ABSTRACT

GONZALES, BRIAN. Energy Differentiating Micro-Computed Tomography System and Energy Axis Reconstruction Algorithms. (Under the direction of Dr. David Lalush).

We developed a novel x-ray micro-computed tomography (μCT) system capable of dense energy-differentiating x-ray measurements using a photon-counting single-pixel detector. This system is presented in detail, with a focus on what is novel about the system. Reconstructed images from this system have high energy axis resolution but suffer an increase in noise resulting from the nature of photon counting. We have developed two methods to suppress the noise along the energy axis, while preserving the increased energy resolution: a Penalized Weighted Least Squares Algorithm (PWLS) for iterative reconstruction along the energy axis, and an Eigenvector Filtering Algorithm (EIGEN) for noise suppression in the energy domain using a set of basis functions. These two algorithms are presented in detail, with a focus on the initial assumptions, rate of convergence, and mathematical relevance of each algorithm. Both algorithms are shown to suppress the noise while preserving energy axis resolution. We present a detailed comparison of the two algorithms, focusing on the noise-energy resolution relationship in both methods: comparing the signal-to-noise ratio (SNR) for both methods. The two methods are also compared to see how each retains key energy-axis information, specifically absorption edges for metallic contrast agents. We investigate combining the two methods forming a hybrid PWLS-Eigenvector method. We show that this hybrid method takes advantage of the best properties of both methods. Once the noise suppression methods have been applied, we demonstrate that the increased energy resolution makes it possible to identify imaged elements based on the specific way each element's attenuation relates to x-ray energy. We show that this

identification allows us to separated two metallic contrast agents imaged at the same time. Using the increased energy resolution, we demonstrate it is possible to accurately estimate the concentration of metallic contrast agents in an imaged object. We demonstrate that increasing the number of energy samples improves the identification of elements based on each element's attenuation-energy relationship, and improves the estimation of concentration of specific metallic contrast agents. This justifies further x-ray energy resolving detector research; accuracy is shown to increase significantly from six to ten energy samples. This work will lead to increased sensitivity in high-resolution molecular-targeted X-ray imaging of biological subjects.

Energy Differentiating Micro-Computed Tomography System and Energy Axis Reconstruction Algorithms

by
Brian Gonzales

A dissertation submitted to the Graduate Faculty of
North Carolina State University
in partial fulfillment of the
requirements for the degree of
Doctor of Philosophy

Biomedical Engineering

Raleigh, North Carolina

2011

APPROVED BY:

_____	_____
Dr. James Brown	Dr. Welsey Snyder
_____	_____
Dr. Otto Zhou	Dr. Mohamed Bourham

_____
Dr. David Lalush
Committee Chair

DEDICATION

To My Mom

BIOGRAPHY

Brian Gonzales obtained his A.A. from Salem Community College, in Carneys Point, New Jersey, in 2001. He obtained his B.S. and M.S. in electrical engineering, with a focus on analog circuit design and signal processing, from Rochester Institute of Technology in Rochester, New York, in 2005. He worked for Harris Communications, R.F. Division, as a radio-frequency design engineer from August, 2005 to July, 2006. In August, 2006 he returned to graduate school at the Joint department of Biomedical Engineering at the University of North Carolina at Chapel Hill and North Carolina State University. His research focuses on medical imaging, specifically x-ray computed tomography. He received his Ph.D. in August 2011.

ACKNOWLEDGEMENTS

No research is done without a network of individuals supporting the researcher. This support is both direct, as collaborating scientists, and indirect, including individuals who help to generate ideas, listen, edit writing and provide an emotional and metal stability throughout the long journey to finish the work. I would like to acknowledge and thank those individuals. First, I would like to thank my advisor, Dr. David Lalush who is partially responsible for many of the novel concepts presented in this dissertation and who was always available with ideas and direction throughout my entire time at N.C. State University and UNC Chapel Hill. I would also like to thank the members of my dissertation committee: Dr. David Lalush, Dr. Mohammed Bourham, Dr. Otto Zhou, Dr. James Brown, and Dr. Wesley Synder. Dr. Mohammed Bourham welcomed me into his lab, Burlington Lab 3113, for the first three years of my work. Dr. Otto Zho provided the carbon nanotube sources for the x-ray system. I would also like to acknowledge Dr. Gouhua Cao, Dr. Ben Moody, Dr. Tuyen Phan, Dr. Michael Altenburg, Dr. Brian Daniel, Sigen Wang, Erin Egan, and Steve Callender. Dr. Gouhua Cao designed the second x-ray source I used and helped me understand, construct, and operate the source. Dr. Ben Moody helped me prepare the contrast agent solutions and helped me with my chemistry throughout my research. Dr. Tuyen Phan helped me develop an understanding of x-ray spectra and x-ray CT concepts. Dr. Michael Altenburg provided the mouse kidneys imaged at the end of the research. Dr. Brian Daniel helped me formulate some of the signal processing ideas in this work. Erin Egan provided the mice imaged in the initial set-up and validation of the x-ray system. Sigen Wang helped me understand how to use the AMPTEK detector to measure the x-ray spectra. Steve Callender help me set-up my

x-ray system in a new lab in Engineering Building III and was consistently helpful when I needed a part for the system.

I would also like to thank all the people who have supported me throughout my research. I would like to thank the members of my Bible study: Dr. Benjamin Redelings, Beth Overman, Bryan and Susana Klingenberg, Casey Letkewitcz, Eric Bulter, Erich and Karli Bain, Emily Ransom, Jared Barnes, Keegan Davenport, and Rebecca and Stewart Thomas. Special thanks to Dr. Benjamin Redelings and Eric Bulter who have consistently listened to me and helped me formulate new ideas. I would like to thank my family: my mom Kathleen Gonzales, who encouraged me to continue my research when I was lonely working by myself long hours in the lab; my brother Kevin Gonzales who also was very encouraging and always listened to me; and my siblings Timothy, John, Elisabeth and Mary who where very supportive and encouraging to me throughout my time at N.C. State. Last I would like to thank my wife, Laura Beth Fitzwater Gonzales, who has edited my entire dissertation, listened to my presentations, helped me formulate new ideas, and consistently encouraged me to persevere as I was finishing my research.

TABLE OF CONTENTS

LIST OF FIGURES

LIST OF TABLES

1. INTRODUCTION

Since X-ray Computed Tomography (CT) was first introduced by Hounsfield in 1973 (Hounsfield, 1973), CT systems have relied on integrating detectors to measure the projected x-rays. These detectors average the incident x-ray spectrum to a single projection value. Early in x-ray CT development, it was shown that most materials could be characterized with only two x-ray energy measurements (Talbert, Brooks, and, Morgenthaler, 1980). Since then, x-ray CT has been limited to either a single integrated projection or two widely separated energy projection measurements. Recently, new integrating x-ray detectors which segment the x-ray spectrum into six energy bins have been developed (Paulus *et. al*, 1998); however, these detectors are still in the initial stages of development and the energy range is only represented by six energy bins. Thus, spectral sampling for x-ray CT is limited to six energy bins or less, and is generally limited to only two energies.

In this dissertation, we present a new x-ray CT system capable of dense spectral sampling; an overview of this system is shown in figure 1.1. In this system, an AMPTEK (Amptek) photon-counting detector is used in place of an integrating detector. This detector is capable of sampling the x-ray spectrum with as many as 1,024 energy bins spaced between 10 and 100keV. However, the detector only has a single detection element. This limits the detector to a one-dimensional (in space) measurement. A single projection ray is defined between the x-ray source and the single detector element. The detector samples the projected x-ray spectrum along this single ray (figure 1.1.A). An object is translated some number of steps through the fixed ray, simulating a strip detector in a parallel beam field, the object is then rotated and translated back through the fixed ray.

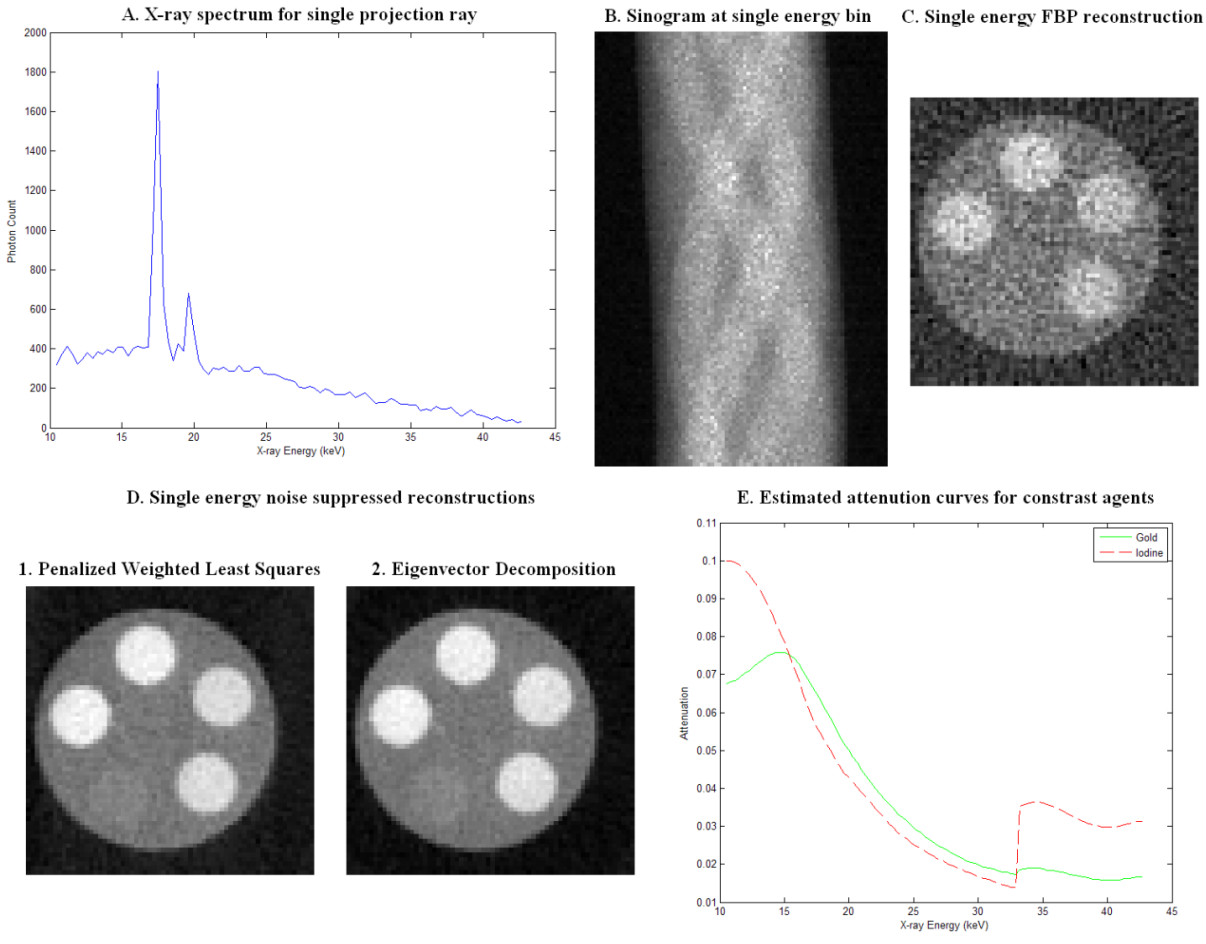

Figure 1.1: System Overview

This builds a sinogram for a single projection ray at a time. This method is similar to the one proposed by Claesoon using a single energy gamma source instead of a polychromatic x-ray source (Claesoon et.al, 2001).

The initial projection data is represented as either an x-ray spectrum for each projection ray in the sinogram (figure 1.1.A) or a sinogram for each energy bin in the sampled x-ray spectrum (figure 1.1.B). Each sinogram is reconstructed using filtered back projection (FBP) to an estimated attenuation map (figure 1.1.C). There will be an attenuation map for each energy bin in the sampled x-ray spectrum. Thus, in this new system, the estimated attenuation is dependent on both x-ray energy and spatial location.

The incident x-ray spectrum is separated into a number of energy bins. The total x-ray flux is divided among all of these bins. Each energy bin will have significantly less x-ray flux than a single integrated measurement. As the number of energy bins increases, the total flux in each bin decreases. Decreasing the x-ray flux increases the noise in each energy bin. Therefore, as the energy axis resolution increases the noise along the energy axis also increases. To suppress this noise, while preserving the energy axis resolution, two noise suppression algorithms were developed: a penalized weighted least squares (PWLS) iterative reconstruction algorithm (Gonzales and Lalush, 2011) and an eigenvector decomposition post reconstruction filtering algorithm (Gonzales and Lalush, 2010). Both of these methods suppress the noise along the energy axis rather than in space. The FBP reconstruction of a single energy bin (figure 1.1.C) has a large amount of noise. This noise is the photon counting noise that the two noise suppression algorithms have been developed to reduce. Suppressing the noise along the energy axis will also reduce the noise distributed in the attenuation maps with no loss in spatial resolution (figure 1.1.D).

The complete x-ray spectrum is sampled for each projection ray. This means that instead of estimating the attenuation in space (figures 1.1.C-D), it is possible to estimate the attenuation as a function of energy for a specific location in space (figure 1.1.E); we call this an attenuation curve. The attenuation curves for elements with atomic numbers 1-93 and selected biological compounds are listed in the National Institute of Standards and Technology (NIST) database (Hubbell, 1996). The shape of each curve is dependent on the element; so the estimated attenuation curves can be used to identify the materials at the specific location in space. Two estimated attenuation curves, from an experiment imaging both gold and iodine contrast agents, are shown in figure 1.1.E. One of these curves is clearly

iodine and the other is clearly gold. The iodine is identified by the absorption edge at 33keV. The gold is identified by the increase in attenuation in the energy region corresponding to three gold absorption edges at: 12keV, 13.9keV, and 14.4keV. Using dense spectral sampling it is possible to differentiate between two contrast agents in the same imaged object. However, the noise along the energy axis distorts the attenuation curves, preventing them from being used to identify materials. This noise must be suppressed while underlying shape of the attenuation curves is preserved. Both noise suppression algorithms suppress noise along the energy axis while preserving energy resolution, specifically the shape and existence of absorption edges.

In this dissertation, we present both noise suppression algorithms in detail. The PWLS uses a penalty which drives neighborhoods along the energy axis to an average attenuation curve. The Eigenvector decomposition method uses known attenuation curves from the NIST database to form a set of orthogonal basis functions separating the signal and noise along the energy axis. These two methods are compared for accuracy, final signal to noise ratio (SNR), speed, and conceptual complexity. The PWLS is conceptually simpler and has better SNR, but it takes longer and has a hard time with absorption edges. The Eigenvector method is faster and preserves absorption edges, but has a worse SNR and takes longer. The combination of both methods is dependent on which is done first: PWLS then Eigenvector combines the best of both, but Eigenvector then PWLS combines the worst of both.

The estimated attenuation curves can be used to identify some material at a specified location once the noise has been suppressed based on the shape of the curves. Using the shape of the attenuation curve rather than the intensity of attenuation to identify materials in

the imaged object means the intensity can be used to identify the concentration of a material at a specified location. Changing the concentration will increase or decrease the average intensity of the curve, shifting the curve up or down, but not changing the overall shape. A number of experiments are presented with different concentrations of either gold or iodine imaged in a single phantom to quantify the affect of concentration on the attenuation curve. This means the dense spectral CT system we present can both identify multiple contrast agents and estimate their concentration in an imaged object. We show that as the energy resolution increase, this identification and estimation becomes more accurate

The majority of the experiments use a technical phantom. To investigate the dense spectral sampling on a more realistic object, a fixed mouse kidney is imaged as the final experiment presented in this dissertation. Gold nanoparticles were injected into the mouse immediately after it was sacrificed; we able to identify some of this gold in the kidney. The spectral CT is compared with an integrated single energy CT, which is unable to identify the gold. This demonstrates the new system's improvement in identifying small concentrations of contrast agents.

In this dissertation we present an energy-sensitive microCT system capable of dense spectral sampling with close to 100 energy bins. This system is not practical, due to use of a single-element detector. As energy resolving detector research continues, an energy-sensitive CT system will become practical. Our system demonstrates the usefulness and importance of developing these systems. We demonstrate that an energy-sensitive CT can reconstruct the sampled attenuation as a spatial distribution of attenuation curves and uses those curves to identify specific materials. These curves can be used to separate two contrast agents, which is not possible with typical CT. This means that multiple organ systems can be imaged

simultaneously. The curves can also be used to separate soft tissues. This might be particularly useful in mammography, using the differences between ducts and cancer attenuation curves to more accurately cancerous tissues. The curves are also used to identify specific concentrations of contrast agents in solution in the imaged object. Gold nanoparticles used for molecular-targeting and the attenuation curves can be used to identify the concentration of those molecules based on the concentration of gold. This will expand the use of contrast agents from simply improving soft-tissue contrast to be used for high-resolution molecular-targeted X-ray imaging of biological subjects.

1.1. References

AMPTEK detector XR-100CT, product information available at: http://www.amptek.com/xr100cr.html

Claesson T., Kerek A., Molnar J. and Novak D., 2001, "A CT demonstrator based on a CZT solid state detector," in IEEE Nuclear Science Symposium Conference Record, vol. 3, pp. 1644-1646.

Hounsfield G.N., 1973, "Computerized transverse axial scanning (tomography).1. description of system," British Journal of Radiology, vol. 46, pp. 1016-1022.

Hubbell J.H. and Seltzer S.M., 1996, Tables of X-Ray Mass Attenuation Coefficients and Mass Energy-Absorption Coefficients from 1 keVto 20 MeV for Elements Z = 1 to 92 and 48 Additional Substances of Dosimetric Interest, National Institute of Standards and Technology, Tech. Rep. 43NANB412756 Available: http://www.physics.nist.gov/PhysRefData/XrayMassCoef/cover.html

Gonzales B. and Lalush D., 2011, "Full-Spectrum CT Reconstruction Using a Weighted Least Squares Algorithm with an Energy-axis Penalty," *IEEE Trans. Med. Imag*., vol. 30, pp. 173-183.

Gonzales B. and Lalush D., 2010 "Performance of Reconstruction and Processing Techniques for Dense Full-Spectrum X-ray Ct," *Proceedings of the 2010 IEEE Nuclear Science Symposium and Medical Imaging Conference*, Knoxville, TN, M09-131.

Paulus M., Sari-Sarraf H., Gleason S., Behel J., Thompson L. and Allen W., 1998, "A new X-ray computed tomography system for laboratory mouse imaging," IEEE Trans. Nuclear Science, vol. 2, pp. 1259-1263.

Talbert A.J., Brooks R.A., and Morgenthaler D.G., 1980, "Optimum energies for dual-energy computed tomography," Phys. Med. Biol., Vol. 25, No. 2, pp. 261-269.

2. BACKGROUND

X-rays are electromagnetic radiation with frequency above $3X10^{16}$Hz, wavelengths below 10nm, and quantum energies above 124eV (Kane, 2003). This radiation is modeled as both a wave with some specific wavelength and magnitude and as a number of particles with some quantum energy. The Planck relation: $E = h \cdot v$ describes this relationship, where $h = 4.135 \times 10^{-15} eV \cdot s$ is a physical constant expressing the correlation between energy E and wavelength v (Burkhardt and Leventhal, 2008). X-rays exist naturally and are emitted by objects such as stars and planets across a range of wavelengths; by observing these signals, scientists study the stars or planets emitting them. The distribution of x-ray magnitude with respect to the wavelength is dependent on the elemental composition of these objects, allowing scientists to study their composition (Grande, Dunkin, and Kellett, 2001). The distribution of x-ray magnitude with respect to wavelength is also used for chemical analysis when imaging the physical constitution of different molecules; this is called x-ray photoelectron spectroscopy (Agarwal, 1991). X-ray radiation is most commonly associated with medical imaging; common uses include: chest scans, broken bone scans, dental scans, and full body computed tomography CT scans. These applications typically use sources which emit x-rays as spectrum of multiple wavelengths, but the measurement is typically averaged to a single wavelength. Including multiple wavelength information in medical scans could increase information about elemental composition of the tissue; similar to the way the distribution of x-ray magnitude with respect to wavelength is used for astronomy or spectroscopy.

In this chapter, we discuss how x-rays are produced for medical imaging and the corresponding x-ray spectrum produced by these sources. We then describe how this

spectrum is attenuated by different materials; defining the continuous spectrum to be related to a specific material via an attenuation curve. This spectrum has historically been sampled using integrating detectors, discussed in this chapter; however, new energy-discriminating detectors are becoming available and are introduced in this chapter. We then discuss how the data from these detectors, collected as computed tomography (CT) data, is reconstructed to form an estimate of the attenuation using via filtered-back projection (FBP) and other statistical and iterative reconstruction methods. We also discuss how these methods are expanded to incorporate energy-discriminated data; first as only two energies, dual-energy CT (DECT), then more than two energies. We finish the discussion with an introduction of two more concepts: carbon-nanotube sources and contrast enhancement agents, both of which are significant to the novel concepts proposed in this dissertation.

2.1.1. X-ray Production for Medical Imaging

X-rays were first discovered by Roentgen as he experimented with early vacuum tubes. Roentgen realized he could create an image of the bones in his wife's hand by passing the radiation produced by the tube through the hand and collecting the radiation on film (Roentgen, 1913). Using x-ray radiation, produced in vacuum tubes, to image bone or other dense tissue is the bias for much of modern medical imaging. To create a sufficient x-ray flux for these images, x-rays are produced by accelerating free electrons in a vacuum through a strong electric field into some metal. The free electrons are typically produced by passing a current through a tungsten filament. The current causes the filament to heat; the heat causes the electrons to escape the tungsten atoms into the vacuum (Lee, 1993), called thermoemission. These electrons are accelerated through an electric field into a target metal. It is the interaction of the free electrons with the metal's atoms which creates x-rays. A large

voltage, in the tens of kilovolt range, is applied to the metal, which becomes the anode of the system. The filament is grounded with respect to the anode and becomes the cathode. The voltage potential between these two creates the electric field through which the electrons are accelerated. The electrons acquire an energy equivalent to the anode voltage upon reaching the metal (Webb, 1996). Vacuum tubes are used for the most medical imaging applications (Eichmeier and Thumm, 2008); however, experimental systems often use a vacuum chamber which can be open and closed repeatedly (Chambers, Fitch, and Halliday, 1998,). X-rays exit the vacuum tube or chamber through a window, typically coated with beryllium to remove low energy x-rays (Rogers, 1947).

2.1.2. X-ray Spectrum

The x-rays exciting the vacuum tube or chamber exist over a range of wavelengths or energies. These are defined by the type of x-ray radiation produced. The free electrons interacting with the metal's atoms create two types of x-ray radiation: fluorescence radiation and Bremsstrahlung radiation (Hyper Physics, 2007). The electrons have the energy acquired passing through the electric field. As they pass through the metal, some of the electrons will collide with the metal's orbiting electrons. If the free electron's energy is greater than the valence energy of the orbiting electron, it will knock the orbiting electron out of its shell creating an empty shell in the atom. An electron orbiting in a higher shell will drop to fill the empty spot, radiating the difference in valence energies as x-ray radiation. This radiation will be at a very specific energy which is the difference in the valence energy between the shells. This is fluorescence radiation, also called characteristic radiation because the x-ray radiation produced is specific to the difference in shell energies. The difference in shell energies will be dependent on the distribution of orbits based on the specific metal atom. This means that

the radiation is also specific to each metal and can be used to identify which metal has been used as the anode metal. This radiation is a form of x-ray radiation used in astronomy (Grande, Dunkin, and Kellett, 2001).

The free electrons that pass through the metal without hitting any orbiting electrons are still affected by the atom's electro-magnetic field. This field will cause the electrons to change their path and lose energy. This energy can be emitted as x-rays. The energy of this radiation will vary from almost nothing to the maximum possible energy, which is the energy of electric field applied between the anode and cathode of the x-ray system, called Bremsstrahlung radiation.

The two forms of x-ray radiation combine to form a continuous x-ray spectrum; this spectrum is the relation between the intensity of the x-rays, or x-ray flux, with the x-ray energy. An example of an x-ray spectrum is shown below in figure 2.1.

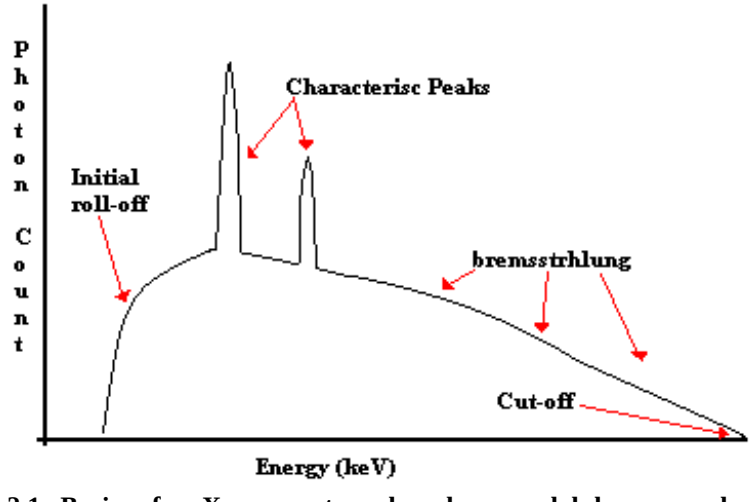

Figure 2.1. Basics of an X-ray spectrum based on a molybdenum anode.

The x-ray spectrum has a continuous triangular shape defined by the Bremsstrahlung radiation. The cut-off point is the voltage applied to the anode; the maximum energy can only be the energy applied to the system. The characteristic peaks are the result of the

fluorescence radiation, in this case characteristic to molybdenum. The initial roll-off is the result of the low energy x-rays that do not escape the vacuum chamber. Figure 2.1 labels the shape of the spectrum as photon counts for each energy; the x-axis could also be labeled more generally as intensity. This overall intensity is dependent on the x-ray flux generated by the source. This flux is dependent on the number of free electrons. Thus it is proportional to the current through the tungsten filament; i.e. the total x-ray flux is proportional to the current.

2.1.3. X-ray Attenuation

As x-rays pass through some material or mixture of materials, the incident x-ray beam I_0 is attenuated to a detected x-ray beam Y. The detected beam Y is dependent on the linear attenuation coefficient of the material μ and the thickness of the material l. The relationship between the incident beam, the detected beam, the linear attenuation, and thickness is defined as:

$$Y = I_0 e^{-l \cdot \mu} \tag{2.1}$$

This relationship defines change in the x-ray intensity through a thickness l of some material. If a single material is used, the thickness l can be varied to investigate the effect of different thickness of that material on the detected x-ray intensity Y. This is for only a single material. The model of attenuation for multiple materials is:

$$l \cdot \mu = l_1 \cdot \mu_1 + l_2 \cdot \mu_2 + \cdots + l_n \cdot \mu_n \tag{2.2}$$

This models the linear attenuation coefficient as the weighted sum of the individual attenuation coefficients along the path. The expression for attenuation (2.1) is modified using the mixture (2.2) to form:

$$Y = I_0 e^{-\sum_i l_i \cdot \mu_i} \quad \textbf{(2.3)}$$

where the same x-ray intensities are again expressed as I_0 for the un-attenuated incident intensity and Y for the measured intensity. The attenuation is now the sum of all the attenuations along the path l, as defined in (2.2). Each will contribute to the total attenuation based on the thickness of each material l_i along the path.

The fundamental equation for relating x-ray attenuation to intensity, expression (2.1), defines the linear attenuation in terms of an incident and exiting x-ray intensity, I_0 and Y respectively. This indicates that linear attenuation is the amount of the x-ray beam that gets absorbed by the object along a path l through the object, in reality, with both absorption and scattering contributing to the linear attenuation coefficient.

2.1.4. X-ray Attenuation Curves

The linear attenuation coefficient μ, for some element, is a function of photoelectric absorption, scattering, and the mass of the material (Christ G., 1984). The mass of the material, also referred to as density and labeled as ρ, is the amount of the element per unit volume. This is affected by the physical state of the element, i.e. a gas is less dense than a solid for the same material, and amount of the material in solution with other materials. This value is dependent on the specific element and is independent of x-ray energy. A mass attenuation coefficient $\frac{\mu}{\rho}$ is defined as the energy-dependent portion of the linear attenuation coefficient with the density term removed. Thus, the mass attenuation relates an elemen's attenuation to x-ray energy based on the nature of the element rather than the amount of element present. Therefore, the mass attenuation is a function of photoelectric absorption and scattering.

Photoelectric absorption is the absorption of x-ray photons by the element's electrons. The x-rays collide with orbiting electrons and knock the electrons out of their shells. To interact with the electrons, the x-rays must have as much or more energy than the valence energy of the electrons. Thus, each element will have a unique photoelectric absorption, relating the atomic number to the x-ray energy (Chantler, 2000). A larger atomic number means more protons and electrons in the atom, and consequently larger photoelectric absorption. The absorption changes with energy, as the x-ray energy increases there is a general pattern of decreasing absorption broken with sudden sharp increases. The increases are labeled absorption edges (Chantler, 2000) and correspond to the energy distribution of the valence electrons. As the x-ray energy increases, it will reach energies equal to these electrons and more x-rays will be absorbed. For lower energies and materials with a large atomic number, the photoelectric effect dominates the attenuation coefficient (Reddy *et. al.*, 1976).

There are two types of scattering: Compton and Rayleigh. Compton scattering happens when an incident x-ray loses a portion of its energy to the atom and is scattered away from its path. By definition the x-ray beam intensities I_0 and Y correspond to a narrow beam through the object. If the x-ray is scattered away from the beam it no longer contributes to the output intensity Y of the beam; even if it is not scattered completely away from the beam it loses energy and may fall out of the energy range being measured. Each element will have a unique atomic cross section for Compton scatter depending mostly on the electron distribution and Coulomb field and is defined by the Klein-Nishina formula (Kirby *et. al*, 2003)

Rayleigh scattering is often included in the different atomic cross sections, but most of the time it is added to the Compton scatter and the two types of scatter are labeled as Compton scattering and left with a single atomic cross section (Reddy *et. al.*, 1976; Hubbell and Seltzer, 1996, Kirby *et. al.*, 2003). Electron pair production could also be included in the model of attenuation, but it happens at higher energies outside x-ray range (Hubbell and Seltzer, 1996) so it is not necessary to include in any model for x-ray attenuation.

The National Institute of Standards and Technology (NIST) have a database (Hubbell and Seltzer 1996) which catalogs the attenuation coefficient for elements with atomic numbers one to ninety-three and some biological compounds. This database defines attenuation coefficient in terms of the mass-attenuation as:

$$\frac{\mu}{\rho} = \frac{\sigma_{pe} + \sigma_{coh} + \sigma_{incoh}}{u \cdot A} \qquad (\mathbf{2.4})$$

Equation (2.4) is expanded into a definition of the linear attenuation coefficient as a function of energy as:

$$\mu(E) = \left(\sigma_{pe}(E) + \sigma_{coh}(E) + \sigma_{incoh}(E)\right) \cdot \frac{\rho}{u \cdot A} \qquad (\mathbf{2.5})$$

In equation (2.5) σ_{pe} is the photoelectric cross section, σ_{coh} is the coherent or Rayleigh scattering cross section, σ_{incoh} is the incoherent or Compton scattering cross section (each of these cross sections is also a function of the x-ray energy E), $u = 1.66054 \cdot 10^{-24}\ g$ is the atomic mass unit, A is the relative atomic mass of the desired element, and ρ which has units of g/cm, is the density or mass of the material.

The attenuation coefficient in expression (2.5) is a function of x-ray energy. This is a continuous function which is defined as an "*Attenuation Curve*". An attenuation curve is defined as the continuous relationship of the attenuation coefficient and x-ray energy. As the

x-ray energy increases, the scattering cross sections σ_{coh} and σ_{incoh} get smaller because increased energy is the same as decreasing wavelength. This means the curves descend with respect to energy except at absorption edges. Absorption edges are the result of the photoelectric cross section σ_{pe}. Several examples of an attenuation curve are shown below in figure 2.2.

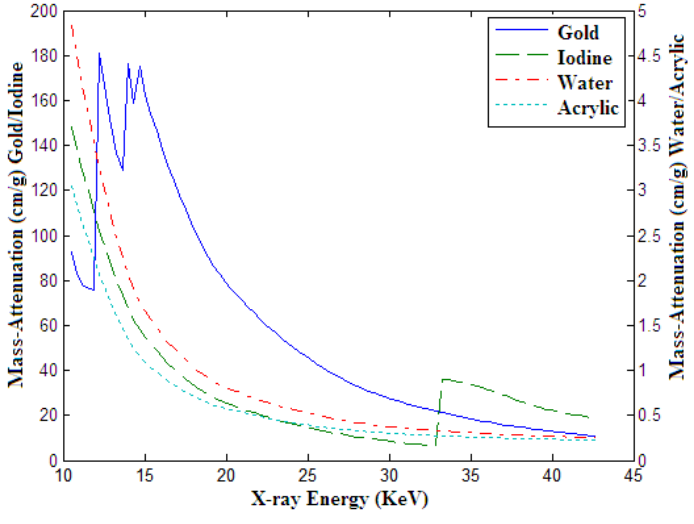

Figure 2.2: Mass attenuation coefficient as a function of energy.

Figure 2.2 demonstrates four different mass-attenuation curves from the NIST attenuation database (Hubbell and Seltzer, 1996). These are graphed on separate axes because of the significant difference in attenuation values. Iodine and gold have much larger mass-attenuation values within the specified energy range than water and acrylic. The values are expressed with units of cm^2/g. The mass or density of the material ρ has units of g/cm^3 or g/ml. The linear attenuation coefficient is found by multiplying the density with the mass attenuation. The linear attenuation coefficient μ has units of inverse centimeters (cm^{-1}) or attenuation per centimeter. The linear attenuation coefficient μ times the distance l in expression (2.1) yields a unit-less value which modifies the incident x-ray spectrum I_0.

2.2. X-ray Imaging

X-ray images are generated as the x-ray intensity through an object, designated as Y in eq. 2.1. This intensity will vary depending on the path l from the source to the detector through the object. Computed tomography (CT) images are reconstructed from multiple x-ray images.

2.2.1.1. X-ray Detectors (Integrating Detectors)

Basic x-ray imaging is called projection imaging. X-rays pass through an object projecting the image of the object onto a detector. X-ray analog detectors use a screen which converts the x-ray photons into light photons which are then imaged on film (Hunger *et. al.*, 1992). Analog detectors are used for chest x-rays, dental x-rays, and other simple projection x-rays. Digital flat panel detectors are now replacing analog screen-film detectors (Kump and Shi, 1999; Nikl, 2006; Kalendar and Kyriakou, 2007). These detectors convert x-ray photons into light using a scintillator and then measure the intensity of the light using a photodiode array (Nikl, 2006). This is basically a digital camera with a scintillator layer to convert the x-rays to visible light.

Both the film and the digital detectors are integrating detectors. A single intensity value is assigned to the entire incident x-ray spectrum. This intensity value is a weighted sum of the incident x-ray spectrum. Both screen-film and integrating detector need to convert the x-ray photons to light photons (Kump and Shi, 1999). When this happens the x-ray spectrum is reduced to a single light intensity level rather than a spectrum of photon counts at different energies (Kalendar and Kyriakou, 2007).

2.2.1.2. X-ray Detectors (Photon-Counting Detectors)

Recently there has been an increased interest in creating photon counting detectors for medical imaging applications using cadmium zinc telluride (CdZnTe) or cadmium telluride CdTe detectors (Szeles, 2004). A small bias voltage is maintained across the CdTe or CdZnTe detector element. Each incident x-ray photon will be absorbed by the element and produce a current proportional to the photon's energy. Thus, each photon can be counted and the energy of the photon measured (Szeles, 2004). By counting the incident x-rays one photon at a time and assigning each an estimated energy, the entire incident x-ray spectrum (figure 2.1) can be measured (Matsumoto, 2002).

These detectors are commonly limited to a single detector element. This makes it challenging to do medical imaging, especially computed tomography (CT) (Giakos *et. al.*, 1998). These detectors have been used to characterize CT systems, characterizing the current and temperature of the x-ray source over time (Ricq, Glasser, and Garcin, 2001). The detectors have also been used to compare x-ray flux to photon counts and noise for medical imaging (Brunner and Clemens *et. al.*, 2009). Both of these applications use the detector to study the x-ray system which will be used with a normal flat panel integrating detector for medical imaging. For medical imaging, these detectors are commonly used with a standard detector to enhance the integrating detector's measurements. These detectors have also been used a single element photon counting detector to measure the noise power spectra, MTF, and DOF for mammography measurements and to investigate the energy response of the tissues in mammography (Lundqvist *et. al.*, 2003).

To acquire multiple-energy data which can be used for medical imaging, hybrid systems have been proposed which combine photon-counting detectors with digital detectors

(Goldan, Karim and Reznik, 2008; Brunner and Khoury *et. al.*, 2009). This work has been focused on the detectors, investigating the noise, frequency, and power responses of the new detectors. The goal is to be able to acquire medical images while increasing the x-ray energy information. These are not true photon-counting detectors for CT or medical applications, but represent a step in that direction.

2.2.2. X-ray Computed Tomography

X-ray detectors measure the distribution of x-ray intensity (designated as Y), over the detector surface. The distribution of x-ray intensity Y is related to the linear attenuation coefficient μ through expression (2.1). Moving the attenuation μ from the exponent by using the natural logarithm log and rearranging expression (2.1) leads to:

$$l \cdot \mu = log(I_0) - log(Y) \quad \textbf{(2.6)}$$

In the ideal case, (i.e. noiseless), the projected attenuation should equal the total attenuation along the projection path expression (2.2). Thus, the ideal projected attenuation measured at the detector is the sum of all the attenuation values along the line from the x-ray source to the detector. This is called an x-ray projection; all attenuation along the line l is projected to a single value, the line l is also called the projection ray. The spatial distribution of the projected attenuation is dependent on the distribution of the measured x-ray intensity. In the case of a single pixel detector, Y is a single element and μ is a single value where the projection ray l is a single line connecting the x-ray source to that point. In the case of a flat panel detector, Y is a plane and μ is a matrix corresponding a collection of projection rays connecting the x-ray source to each detector element.

The summing of all attenuation along the projection ray means that it is impossible to tell how the materials are distributed along the projection ray. For example, consider an x-ray projection image of a broken bone: the physician can tell if the bone is broken by looking at the spatial distribution of attenuation in the image; however, the physician can't see the damaged tissue around the broken bone because the attenuation of the tissue is added to the bone along the projection rays. To estimate the distribution of the materials along the projection rays, multiple projections are required. This is the foundation of x-ray computed tomography (CT) (Hounsfield, 1979), where multiple x-ray projections are acquired with different source detector orientations to estimate the distribution of the materials in three dimensions. First proposed by Hounsfield, CT has become one of the most commonly used medical imaging modalities (Gonzalez *et. al.*, 2009).

X-ray CT builds three-dimensional estimated attenuation maps from a set of x-ray projections taken with different source-detector-object orientations around some imaged object. An attenuation map is the spatial distribution of attenuation corresponding to a slice through the imaged object. The distribution of attenuation within the slice will correspond to the distribution of materials in the slice. The most intuitive way to describe CT is in a parallel beam field; where all the projection rays for a single projection are parallel and have equal initial intensity. Figure 2.3.A demonstrates a parallel beam field with a strip detector. The source detector orientation changes by rotating the source and detector; thus, the projection rays are rotated, passing through a different combination of materials for each angle of rotation. The projected attenuation for each angle (figure 2.3.B and eq. 2.6) is projected back along the projection rays (figure 2.3.C) to estimate the spatial distribution of attenuation, which is called an attenuation map. As the number of projection angles increases, the

different attenuation measurements will overlap according to the distribution of the materials in the object. The projection angles must span 180° to be complete a tomographic span; after 180° projection rays will begin repeating combinations of materials, in reverse order, so no new information is acquired. This concept of projection along rays with a number of different angles covering a span of 180° and then back-projecting along the same rays to estimate the attenuation map, is the basis for CT imaging; this is not dependent on the source-detector geometry, it works for multiple geometries, including but not limited to parallel beam (Kak and Slaney, 1989).

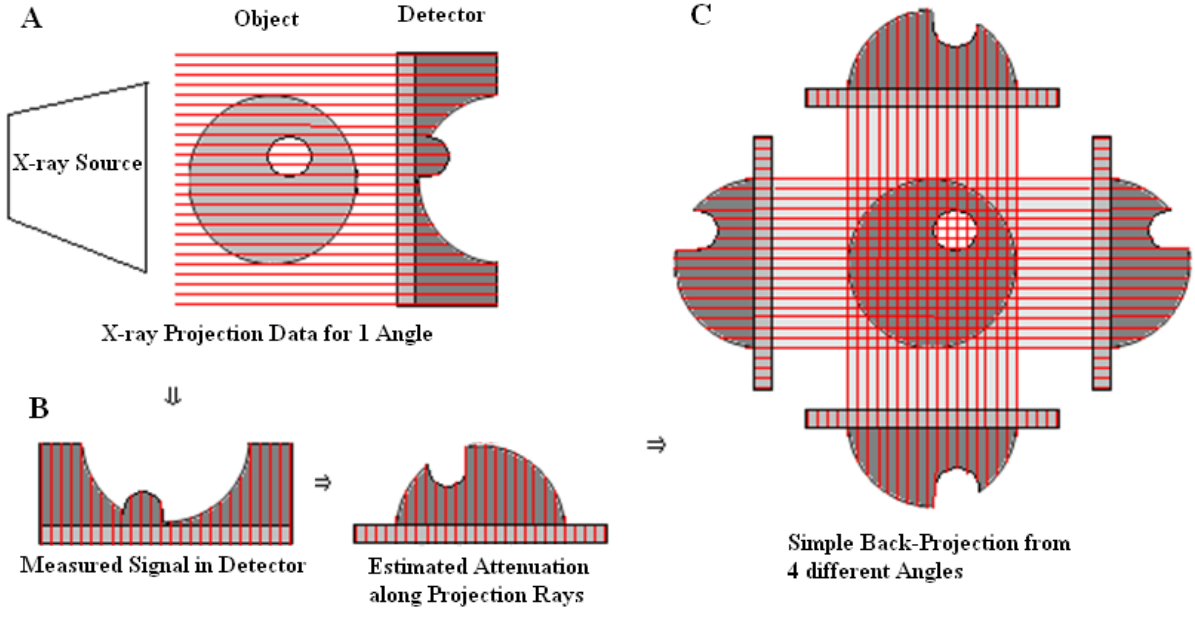

Figure 2.3: Basics of X-ray projection and back-projection for CT. A. is x-ray projection of a circular object with circular hole in a parallel beam field. B. is the acquired projection and corresponding estimate attenuation. C. is back-projection of estimate attenuation from 4 different angles spanning 360°.

X-ray projections are transformed from the spatial to frequency domain to make back-projection mathematically simpler. The Fourier transform of a single angle along the whole strip detector in a parallel beam projection is a sampling a slice through two-dimensional frequency corresponding to the angle of projection (Kak and Slaney, 1989). As

the number of projection angles increases this frequency space is filled. A full 180° scan fills the two-dimensional frequency space. Taking an inverse Fourier transform of this two-dimensional frequency space creates an estimate of the two-dimensional space corresponding to a slice through the imaged object (figure 2.3.C).

The Fourier transform of each of the projection line will cross the zero frequency point. This means there is an overlap at the DC frequency. The density of information in frequency is dependent on the number of projections acquired; as more projection angles are measured between 0 and 180° the frequency space is more densely sampled and estimated spatial distribution, the inverse Fourier transform of frequency space, is more accurate. A filter is imposed on the projection data in the frequency domain. Typically this is a ramp filter with zero at DC and increasing as frequency increases. This removes the common DC term and emphasizes higher frequencies (Ramachandarn and Lakshminarayanan, 1971). The process of converting the projections to the frequency domain, applying a filter to remove the DC term and emphasize high-frequencies, arranging all projections according to angle in two-dimensional frequency space, and taking the inverse Fourier transform of that two-dimensional frequency space to get an estimate of the attenuation map is called filtered-back-projection (FBP) (Brooks and DiChiro, 1975). The filter part is the ramp filter applied in frequency domain of each projection; the back-projection is the arranging of each projection in frequency space and inverse Fourier transform of the two-dimensional frequency space.

The FBP outlined is for a parallel beam field. To generate a true parallel beam field, the x-ray source would need to have the same dimensions as the detector. This is not practicable because it requires either a very large x-ray source or a very small detector; both limit the functionality of a CT system. Actual x-ray sources are more accurately modeled as

point sources. If the same sort of strip detector used for the parallel beam field (figure 2.3) is used, the x-ray projection rays fan out from the point source to the detector elements. This is called fan-beam projection. FBP is used for fan-beam projection, but the change in the geometry from parallel beams to fan beams has to be taken into account. This will change how the angles of projection relate to the frequency space; the back-projection has to be done along fan lines rather than parallel lines (Kak and Slaney, 1989). If instead of a strip detector a flat panel detector is used, the projection rays will fan out as a cone. This is called cone-beam CT. The cone geometry is more complicated than either the fan or parallel beam. So a faster approximation is made using fan-beam properties to speed up the FBP; this approximation is called the Feldkamp algorithm and is a fast and accurate approximation for cone-beam back-projection (Feldkamp *et. al*, 1984).

2.2.3. Statistical Reconstruction Algorithms

Iterative reconstruction methods are also used to reconstruct the estimated spatial distribution of attenuation for x-ray CT. Iterative reconstruction methods follow a four-step processes starting with some initial estimate of the attenuation map. First, the initial estimate is projected using the x-ray projection. The estimated projection is compared with the measured x-ray projection, creating some measure of error. This error is back-projected to form a reconstruction of the error. The error reconstruction is then used to update the initial estimate of the reconstruction. This whole process is then repeated until the process converges on a final estimate of the attenuation map, until the user designates a stop, or for a set number of iterations.

Iterative reconstruction algorithms produce attenuation map estimates which are based on measured x-ray projection data which are inconsistent due to noise in the projection

measurements. Statistical reconstruction algorithms use the same process as iterative reconstruction methods, changing the process by introducing a criterion to decide which are the optimal solutions. The choices of criterion used for x-ray CT include: maximum likelihood (ML), weighted least squares (WLS), and maximum a posteriori (MAP).

To select the appropriate criterion, a model of the noise in the x-ray projections is required. The noise is the result of the random nature of the x-ray projection and x-ray detection. The projections are commonly modeled as a Poisson random process starting from the model of x-ray attenuation expressed in equations (2.1) and (2.2). To define a Poisson random variable, the expectation of the measured x-ray signal is:

$$Y_i = I_{0i} e^{-\sum_j l_{ij} \mu_j^{true}} = E[Y_i] \quad \textbf{(2.7)}$$

The expected value $E[Y_i]$ is used as the mean for the Poisson distribution. The mean is simply the projection of the true attenuation distribution μ_j^{true}. This means that the mean is the actual signal in a noiseless system. Equation (2.7) is expressed with an i index to indicate the specific projection ray and index j to indicate the specific reconstructed pixel or voxel. Thus, the element l_{ij} relates the contribution of the pixel j to the i^{th} projection ray. This means the expression (2.7) can apply to any geometry. This Poisson model is for a single wavelength, μ_j^{true}, is considered independent of energy. A compound Poisson model (Elbakri, 2003) can also be used to account for the polychromatic nature of the emitted x-ray spectrum. This model is typically used to account for noise due to an integration of the x-ray spectrum.

The Poisson model has the same mean and variance $E[Y_i]$, this model can be approximated with a Gaussian using the same mean and variance $E[Y_i]$. Poisson estimation

leads to a maximum likelihood (ML) criterion, Gaussian estimation could also be used for a ML criterion because it is an approximation of the Poisson. However, a Gaussian model in general leads to a weighted least-squares (WLS) criterion. The MAP criterion can use either estimation for the noise and is different in the inclusion of prior knowledge to select optimal solution.

The maximum likelihood (ML) criterion can be solved using an expectation maximization (EM) algorithm; this was first proposed for emission tomography (Lange and Carson, 1984). ML-EM works well for tomographic reconstructions, but it takes a long time and many iterations to arrive at a final solution. To speed up the convergence of the algorithm, ordered-subsets are commonly used. This was first introduced for emission tomography ML (Hudson and Larkin, 1994). Ordered subsets (OS) break up the measured projections into a number of ordered subsets; the iterative step is performed for one of the subsets at time. Once all subsets have been included, the algorithm is considered to have finished a complete iteration. However, each subset iteration brings the estimate closer to a final solution, speeding up the entire algorithm. This can also be done by breaking the projection space into blocks, similar to subsets (Lalush and Tsui, 2000). Each block is then reconstructed in order to form a complete iteration. This is expressed in the following equation from (Lalush and Tsui, 2000):

$$\mu_j^{new} = \mu_j^{old} + t \cdot \mu_j^{old} \left(\frac{\sum_{i \in S_n} l_{ij} \left(I_{0i} e^{-\sum_j l_{ij} \mu_j^{old}} - Y_i \right)}{\sum_{i \in S_n} l_{ij} \left(\sum_j l_{ij} \mu_j^{old} \right) I_{0i} e^{-\sum_j l_{ij} \mu_j^{old}}} \right) \quad \textbf{(2.8)}$$

The new attenuation map is μ_j^{new} the old attenuation map μ_j^{old} updated by a gradient, the expression in the parenthesis, multiplied by a step size t and the old attenuation map. The

gradient is defined as the back-projection $\sum_{i\epsilon S_n} l_{ij}$ over the n^{th} subset S_n of projections lines of the difference between the projection of the old attenuation map $I_{0i}e^{-\sum_j l_{ij}\mu_j^{old}}$ and the measured x-ray projections Y_i over a the back-projection of just the attenuation term $\sum_j l_{ij}\,\mu_j^{old}$ multiplied the projection of the old attenuation map. The total number of projections are broken into N ordered subsets S. The gradient term is only applied to single set of these subsets S_n for each iteration, speeding up the time it takes to calculate the gradient. The numerator term of the gradient is the back-projection of the error; the error is the difference between the projected attenuation estimate and the x-ray projections. The denominator is a normalization term weighting the gradient by the old attenuation estimate.

For a Gaussian model of the noise, a weighted least-squares (WLS) criterion is optimal. WLS is commonly done with MAP by adding a penalty to the WLS based on some prior knowledge. This process is called penalized weighted least-squares (PWLS) (Wang et. al, 2006; Anderson et. al, 2005; Fessler et. al, 1997).

The WLS criterion applies a least-squares form to the Gaussian model of the x-ray projection data. The criterion typically leads to an objective function similar to:

$$\varphi(\hat{\mu}_{est}) = (l \cdot \mu - [L\hat{\mu}_{est}]_i)^T Y_i (l \cdot \mu - [L\hat{\mu}_{est}]_i) - \beta \cdot T(\hat{\mu}_{est}) \qquad \textbf{(2.9)}$$

In this objective function $\varphi(\hat{\mu}_{est})$ represents the PWLS minimized to solve for an estimate of the attenuation$\hat{\mu}_{est}$. This is the difference between the measured log corrected projections $l \cdot \mu$ (expression 2.6) and the projection of the estimated attenuation $[L\hat{\mu}_{est}]_i$ squared, this is the least squares portion. The L is a matrix with elements of length l_{ij}, $[L\hat{\mu}_{est}]_i$ is another way of expressing $\sum_j l_{ij}\mu_j$. The weight is the measured projection Y_i. A penalty is added with some weight β and some penalty function T$(\hat{\mu}_{est})$ which is some function of the estimated

attenuation. This is a basic objective function which is minimized using a variety of different methods.

One example of a PWLS algorithm is proposed by Elbakri and Fessler to solve for a single energy x-ray CT scan (Elbakri and Fessler, 2002). This algorithm is:

$$\hat{\mu}_j = \left[\hat{\mu}_j - \frac{N \sum_{i \in S_n} l_{ij} Y_i \cdot \left([L\hat{\mu}]_i - \frac{log(I_0)}{log(Y_i)} \right) + \beta \frac{\partial \mathrm{T}(\hat{\mu}_{est})}{\partial \mu_j}}{\sum_i \frac{l_{ij}^2 Y_i}{l_{ij}} + \beta \frac{\partial^2 \mathrm{T}(\hat{\mu}_{est})}{\partial \mu_j^2}} \right] \qquad (\mathbf{2.10})$$

The numerator in the expression is the first derivative of the PWLS objective function and the denominator is the second derivative of the PWLS objective function. The value $\frac{log(I_O)}{log(Y_0)}$ is substituted for $l \cdot \mu$ based on expression (2.6). This is a PWLS using ordered projection subsets S_n. This algorithm is used as an example of PWLS because it serves as the bais for the PWLS presented in this dissertation.

A PWLS approach is not limited to attenuation map reconstruction and estimation. It can also be applied to the sinogram projections prior to a FBP reconstruction (Wang *et. al*, 2006). This is done to improve the projection data to account for low dose and high noise situations. This mode is not commonly used because it leaves out a reconstruction stage. Leaving this out does not result in any significant improvement over including the reconstruction in the algorithm. This work demonstrates the PWLS improvement in noise suppression.

ML solves for a maximization looking for the most the solution which is most likely given the measured data, but fails because it tends to increase the noise in the reconstructions after a number of iterations. A penalty is commonly added to a WLS approach to account for the noise. Work done by Anderson (Anderson *et. al*, 2005) compares both methods with FBP

for noise suppression. Both methods have some improvement over simple FBP, because of the statistical nature of both methods modeling the projections.

One other possible criterion is a maximum a posteriori (MAP); this criterion incorporates information known about the imaged object prior to the scan. This prior is typically modeled as a Gibbs-Markov random field (Lopez *et. al*, 2006). Typically it is assumed that any large variation across the reconstruction or projection space must be from noise or an edge, this can be modeled using a Gibbs random field. These variations are penalized with some weight each iteration. MAP can be done as its own independent iterative reconstruction algorithm or as a piece of the other iterative statistical reconstruction algorithms. This includes PWLS (Wang *et. al*, 2006; Anderson *et. al*, 2005; Fessler *et. al*, 1997) or adding a penalty to ML (LaRiviere and Billmire, 2005; Sheng and Ying, 2005). Adding a penalty to ML can be done by smoothing the projection space and then reconstructing using an ML algorithm (Riviere and Billmire, 2005), or by adding a penalty step to an OS-EM algorithm (Sheng and Ying, 2005).

Maximum a posteriori (MAP) changes the probability function from the probability of the measured projections Y given an estimate of attenuation $\hat{\mu}_{est}$ to the probability of an estimate of attenuation given the projection data and some prior knowledge. This probability is then maximized. This means that the function is now looking for the estimate of attenuation which has the highest probability given a set of projections.

The advantage of using MAP is that it allows the user to incorporate prior knowledge about the attenuation map into the estimated attenuation map. This is different than other statistical methods, iterative filtered back projection (IFBP), WLS, and ML, which try to find the best match between the measured projection data and the estimated attenuation map. If

the user knows something about the true attenuation map, it can be incorporated as a prior, even if the noise is preventing it from being reconstructed using other methods.

The posterior $P(\hat{\mu}_{est}|Y)$ is related to the prior $P(\hat{\mu}_{est}|Y)$ via Bayes rule:

$$P(\hat{\mu}_{est}|Y) = \frac{P(Y|\hat{\mu}_{est})P(\hat{\mu}_{est})}{P(Y)} \tag{2.12}$$

The MAP is found by maximizing the posterior for a given prior. Taking the log of the posterior:

$$log\big(P(\hat{\mu}_{est}|Y)\big) = log\big(P(Y|\hat{\mu}_{est})\big) + log\big(P(\hat{\mu}_{est})\big) - log\big(P(Y)\big) \tag{2.13}$$

The first term is the log likelihood, or the log of the probability of a projection Y given some estimated attenuation $\hat{\mu}_{est}$. The second term is the log likelihood of the prior. The final term is the log likelihood of the projection. If the first term is expressed as a WLS:

$$log\big(P(\hat{\mu}_{est}|Y)\big) = -(l \cdot \mu - [L\hat{\mu}_{est}]_i)^T Y_i (l \cdot \mu - [L\hat{\mu}_{est}]_i) \tag{2.14}$$

And the second term can be expressed as the penalty term

$$log\big(P(\hat{\mu})\big) = -\beta \cdot T(\hat{\mu}) \tag{2.15}$$

Then the MAP looks like a WLS with an added $log\big(P(Y)\big)$ term. The other difference between the MAP and WLS is the sign. PWLS is looking for the minimum squared error modified by prior knowledge. MAP is looking to maximize the probability of an attenuation estimate given a set of projections and some prior knowledge about those projections. The negative in (2.13) and (2.14) accounts for this difference. MAP is the same as a negative PWLS criterion when a negative WLS criterion is used for the log likelihood; because MAP is maximizing the criterion and WLS is minimizing the criterion.

For MAP criterion the prior knowledge is added to the estimate of attenuation. MAP can use either ML or WLS for the log likelihood criterion. PWLS and MAP are basically the same only when a WLS criterion for MAP is used. This means PWLS is a special case of MAP.

2.3. Energy-discriminating X-ray CT Reconstruction

This section covers different forms of energy-discriminating x-ray CT reconstructions. Initially this was regulated to only two energies and labeled dual-energy x-ray. This has recently been extended to five energies. The new work has been divided between theoretical work and system design using new energy-discriminating detectors. The work presented in this dissertation represents the first attempt to combine these two pieces incorporating a novel energy differentiating system with new algorithms designed specifically for energy-discriminated x-ray CT reconstruction and noise suppression.

2.3.1. Dual-Energy X-ray Measurements

There are two established methods for collecting dual-energy x-ray measurements: two separated energy measurements and dual energy detectors. The first method is commonly a dual exposure technique (Rebuffel and Dinten, 2007). In this method two separate x-ray projections are measured, one with a very high anode voltage setting (typically in the range of 80-100kV) and the other with a very low anode voltage (typically in the range of 40-50kV) (Talbert *et. al.*, 1980). Each of these x-ray projections will be emitted as an x-ray spectrum, but the different cut-off voltages will make the average x-ray energy of each spectrum different. The two average energies are the dual energies required. This is dual exposure because the patient is exposed to x-rays twice, rather than a single x-ray exposure with a single anode voltage. The second method is a single exposure technique (Rebuffel and

Dinten, 2007). In this method a single x-ray projection with a high anode voltage is measured with a detector which has two detecting elements separated by an x-ray filtering material (Allec and Karim, 2010). Two integrating detectors sandwich the x-ray filter. The low energy x-rays are absorbed and measured in the first detector. The filter removes the remaining low energy x-rays. The high energy x-rays are absorbed and measured in the second detector. An example of this is the top layer has thin scintillator which only converts the low energy x-rays into light photons the second layer has a thicker scintillator which converts the high energy x-ray photons into light photons (Allec and Karim, 2010). The single exposure method has the advantage of only one x-ray measurement. This reduces artifacts due to any small changes in patient alignment between scans. However, the filter between detectors can attenuate much of the total x-ray signal reducing the signal in the high energy scan and increasing the system's noise (Rebuffel and Dinten, 2007).

2.3.2. Dual-Energy X-ray Reconstructions

When x-ray CT was first developed, there was interest in extending measurements from single energy to dual-energy projection measurements (Rutherford, Pullan, and Isherwood, 1976). Early x-ray CT defined x-ray projection in terms of a single absorption coefficient, which makes sense because expression (2.1) is an application of the Beer-Lambert law for absorption of light passing through a material, where the absorption coefficient becomes the attenuation coefficient. It was proposed in (Christ, 1984) that the attenuation of an tissue is the sum of the photoelectric absorption and Compton scattering rather than just absorption. Thus, dual energy x-ray imaging attempted to use two energies to create two sets of equations to solve for these two values rather than a single energy and single equation (2.1) to solve for attenuation (Talbert, Brooks, and Morgenthaler, 1980).

The initial work in dual energy x-ray imaging focused on the using two energies to measure Compton scatter and photoelectric absorption of different tissue. Marshall showed that this was possible for a number of different typical clinical tissues including: specimens of brain and other body tissues (Marshall, Alvarez and Macovski, 1981). This work was done for each tissue individually, showing it was possible to use dual energy to identify the atomic number and atomic density of each of these tissues. Using dual energy imaging in this is still used for applications where identifying tissues is more challenging and more information is helpful, such as mammography (Bliznakova, Kolitsi and Pallikarakis, 2006). However, it is not possible to find the atomic number and atomic density for more than a single tissue using dual-energy imaging without additional prior information (Shikhalie, 2008).

Using dual-energy x-ray imaging to identify tissues based on the way the x-ray photons interact with them, i.e. Compton scatter and photoelectric absorption, is the same basic concept presented in this dissertation. The attenuation curves used in this work are an extension of the two values representing a tissue. This dissertation use of multiple energies overcomes the dual-energy limit.

Dual energy x-ray imaging commonly uses the differences between the two polychromatic energy images rather than using the measurements to calculate the atomic number and atomic density. An early look at the difference between two projection x-rays is presented by Kruger (Kruger *et. al.*, 1981). In his work, Kruger proposes taking two chest exposures one at 65KVp and a second at 130KVp and subtracting the first from the second to remove the soft-tissue from the images and increase the contrast in the final image. The differences were used to identify calcifications in the lungs, which are distorted by the soft tissue around them. The lower energy x-ray images will include more information about the

soft tissue than the higher energy x-rays. This is because the attenuation of soft tissue decreases faster with respect to energy than dense tissue, such as bone. For this reason subtracting the low-energy image from the high energy image reduces the effect of soft tissue, removing it from the images. This idea is extended to digital mammography and CT.

Dual-energy subtraction is used in digital mammography, where the method is used to enhance mammography images by subtracting projections measured with two energies. An example of this is a simulation study, focusing on identifying known calcifications and tumors within a simulated breast using dual-energy rather than single-energy digital mammography (Bliznakova, Kolitsi and Pallikarakis, 2006). Another example focuses on increasing the signal-to-noise ratio using (SNR) real dual-energy digital mammography based on commercially available mammography systems (Brandan and Ramirez, 2006). Mammography is complicated by the need to find very small masses and calcifications in the breast which have a system of ducts that appear very similar to small masses in standard single-energy x-rays. Increasing the information by taking two energies improves the SNR and helps to identify the masses in the breast. These are just two examples of dual-energy subtraction being used to improve mammography. This is not directly applicable to the CT research presented in this dissertation; however, it shows other examples of energy-discriminating x-ray uses.

Dual-energy subtraction is also used in x-ray computed tomography. This includes: subtraction of x-ray CT projections or reconstructions at different energies is used to improve SNR and contrast within the final reconstruction image. Work proposed by Shikhalie, has a theoretical focus using simulations rather than real experiments (Shikhalie, 20078). Shikhalie looks at subtraction to increase SNR when comparing calcium and iodine in simulation.

Work proposed by Uotani is more focused on experimental results (Uotani, 2009). Uotani looks at using dual-energy imaging to remove head bone in cranial CT scans and hard plaque in calcified carotid stenosis. In both cases the more dense tissue is removed so that the softer tissue, visible at lower energies, is highlighted. Both Shikhalie and Uotani present a set of convincing images justifying the use of dual-energy CT.

Dual energy x-ray CT is not limited to simple subtraction; more advanced segmentation methods have been proposed. Work proposed by Sukovic and Clinthorne presents a penalized weighted least-square (PWLS) method for reconstructing x-ray attenuation collected as dual-energy x-ray CT (Sukovic and Clinthorne, 2000). The Sukovic and Clinthorne assume that every pixel in the attenuation map is a mixture of densities distributed spatially. Their goal was to use two measurements of attenuation at different energies to solve for the spatial distributions of the different densities of bone and soft tissue. They created a PWLS objective function based on the two energy measurements. A simple quadratic smoothing penalty is used. Minimizing the objective function finds the best estimate of density distributions of the two tissues.

The unique part of the PWLS algorithm proposed by Sukovic and Clinthorne was the use of a mixture model for the attenuation model. This allows the algorithm to be solved for bone and soft tissue creating images very similar to digital subtraction results. This method was tested in the presence of noise and compared to a dual-energy FBP subtraction method. It was shown to be significantly better than the FBP in the presence of noise. This makes sense because of the penalty term which will smooth the final images. It was also tested with two small ultra-dense regions added. These regions introduced beam-hardening in the filtered

back projection reconstructions, but the PWLS was able to compensate because it used estimates of density rather than attenuation.

Work proposed by Bazalova attempts to use two energies to automatically determine the atomic numbers and electron densities based on two attenuation measurements (Bazalova *et. al.*, 2008). An attenuation expression very similar to (2.2) was used, and then a difference in ratios was defined to be zero. The x-ray spectrum is represented by the weights and for the photoelectric and Compton effects. Then attenuation expression can be solved for the atomic number of a given tissue, and the density can be found by plugging the found atomic number back into the attenuation expression. Bazalova simulates a number of different phantoms and decomposes them into the appropriate tissues. This method is more complicated but generates more useful results than the PWLS if there is enough information about the existing tissues and if the dual-energy projections are complete.

Another algorithm proposed by Goh uses a similar mixture model as the PWLS but defines the attenuation in terms of a more generalized basis function (Goh, Liew, and Hasegawa, 1997). Rather than defining attenuation as a sum of two mass-attenuation coefficients with two density distributions, this algorithm defines the attenuation as a sum of two basis functions and two corresponding weights. The basis functions are chosen to be linear attenuation coefficients. However, the basis functions are assumed to be linearly independent. This makes a system of equations which is easier to solve, but also introduces error because linear attenuation coefficients are not truly independent of one another. The authors claim that as long as the atomic number of the basis functions is not too high, the error will small. Goh selected an aluminum and acrylic basis function into which the images are decomposed.

A final algorithm proposed by Kalender uses the same mixture model as the PWLS (Kalender, Klotz and Kostaridou, 1988). This algorithm focuses on noise suppression. Kalender developed an adaptive algorithm which defines an average attenuation as the average of the high-energy and low-energy attenuation maps. Then it looks at these attenuations, using a PWLS expression and allows the densities to vary as long as the average attenuation remains constant. This prevents the algorithm from biasing the data while suppressing the noise. The algorithm passes an adaptive filter over the tissue equivalent images. The adaptive filter is based on the average attenuation. This adaptive filter preserves edges and other important information while suppressing the noise.

These algorithms represent automatic tissue segmentation based on a mixture model where the attenuation has been sampled at two separate x-ray energies. In all of these cases the algorithms are severely limited by the fact that there are only two energies. The mixture models are simple because only two basis functions can be used. If more than two basis functions were used it would result in an underdetermined set of equations with more unknowns then equations. The justification for only two energies goes back to (Christ, 1984) which says that complete information for the polychromatic x-ray spectrum is in the photoelectric and Compton effects. However, this is really only true for a single tissue. As the number of tissues is increased, more x-ray energies are required to decompose the x-ray signal.

2.3.3. Dual-Energy X-rays Limitations

The limitations of dual-energy imaging are addressed by Rebuffel and Nazarian (Rebuffel and Dinten, 2007; Nazarian *et. al.*, 2008). A key limitation of dual-energy imaging is an increase in the dose received by the patient (Rebuffel and Dinten, 2007) if a dual-

exposure technique is used. A dual-exposure technique is the use of two separate x-ray measurements to generate dual-energy x-ray data. The patient receives an x-ray dose at high energy and then a second one at low energy. Both contribute to the total patient dose. To avoid this problem a single exposure technique can also be used (Rebuffel and Dinten, 2007). This method uses overlapping detectors with a filter in-between. The upper layer will have higher average x-ray energy than the lower one which has filtered out the lower energies. This method reduces the x-ray flux to the lower detector and limits the separation between the two energies. The problem of dual exposure is that the patient receives double the x-rays. This can be overcome by controlling the dose in each of the different energy exposures (Nazarian *et. al.*, 2008). However, without exposure control the patient receives a greater dose with dual-energy imaging, even if it is not double the exposure.

Other limitations discussed by Rebuffal and Nazarian include the noise in the dual-energy system and the limitation of only two energies. Dual-energy imaging is used to decompose an image based on the distribution of tissues. This is based on the attenuation properties of the tissues, i.e. Compton and photoelectric effects. The more alike these tissues are the more decomposing the image will magnify the noise. If two tissues' attenuation properties are very close, insufficient data has been collected or imaging energies which are too close then dual-energy reconstructions will increase the noise. Dual-energy users need to be careful in selecting the target tissues and the image energies.

The final and most important limitation of dual-energy X-ray is that only two energies are measured. Both of these measurements are still an averaged polychromatic x-ray spectrum. Modeling a polychromatic spectrum with two energies allows for the formation of two equations to decompose the tissues in the image. If there are more than two tissues in the

object dual energy can not decompose them without an additional equation (Nazarian *et. al.*, 2008). For this reason dual-energy can be used to separate bone and soft tissue (Bazalova *et. al.*, 2008) but not multiple soft tissues.

Dual-energy imaging offers additional information by increasing the data acquired. This is useful because a material has attenuation which is a combination of two quantum effects: Compton scattering and photoelectric absorption, both of which are dependent on the x-ray energy. For two materials having two energies allows decomposition of the reconstructed images based on their quantum effect (equations 2.4 and 2.5). However, taking two energy measurements increases the patient dose. If the materials or the energies are not well separated the noise will actually be increased using a dual-energy method. Taking two energy measurements only allows for a two material decomposition, and most real world applications have multiple elements.

2.3.4. Energy- discriminated X-ray Reconstruction

Recently there has been a surge of interest in extending dual-energy x-ray CT to a more accurate energy-discriminated x-ray CT. This work is separated into theoretical simulated energy-discriminated reconstructions, new energy discriminating x-ray photon counting detectors, and new CT systems designed to incorporate these x-ray detector. Each of these will be briefly discussed.

An algorithm proposed by Schlomka (Schlomka *et. al.*, 2008) divides the energy spectrum based on absorption edges and uses one more energy measurement than the number of absorption edges existing in the materials being imaged; attempting to separate simulated data on the basis of absorption edges. This algorithm uses the same principles as dual energy imaging subtraction, where differences in the materials' attenuation coefficients are used to

produce increased contrast with increased energy axis resolution. This algorithm is limited by the number of absorption edges available. However, it presents an algorithm capable of imaging multiple contrast agents. This work gives a good overview of a number of potential contrast agents with different absorption edges within the typical clinical x-ray energy range.

An algorithm proposed by Yan (Yan *et. al*, 2000) uses theoretical energy-discriminated data to improve beam-hardening artifacts. This work focuses on the differences in attenuation coefficients of typical imaged tissues with respect to x-ray energy. Yan proposes using known information about the attenuation curves to correct for beam-hardening artifacts in the reconstructions. This work focuses only on the issue of artifacts in the reconstructions and used theoretical attenuation curves to correct this issue, no real reconstruction algorithm is proposed. However, it introduces attenuation curves and the way these changes in attenuation impacts x-ray CT.

Elbakri and Fessler (Elbakri and Fessler, 2002) propose an energy-discriminated PWLS algorithm and then apply it to simulated data. This work presents a detailed description of the measured x-ray spectrum as a Poisson random variable, similar to expression 2.3. The spectrum is then approximated as a compound Poisson random variable. The following objective function was approximated to a solvable PWLS algorithm for a single energy signal. This PWLS is extended to cover a complete spectrum. This was done to incorporate the change in x-ray intensity and material attenuation with respect to energy. The single energy PWLS proposed by Elbakri and Fessler serves as the bases for the PWLS algorithm proposed in this dissertation.

These different algorithms all use simulated rather than experimental data. This is because experimental systems capable of acquiring energy-differentiated x-ray projections

are in the initial phases of development. Bazalova and Verhaegen propose a detailed Monte-Carlo simulation of an x-ray spectrum for CT (Bazalova and Verhaegen, 2007). This is a detailed work comparing the simulation to actual data and demonstrates the accuracy of x-ray spectrum modeling. However, no work has been done modeling the interaction of a clinical x-ray spectrum with the attenuation of different materials. Rather, the spectrum is investigated or the materials attenuation response to different photon energies is investigated (Hubbell and Seltzer, 1996).

There has been significant development in new energy-discriminating photon counting cadmium zinc telluride (CdZnTe) detectors. These detectors have been used for x-ray computed tomography applications (Ricq, Glasser, and Garcin, 2001; Giakos *et. al.*, 1998). These detectors count each incident x-ray photon and estimate the energy of each counted photon, assigning each photon to an energy bin to determine a spectrum of photon energies reaching the detector. This makes these detectors different from other x-ray detectors, such as analog film or flat panel and strip digital CCD based detectors (Hoheisel, 2006), which assign a single value to the entire incident x-ray field at a given location in space.

These detectors tend to be either single pixel detectors with high energy resolution or strip detectors with limited energy resolution. No x-ray CT has been done with the single pixel detectors with high energy resolution. A CT demonstrator has been built using a CZT single pixel detector (Claesson *et. al.*, 2001). This demonstrator was designed to show undergraduate students how basic CT concepts worked via a monochromatic beam and radon parallel beam data. Thus, this demonstrator uses a single energy gamma ray source rather

than an x-ray source. This is the only use of a single pixel CZT detector for any CT measurements.

The strip detectors are more like detectors commonly used for typical CT systems. However, these detectors only bin up to six energies (Medipix). Medipix is one of the leading energy resolving detectors. The Medipix 2 is a digitial flat panel detector capable of segmenting the x-ray spectrum into six energy bins. This is a significant improvement over single energy integrating detectors and two energy measurements. Several different systems have been proposed using these energy resolved detectors. Paulus and Gleason propose a novel energy-differentiating system using a CdZnTe detector (Paulus *et. al.*, 1998; Gleason *et.al.*, 1999). This system is demonstrated using a mouse and the reconstructions are done using FBP. The work by Paulus and Gleason is proof of concept. This work was done a while ago, yet there does not seem to be any further development of the initial concepts. This may be because there has not been any further development beyond six energy ranges.

The work done thus far on energy-discriminating is clearly divided between algorithms which are validated with simulated data and experimental systems limited to six energy bins and reconstructed using FBP. This is all limited to proof of concept and makes limited use of additional energy axis information. The work presented in this dissertation extends both of these concepts. A novel x-ray energy-discriminating CT system is presented and reconstruction algorithms focused on noise suppression on tissue segmentation are also presented.

2.4. Other Important Background Issues

There are two other important background topics: carbon nanotube field emission sources and x-ray contrast agents. The carbon nanotube field emission sources replace the

tungsten filament in the x-ray source used for this work. The contrast agents are used to improve tissue contrast in CT reconstructions.

2.4.1. Carbon Nanotube Sources

Carbon nanotube field-emission sources have recently been proposed as an alternate method for the generating electrons used for x-ray production (Zhang *et. al.*, 2005). This electron emission source replaces the tungsten filament usually used to produce free electrons using thermal emission. Electrons are emitted from the tips of the carbon nanotubes when an electromagnetic field is applied over the tips of the nanotubes. The field warps the barrier which keeps the electrons bound to the carbon; the electrons tunnel through the warped surface potential barrier rather than passing over it. This is different from other forms of electron emission, such as thermionic emission and photoemission, each of which add enough energy to electrons to get them over the potential barrier (Gomer, 1993).

Field emission using carbon nanotubes was first proposed by Heer and Rinzler in 1995 (Heer *et. al.*, 1995, Rinzler *et. al.*, 1995). Heer and Rinzler proposed using carbon nanotubes as electron emitters because carbon nanotubes operated very well in field emission. The carbon nanotubes are already good conductors and the tips have very small surface areas. However, the very small dimension of the nanotubes limits the emission current. This is overcome by using an array of nanotubes rather than a single one (Rinzler *et. al.*, 1995). Further research using carbon nanotubes has increased the emission current to a point where the carbon nanotubes can be used as an x-ray electron source (Cheng and Zhou, 2003). Experiments and data presented by Cheng and Zhou indicate that carbon nanotube emitters can be designed to have a stable electron emission current over a long period of time.

The carbon nanotubes are clustered as an array on some conductive substrate. A this substrate is grounded through a 100kΩ resistor. A metal grid is placed some distance above the nanotubes. When a voltage is applied to the metal gird, the carbon nanotubes are subject to an electromagnetic field determined by the voltage applied to the gird relative to the grounded substrate; the voltage applied to the gird is called the "gate voltage". The x-ray flux resulting is related to the voltage applied to the carbon nanotubes rather than a current through a filament. A negative voltage could be applied to the substrate the nanotubes are mounted to if the metal grid above the nanotubes is grounded (Yuan *et. al.*, 2003). This maintains the same field over the nanotubes for the same voltages as the arrangement proposed in (Yuan *et. al.*, 2003). If there is no field, the nanotubes will not emit electrons due to the work function of the carbon nanotubes, the electron remain bound the carbon nanotubes. As soon a field is applied, the carbon nanotubes will start emitting electrons. The field is controlled by the gate voltage which can be turned on and off almost instantaneously. This means that the emission current can be turned on and off almost instantaneously as well (Yue *et. al.*, 2002; Cheng *et. al.*, 2004; Zhang *et. al.*, 2005). This produces x-rays which can be pulsed on and off (Zhang *et. al.*, 2005).

Field emission carbon nanotubes for X-ray sources can also be arranged as multi-beam carbon nanotube sources sources. A multi-beam source is an x-ray source that can produce multiple x-ray beams with different orientations. Carbon nanotubes sources have been used to create multi-beam sources (Zhang *et. al.*, 2006) which can control the orientation of the x-ray beam (Wang *et. al.*, 2008) or be used for tomosynthesis (Yang *et. al.*, 2008). Field emission carbon nanotubes can be used for multi-beam x-ray imaging, as an array with the same anode (Zhang *et. al.*, 2006), a matrix on a chip (Wang *et. al.*, 2008), or

an array of independent sources (Yang *et. al.*, 2008) because of their reliance on an electromagnetic field for electron emission. The sources only emit electrons in the presence of a field. As soon as the field exists there is full electron emission. This binary nature allows a rapid transition from emission source to emission source. This transition becomes a rapid transition from x-ray beam to x-ray beam, making a multi-beam x-ray source practical.

The principal advantage of the carbon nanotube sources for x-ray production is the speed with which the sources can be turned on and off. This allows the source to be pulsed which opens the door to high-speed x-ray imaging. Carbon nanotube sources were initially incorporated with the hope to pulse them in a dual-spectrum system. However, this turned out to be unachievable; a single pixel photon counting detector was used instead. The new system presented in this dissertation used unique pulsing property of the carbon nanotube sources to synchronize x-ray source with the detector and the motion control required to acquire tomographic data.

2.4.2. Attenuation Contrast Enhancement Agents

X-ray CT for human medical applications creates estimates of the spatial variation of attenuation for tissues within a slice through the body. Each slice is displayed as an image of the spatial variation of the attenuation; contrast in these images is the result of large differences in attenuation. Dense tissues such as bone will have a large attenuation coefficient and less dense or soft tissues, such as soft tissue or blood, will have smaller attenuation coefficients. When bone and soft tissues are compared there is sharp contrast; when two soft tissues are compared, the contrast is significantly smaller. To increase the contrast in a specific soft tissue, contrast agents are introduced (Ramm *et. al.*, 2001).

Contrast agents are elements which have a large attenuation coefficient and are added into the body to increase the attenuation contrast for a specific tissue, organ, or system (Ramm *et. al.*, 2001). These include barium which is used to image the gastro-intestinal tract (Swanson and Halpert, 1990) and iodine which is used to image the cardiac system (Cardinal *et. al.*, 1993). Iodine is injected into the blood stream and then cycles rapidly through the kidneys. Barium is ingested into the gastro-intestinal tract and imaged as it passes through the tract. Both are minimally reactive, meaning that they do not chemically react with anything in the body; therefore, both are non-harmful to the patient. Iodine occasionally reacts with patients but this is rare. Iodine contrast agents are also used for imaging tumors and tumor growth (Shibamoto *et. al.*, 2007). Both of these contrast agents have been used for quite some time and are well understood. Iodine is included in this work to demonstrate the result of absorption edges on the proposed system. Iodine has an absorption edge in the middle of the energy range investigated in this dissertation. The iodine used is Visipaque™ which is a commercial contrast agent produced by General Electric for cardiac imaging (Visipaque).

Gold nanoparticles are currently being investigated as a new X-ray contrast agent (Hainfield *et. al.*, 2006). Gold is non-reactive with biological compounds so it makes a great contrast agent (Hainfield *et. al.*, 2006). Here gold is proposed as a biological contrast agent and demonstrated using gold nanoparticles as contrast agents on a CT of mice. The principal focus of gold nanoparticles has been cancer research (Xu, Tung, and Sun, 2008) because gold stays in the body longer than iodine and smaller concentrations are required to create contrast in CT images (Wang, Muszynski, and Simonsen, 2007). This has also been tested for non-biological x-ray CT as well (Popovtzer *et. al.*, 2008). Popovtzer mixes gold nanoparticle with

wood pulp to take a CT of the construction of different types of plywood. This demonstrates the increased attenuation of gold nanoparticles.

Researchers are investigating the ability to tag gold nanoparticles with proteins to be used for functional imaging (Rabin *et. al.*, 2006; Kim *et. al.*; 2007, Alric *et. al.*, 2008). These papers look at different proteins which are attached to the gold nanoparticles and then demonstrate the improvements in petri-dish x-ray images (Kim *et. al.*, 2007; Alric *et. al.*, 2008). These are also tested for lymph-node imaging in mice (Rabin *et. al.*, 2006). All of this work is preliminary investigations of gold nanoparticles tagged with proteins for functional imaging.

The concentration of the gold nanoparticles is important (Wang, Muszynski, and Simonsen, 2007). A small concentration makes it very hard to identify the gold from the background materials. This was shown for integrating detectors. The system proposed in this dissertation is a new multi-energy system. We believe this new system and algorithms will be able to measure smaller concretions of gold nanoparticles. Gold is used in this dissertation to demonstrate and study the effect of multiple absorption edges on the algorithm. Gold nanoparticles with a 1.9nm diameter were used in this experiment, trade-named AuroVist^{TM} (AuroVist).

2.5. References

Agarwal B.K., 1991, X-ray spectroscopy: an introduction 2nd ed., New York, Springer-Verlag

Allec N. and Karim K.S., 2010, "Multilayered x-ray detector for contrast-enhanced digital subtraction mammography," *Presented at Proceeding of SPIE Medical Imaging*, vol. 7622, 76221M-1.

Alric C., Taleb J., LeDuc C., Mandon C., Billotey C., Le Meur-Herland A., Brochard T., Vocason F., Janier M., Perriat P., Roux S. and Tillement O., 2008, "Gadolinium

chelate coated gold nanoparticles as contrast agents for both x-ray computed tomography and magnetic resonance imaging," *Journal of the American Chemical Society*, vol. 130, pp. 5908-5915.

Anderson J.M.M, Srinivasan R., Mair B.A., and Votaw J.R., 2005, "Accelerated penalized weighted least-squares and maximum likelihood algorithms for reconstrurction transmission images from PET Transmission data," *IEEE Trans. Med Imag.*, vol. 24, pp. 337-351.

AuroVist™, A Nanoprobes Product, Information available: http://www.nanoprobes.com/AuroVist.html

Bazalova M., Carrier J.F., Beaulieu L. and Verhaegen F., 2008, "Tissue segmentation in Monte Carlo treatment planning: a simulation study using dual-energy CT images," *Radiotherapy and Oncology*, vol. 86, pp. 93-98.

Bazalova M. and Verhaegen F., 2007, "Monte Carlo simulation of computed tomography X-ray tube," *Phys. Med. Biol.*, vol. 52, pp. 5945-5955.

Bliznakova K., Kolitsi Z. and Pallikarakis N., 2006, "Dual-Energy mammography: simulation studies," *Phy. Med. Biol.*, vol. 51, pp. 4487-4515.

Borisov A.A, Veip, Mazurov A.I., and Elinson M.B., 2006, Two technologies for designing digitial X-ray image detectors. *Biomedical Engineering*, vol. 40, pp. 219-222.

Brandan M. and Ramirez V., 2006, "Evaluation of dual-energy subtraction of digital mammography images under conditions found in a commercial unit," *Phys. Med. Biol.*, vol. 51, pp. 2307-2320.

Brooks R.A and DiChiro G., 1975, "Theory of image reconstruction in computed tomography," *Radiology*, vol. 117, Is. 13, pp. 561-572.

Brunner F.C., Clemens J.C., Hemmer C., and Morel C., 2009, "Imaging performance of the hybrid pixel detectors XPAD3-S," Phys. Med. Biol, vol. 54, pp. 1773-1789.

Brunner F.C., Khoury R., Benoit D., Meessen C., Bonissent A. and Morel C., 2009, "Simulation of PIXSCAN, a photon counting micro-CT for small animal imaging," *IOP Publishing for SISSA*, pp. 1-5.

Burkhardt C. E. and Leventhal J. J., 2008, Foundations of quantum physics, New York, Springer.

Cardinal H.N., Holdsworth D.W., Drangova M., Hobbs B.B., and Fenster A., 1993, "Experimental and theoretical x-ray imaging performance comparison of iodine and lanthanide contrast agents," *Medical Physics*, vol. 20, no. 1, pp. 12-31.

Claesson T., Kerek A., Molnar J. and Novak D., 2001, "A CT demonstrator based on a CZT solid state detector," in *IEEE Nuclear Science Symposium Conference Record*, vol. 3, pp. 1644-1646.

Chambers A., Fitch R.K., and Halliday B.S., 1998, *Basic vacuum technology 2nd ed.*, Philadelphia, Penn: Institute of Physics Pub.

Chantler C.T., 2000, Detailed Tabulation of Atomic form Factors, Photoelectric Absorption and Scattering Cross Sections, and Mass Attenuation Coefficients in the Vicinity of Absorption edges in Soft x-ray (Z=30-36, Z=60-89, E=0.1 KeV-10KeV, addressing Convergence Issues of Earlier Work, *Journal of Physical Chemistry*, vol. 29, No. 4.

Cheng Y., Zhang J., Lee Y.Z., Gao B., Dike S., Lin W., Lu J.P. and Zhou O., 2004,"Dynamic radiology using carbon-nanotube-based-field-emission x-ray source," *Review of Scientific Intrstuments*, vol. 75, no. 10.

Cheng Y. and Zhou O., 2003, "Electron field emission from carbon nanotubes," *C.R. Physique 4*, pp. 1021-1033.

Christ G., 1984, Exact treatment of dual-energy method in CT using polyenergtic x-ray spectra, *Phys. Med. Biol.*, vol 29, pp. 1501-1510.

Eichmeier J.A. and Thumm M.K., 2008, *Vacuum electronics: components and devices*, New York, Springer

Elbakri I. and Fessler J., 2002, "Statistical image reconstruction for polyenergetic X-ray computed tomography," *IEEE Trans. Med. Imag.*, vol. 21, no. 2, pp. 89-99.

Elbakri I, 2003, "Statistical Reconstruction Algorithms for polyenergetic x-ray computed tomography," Dissertation…

Feldkamp L.A., Davis L.C., and Kress J.W., 1984, "Practical cone-beam algorithm," *Journal of Opt. Soc. Am.*, Vol. 1, No. 6, pp. 612-619.

Fessler J.A., Ficaro E.P., Clinthorne N.H., and Lange K, 1997, "Grouped-corrdinate ascent algorithms for penalized likelihood transmission image reconstruction," *IEEE Trans. Med. Imag.*, vol. 16, pp. 166-175.

Giakos G.C., Guntupalli R.K., Vedeantham S., Chowdhury S., and Pillai B., 1998, "A computed tomography CdZnTe based scanning detector," *IEEE Instrument and Measurement Technology conference*, May 18-21, pp. 462-465.

Grande M., Dunkin S.K., and Kellett B., 2001, Opportunities for X-ray remote sensing at Mercury, Planetary and Space Science, vol. 49, pp. 1553-1559.

Goh K.L., Liew S.C., and Hasegawa D.H., 1997, "Correction of Energy-Dependent Systematic Errors in Dual-Energy X-ray CT using a Basis Material Coefficients Transformation Method," *IEEE Trans. Med. Imaging*, vol. 44, no. 6, pp. 2419-2424.

Goldan A.H., Karim K.S., Reznik A., Caldwell C.V., and Rowlands J.A., 2008, "Photon counting readout pixel array in 0.18um CMOS technology for on-line gamma-ray imaging of palladium seeds for permanent breast seed implant (PBSI)." *Proc. of SPIE*, vol. 6913, pp. 69130-1-11.

Gomer R., 1993, *Field Emission and Field Ionization*, American Vacumm Society Classics, University of Chicago, 1993

Gonzalez A.B., Mahesh M., Kim K.P., Bhargavan M, Lewis R., Mettler F., and Land C., 2009, "Projected cancer risks from computed tomographic scans performed in the United States in 2007," *Ach. Intern. Med.*, vol. 169, pp. 2071-2077.

Hainfeld J. F., Slatkin D.N., Focella T.M. and Smilowitz H M, 2006, "Gold nanoparticles: a new X-ray contrast agent," *British Journal of Radiology*, vol. 79, pp. 248-253.

Heer W.A.D, Chatelain A. and Ugarte D., 1995, "A carbon nanotube field-emission electron source," *Science*, vol. 270, pp. 1179-1180, 1995

Hoheisel M., 2006, "Review of medical imaging with emphasis on X-ray detectors," *Nuclear Instruments and Methods in Physics Research*, vol. 563, pp. 215-224.

Hounsfield G.N., 1973, "Computerized transverse axial scanning (tomography).1. description of system," *British Journal of Radiology*, vol. 46, pp. 1016-1022.

Hubbell J.H. and Seltzer S.M., 1996, Tables of X-Ray Mass Attenuation Coefficients and Mass Energy-Absorption Coefficients from 1 keVto 20 MeV for Elements Z = 1 to 92 and 48 Additional Substances of Dosimetric Interest, *National Institute of Standards and Technology*, Tech. Rep. 43NANB412756 Available: http://www.physics.nist.gov/PhysRefData/XrayMassCoef/cover.html

Hudson H.M. and Larkin R.S., 1994, "Accelerated image reconstruction using ordered subsets of projection data," *IEEE trans. Med. Imag*., vol. 13, pp. 601-609, 1994.

Hunger J., Wust P., Claussen C. and Felix R., 1992, "Evaluation of x-ray beam quality and film-screen combinations for detection of small low-contrast objects." *Phys. Med. Biol.*, vol. 37, pp. 343-355.

Hyper Physics, 2007, Characteristic X-rays available at: http://hyperphysics.phy-astr.gsu.edu/Hbase/quantum/xrayc.html#c1.

Kak A.C. and Slaney M.,1989, “Principles of Computerized Tomographic Imaging,” *IEEE Press*.

Kalender W.A and Kyriakou Y., 2007, “Flat-detector computed tomography (FD-CT),” *Eur. Radiol*., vol. 17, pp. 2767-2779.

Kalender W., Klotz E. and Kostaridou L., 1988, “An Algorithm for Noise Suppression in Dual Energy CT Materail Density Images,” *IEEE Trans. Med. Imag.*, vol. 7. no. 3. pp. 218-224.

Kane S. A. 2003, Introduction to physics in modern medicine, New York, Taylor and Francis.

Kim D., Park S., Lee J. H., Jeong Y.Y., and Jon S., 2007, “Antibiofouling polymer-coated gold nanoparticles as a contrast agent for in-vivo x-ray computed tomography imaging.” *Journal of American Chemical Society*, vol. 129, pp. 7661-7665.

Kirby B.J., Davis J.R., Grant J.A. and Morgan M.J., 2003, Extracting material parameters from x-ray attenuation: a CT feasibility study using kilovoltage synchrotron x-rays incident upon low atomic number absorbers, *Phys. Med Biol*., vol. 48, pp. 3389-3409.

Kolditz D., Kyriakou Y, and Kalendar W.A., 2010, “Volume-of-interest, (VOI) imaging in C-arm flat-detector CT for high image quality at reduced dose,” *Medical Physics*, vol. 37, Is. 6, pp. 2719-2730.

Kruger R., Armstrong J., Sorenson J., and Niklason L.T., 1981, “Dual Energy Film Subtraction Technique for Detecting Calcification in Solitary Pulmonary Nodules,” *Radiation Physics*, pp. 213-219.

Kump K.S. and Shi S., 1999, “Clinical comparison of new digital x-ray detector system with a conventional screen film system.” *Percent at SPIE Conference on Physics of Medical Imaging*, vol. 3659, pp. 464-470, 1999

Lange and Carson R., 1984, “EM Reconstruction algorithms for emission and transmission tomography,” *Journal of Computer Assisted Tomography*, vol. 8, pp. 306-316.

LaRiviere P.J., and Billmire D.M., 2005, “Reduction of noise-induced streak artifacts in x-ray computed tomography through spline-based penalized likelihood sinogram smoothing.” *IEEE Trans. Med. Imag.*, vol. 24, pp. 105-111.

Lee R, 1993, *Scanning electron microscopy and x-ray microanalysis*, Englewood Cliffs, NJ, PTR Prentice Hall

Lopez A., Martin J.M., Molina R., and Katsaggelos A.K., 2006, "Transmission tomography reconstruction using compound gibbs-markov random field and ordered subsets," *LNCS*, vol. 4142, pp. 559-569.

Lundqvist M., Danielsson M,, Cederstrom B., Chmill V., Chuntonov A., and Aslund M., 2003, "Measurement on a full-field digital mammography system with a photon counting crystalline silicon detector," *Medical Imaging Physics of*, vol. 5030, pp. 547-552.

Marshall W.H., Alvarez R. and Macovski A., 1981, "Initial Results with Prereconstruction Dual-Energy Computed Tomography (PREDECT)," *Ragiology*, pp. 421-430.

Matsumoto M., Miyajima S., Yamamoto A., Yamazaki T. and Kanamori, 2002, "Measurement of diagnostic X-ray spectra using CdZnTe detector," *IRPA Proceedings*, vol. 7, no. 43.

Medipix™ a Collaboration effort in photon counting detector development, information available at: http://medipix.web.cern.ch/medipix/index.php

Nazarian A., Cory E., Muller R., and Snyder B.D., 2008. "Shortcomings of DXA to assess changes in bone tissue density and microstructure induced by metabolic bone diseases in rat models," *Osteoporos Int.*, Vol. 20, pp. 123-132.

Nikl M., 2006, "Scintillation detectors for x-rays, Review Article," *Meas. Sci. Technol.*, vol. 17, pp. 37-54.

Popovtzer R., Agrawal A., Kotov N.A., Popovtzer A., Balter J., Carey T.E., and Kopelman R., 2008, " Targeted gold nanoparticles enable molecular CT imaging of cancer," *American Chemical Society*, vol. 8, pp. 4593-4596.

Rabin O., Perez J.M., Grimm J., Woljtkiewicz G. and Weissleder R., 2006, "An X-ray computed tomography imaging agent based on long-circulating bismuth sulphide nanoparticles," *Nature Materials*, vol. 5, pp. 118-122.

Ramachandran R.A. and Lakshminarayanan A.V, 1971, "Three dimensional reconstruction from radiographs and electron micrographs: Application of convolution instead of Fourier transforms," *Proc. Nat. Acad.*, vol. 48. Pp. 2236-2240.

Ramm U., Damrau M., Mose S., Manegold K.H., Rahl C.G., and Bottcher H.D., 2001, "Influence of CT contrast agents on dose calculations in 3D treatement planning system." *Phys. Med. Biol.*, vol. 46, pp. 2631-2635.

Rebuffel V. and Dinten J.M., 2007, "Dual Energy X-ray imaging: benefits and limits," *Insight*, vol 49, no. 10.

Reddy D.S., Premachand K., Radha V., Murty K, Rama Rao J., and Lakshminarayana V., 1976, Photoelectric interaction below the K-edge," *Physical Review A*, vol. 13, no. 1.

Rinzler A.G., Hafner J.H., Nikolaev P., Lou L., Kim S.G., Timanek D., Colbert D. and Smalley R.E., 1995, "Unraveling nanotubes: field emission from an atomic wire," *Science*, vol. 269, pp. 1550-1553.

Ricq S., Glasser F., and Garcin M., 2001, "Study of CdTe and CdZnTe detectors for X-ray computed tomography," *Nuclear Instruments and Methods in Physics Research*, vol. 458, pp. 534-543.

Roentgen, 1913, An interview with Dr. Roentgen, American Journal of Roentgenology, vol. 1, pp. 325-325.

Rogers T.H., 1947, High-Intensity radiation from beryllium window x-ray tubes, *Radiology*, vol. 48, pp. 594-603.

Rutherford R.A., Pullan B.R., and Isherwood I., 1976, "Measurement of Effective Atomic Number and Electron Density Using and EMI Scanner," *Neuroradiology*, vol 11., pp.15-21.

Schlomka, Roessl E., Dorscheild R., Dill S., Martens G., Istel T., Baumer C., Herrmann C., Steadman R., Zeitler G., Livne A. and Proksa R., 2008, "Experimental feasibility of multi-energy photon counting K-edge imaging in pre-clinical computed tomography," *Phys. Med. Biol*., vol. 53, pp. 4031-4047.

Sheng J., and Ying L., 2005, "A fast image reconstruction algorithm based on penalized-likelihood estimate," *Med. Engineering Physics*, vol. 27, pp. 679-686.

Shibamoto Y., Naruse A., Fukuma H., Ayakawa S. and Tomita N., 2007, "Influence of contrast materials on dose calculation in radiotherapy planning using computed tomography for tumors at various anatomical regions: A prospective study." *Radiotherapy and Oncology*, vol. 84, pp. 52-55.

Shikhalie P., 2008, "Computed Tomography with energy-resolved detection: a feasibility study," *Phys. Med. Biol.*, vol. 53, pp. 1475-1495.

Sukovic P. and Clinthorne N.H., 2000, "Penalized Weighted Leat-Square Image Reconstruction for Dual Energy X-ray Transmission Tomography," *IEEE Trans. Med. Image.*, vol. 19, No. 11, pp. 1075-1081.

Swanson, D. P. and Halpert, R. D., 1990, "Gastrointestinal Contrast Media: Barium Sulfate and Water-Soluble Iodinated Agents. In Pharmaceuticals in Medical Imaging. Radiopaque Contrast Media, Radiopharmaceuticals, Enhancement Agents for

Magnetic Resonance Imaging and Ultrasound," *Macmillan Publishing Co*.: New York, NY, pp 155-183.

Szeles C., 2004, "CdZnTe and CdTe materials for X-ray and gamma ray radation detector applications" *Phys. Stat. Sol.*, vol. 241, pp. 783-790.

Talbert A.J., Brooks R.A., and Morgenthaler D.G., 1980, "Optimum energies for dual-energy computed tomography," *Phys. Med. Biol.*, Vol. 25, No. 2, pp. 261-269.

University of Maryland Medical Center, "Radiology, what are barium x-rays," available at: http://www.umm.edu/radiology/barium.htm

Uotani K., Watanabe Y., Higashi M., Nakazawa T., Kono A., Hori Y., Fukuda T., Kanzaki S., Yamada N., Itoh T., Sugimura K. and Naito H., 2009, "Dual-energy CT head bone and hard plaque removal for quantification of calcified carotid stenosis: utility and comparison with digital subtraction angiography," *Eur. Radiol.*, vol. 19, pp. 2060-2065.

Visipaque™ (iodixanol), A GE Product, Information available: http://md.gehealthcare.com/visipaque/

Wang J., Li T., Lu H., and Liang Z., 2006, "Penalized weighted least-squares approach to sinogram noise reduction and image reconstruction for low-dose x-ray computed tomography," *IEEE Trans. Med. Imag.*, vol. 25, pp. 1272-1283.

Wang S., Lu Z., An L., Zhou O. and Chang S., 2008, "Fabrication and characterization of Individually Controlled Multi-pixel Carbon Nanotube Cathode Array Chip for Mirco-CT Application for Cancer Research," *Mater. Res. Soc. Symp. Proc.*, vol. 1065.

Wang Y., Muszynski L. and Simonsen J., 2007, "Gold as an x-ray CT scanning contrast agent: effect on mechanical properties of wood plastic composites," *Holzforschung*, vol. 61, pp. 723-730.

Webb S. 1996, *The Physics of Medical Imaging (Medical Science Series)*, IOP Publishing, 1996.

Xu C., Tung G. A., and Sun S., 2008, "Size and concentration effect of gold nanoparticles on X-ray attenuation as measured on computed tomography," *Chemistry of Materials*, vol. 20, pp. 4167-4169.

Yan C., Whalen R., Beaupre G., Yen S. and Napel S., 2000, "Reconstruction algorithm for polychromatic CT imaging: application to beam hardening correction," *IEEE Trans. Med. Imag.*, vol. 19, no. 1, pp. 1-11.

Yang G., Rajaram R., Cao G., Sultana S., Liu Z., Lalush D., Lu J, and Zhou O., 2008, "Stationary digital breast tomosynthesis system with multi-beam field emission x-ray array," *SPIE Medical Imaging conference proceeding*

Zhang J, Cheng Y, Lee Y.Z, Gao, B., Qiu Q., Lin W.L., Lalush D., Lu V, and Zhou O, 2005, "A nanotube-based field emission x-ray source for microcomputed tomography," *Review of Scientific Instruments*, vol. 76.

Zhang J., Yang G., Lee Y.Z., Cheng Y., Gao B., Lu J.P. , and Zhou O., 2006, "A multi-beam x-ray imaging system based on carbon nanotube field emitters," *SPIE*, Vol. 6142, 614204.

Zeng GSL and Gullberg G.T., 1992, "A cone beam tomography algorithm for orthogonal circle and line orbit," *Phys. Med. Biol.*, vol. 37, pp. 563-577, 1992.

Yue G.Z., Qiu Q., Gao B., Cheng Y., Zhang J., Shimoda H., Chang S., Lu J.P and Zhou O., 2002. "Generation of continuous and pulsed diagnostic imaging x-ray radiation using carbon nanotube-based-field-emission cathode," *Applied Physics Letters*, vol. 81, no. 2.

3. SYSTEM DESCRIPTION

This section describes a new x-ray micro-computed tomography (μCT) system capable of dense spectral measurements. The x-ray system was initially designed as μCT for dual-spectrum measurement. The development of this system is described in detail and initial results validating the functionality of the system are presented. Modifications made to the initial system are then discussed along with changes to the experimental procedure to incorporate these modifications. A further modification to the original x-ray source, a redesign of the original source, is also presented.

3.1. Original Micro-Computed Tomography System

The dual-spectrum x-ray micro-computed tomography system is presented in this section.

3.1.1. Original Concept

The original system was designed as a dual-spectrum micro-computed tomography system using a field-emission carbon-nanotube x-ray source. Field emission carbon nanotube field emission x-ray sources have been developed by Dr. Zhou at UNC (Cheng and Zhou, 2003). These sources can be pulsed on and off almost instantaneously, due to the nature of field emission. The original concept was to turn two separate spectra on and off intermittently using the pulsing capabilities of the carbon nanotube sources, using the differences between the two spectra to increase contrast in the two x-ray images.

Dual-energy computed tomography (DECT) takes two x-ray projections with two different tube voltages; one at a lower voltage and one at a higher voltage. The separation between the two x-ray energies produces different measures of projected attenuation. This difference is used to enhance the contrast in the reconstructed attenuation estimate. Dual-

spectra CT is similar, taking two x-ray projections with two different x-ray spectra. Each x-ray spectrum will have unique distribution of x-ray intensity with respect to x-ray energy, mostly due to the location of characteristic peaks for the anode material used to produce the spectrum. The differences in the x-ray spectra are used to create different measures of projected attenuation. Both x-ray spectra will cover the same energy range; thus, the flux distribution of both will be much closer than dual-energy. To use two spectra, both spectra must have characteristic peaks within the energy range and there must be some way to switch rapidly between two anodes. To meet the first requirement, molybdenum and tungsten sources were used as the two target anodes. The molybdenum has a group of low energy characteristic peaks (around 16KeV) and the tungsten has high energy peaks (around 60KeV).

The principal limitation preventing dual-spectrum imaging in the past was the rapid switch between anodes. Typical clinical x-ray systems use thermoemission to generate the free electrons needed to create x-rays. This takes time to warm up and cool off, so changing the anode in the middle of a scan is not practical. The new carbon-nanotube sources can be pulsed on off nearly instantaneously. Two different anodes can be placed side by side with two different carbon nanotube electron sources which are pulsed on and off to transition instantaneously between spectra. Thus, field emission carbon nanotube field emission sources make it possible to do dual-spectrum imaging.

3.1.2. Original System

The original system was designed as a dual-spectrum micro-computed tomography (μCT) system with carbon-nanotube field emission sources. The system has three parts: the x-ray source, the positioning system, and the detector.

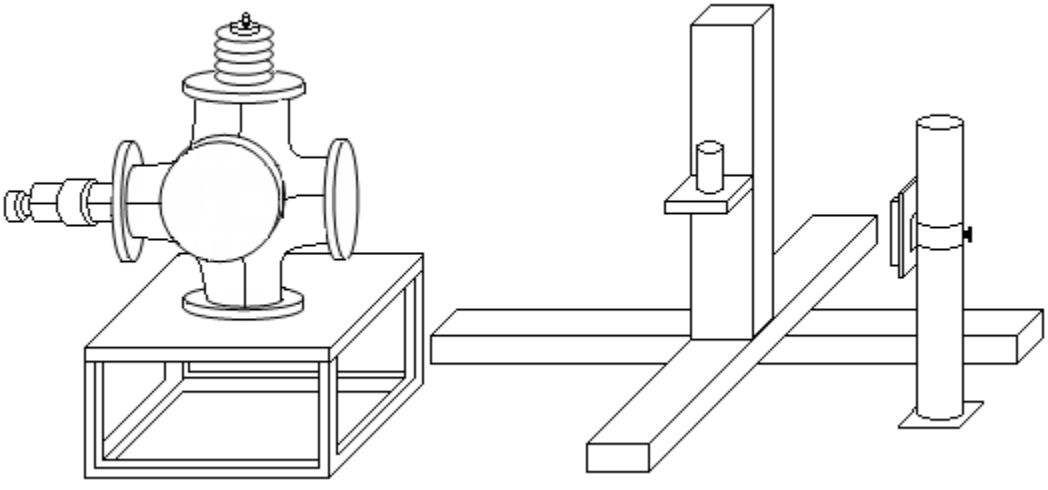

Figure 3.1: Schematic representation of original x-ray system. Source is housed in vacuum system on right of image and molybdenum and tungsten anodes are attached to high voltage line shown in figure. Velmex positioning system as shown in center is controlled by step motors in lower right-hand corner. Hamamatsu flat panel digital detector is shown on the left.

These different parts are all controlled via a central computer using Labview software (Labview). The original system is shown below in figure 3.1. Each of the parts is described individually in the following sections.

3.1.2.1. Positioning system

The positioning system consists of three linear Velmex slides and a Velmex rotating table. These slides are arranged as a set of axes in three-dimensional space with the rotating table mounted on the vertical slide. The slides are controlled remotely via stepper motors connected to the computer through a serial cable. The slides provide motion with 0.01mm accuracy in three dimensions and 0.1° accuracy in rotation. However, this flexibility is not fully utilized in the system.

The system was designed as a simple step-and-shoot CT. The object is rotated 1°, x-rays are collected for a period of time, and then the object is rotated 1° again. The x-rays are

only collected when the object is not in motion; the step is the rotation, the shoot is when the object is exposed to radiation and imaged. The computer program sets the motion to be in-between measurements. The Hamamatsu detector has a collecting phase and reading phase; thus, the positioning system is timed to move during the reading phase when the detector is not collecting x-ray data. The linear slides are not used during a step and shoot. The slides are used to move the object to a precise location prior to CT.

3.1.2.2. Detector

The original design used a Hamamatsu C9321CA-02 flat panel detector (Hamamatsu), which has a high resolution and a high imaging rate, but a very small field of view. The imaging field of view is 5.16cm by 5.06cm with 1032x1012 pixels. This means that each pixel is 50μm^2. Ideally the resolution is 50μm both directions; however, there is noise in each measurement, suppressing this noise will distort the resolution. The detector can take eight frames per second when in full resolution. If the resolution is reduced by combining four pixels into one, making the detector 258 x 253 with 200μm square pixels, the speed is increased to 27 frames per second. This detector is shown below in figure 3.2 from the schematic in the detector's data sheet.

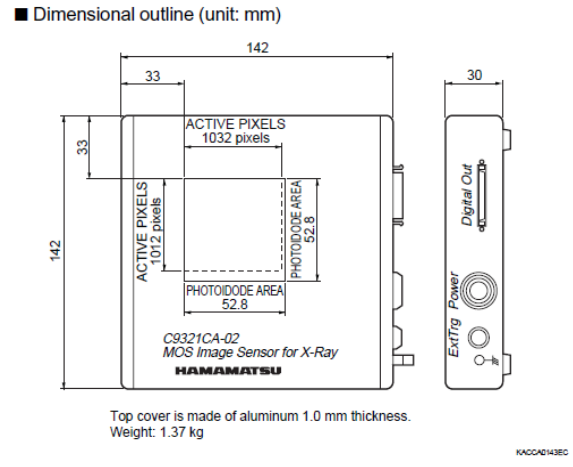

Figure 3.2: Hamamatsu C9321CA-02 flat panel detector

The detector has two modes: collect and read, controlled by a control input labeled read on the detector computer interface. If the read input is low, the detector is in collect phase. This means that the photons collect on the photodiodes until there is a read signal. The detector will read even if there is no x-ray flux, resulting in almost no measured flux, only measuring background counts. The photons continue to collect on the photodiodes until the read line is activated. When this happens the charge collected on the diodes is read as the intensity of the x-ray spectrum at that location. The frame rate is limited because there must be enough time for a readable charge to collect on the surface of the photodiodes, and there must be enough time to read that charge. If the pixels are larger, the total number of pixels is reduced; thus, increasing pixel size increases frame rate.

The detector also has an external trigger. The detector continuously reads the charge on the photodiodes at a rate defined by the user and limited by the max frame rate. If the user wants a better image (i.e., high resolution with less noise) the frame rate can be slowed to allow more photons to collect between each measurement. The trigger line acts as an external control on the read line. The read line can only be active when the trigger line is high. When

the trigger is high the detector reads at the rate the user has specified. The trigger also allows for synchronization of the detector with the rest of a system.

The particular Hamamatsu detector used has two dead pixel lines in the field of view. A dead pixel line is a full array of non-functioning pixels rather than a single random dead pixel. These lines of photodiodes are always oversaturated reading the maximum possible value for every measurement. This is within operational specs for Hamamatsu detectors, and must be worked around. The alignment of the detector with the source is critically important for computed tomography. It negates the alignment to remove these dead pixel lines (Cho *et. al.*, 2005). The data in the lines are estimated as the average of the pixels on either side of the dead pixel line. These data are not correct but provide a smooth image in the final result, and the loss of data is tolerable.

3.1.2.3. Vacuum system

For x-rays to be produced the source must be placed in a vacuum to allow a high-voltage potential between the cathode and anode to remain stable and prevent arcing. In clinical x-ray systems this is a sealed vacuum tube (Eichmeier and Thumm, 2008). However, once sealed, the x-ray system cannot be modified. To bypass this constraint, a steel vacuum system is used which can be opened and resealed so that the system can be periodically modified.

The system has a sealable door on the side which allows for easy access to the x-ray system. The system is pumped from atmospheric pressure to a vacuum in two stages. The first stage is a roughing pump which pumps out the air for about a day, bringing the internal vacuum chamber to 10^{-4} TORR. The first stage also includes a heating element which bakes the system, which ionizes the remaining air in the system. The second stage is an ion pump

which takes another day to bring the internal vacuum chamber to 10^{-9} TORR. The valve of the roughing pump is sealed shut when the ion pump is turned on. The ion pump remains on as long as the chamber remains sealed and maintains the vacuum.

A Varian StarCell ion pump is connected at the bottom of the vacuum chamber and controlled via a Varian MidiVac ion pump controller. The controller maintains a 3kV DC voltage to the ion pump to keep the pump operating. The controller displays the ion current collected by the pump. The current is proportional to the chamber's internal vacuum; a lower ion current means there is a better vacuum. There is no computer control or read out from the ion pump controller. The controller uses a set voltage to control the ion pump and displays a current. As long as the vacuum is maintained, it is not necessary to record the exact vacuum level; thus, there is no reason to connect the ion controller to the computer.

A Varian MiniTask roughing pump is used for the first pumping stage. This is a highly efficient pump which operates in a simple binary mode: either on or off. The pump has no output to monitor the vacuum level in the chamber. The ion pump cannot be turned on until the chamber has been pumped down to 10^{-4} TORR. To monitor the chamber, a Varian IMG-100 vacuum meter is placed after the valve. The meter is connected via a BNC cable to the Varian multi-gauge. This gauge is only used when the roughing pump is functioning; thus, it is not connected to the computer and monitored manually until the vacuum in the chamber is pumped down and the ion pump engaged.

3.1.2.4. X-ray source

X-rays are produced as free electrons in a vacuum are accelerated through a voltage potential into some heavy metal. The metal has large atoms arranged densely. As the free electrons interact with the electrons orbiting these atoms, the free electrons will lose all or

part of the energy they acquired in the voltage potential. This energy is lost as x-ray energy. The system uses a field emission carbon nanotube source to produce the free electrons. This is shown schematically in figure 3.3.

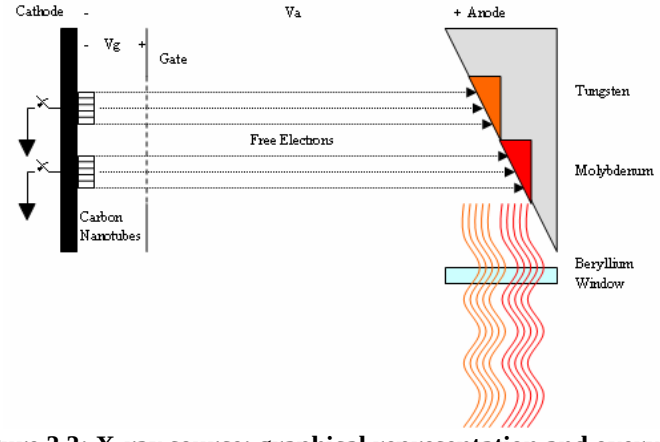

Figure 3.3: X-ray source: graphical representation and overview

The source has two groups of carbon nanotubes placed on a substrate, labeled "cathode" in figure 3.3. The substrate is grounded through a 100kΩ resistor; grounding the substrate the carbon nanotubes are anchored to. A metal plate, labeled "gate" in figure 3.3, is placed over the cathode. The gate plate has small holes cut directly over the carbon nanotubes; these holes are covered with very fine wire mesh designed to create a voltage over the carbon nanotubes, but not to inhibit the flow of free electrons. When a voltage, V_g in figure 3.3, is applied to the gate, an electric field is created between the gate and the grounded carbon nanotubes. This field causes the carbon nanotubes to emit free electrons with an emission flux proportional to the voltage applied to the gate. For this design, there is only one gate over both sets of carbon nanotubes. There is a switch between each set of carbon nanotubes and ground. If the switch is open, the nanotubes are isolated from the ground and no electric field exists; hence, there is no electron emission. These switches are used to select which carbon nanotube source is used.

The free electrons emitted by the carbon nanotubes are accelerated through a larger electric field, defined by the anode voltage, V_a in figure 3.3. The anode has two target materials: tungsten and molybdenum. Each set of carbon nanotubes is placed directly under one of these materials. These will each produce a different x-ray spectrum, for dual-spectra CT. The spectrum is selected by closing the switch between the carbon nanotubes and ground the under the desired anode material. Therefore, it is possible to switch the x-ray spectra by simply opening and closing a switch.

The x-rays produced in the interaction of the free electrons and target material exit the steel vacuum chamber via a beryllium coated window. The layer of beryllium filters low energy x-rays from the emitted spectrum.

This source design assumes each of the emitted electron paths is independent of each other. This assumption means that no electrons emitted from one source cross over and interact with the target material over the other source; if this is true, then this design produces two independent x-ray spectra. However, this is not completely accurate. There is some spreading of free electrons as they leave the carbon nanotubes, and a small amount of the free electrons interact with the wrong target material. However, this does not appear to be a significant problem in the final x-ray spectra. When the two spectra are compared (figures 3.7 and 3.8), the key differences between the spectra, the characteristic peaks, are preserved. If a large number of free electrons were leaking over to the other source, both spectra would have the same characteristic peaks. This demonstrates a separation between the two electron paths from the sources to the anode target materials.

3.1.2.5. System Control

The x-ray source, figure 3.3, is controlled with two voltages: an anode voltage and a gate voltage; and by two switches: one for each set of carbon nanotubes or one for each spectrum. The anode voltage is controlled by a Matsusada Precision AU Series power supply capable of generating a DC voltage from 1kV-60kV. The power supply has a high power voltage line connected to the x-ray source. The power supply has 25 pin serial connections for source control. To control the power supply the serial connections are connected via a National Instruments USB 6006 Digital to Analog converter (DAC) to the computer. The serial connections are controlled using analog voltages. The high voltage is controlled with an analog 0 to 10 volt input. A LABVIEW function was written to write the correct analog voltage to the power supply based on a user specified anode voltage. Another LABVIEW function monitors the anode voltage produced by the voltage source. A final LABVIEW function turns the source on or off.

The gate voltage has a more complicated control, because the source is turned on or off via the gate. If the gate voltage is on, x-rays are produced with a total flux related to the gate voltage. If the gate voltage is off, no x-rays are produced, even if the anode voltage is on. Therefore, the gate is connected to voltage supplies through a high-voltage pulse generator. A DEI PVX-4140 pulse generator is used. The pulse generator has two high-voltage (HV) inputs, a +HV and –HV input which is capable of up to a 3000 volt differential. A single HV output is connected to the gate of the x-ray source. The –HV input is connected to ground the x-ray system. The +HV is connected to a Stanford PS350/5000V power supply. The pulse generator has a gate input which controls the shape of the output HV signal. The

gate input is connected to a Directed Energy PDG-2515 function generator, which has a binary (high or low) output.

The Stanford PS350 is a DC voltage source with a 5000V maximum voltage. This source can be controlled manually: the user can input a desired voltage, a cut-off current, and turn the source on or off via a touch pad on the face of the source. The face also has two large and one small LED displays, which show the voltage, current, and settings, respectively. The source can also be controlled remotely via a GPIB cable. A LABVIEW function has been written which controls the voltage setting and turns the source on and off.

The PDG-2515 has two output lines which can operate independently or together with six different modes of operation. These modes include: a continuous mode, trigger mode, pulse count mode, divide by N mode, burst mode, and counted burst mode. The continuous mode creates a square wave with some specified frequency and pulse duration; the frequency range is 100mHz to 3MHz. The trigger mode operates the same as the continuous mode, limited by a trigger input line. The pulse count operates the same as the continuous with a specified number of pulses; this mode can be started based on an external or internal trigger. The divide by N mode operates one channel continuously and the other channel every N of the first channel. The burst mode has a burst of pulses with some burst frequency and some pulse frequency. The burst count mode is the same as the burst mode, with some specified number of bursts. All of this is controlled with six buttons and an LED interface; this is not a very functional interface. However, the pulse generator can be remotely controlled via a GPIB cable. A LABVIEW code was written to choose the mode, set the frequency, set other settings such as count number, and turn the pulsing on or off.

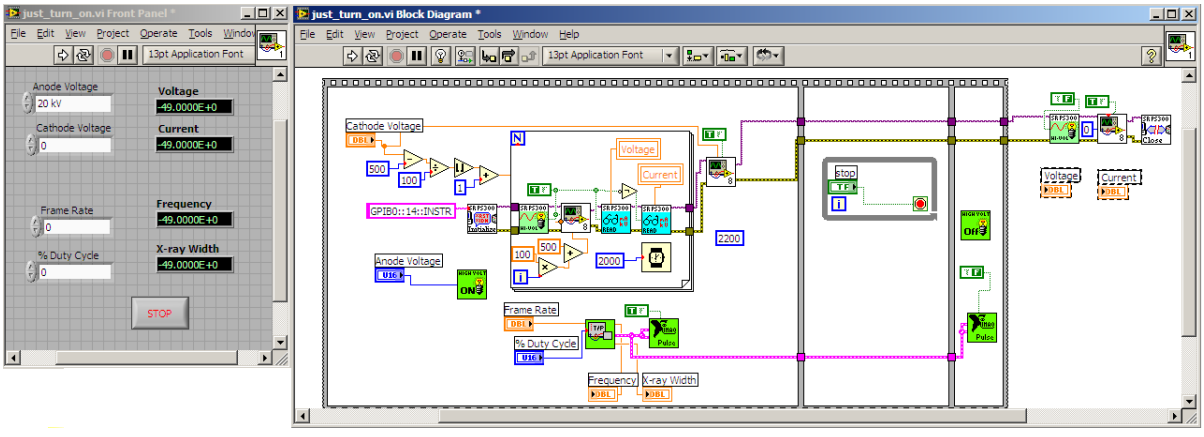

Figure 3.4: Simple "Just Turn On" LABVIEW control function

The simplest form of overall control code is shown below in figure 3.4 which simply turns all of the sources on with a user specified settings. The left part of figure 3.4 is the user interface where an anode voltage, cathode voltage, frame rate and duty cycle are selected. The pulse generator is set in continuous mode with frequency defined as "frame rate" and the pulse length is based on duty cycle setting. The cathode voltage is the gate voltage; this value is slowly ramped up, increasing 100V every two seconds until the gate voltage reaches its specified setting. This prevents arcing which could result from rapidly changing the gate voltage. The function runs until the stop button is pushed. The code to run this is shown on the right side of figure 3.4 as LABVIEW source code. Each of the smaller boxes in the figure is a function to control the different voltage sources and the pulse generator. The specific functions are not shown for the sake of simplicity.

The switches connecting the carbon nanotubes to ground are controlled manually. To switch rapidly between the two spectra for dual-spectrum imaging, a remote switch controllable by the computer would need to be designed. For the initial experiments, investigating the differences between the spectra, it was not necessary to rapidly switch between spectra. These experiments demonstrated that it would not be possible to do dual-

spectra CT with this system. Thus, no remote switch was designed and the switching was done manually.

For the original design, this function is used as part of a larger function (not shown) which also controls the linear slides and the Hamamatsu detector. The larger function uses the pulse generator in burst mode to turn the gate on when the object is stopped in front of the detector and turn the gate off when the object is moving. The linear slides are in sync with the rest of the system through the LABVIEW function, which tells them when and how far to move. The Hamamatsu detector is also controlled by the LABVIEW function and user interface displays the projected image collected.

3.1.2.6. Initial Results and Problems

Numerous initial experiments were done with the original system to perfect and calibrate the initial design. These included imaging a designed calibration phantom (Claesson *et. al.*, 2001), a bell pepper, a soft-tissue step phantom, and a dead mouse. The calibration phantom was a cylindrical acrylic phantom with small steel balls arranged circularly at different heights along the cylinder. This phantom was used to calibrate the flat panel detector with the positioning system and the x-ray source for tomographic data. The bell pepper was used as the first imaged object with an unknown attenuation distribution. It demonstrated that the system was working after the calibration experiment. A dead mouse was used to compare the system to existing μCT systems.

A dead mouse was obtained from the North Carolina State University Veterinary School, courtesy of Erin Egan, and was imaged using the Hamamatsu detector. Projections were reconstructed using Cobra Exxim (Cobra Exxim) CT reconstruction software which uses a Feldkamp algorithm to reconstruct slices through the imaged object. These slices

correspond to attenuation distribution of a specific height along the mouse, showing a distribution of tissues in that slice. Two example slices are shown in figure 3.5.

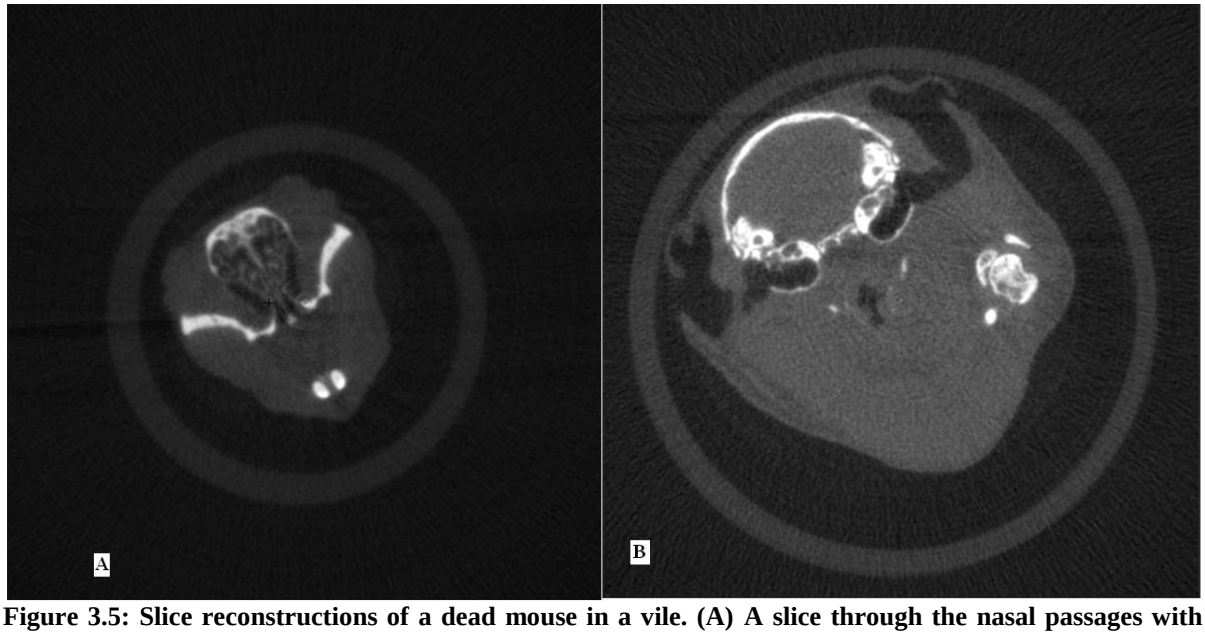

Figure 3.5: Slice reconstructions of a dead mouse in a vile. (A) A slice through the nasal passages with sinus detail shown. (B) A slice through the back of the head, with the upper shoulder also visible.

Figure 3.5 demonstrates the accuracy of the µCT system using the Hamamatsu detector. Detail in the bone structure of the nasal cavity, figure 3.5.A is clearly visible; this includes the swirling bone structures and the small holes in the bones in the nose. Figure 3.5.B shows the inner ear near the back of the mouse's head. This figure also shows the back of the throat and the top of the shoulder.

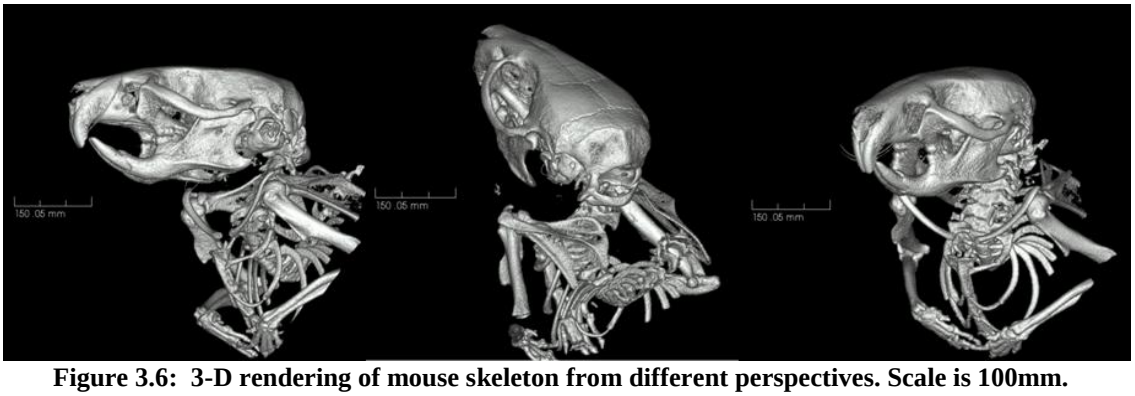

Figure 3.6: 3-D rendering of mouse skeleton from different perspectives. Scale is 100mm.

In figure 3.5, it is hard to see any soft-tissue detail; only the bone has the very fine detail. A three-dimensional volume rendering was done using 3D-Doctor (3-D Doctor), a three-dimensional rendering program designed to reconstruct bones from CT scans. These reconstructions are shown from different perspectives in figure 3.6.

The three dimensional rendering takes all of the reconstructed slices and interpolates between each slice to create an estimate of a continuous object. To create this rendering, all the soft tissue is removed from the images by applying a threshold to each slice. The bone has much greater attenuation and remains when the soft-tissue is removed. The final three-dimensional rendering is just the skeleton. This figure shows remarkable detail in the bone, the sutras in the skull can be clearly identified, along with nasal bones and individual teeth. These results are similar to the work published by Paulus (Paulus *et. al.*, 1998) for μCT systems.

The CT reconstruction of the mouse, both the individual slices (figure 3.5) and the three dimensional rendering (figure 3.6), demonstrates that the original system is comparable with other μCT systems. The mouse experiment was done as the final validation of the original system. By itself, this experiment is not significant, μCT with carbon nanotube sources have already been done by Dr. Zhou's research group at UNC (Zhang *et. al.*, 2005); however, this experiment validates the functionality of our system.

One of the main goals for the dual-spectrum design was to improve the contrast in soft-tissue imaging by using the differences in the distribution of the x-ray spectra with respect to x-ray energy. The mouse experiment demonstrated the system design worked as well as existing μCT single spectrum systems; making it possible to compare possible improvements in image contrast to a single spectrum source. To begin investigating the affect

of the two spectrums on soft-tissues, a soft-tissue contrast phantom was developed. This was a simple step projection phantom.

The soft-tissue phantom was block of gelatin cut in four steps with the thickest step on the bottom and each step less thick than the one preceding it. This is a projection phantom; as x-rays are passing through the phantom, different attenuation values will be projected onto the detector based on the attenuation of the gelatin and the different thickness of the phantom. This phantom was only used for single projection images. Each spectrum was used when imaging this phantom and the results were compared. The results were almost identical. This demonstrated that this phantom was a bad test for dual-spectrum imaging because it was a single material. Dual-spectrum, like dual-energy, imaging segments based on the way different x-ray energies affect the attenuation of different materials; thus, a single material phantom is not very useful.

After the soft-tissue block phantom failed, to find new direction, the system was characterized using a single pixel photon counting AMTPEK detector (Amptek). This was done to characterize the two spectra in the source. Originally there was no specific knowledge of the distribution of x-ray flux with respect to x-ray energy. Thus, characterizing the energy spectra would help in designing a better soft-tissue phantom and provide direction for optimizing a dual-spectra system.

The AMPTEK detector counts each incident x-ray photon and assigns it to an energy bin based on the estimated energy of the photon. Over time, an image of the spectrum is collected as the number of photons in each energy bin. This was done for each of the two spectra. The first spectrum was from the Molybdenum anode, shown figure 3.7.

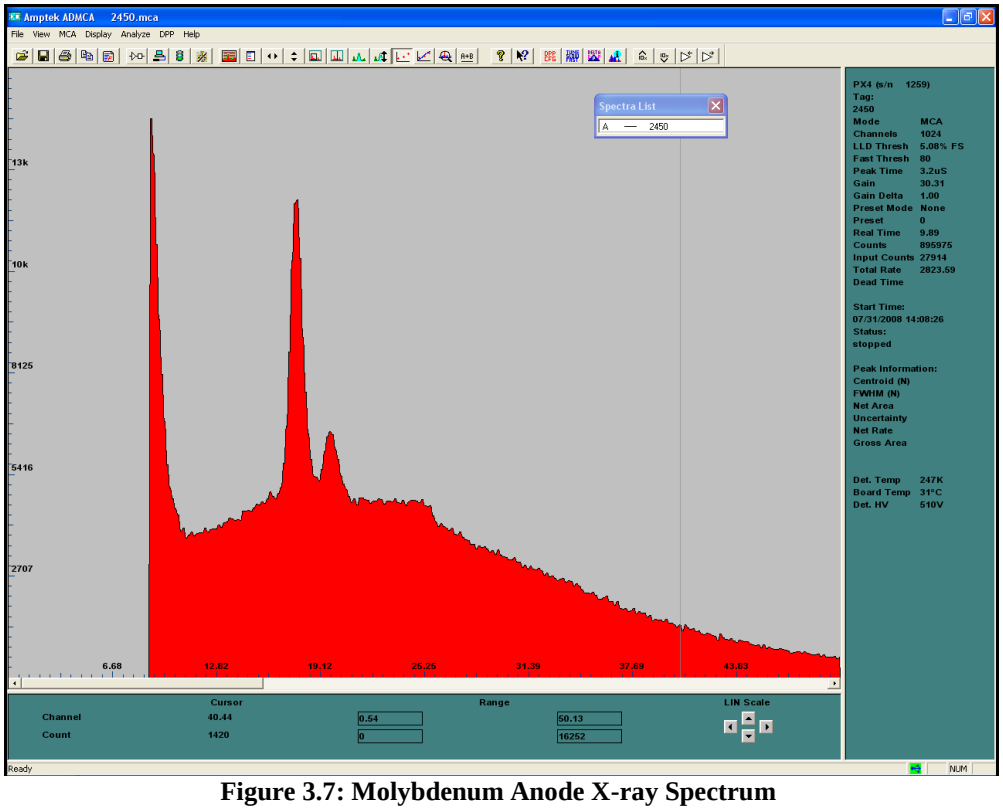

Figure 3.7: Molybdenum Anode X-ray Spectrum

The x-ray spectrum is measured as photon count over 1056 energy bins. The spectrum is displayed as screen capture of the measured spectrum as the red in the image. The total collection time for this experiment was one minute. The x-ray tube anode voltage was 45KV. The detection bins have been calibrated to correspond to the specific energies for each bin based on the known characteristic peaks. The x-ray spectrum has several key features: the overall Bremsstrahlung shape, the cut-off points, and the distinct peaks. The detector can only measure x-ray energy to 8KeV. The detector puts all photons below 8KeV into the 8KeV bin. This causes the first peak at 8KeV. This peak represents all the detected photons around and below 8KeV. This is an artificial peak and can be ignored. The other peaks in the image are at energies 17.5KeV and 19.6KeV. These are the two characteristic

peaks for molybdenum and used to identify the anode material. The second spectrum was a tungsten anode, shown in figure 3.8.

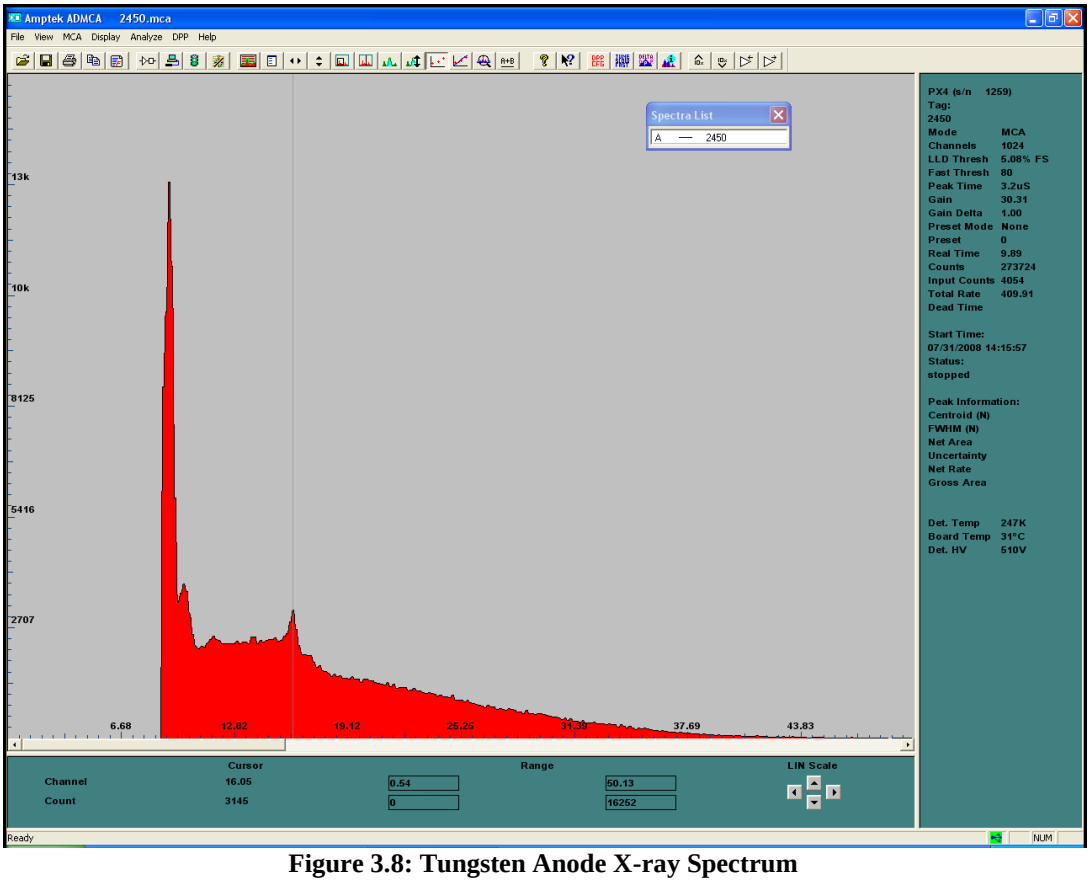

Figure 3.8: Tungsten Anode X-ray Spectrum

The overall shape of tungsten is similar to molybdenum, with no characteristic peaks. There is a large peak again at 8KeV and a basic triangular Bremsstrahlung shape with an end point at 45KeV. The overall x-ray flux for the tungsten is much smaller for the same collection time. The carbon nanotubes for the tungsten source in the original system design appear to have been damaged upon installation. This prevented an equal flux in both spectra. Tungsten has no characteristic peaks in the specified energy range. Tungsten has a peak at 60KeV, but that is above the maximum energy for the system design.

There are only two significant differences between the molybdenum spectrum and the tungsten spectrum, comparing figure 3.7 to 3.8. This difference is the characteristic peaks: molybdenum has two and tungsten has none within the specified energy range. In a dual spectra system, the molybdenum spectrum will have a lower average energy than the tungsten. However, this is not really true; the Hamamatsu detector energy range is 20KeV to 100KeV, with no x-ray detection below 20KeV. This means the two characteristic peaks are removed from the energy spectrum and the two spectra are almost identical in the detector energy range. The only other difference is the total x-ray flux. This is not a true difference because a dual-spectra system would like to use an approximately equal total x-ray flux for each spectrum.

The original design was shown to operate as a functional μCT system but not as a dual spectra CT system. The design was capable of replicating work already published but could not extend into a spectral comparison as was hoped. The design was limited by the detector which could only image x-ray energies above 20KeV and by the high-voltage, which was only rated to 60KV. This limited the x-ray spectra to an energy region where the two spectra where very similar. Thus, the system needed to be redesigned.

3.2. Energy Discriminating Micro-Computed Tomography System

The original design included two anode materials to do dual spectra CT. The original system relied on an integrating detector which could not identify many differences in the spectra. The initial experiments seeking to identify differences in the spectra with the integrating detector failed. After identifying the differences in the spectra as outside the range of the system, the system was redesigned. The new system was based on the AMPTEK detector replacing the Hamamatsu detector. This is a single pixel detector and required an

extensive system redesign to acquire tomographic data. This section presents the new detector and the system redesign required to acquire tomographic data.

3.2.1. Amptek Detector

When the original system was first designed, an Amptek XR-100T-CdTe single-pixel photon-counting detector and a PX4 amplifier/signal processor were used to examine x-ray spectra (results shown in figure 3.7 and 3.8); the detector is shown in figure 3.9 (image provided from vendor) (Amptek). These came as part of a set which also included the cables to connect the different components, a stand on which to mount the detector, and a collimator with a set of pinholes to protect the detector window.

Figure 3.9: Amptek Detector: images from vendor (Amptek)

The Amptek detector, shown in figure 3.9, is a single 3mmx3mmx1mm Cadmium telluride (CdTe) diode detector (Giakos *et. al.*, 1998; Matsumoto *et. al.*, 2002; Szeles, 2004; Brunner *et. al.*, 2009) Each x-ray photon creates a current across the diode proportional to its x-ray energy. The current across the diode is amplified internally in the detector unit and then passed to the PX4 amplifier which processes the current and assigns it to an energy bin. In this way, each individual x-ray photon is recorded individually and assigned to an energy bin. The x-ray spectrum is reflected in the number of x-ray photons in each energy bin.

In order to measure x-ray energy for each photon the photons must be measured individually. The detector was designed to measure multiple types of radiation, most of which emit a small number of high-energy photons. X-rays are emitted in much larger quantities than these other forms of radiation; medical x-rays have very high flux compared to other forms of radiation. To reduce the x-ray flux incident on the detector, a pinhole collimator is used, shown in figure 3.10 (image from vendor).

Figure 3.10: Collimator kit: image from vendor (Amptek)

The pinhole collimator consists of one or two tungsten pinholes placed on either side of a round brass spacer. The column is defined as the line through the two pinholes. Only x-ray photons which are within this column can be recorded and counted, the rest of the x-ray photons are absorbed or scattered by the collimator. The pinholes also define the width of the projection rays. The pinholes are much smaller than the CdTe diode.

The detector is plugged into the PX4 amplifier/signal processor which assigns each incident x-ray photon to a detector bin. The PX4 is connected to a computer and has an operating program which comes as part of the detector kit. This detector is controlled, and the results from the photon counts are displayed in this program. The program is fairly simple; most of the functions are focused on defining the detector parameters and stopping and starting photon counting.

The program, named ADMCA, allows a user to choose between 256, 512, 1024, 2048, or 4096 energy bins, called channels, spanning the energy range of the detector. The range of the detector is set between 10KeV and 100KeV based on the thickness of the CdTe diode. In this range the detector is almost 100 percent efficient, with less than one percent of variation in this range. The program also allows the operator to set the amount of time the detector collects photons. The program displays the output as the number of photon counted in each channel for the specified length of time. This output can be calibrated using two known sources with different energies to assign specific energy values to each channel. These values represent the average energy which the channel spans based on the two calibration energies. This calibration can be saved and used again for the particular setting. The calibrated measurement is the radiation spectrum for the measured x-ray field through the collimator.

The measured spectrum can be saved in two different ways: as a .mca file, which is specific to the ADMCA program, or as an EXCEL file. The first is a file which can only be opened by ADMCA programs and is useful for comparing two or more spectral measurements. The .mca file saves all of the information: the counts, the calibration, the time, the total counts, the count rate, and peak information. The second is as an EXCEL file which saves each channel to a row in an EXCEL spreadsheet. This saves the same information, but it is entirely numerical with no graphical display. This is more useful because it allows the data to be ported to other programs or investigated numerically.

The ADMCA program also has an automated collection feature. This allows the operator to set up a specified number of measurements. Each measurement has an operator designated collection time ranging from one second to two hours and a specified rest time

between each measurement. Each measurement is automatically saved to a designated file. There is an individual file for each measurement. Each of these files has the same name with the measurement number added to the name. The PX4 has a digital output line which is high when the detector is collecting and low when it is reading.

The AMDCA program was written to operate the detector independent of other programs and it does not interface with LABVIEW at all. To interface with LABVIEW the digital output line of the PXA is connected to the DAQ. This allows for basic communication between the detector and LABVIEW. The LABVIEW program knows when the detector is reading. The data collected are either processed in AMDCA or read to an EXCEL file and processed with another program.

This detector was designed to measure a radiation spectrum. The electronic noise in the system is very small and there is almost no scatter due to the collimator; thus, the only significant noise is due to the random nature of photon counting. As the number of channels increases, this noise increases relative to the signal. This is a normal noise/resolution trade-off. As the energy resolution increases so does the noise in the channels. As the total collection time increases the noise decreases, due to the nature of photon counting. This is because the variation is less significant if there are a large number of photon counts in each channel. The initial measurements were collected over a long period of time (figures 3.7 and 3.8) so there is not a lot of noise in these images. Noise becomes a problem when the detector is used for CT measurements. These measurements require a much shorter collection time.

3.2.2. Single Pixel CT

The Hamanatsu flat-panel integrating detector is replaced with the Amptek XR-100T single-pixel photon-counting detector. A photo of the new system is shown below in figure 3.11.

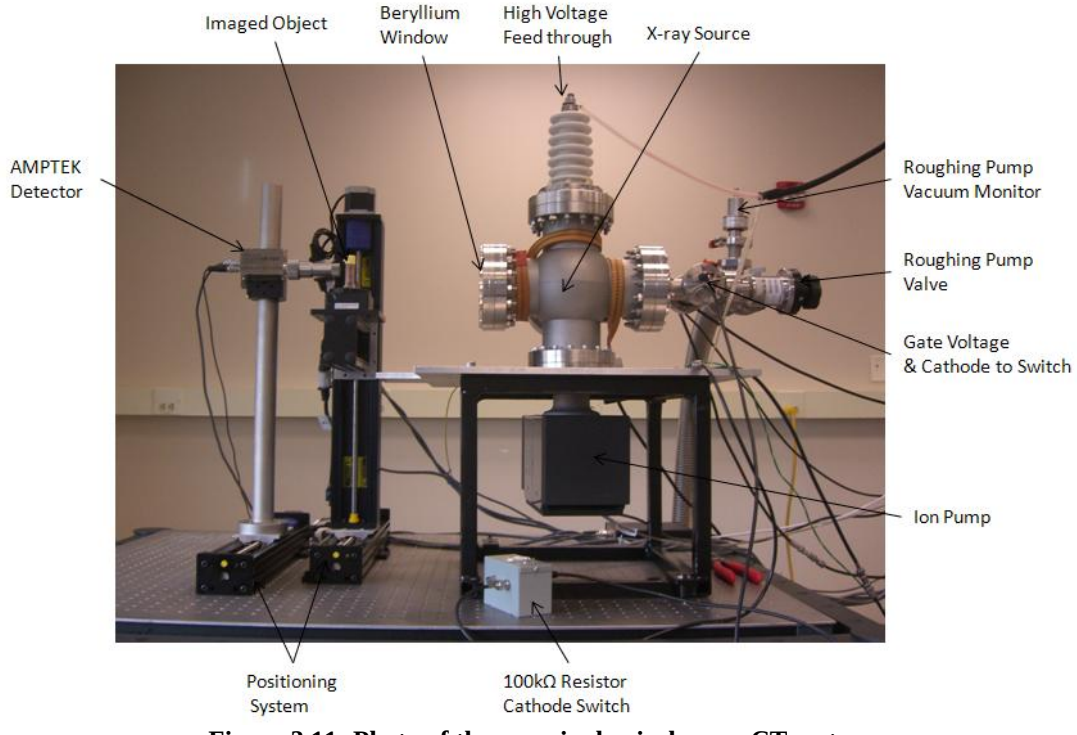

Figure 3.11: Photo of the new single pixel x-ray CT system

The right side of figure 3.11 is the x-ray source. This has not changed from the original design. The same vacuum chamber is used, with a roughing pump and ion pump. The source has the same high voltage feed through and beryllium window. Therefore, the right side of this picture is also a representation of the original system. The left side of the picture shows the Velmex linear slides in a new orientation (labeled as positioning system) and the AMPTEK detector. There are now only two dimensions of motion, with the detector on a moveable axis. The third dimension is removed because it is no longer necessary and because it is useful to move the AMPTEK detector to find an optimum imaging location. There are no

further changes to the physical implementation of the system. The majority of the redesign is in the way tomographic data are acquired.

3.2.2.1. System Theory

The changes in the system were inspired by Claesson (Claesson *et. al.*, 2001). In this paper the authors built an x-ray CT demonstrator based on a single energy gamma source and an Amptek XR-100T CdZnTe detector. This system was designed to demonstrate first generation CT concepts, specifically parallel beam projection data. To demonstrate this, the system was designed to be simple and obvious to students rather than efficient.

The system proposed by Claesson measured a single projection ray at a time, defined from a single energy gamma source through the object to the Amptek detector. The source and detector configuration was then translated some distance alongside the imaged object and another projection ray was measured. This was repeated a number of times. This built a set of parallel projection measurements, as defined in classical CT as a strip of projection rays. The source and detector were then rotated some degree and the process was repeated for the same number of projection rays, measured individually again. Measuring each projection ray individually allows the students to grasp parallel-beam projection data. The detector and source are rotated 360°, completing the computed tomography projection data. The collected data are a photon count for a single energy along each projection ray. These data are plugged into MATLAB (Matlab) which uses an inverse radon transform to reconstruct a slice through the imaged object. The MATLAB function was designed to demonstrate to students how the radon and inverse radon transform works with simple data. This system was designed to provide students with an empirical understanding of CT.

The source and detector were mounted on a gantry which rotated around the subject. The detector is a single-pixel detector, so the source-detector gantry is also translated laterally on the side of the subject to build a set of projection rays simulating a set of parallel pencil beams and a strip detector. This system served as starting point for the redesigned source.

The new system is designed around a detector capable of only measuring a single projection ray. This redesign was based on the CT demonstrator proposed by Claesson (Claesson *et. al.*, 2001). However, rather than a single energy gamma source, the new system has a polychromatic x-ray source. Thus, the AMPTEK detector acquires photon counts for multiple energy bins rather than just at a single energy. The other significant difference between the redesigned system and the one proposed in (Claesson *et. al.*, 2001) is the source and detector are stationary and it is the object that moves to create tomographic data.

For this new system, a projection ray is defined as the path from the x-ray source through the pinhole collimator to the detector. This projection ray remains stationary, the source and detector are not moved, during an entire CT scan. The object is placed on the rotation table mounted on the Velmex linear slides (figure 3.11). The linear slides are used to translate the object through the projection rays with some user designated step size. The table starts the object on one side of the projection ray and moves it through the projection ray until the object is fully on the other side of the ray. The table then rotates the object some designated angle and translates the object back through the projection ray. This is repeated for a span of 180°. After each table step, the object pauses for some collection time. During this collection time, the x-ray spectrum is measured along the projection ray. This process is demonstrated schematically in figure 3.12.

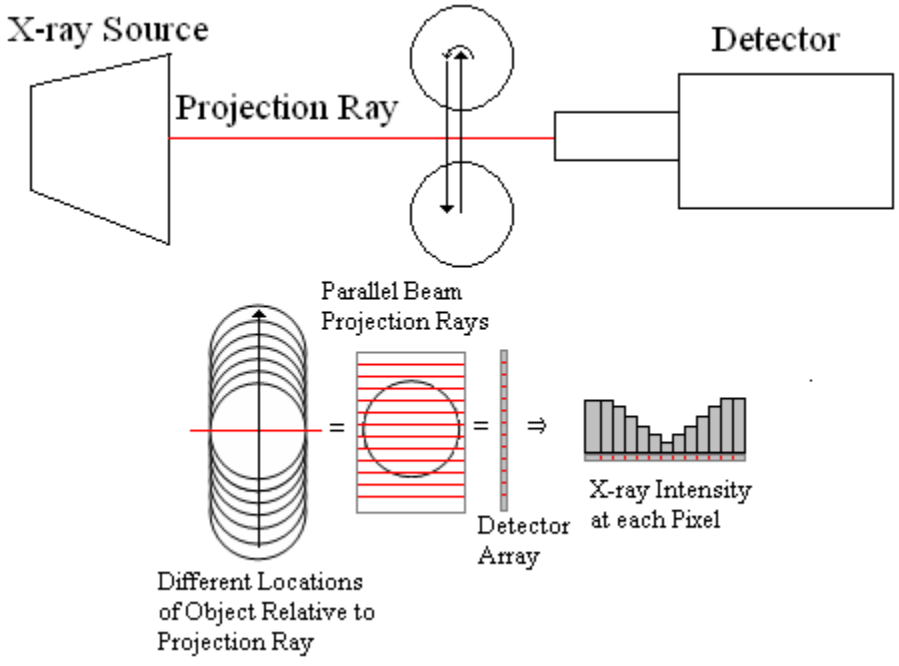

Figure 3.12: Graphical description of a single-projection ray CT implementation.

As the object is translated through the projection ray, each measurement is a projection ray through a different portion of the imaged object. Therefore, this system could be described as a set of parallel projection rays passing through a stationary object and collected on a line detector. This is shown in the bottom-left of figure 3.12; the object translated through the projection ray is the same as a set of parallel beam projections to a line detector array. Translating the object through the projection ray is a projection of the object to a line for one angle. Repeating this for multiple angles over a span of 180° builds a set of tomographic data for a slice through the object at the height the of the projection ray.

3.2.2.2. System Implementation

The system was redesigned to create a CT scan one projection ray at a time, shown in figure 3.11. The linear slides are rearranged from the three-dimensional orientation (figure 3.1) to a two dimensional orientation. The two dimensions are perpendicular to the projection ray, one moves the object through the ray transversely and the other vertically. The

remaining linear slide is used to mount the detector. The detector is fixed vertically on a cylindrical stand but it has freedom of motion in transverse direction because the stand is mounted on the linear slide.

The first step implementing the single projection CT is finding the best fixed projection ray. The detector's fixed vertical location is chosen to place the projection ray in the center of the vertical x-ray emission, found with the prior knowledge of the source geometry. The detector is then translated through the x-ray field to find a location with the highest x-ray flux for a set gate and anode voltage. Once an optimal location is identified, the detector remains fixed for the CT scan.

The rest of the implementation is new software to control the CT motion, source voltages, and detector. This new program is shown in figures 3.13 and 3.14 for the user interface and source code respectively.

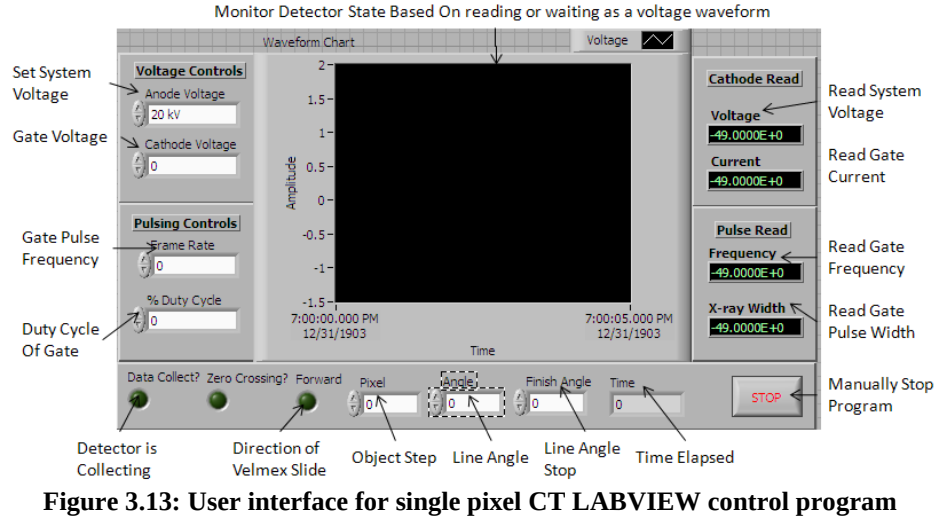

Figure 3.13: User interface for single pixel CT LABVIEW control program

The user interface allows a user to set all of the key voltages and timing for the source. The anode voltage, gate voltage, and gate pulsing are all set and read in the same way as the simple source control (see figure 3.4). The linear slides are controlled by the direction

of the slide, object step and angle settings at the bottom of the program. The Amptek detector is not directly monitored using this program, the AMDCA program is used; this program interface is shown in figures 3.7 and 3.8. However, the detector communicates with the program through a DAQ and that communication is shown as a continuously sampled waveform in the center of the user interface.

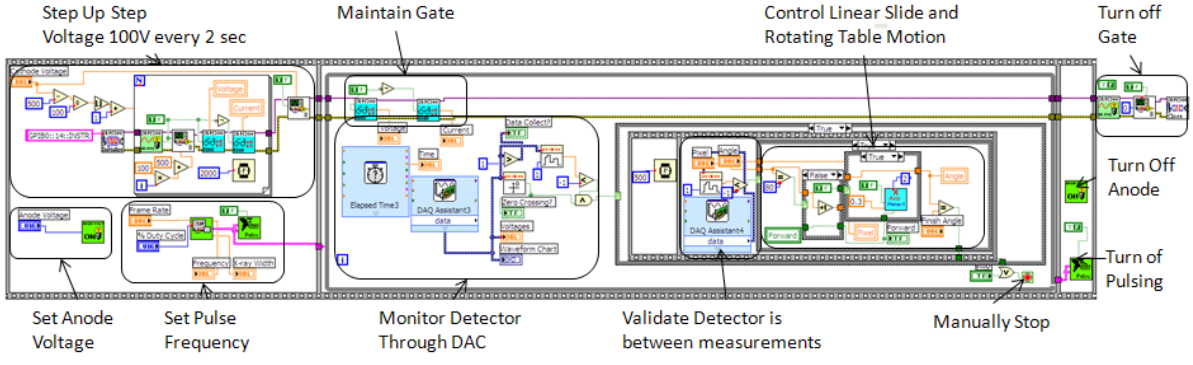

Figure 3.14: LABVIEW source code for single pixel CT control program

The LABVIEW code uses a sequence control to first set the anode voltage, gate voltage, and gate pulsing; again this is similar to the simple code in figure 3.4. The next step is the bulk of the control code; this is placed in a loop and operates continuously until either the manually stop button is pressed or the specified number of projection lines have been acquired. The final step is turning off all voltages and pulse generator.

This program (figures 3.13 and 3.14) relies on an interface through a DAC with AMDCA program to control the detector. The AMDCA program is set to take a specified number of measurements with a user defined measurement time and wait time between each measurement. Once the voltages are set, the program waits until the AMDCA program has started; if this does not happen the program will not work. Thus, both programs run simultaneously. To run both programs, the PX4 signal processor outputs a voltage which is connected to a DAQ which communicates with the LABVIEW program. The LABVIEW

program monitors the voltage on the read line, figure 3.14 labeled “Monitor detector through DAC,” the program displays this voltage on the user interface, figure 3.13 labeled “Monitor detector state based on reading or waiting as a voltage waveform.” When this voltage goes from high to low the next sequence is initiated. The program waits half a second and then checks to make sure the read line is still low. The read line often goes low for a moment in the middle of a measurement. The program waits and checks to ensure this does not trigger a movement. If the read line remains low for half a second, the object is moved. After the object is moved the process starts again.

The program is designed to acquire CT data one projection ray at a time (figure 3.12). When the read line is low, the LABVIEW program (figure 3.14) moves the object. There is some set step size and number of steps. The step size is the distance the object is translated during a single step. The number of steps is the number of projection rays acquired for each angle. The program begins at zero and counts by one each time the object is moved, checking each time to make sure the step number is below the programmed number of steps. If the step number is equal to the number of steps, the program rotates the object and sets the step number back to zero. Each time the object is rotated, the direction of the slide is changed. This allows the object to move back and forth through the projection ray. One direction is labeled positive and the other negative. The angle the object is rotated is determined by the user to give full tomographic coverage. This movement continues until the finish angle is reached. The finished angle determines the number of projection lines the program detects.

A complete CT scan spans 180°; however, the finished angle is not necessarily set to 180°. As x-rays are produced, the vacuum slowly breaks down over time. This program takes a long time to acquire data, due to only measuring a single projection ray at a time. As the

vacuum breaks down, the source begins to arc; this can damage the carbon nanotube sources and create inconsistent flux density. Therefore, the program is set to only collect the projections for two to ten angles at a time. After the program has run, the source is allowed to rest before another two to ten angles are run. This process is repeated until the full 180° span has been covered.

The data acquired by this program (figures 3.13 and 3.14) are collected using the AMDCA program and stored as an EXCEL file for each projection ray. These EXCEL files are read into a MATLAB function which places all of the projection rays into a matrix indexed to the projection ray number by the number of energy bins. These data are then reformatted into a sinogram for each energy bin. For a single energy, a sinogram is defined as a matrix where each row represents a different angle and each column a different transverse position of the object for the given angle. A sinogram is a typical data form for CT data (Hounsfield, 1979).

The initial data in MATLAB were a sinogram for each energy bin. Each sinogram is reconstructed using the IRADON function in MATLAB. This is the inverse radon transform with a Ram-Lak filter; this is the same as simple filtered back projection (FBP) for a parallel beam x-ray field. The reconstruction creates an attenuation map for each energy bin corresponding to the slice through the object. The set of sinograms and corresponding FBP reconstructions for each energy bin are the final data forms for the new x-ray system.

3.3. New Source Design

The original system design and the new single pixel CT system used the same simple carbon nanotube source. This source burned out with time and use; the carbon nanotubes emit fewer electrons for the same gate voltage over time, slowly reducing the x-ray flux.

After a number of CT scans, the carbon nanotube sources ceased producing sufficient x-ray flux to do imaging. Thus, it was necessary to replace the carbon nanotubes in the original x-ray source. However, rather than simply replacing the sources, the entire x-ray source was redesigned. This was done to make it easier to replace the sources in the future and to incorporate advancements made by Dr. Zhou's group (Liu *et. al.*, 2006; Yang *et. al.*, 2008, Cao *et. al.*, 2009) since the beginning of this project.

3.3.1. Source Theory

The field emission carbon nanotube sources have been used to design a new stationary tomosynthesis system (Yang *et. al.*, 2008). Tomosynthesis is a limited angle tomographic reconstruction, typically used in mammography where a full circular scan is less practical (Andersson *et. al.*, 2008). The source or detector is translated to create a limited number of different source detector orientations with respect to the imaged object. Each of these orientations is a different projection angle, creating a limited angle scan of the object. The additional information acquired in these different angles helps in identifying the depth, location, and composition of the different materials in the imaged object in less time and less dose than a full tomography; although with less accuracy as well. Rather than translating a source or detector to gather the tomosynthesis data, an array of carbon nanotube sources (Liu *et. al.*, 2006) is used create the different source detector orientations.

The source is designed as an array of field emission carbon nanotube sources. Rather than translating the source, each element in the array turns on in sequence to create the sweep. This is possible because it is easy to rapidly turn each of these sources on or off using the gate voltage for each source. For this to work each of the sources needs a narrow focal

spot; thus, an electron steering stage is added to control the focal spot for each carbon nanotube source element.

The electron steering stage consists of two focusing elements, shown in figure 3.15. The source has a layered design. The first layer is the substrate the carbon nanotubes sit on. This layer is grounded to create a potential between the cathode and the gate and the cathode and the anode. The next layer is the gate; this is a metal plate with holes directly over the carbon nanotubes. The whole plate has a set gate voltage which creates the electric field over the nanotubes for field emission. The next two layers are another two metal plates with holes in line with the gate and carbon nanotubes. A voltage applied to each of these plates modifies the electric field between the carbon nanotubes and the anode to prevent the electrons from spreading out in the vacuum and forces them into a beam. The dimensions of this electron beam determine the dimensions of the focal spot

3.3.2. Source Design

The new source was based on a design by Gouhua Cao (Cao *et. al.*, 2009), with modifications to the anode to incorporate two materials and changes to fit our chamber. This new design is shown in figure 3.15. The carbon nanotube source and the electron steering elements sit in a ceramic shell on an aluminum base. A ceramic pillar keeps the anode at a fixed height above the source and steering elements. There are two anode materials: tungsten and molybdenum, which sit on the lower part of the copper anode facing the carbon nanotube source. The aluminum base is designed to sit in the base of the vacuum chamber; the circular shape matches the circular shape of the chamber (figure 3.11). This base is electrically isolated from the source by the ceramic spacer and ceramic shell. The carbon nanotube

source and electron steering elements in the ceramic shell are shown in more detail, from multiple angles, in figure 3.16.

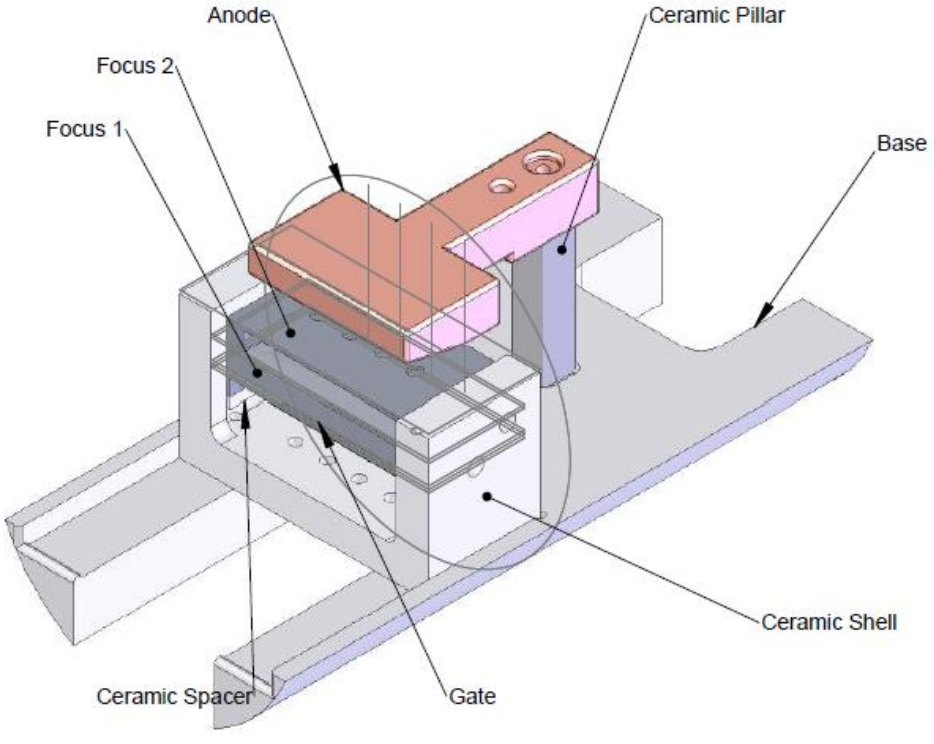

Figure 3.15: New x-ray source assembly. This image shows all of the pieces for the new assembly including: gate, focusing, and anode along with the spacers, shell and base. To see where carbon nanotubes are placed, see figure 3.16.

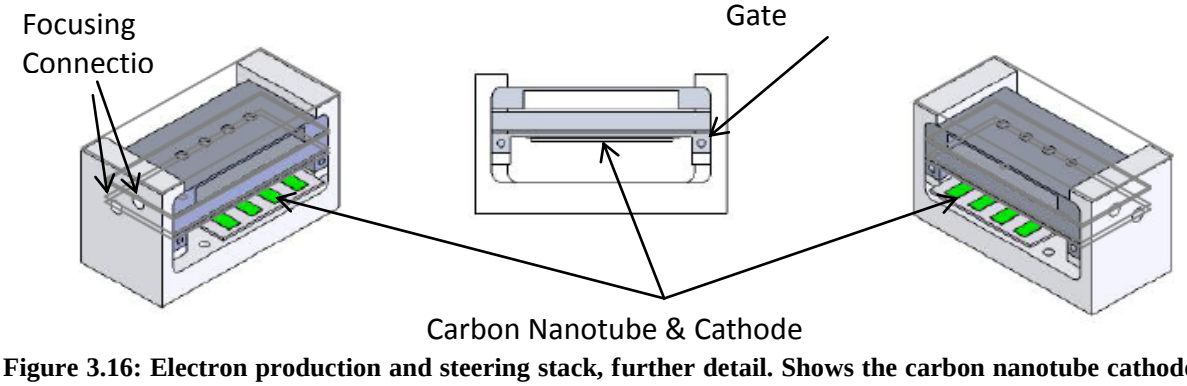

Figure 3.16: Electron production and steering stack, further detail. Shows the carbon nanotube cathode, gate, and two to focusing elements along with the ceramic shell these are housed in.

The new source has four carbon nanotube source elements, each mounted on its own substrate, shown as the green strips in figure 3.16. These are all mounted on a glass slide to hold them in place and electrically isolate them from each other. The carbon nanotubes sit directly under the gate; there is a thin glass separator between them, with a 150μm gap between them. The gate has four circular holes each directly above one of the carbon nanotube source elements. A wire mesh covers the hole. The wire mesh keeps the electric field over the nanotubes, but allows the electrons to pass through. The wire mesh is spot-welded onto the gate using a laser spot-welder. The first focusing element sits directly above the gate and is a thick plate of metal. The first focus has cone-shaped holes which have a smaller radius closer to the gate and a larger radius further away from the gate. This allows the electrons to spread a little but controls how they spread. The second focus element has more empty space between the element and the previous focus. The second focus has circular holes in line with the gate holes and with the same radius as the upper radius of the first focusing element. The first focusing element allows the electrons to spread in a controlled shape, the pulls them back and focuses them on the anode. Ceramic shapers keep each of the metal plates electrically separated and in the correct location in the stack.

Kapton-coated wires are used to control each of the different elements in the source. Kapton coating keeps the wires electrically isolated in a vacuum. Alligator clips connect the wires to the different substrates. Banana plugs connect the wires to the gate and focusing elements. There are plugs in the gate and focusing elements, through the ceramic shell (shown in figure 3.16). The wires exit the vacuum via BNC connectors at the back of the vacuum chamber (figure 3.11, labeled “Gate Voltage”).

3.3.3. Implementation Issues

The source was produced in the machine shop at the University of North Carolina Chapel Hill. However, there were a few key issues in installing the source in the vacuum chamber. These included: electro-polishing the source, how to actually install the source in the vacuum chamber, and finally turning the source on and finding optimal focusing voltages.

3.3.3.1. Electro-Polishing

The source stack (figure 3.16) is three metal plates in an electric field between the anode and cathode. Any impurities on the surface of one of these plates could cause arcs from the anode to the metal plate or from the metal plate to the cathode. This damages the carbon nanotubes, causing them to burn out faster. Therefore, prior to installation of the system, all of the metal pieces in the source are polished using electro-polishing.

The first step in electro-polishing the metal plates is scrubbing each of the metal plates with sandpaper to apply an initial rough polish. The plates are then cleaned with distilled water. Each metal plate is then immersed in an electro-polishing solution (EPS) and electrically charged with a DC voltage. The EPS is a strong acid. Each plate is connected to a positive DC voltage of between 1000 and 1500 volts. A second metal plate, made of the same material of the source plate (if the source plate is steel the second plate is also steel) is connected to the ground of the DC source. This makes the source plate the anode and the second plate is the cathode, both immersed in the acid. The acid is heated to increase the chemical reactions. The acid and the electric field strip the top layer off the metal plate and deposit it on the second plate. This removes any impurities on the surface of the metal plate. The acid is cleaned off the plate by soaking the plate in acetone and sonicating it for an hour.

After the acid is cleaned off, the plates are cleaned with distilled water, dried with forced air, and placed in a temporary vacuum chamber.

This process is repeated for the steel gate and focusing plates, the copper anode, and the aluminum base. The molybdenum and tungsten anodes in the copper base are cleaned with the copper electro-polishing. There is no real effect on the molybdenum or tungsten due to this process. The ceramic spacers and shell are scrubbed with sandpaper, sonicated in acetone, and rinsed with distilled water. After the gate is electro-polished, the gate mesh is attached to the lower surface using a laser spot-wielder.

3.3.3.2. Vacuum System

To install the new source, the vacuum chamber must be opened and the old source removed. However, the new source was too large to use the door. Thus the vacuum chamber had to be disassembled. The vacuum chamber has a round T-shaped central chamber where the x-ray source sits. Each of the arms is bolted to a round plate: one houses a beryllium window for the x-rays to exit the system, another has the high-voltage anode connection, another is the door, and the final one houses the output/input for the wires controlling the source and links to the roughing pump valve. Each of these plates is bolted to the main chamber with 16 large bolts and sealed with a round copper seal between the plate and the chamber. The anode plate and the plate housing the wires and valve are taken off to open the main chamber. The source is then placed in the main chamber. Wires are attached to each of the source elements and the high-voltage line is connected to the anode. The plates are then bolted back on the main chamber. New copper seals are used so that no leaks will develop when the vacuum is reestablished. Once the plates are bolted on again, the only access to the chamber is through the door. This is not very useful; to change the carbon nanotubes the

entire source must be removed because the carbon nanotubes sit at the base of the stack and cannot be removed without pulling the entire stack. The stack is too large to be pulled out of the door. Once the source is in place, the system is roughed using the roughing pump for a day. The ion pump is then turned on again and the system is baked for a day. Overall, replacing the source, or making a change to the source, takes two days just to reestablish the vacuum.

3.3.3.3. Source Voltages

There are three DC voltages, besides the high-voltage anode, which control the source. These are connected to the source via banana plugs and Kapton wires which exit the vacuum chamber through BNC cables. There are plugs for these designed in the source. The cathode is connected to the ground using alligator clips and Kapton wires. The alligator clips attach to the substrate, shown as green strips in figure 3.16. It is very important to have a good electrical connection, so a piece of aluminum foil is placed between the clips and the substrate.

The gate voltage determines the electron flux from the carbon nanotubes. The gate voltage varies from 1000 volts to 2000 volts depending on the desired x-ray flux for a given experiment. If the voltage goes higher than 2000 volts, the carbon nanotubes may be damaged, due to the electric field produced by that voltage with 150μm gap between the gate and the carbon nanotubes.

The focusing elements have a fixed voltage on each of the plates. The voltage on the plates determines the focal spot.

3.4. Initial Data

This new system acquires data as an x-ray spectrum (figure 3.7) projected through an imaged object onto a single-pixel photon-counting detector (figure 3.9). This projection is along a single projection ray (figure 3.12). The object is moved through this ray, simulating a strip detector. Therefore, the initial data are a set of x-ray projections which are arranged as a set of sinograms (figure 3.17).

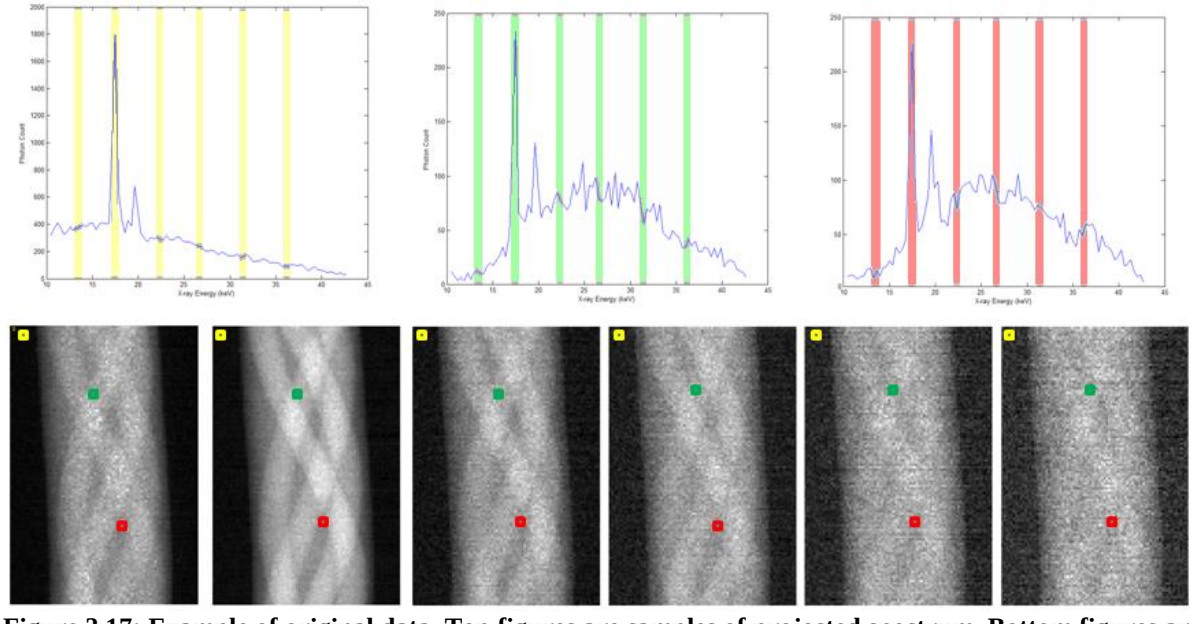

Figure 3.17: Example of original data. Top figures are samples of projected spectrum. Bottom figures are sinograms as selected energy bins.

The original data are first collected as projected spectrum (top three images in figure 3.17). The first image (top left) is the projected spectrum with no object. This is the molybdenum spectrum through the air (same as figure 3.7). The maximum photon count, in the peaks, is near 2000. The second two images in the top of figure 3.17 are the same x-ray spectrum projected through an object. These images show a much lower photon count, the maximum photon count is now close to 250. The object attenuates the x-ray spectrum as it is projected through the object, resulting in a much lower photon count. These images also show a

significant amount of noise along the energy axis. This is illustrated by the sharp variations in projected x-ray spectra (figure 3.17, top three images).

A different sinogram is created for each energy bin in the projected spectrum. Six of these sinograms are shown at the bottom of figure 3.17. Each pixel in these sinograms represents a different projected x-ray spectrum. The three spectra shown in the figure correspond to the three pixels shown in the sinograms; each spectrum is color-coordinated with the corresponding pixel in the sinogram. The six colored bars in each projected spectrum correspond to the energy bins for the six sinograms; the six sinograms are in the same order as the six bars in each spectrum. In actuality, there is a sinogram for every energy bin in the spectrum; but this would be too much data to show in a single figure.

The initial projected x-ray spectra and corresponding sinograms demonstrate the most significant shortcoming of this new system: noise. The detector segments the incident x-ray spectrum into a number of energy bins. As the number of energy bins increase, the noise will also increase relative to the signal. Both the spectra and the sinograms in figure 3.17 demonstrate that as the photon count decreases, the noise increases. The energy bin with the highest photon count, at the molybdenum peak, has the least noise in the corresponding sinograms. The energy bins with the lowest photon counts, ones at higher energies (right of each spectrum in figure 3.17) have the most noise in the corresponding sinograms. The spectrum projected through the object has a very low photon count at low energies (energies 10-16keV in right two spectra in figure 3.17), however, the spectrum through the air has a much higher photon count in the same region. Therefore, there is a higher attenuation signal here.

The sinograms at different energy bins represent a completion of the new CT system. The system is capable of collecting tomographic projection data (the sinograms) and densely sampling the projected x-ray spectrum. The reconstruction of attenuation from these sinograms is discussed in subsequent chapters, along with noise suppression algorithms.

3.5. References

3-D Doctor, A freeware available at: http://www.ablesw.com/3d-doctor/

Andersson I, Ikeda D.M., Zackerisson S., Ruschin M., Svahn T., Timberg P, and Tingberg A., 2008, "Breast tomosynthesis and digital mammography: a comparison of breast cancer visibility and BIRADS classification in a population of cancers with subtle mammographic findings," *European Society of Radiology*, vol. 18, pp. 2817-2825.

AMPTEK detector XR-100CT, product information available at: http://www.amptek.com/xr100cr.html

Brunner F.C., Clemens J.C., Hemmer C., and Morel C., 2009, "Imaging performance of the hybrid pixel detectors XPAD3-S," Phys. Med. Biol, vol. 54, pp. 1773-1789.

Cheng Y. and Zhou O., 2003, "Electron field emission from carbon nanotubes," *C.R. Physique 4*, pp. 1021-1033.

Cho Y., Moseley D.J., Siewerdsen J.H. and Jaffray D.A., 2005, "Accurate technique for complete geometric calibration of cone beam computed tomography systems." *Med. Phys.*, vol. 32, pp. 968-983.

Claesson T., Kerek A., Molnar J. and Novak D., 2001, "A CT demonstrator based on a CZT solid state detector," in *IEEE Nuclear Science Symposium Conference Record*, vol. 3, pp. 1644-1646.

Corba_exxim, http://exxim-cc.com/products_cobra.htm

Eichmeier J.A. and Thumm M.K., 2008. *Vacuum electronics: components and devices*, New York, Springer.

Giakos G.C., Guntupalli R.K., Vedeantham S., Chowdhury S., and Pillai B., 1998, "A computed tomography CdZnTe based scanning detector," *IEEE Instrument and Measurement Technology conference*, May 18-21, pp. 462-465.

Hamanatsu Detector, Flat Panel Sensor C9321CA-02, information and datasheet available at: http://nationalxray.thomasnet.com/viewitems/digital-image-detectors/hamamatsu-x-ray-flat-panel-sensor?&forward=1

Hounsfield G.N., 1973, "Computerized transverse axial scanning (tomography).1. description of system," *British Journal of Radiology*, vol. 46, pp. 1016-1022.

LABVIEW version 8.2.1, National Instruments, 2007.

MATLAB version 7.7.0.471 2008 B Natick, Massachusetts: The MathWorks Inc., 2008.

Matsumoto M., Miyajima S., Yamamoto A., Yamazaki T. and Kanamori, 2002, "Measurement of diagnostic X-ray spectra using CdZnTe detector," *IRPA Proceedings*, vol. 7, no. 43.

Ohara H., Honda C., Ishisaka A., and Shimada F., 2002, "Image quality in digital phase constant imaging using a tungsten anode x-ray tube with a small focal spot size," *Physics of Med. Imag.*, vol. 4682, pp. 713-723.

Paulus M., Sari-Sarraf H., Gleason S., Behel J., Thompson L. and Allen W., 1998, "A new X-ray computed tomography system for laboratory mouse imaging," *IEEE Trans. Nuclear Science*, vol. 2, pp. 1259-1263.

Szeles C., 2004, "CdZnTe and CdTe materials for X-ray and gamma ray radation detector applications" *Phys. Stat. Sol.*, vol. 241, pp. 783-790, 2004

Zhang J, Cheng Y, Lee Y.Z, Gao, B., Qiu Q., Lin W.L., Lalush D., Lu V, and Zhou O, 2005, "A nanotube-based field emission x-ray source for microcomputed tomography," *Review of Scientific Instruments*, vol. 76.

Liu Z., Yang G., Lee Y.Z., Bordelon D., Lu J., and Zhou O., "Carbon nanotube based microfocus field emission x-ray source for microcomputed tomography," *Applied Physics Letters*, vol. 89, no. 10, 2006.

Yang G., Rajaram R., Cao G., Sultana S., Liu Z., Lalush D., Lu J, and Zhou O., "Stationary digital breast tomosynthesis system with a multi-beam field emission x-ray source array," *Physics of Medical Imaging, Proc. Of SPIC*, Vol. 6913 6913, 69131A (2008); doi:10.1117/12.770622

Cao G., Lee Y.Z., Peng R., Liu Z., Rajaram R., Calderon-Colon X., An L., Phan T., Sultana S., Lalush D.L., Lu J.P., and Zhou O., "A dynamic micro-CT scanner based on carbon nanotube field emission source," Phys. Med. Bio., vol. 54, pp. 2323-2340, 2009.

4. First Paper: Full Spectrum CT Reconstruction Using a Weighted Least Squares Algorithm with an Energy-Axis Penalty

This is the first paper published using the new energy-sensitive CT system presented in this dissertation. The paper was accepted for publication on March 28, 2010 to IEEE Transaction on Medical Imaging. This paper was published in February, 2011 in Volume 30, Number 2, pages: 173-183. The paper presents a method for noise suppression along the energy axis using a penalized weighted least squares approach. Noise suppression is the first step in analyzing the energy-sensitive CT data.

4.1. Abstract

Recent developments in X-ray detectors have created the potential to perform energy-sensitive X-ray computed tomography (CT); that is, to reconstruct a series of CT images associated with different X-ray energies from a single scan. In this paper we propose a penalized weighted least squares (PWLS) algorithm for reconstruction of polychromatic energy-differentiated X-ray CT data and a unique experimental setup to take energy differentiated X-ray CT data. The experimental set-up is designed to acquire a complete X-ray spectrum for every projection ray. We use this data to estimate the linear attenuation coefficient as a function of energy for every pixel in the reconstructed attenuation map. We use prior knowledge of the properties of attenuation spectra to smooth the reconstructions, significantly reducing the noise and improving the contrast-to-noise ratio (CNR) in the reconstructed images without significantly biasing the data. We conclude that this algorithm is an effective method for reconstructing energy-sensitive CT data, and provides justification for further research in energy sensitive CT systems.

4.2. Introduction

Most X-ray computed tomography (CT) systems use digital integrating detectors which assign a single value to the intensity of the incident X-ray field, integrating all X-ray photons weighted by energy. Image reconstruction from this data reduces the signal estimation to a single effectively monochromatic attenuation parameter. In reality, X-ray fields are polychromatic: a spectrum of intensities spread over a range of energies. The contrast in X-ray images is related to the linear attenuation coefficient; this is a product of the mass attenuation coefficients and the densities of the different materials in the imaged object (Webb, 1996). The mass attenuation coefficient, independent of density, varies with X-ray energy (Hubbel and Seltzer, 1996). Integrating detectors reduce the attenuation information to an average energy value, resulting in a single linear attenuation coefficient. Any additional information provided by the change in mass-attenuation with respect to energy is lost.

Statistical reconstruction methods have been developed to include a spectral model into the reconstruction from integrated detectors, to account for the polychromatic nature of the real X-ray signal (Lasio *et.al*, 2007; Whiting *et.al*, 2007). This generally incorporates some piece of the missing energy information into a statistical reconstruction model. In (Lasio *et.al*, 2007), a more accurate compound Poisson model is used to account for the energy integration of the detector, reducing artifacts in the reconstructions. In (Whiting *et.al*, 2007) properties of the integrating detector are used to create more accurate estimates of the projections in the sinogram. In both of these papers the polychromatic nature of the x-rays is considered for noise modeling.

It has been shown that the energy information in X-ray attenuation, for a single material, can be reduced to photoelectric absorption and Compton scattering (Christ, 1984)-

(Alvarez and Macovski, 1976). If one uses well separated energies it is possible to find these two components of attenuation for most materials (Talbert *et.al*, 1976). This is the justification for dual energy computed tomography (DECT). DECT takes two X-ray CTs, one at low energy and one at high energy. This method is used to separate specific materials and tissues based on the different combinations of photoelectric absorption and Compton scattering (Marshall *et.al,* 1981; Bazalova *et.al*, 1981; Tsunoo *et.al*, 2004) or to separate dense and soft tissue (Taibi *et.al*, 2003; Sukovic and Clinthorne, 2000). The typical clinical use is for separation of soft tissue from dense tissue in X-ray CT images. This is done by subtracting the low energy image from the high energy image (Taibi *et.al*, 2003) producing a cleaner image of either bone or contrast agents.

DECT increases the energy information available, but is still limited to only two measurements. This has been shown sufficient for some material decomposition (Christ, 1984; Alvarez and Macovski, 1976). However, for an object composed of more than two materials, two energy measurements are insufficient. DECT often assumes a mixture model of two or more basis materials which comprise the image object. Simple models can often corrupt the reconstructed image; more complicated models may be needed (Goh *et.al*, 2008). The other limitations to DECT are a potential decrease in signal-to-noise ratio and an increase in patient dose (Lohan *et.al*, 2008).

Recently there has been a surge of interest in extending DECT to a more accurate polychromatic X-ray CT method. These works have been divided between theoretical simulated polychromatic reconstructions (Schlomka *et.al*, 2008; Yan *et.al*, 2000; Elbakri and Fessler, 2002; Bazalova and Verhaegen, 2007), new energy differentiating X-ray photon counting detectors (Szeles, 2003; Matsumoto *et.al*, 2003; Ricq *et.al*, 2001; Giakos *et.al*,

1998; Hoheisel, 2006), and new CT systems designed to incorporate these X-ray detectors (Elbakri and Fessler, 2003; Paulus *et.al*, 1998; Gleason *et.al*, 1999; Hudson and Larkin, 1994). The algorithm proposed in (Schlomka *et.al*, 2008) divides the energy spectrum based on absorption edges and uses one more energy than absorption edges, attempting to separate simulated data on the basis of absorption edges. The algorithm proposed in (Yan *et.al*, 2000) uses theoretical polychromatic data to improve beam-hardening artifacts. The authors of (Elbakri and Fessler, 2002) propose a polychromatic PWLS algorithm and then apply it to simulated data. The monochromatic version of the PWLS in (Elbakri and Fessler, 2002) served as the base model for a PWLS method described in this paper. All of these papers use simulated data, rather than experimental data, to validate the algorithms. The authors of (Bazalova and Verhaegen, 2007) work to with create a valid Carlo simulation of polychromatic data.

There has been significant development in new energy-differentiating photon counting cadmium zinc telluride (CZT) detectors (Szeles, 2003; Matsumoto *et.al*, 2003). These detectors have been used for X-ray computed tomography applications (Ricq *et.al*, 2001; Giakos *et.al*, 1998). The detectors count each incident X-ray photon and estimate the energy of each counted photon, permitting the binning of photon data to determine a spectrum of photon energies reaching the detector. This makes these detectors different from other X-ray detectors, such as analog film or flat panel and strip digital CCD based detectors (Hoheisel, 2006), which assign a single value to the entire incident X-ray field at a given location in space.

Some work has been done creating an energy differentiating CT system. These systems incorporate the new photon counting detectors. The system proposed in both (Paulus

et.al, 1998) and (Gleason *et.al*, 1999) uses a CZT detector with 6 energy ranges and reconstructs images of mice. The system proposed in (Elbakri and Fessler, 2003) also uses a CZT detector with 6 energy ranges and experiments with a technical phantom. All of these papers only increase the energies to 6 energy ranges and show simple reconstruction images with the focus on the experimental procedure.

In this paper, we bring together a new energy differentiating X-ray CT system (Section 4.4) with a new polychromatic X-ray CT reconstruction algorithm (Section 4.3). The system uses a CdTe photon counting detector to measure the multiple X-ray energies for each projection ray in the sinogram. Each incident x-ray photon is assigned to an energy bin, sampling the x-ray spectrum incident on the detector. The reconstructed image provides an estimate of the linear attenuation coefficient in each spatial pixel for each energy bin.

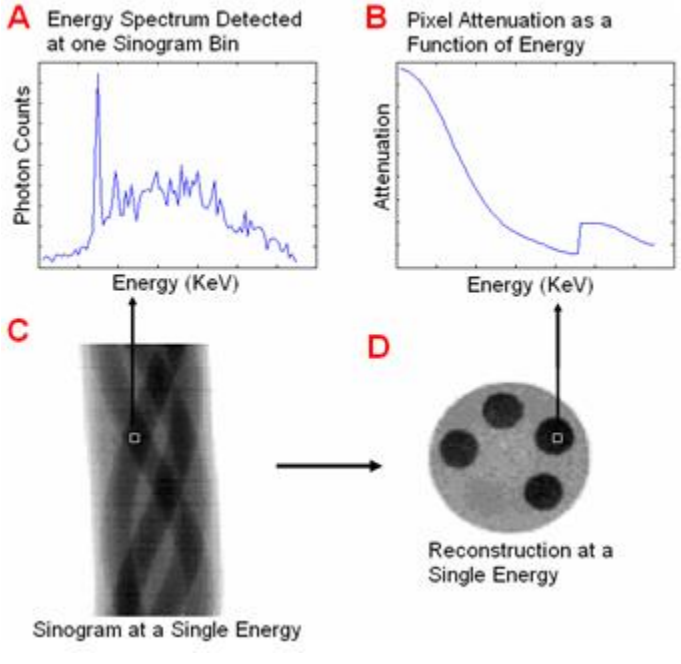

Figure 4.1 Overview of data types in the proposed system. Figure (A) is the detected energy spectrum at a single projection ray, each projection ray in the sinogram has its own spectrum. Figure (B) is the attenuation curve for a single pixel in the reconstructed attenuation map. Figure (C) is the acquired data as a sinogram, where all collected projection rays are shown at a single energy. Figure (D) is the reconstruction of (C) to an attenuation map at a single energy.

The measured x-rays can be represented at each projection ray as an x-ray spectrum (figure 4.1A) or as a sinogram for each detector energy bin (figure 4.1C). These measurements can be reconstructed into an attenuation curve for each reconstruction pixel (figure 4.1B) or into an attenuation map for each detector energy bin (figure 4.1D). We define an attenuation map as the spatial distribution of the estimated attenuation. We define an "attenuation curve" as the X-ray attenuation coefficient as a function of x-ray energy for a given material or image pixel. This is a continuous relationship, which we estimate as a discrete vector. Standard data for these curves, as mass-attenuation, can be found for many materials at the NIST X-ray mass-attenuation database (Hubbel and Seltzer, 1996).

As a practical matter, the individual energy bins in the projection data are noisy due to the random nature of photon counting. To smooth the reconstruction images, we use known properties of material X-ray attenuation coefficients as a function of energy to provide significant noise reduction. This smoothing method suppresses the noise in the reconstructed attenuation maps for each energy bin and in the reconstructed attenuation curves.

In this paper we present an algorithm which reconstructs the projection data using a PWLS algorithm with an energy axis attenuation curve penalty to smooth the reconstructions (Section 4.3). We also describe the experimental system developed to acquire the polychromatic X-ray CT data using a photon-counting CdTe detector (Section 4.4). We then validate both the new system and the algorithm with experimental data (Section 4.5).

4.3. Algorithm

Here we describe the algorithm developed to control the noise in the reconstructions.

4.3.1. Penalized Weighted Least Squares (PWLS)

The projection data Y_{iE} is acquired as an array of photon counts corresponding to $i = [1,2,\cdots, N \cdot D]$ projection rays and $E = [1,2,\cdots, K]$ energy bins; *N* is the number of rays at each projection angle, *D* is the total angles measured, and *K* is the total number of energy bins. For each energy E, there is a complete set of projections Y_{*E} which corresponds to a sinogram (Figure 4.1 C) that can be reconstructed into an energy-specific estimated attenuation map $\hat{\mu}_{*E}$(Fig.1 D) with $j = [1,2,\cdots, N^2]$ as the pixel spatial location. We model the projection as a function of the real attenuation map at some energy *E* and ray *i* as:

$$Y_{iE} = I_{iE}\exp\left(-\sum_j a_{ij}\mu_{jE}\right) + n_{iE} \tag{4.1}$$

I_{iE} is the signal at projection ray *i* and energy bin *E* with the object removed, called the "blank scan". In this expression $\sum_j a_{ij}\mu_{jE}$ is the projection of the attenuation map μ at energy *E* at pixel *j* onto ray *i*. Every element of a_{ij} is the contribution of the j^{th} pixel in the attenuation map to the i^{th} projection ray. We assume that a_{ij} is not energy-dependent. Ours is a parallel-beam system, so this is a very straightforward model, but the treatment applies to any projection geometry. The added component n_{iE} is the noise distributed across space and energy. The noise is modeled such that Y_{iE} varies as a normal variable, approximating the Poisson distribution, as in (Elbakri and Fessler, 2002), resulting in a weighted least squares (WLS) approach.

Our goal is to form an accurate estimate $\hat{\mu}_{jE}$ for the true linear attenuation coefficient from a given a set of projection data Y_{iE}. To do this we used the monochromatic PWLS algorithm proposed in (Elbakri and Fessler, 2002). In (Elbakri and Fessler, 2002), the proposed weight is $w_{ie} = (Y_{iE} - r_{iE})^2/Y_{iE}$; r_{iE} is the mean

number of background events in the model used for Y_{iE} in (Elbakri and Fessler, 2002). We assume $r_{iE} = 0$, no background events, reducing the proposed weights to: $w_{iE} = Y_{iE}$the measured signal. This algorithm is shown below in expression (4.2):

$$\hat{\mu}_{jE}^{new} = \left[\hat{\mu}_{jE}^{old} - \frac{M \sum_{i \in S_m} a_{ij} Y_{iE} \cdot \left(\sum_j a_{ij} \hat{\mu}_{jE}^{old} - log\left(\frac{I_{iE}}{Y_{iE}} \right) \right) + \beta \frac{d}{d\hat{\mu}_{jE}} U\left(\hat{\mu}^{old} \right)}{\sum_i \sum_j a_{ij} Y_{iE} + \beta \frac{d^2}{d\hat{\mu}_{jE}{}^2} U\left(\hat{\mu}^{old} \right)} \right] \quad (4.2)$$

We use the PWLS in form of (4.2) because it was derived from a simple monochromatic model similar to (4.1) and the penalty is expressly separated from the rest of the algorithm. The algorithm, as expressed in (4.2) has a weighted least squares (WLS) portion (first term) and a penalty portion (second term) in the numerator. The penalty is weighted by the parameter β which is found empirically to balance the prior term with the WLS portion of the algorithm. The denominator of (2) is a normalization term.

The PWLS algorithm (expression 4.2) is an ordered subsets approximation to a true PWLS. The projection data is broken into M ordered subsets with S projections in each subset. The WLS part of the algorithm is applied to only one subset at a time and used to modify the estimate of the attenuation map $\hat{\mu}_{jE}$. Iterating through all subsets S_m forms one complete iteration. The penalty portion is separable with respect to reconstruction pixels, being applied only along the energy axis in the reconstruction domain, discussed in the next section. While there is no proof of convergence, the algorithm arrives at a solution in a similar fashion to OSEM (Hudson and Larkin, 1994) solutions used for emission CT. We use ordered subsets because it speeds up the algorithm, which has to run for each energy bin. The algorithm has a non-negativity constraint, indicated by the positive sign in (expression 4.2).

This is enforced by rejecting any update which causes the algorithm to return a negative new estimate of attenuation.

The PWLS is applied simultaneously for each energy bin E in Y_{iE} to update the estimate for $\hat{\mu}_{jE}$ the linear attenuation for each energy bin. Each energy bin is assumed to be independent of all other energy bins for the WLS part of the algorithm, the only relationship between energy bins is in the penalty, discussed in the next section.

Although we use the same form of the monochromatic PWLS algorithm as in (Elbakri and Fessler, 2002), ours is different in the penalty we propose. Our penalty operates in the energy dimension of the polychromatic data and not in the spatial dimension as is typical. We use the PWLS in the form of (Elbakri and Fessler, 2002) because it provides a simple structure where only the penalty must be modified. A spatial penalty could be added to our proposed method; we do not do so in this paper in order to demonstrate that the noise suppression is solely a result of the energy penalty.

4.3.2. Penalty Function

To form a penalty function for the PWLS algorithm it is useful to think of the vector $\hat{\mu}_{jE}$, in space for a specific energy, (Figure 4.1D):

$$\hat{\mu}_{*E} = \left[\hat{\mu}_{1E}, \hat{\mu}_{2E}, \cdots, \hat{\mu}_{jE}, \cdots, \hat{\mu}_{N^2E}\right] \tag{4.3.a}$$

Or in energy at specific location in space (Figure 4.1B):

$$\hat{\mu}_{j*} = \left[\hat{\mu}_{j1}, \hat{\mu}_{j2}, \cdots, \hat{\mu}_{jE}, \cdots, \hat{\mu}_{jK}\right] \tag{4.3.b}$$

The first vector represents a single energy attenuation map. The second vector represents the attenuation curve for a single pixel. An attenuation curve is the attenuation of some material as a function of energy, represented as a vector of discrete energy elements.

The unique aspect of our proposed penalty is that it smoothes the attenuation curves rather than the attenuation map using several known properties common to attenuation curves.

An attenuation curve's properties are a combination of the elemental composition of a material and the density of that material. However, all attenuation curves have several common properties. We will define these properties as statements and mathematically. To define mathematically, we define a change in attenuation along the energy axis as $\Delta_{jE} = \hat{\mu}_{j(E+a)} - \hat{\mu}_{jE}$: where the index *j* is the pixel location and index *E* represents the energy bin. We define the properties of attenuation curves as:

1. The curve is always descending with increasing energy, unless there is an absorption edge (Section 4.3.5) within the energy range.

$$\hat{\mu}_{jE} > \hat{\mu}_{j(E+a)} \text{ or } \Delta_{jE} < 0 \text{ if } a > 1 \tag{4.3.c}$$

2. The curve will have some expected slope, defined by physical properties of materials represented in the pixel; the slope may also be affected by absorption edges (Section 4.3.5).

$$\Delta_{jE} \approx \delta_E \tag{4.3.d}$$

3. The curve will be smooth, except when there is an absorption edge.

$$\frac{\partial}{\partial E}\Delta_{jE} \text{ is small} \tag{4.3.e}$$

The slope of the attenuation curve changes slowly. The penalty is formed to enforce these properties on the data. Elements of the data which do not follow these properties are considered noise and suppressed to smooth the overall attenuation map.

4.3.3. Penalty Function Implementation

We derive the penalty from a Gibbs prior distribution (Geman and Geman, 1984) of the form:

$$P(\mu) = \frac{1}{Z}\exp\left(-\beta \cdot U(\mu)\right) \tag{4.4}$$

Where Z is a normalization constant, β is the weighting parameter, and $U(\mu)$ represents the total energy of the pixel lattice. The penalty is then applied from the term in the exponential. The lattice term of the penalty is the weighted sum of penalty functions over individual neighborhoods. We define these neighborhoods along the energy axis, over attenuation curves $\hat{\mu}_{*E}$. We define the penalty function over pairs of attenuation coefficients at the same spatial location but different energies:

$$U(\mu) = \sum_{a\in M} w_a \sum_j V\left(\hat{\mu}_{j(E+a)}, \hat{\mu}_{jE}\right) \tag{4.5}$$

The weights *w* can be defined individually for each pair of energies, and could even be spatially-varying w_{ja}, though we have chosen not to make them so. Expression (4.5) represents smoothing along the attenuation curve only, but we could introduce spatial-smoothing neighborhoods into the total penalty function here. The weights are defined over a neighborhood *M* defined as varying from the E^{th} energy bin.

The penalty function on each neighborhood is assumed to remain constant across the image and to be a function of only the difference in linear attenuation coefficients at neighboring energies, a difference we label Δ_{jE}:

$$V\left(\hat{\mu}_{j(E+a)}, \hat{\mu}_{jE}\right) = V\left(\hat{\mu}_{j(E+a)} - \hat{\mu}_{jE}\right) = V\left(\Delta_{jE}\right) \tag{4.6}$$

To enforce the properties of attenuation curves, proposed in (Section 4.3.2), on individual attenuation curves, we choose a shifted quadratic form for the penalty function:

$$V(\Delta_{jE}) = \tfrac{1}{2}\Delta_{jE}^2 - \tfrac{\delta_2}{2}\Delta_{jE} \tag{4.7}$$

A normal quadratic penalty function in space penalizes any variation in a neighborhood, smoothing the neighborhoods to an average value. We do not want the neighboring pixels to be the same value; therefore, we assume that the neighborhood in energy represents a curve. To smooth to a curve we shift the quadratic penalty by introducing an expected local slope δ_E into the penalty. The penalty increases as the estimated slope differs from the expected slope; this is justified by the second property of attenuation curves. The shift to slope δ_E also increases the penalty in the region where $\Delta_{jE} < 0$, the further δ_E is from 0, the greater this part of the penalty becomes. This enforces the first property of attenuation curves. The lack of any edge preservation keeps the penalty function continuous enforcing the third property of attenuation curves. The penalty causes the curves to be smooth because the penalty is continuous and smooth, forcing the energy differences toward the expected slope δ_E. The derivative of the total penalty, which is used in the implementation, is then given by the following:

$$\frac{d}{d\hat{\mu}_{jE}} U(\hat{\mu}) = \sum_{a\in M|a<0} w_a\left(\Delta_{jE} - \tfrac{1}{2}\delta_E\right) + \sum_{a\in M|a>0} w_a\left(-\Delta_{jE} - \tfrac{1}{2}\delta_E\right) \tag{4.8}$$

Expression (4.8) is split to keep the penalty term positive. The energy-pair neighborhoods are defined to be those within two consecutive energy bins:

$$w_a = \begin{cases} 1 \text{ if } a = \pm 1 \\ .5 \text{ if } a = \pm 2 \\ 0 \text{ else} \end{cases} \tag{4.9}$$

This makes an effective energy neighborhood of 5 energy bins; the current pixel with two energies below and above the current energy pixel E. This was found experimentally to offer good results. Larger neighborhoods result in increased smoothing along the energy axis,

and also increasing the processing time. The penalty is applied to every energy bin simultaneously in the PWLS, Eq. (2). Methods for estimating δ_E and accounting for absorption edges are presented in the next sections.

4.3.4. Slope Estimations

The expected slope δ_E is a function of energy rather than a single value because the relationship between the attenuation coefficients and X-ray energy is non-linear. The estimated slope is applied to all pixels $\hat{\mu}_{jE}$ in the attenuation map at energy bin E. A spatially varying expected slope δ_{jE} could be used but we do not do so in this paper. The use of a single spatially invariant slope estimate means that it will be applied to a number of different materials. Figure 4.2 shows the attenuation curves for the different materials used in the paper from the NIST database (Hubbel and Seltzer, 1996).

This figure demonstrates the differences in predicted attenuation curves. The expected slope for each material is the slope of each predicted attenuation curve. To create an expected slope which is not dependent on knowing the materials present and is applicable to all pixels in the attenuation map we form the spatial average of the attenuation map:

$$\breve{\mu}_E = \frac{1}{N^2}\sum_j^{N^2} \hat{\mu}_{jE} \tag{4.10}$$

The δ_E parameters are then determined from the corresponding energy-pair differences in the average attenuation map:

$$\delta_E = \breve{\mu}_{(E+1)} - \breve{\mu}_E \tag{4.11}$$

This keeps the expected slope right in the middle of possible material slopes, allowing us to smooth the attenuation curves without significantly biasing the data.

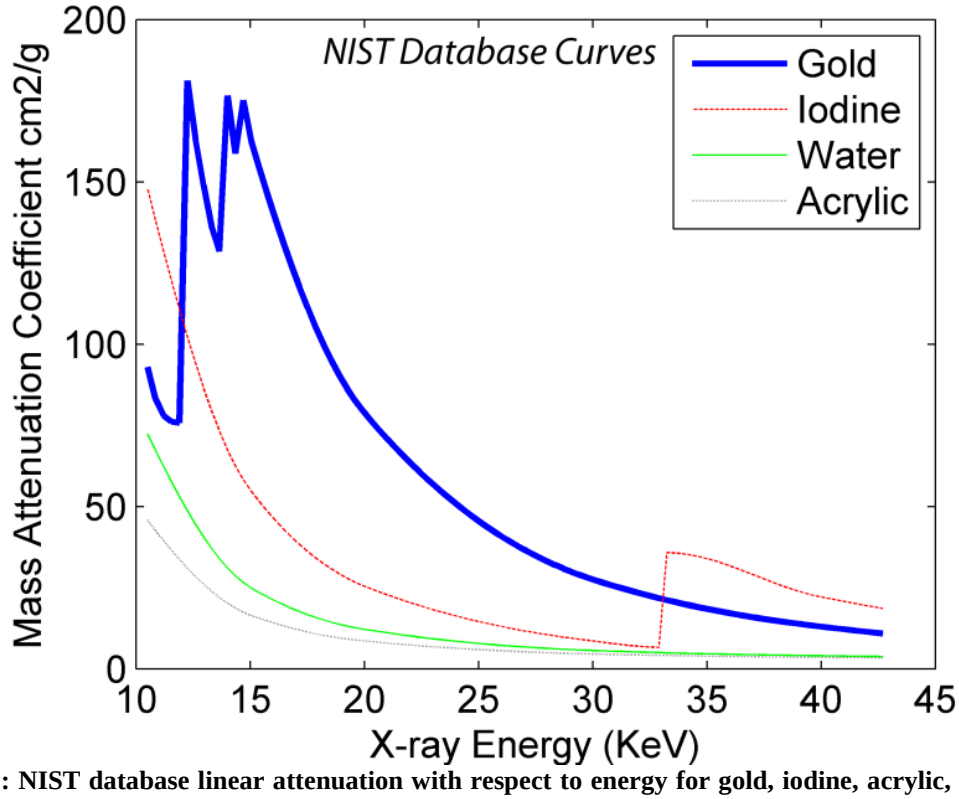

Figure 4.2: NIST database linear attenuation with respect to energy for gold, iodine, acrylic, and water. These are the expected attenuation curves for the different materials in our phantom.

4.3.4. Absorption Edges

The attenuation curve properties used to create the penalty function do not hold true at absorption edges. To account for absorption edges, a new assumption is introduced to the original three properties:

4. Any absorption edge in a biological X-ray CT is from a contrast enhancement material and exists at a known energy location E_{edge}.

This assumption is reasonable at the energies used in biological imaging since the absorption edges of materials in biological tissues are well below these energies. This means that the algorithm only has to deal with known edges and that, except for those known edges, the attenuation curve properties always hold. The algorithm can be modified in one of two ways to preserve absorption edges in the attenuation curve:

Modification Option 1: The penalty ends at E_{edge-1} and begins again at E_{edge+1}, completely ignoring $E_{edge}$for all pixels in the attenuation map, weighting those energy-neighborhoods that cross the absorption edge to zero.

Modification Option 2: The algorithm includes the absorption edge in the estimation δ_e.

The first modification separates the continuous energy range into two or more separate continuous energy ranges: $\{E_1, \cdots, E_K\} \rightarrow \{E_{1,\cdots,}E_{edge-1}\}\{E_{edge+1}, \cdots, E_K\}$. The penalty is then applied separately to each. This modification is very effective for sharp large edges, such as the iodine edge. However, this modification is applied for the entire attenuation map and creates a discontinuity in the attenuation curves for all pixels in the image.

The second modification keeps the complete energy range but forces a non-smooth difference on all the data. The difference is smoothed out a little because it only exists at a single energy; the penalty is applied over a neighborhood of 5 energies. This makes this method less effective for sharp edges but preserves the continuity of the attenuation curves. It is most effective for smaller edges, such as low-energy gold edges. In the data presented in this paper, we use both methods. We use the first method for the iodine edge and the second method for the gold. Both can be used simultaneously because the edges for these materials exist at different energies.

4.4. Experimental Setup

To acquire data in energy specific bins, a unique computed tomography system has been designed. The system has both a unique physical setup and experimental procedure. The physical setup describes the components of the X-ray CT system and how they are

configured. The experimental procedure describes how the system operates to collect CT data. This setup and experimental procedure is an extension of the setup and procedure described in (Claesoon *et.al*, 2001).

The authors of (Claesoon *et.al*, 2001) propose a system with a single energy gamma-source and a photon counting detector measuring a single projection ray at a time. The source detector is rotated around an imaged object building a complete CT data set for a single slice. We use a similar photon counting detector with a polychromatic x-ray source. We move the imaged object rather than the source-detector configuration.

4.4.1. Physical Setup

The computed tomography system consists of a field emission carbon-nanotube X-ray source *(Gao et.al, 2001)* with a molybdenum anode, a remotely controlled positioning system, and an AMPTEK energy-differentiating photon counting single pixel detector. These are shown in figure 4.3. The source accelerates free electrons through an electric field into a molybdenum anode to produce X-rays. Carbon nanotubes replace a tungsten filament as the source for the free electrons. The overall X-ray flux is proportional to the electric field between the carbon nanotubes and a gate electrode. More detail on carbon nanotube sources can be found in (Gao *et.al*, 2001; Yue *et.al*, 2002; Zhang *et.al*, 2005). The source has no significant filtration; the x-rays exit the vacuum chamber through a thin beryllium window.

The positioning system consists of two Velmex linear slides, arranged as shown in figure 4.3, and a Velmex rotation table on which the subject is mounted. The linear slides allow for precise uniform movement in the both the vertical, z, and horizontal, x, directions. The rotation table is mounted on these slides and can rotate the imaging object with 1/10 degree accuracy. The positioning system is controlled via a computer.

The detector is an AMPTEK XR-100 CdTe detector with a PX4 signal processor and a pinhole collimator. This detector counts each photon and assigns it to a specific energy bin over the collection time. The detector builds an X-ray energy spectrum as the number of incident photons in each energy bin for a given period of time. The collimator has two pinholes and limits the incident X-ray photons to a single line with a diameter defined by the pinholes. The projection line is defined as a line from the source through both pin holes to the detector. The detector is located where the projection line will have the maximum X-ray photon flux for the given source to detector distance. The resulting system is functionally equivalent to a scanning pencil-beam X-ray CT.

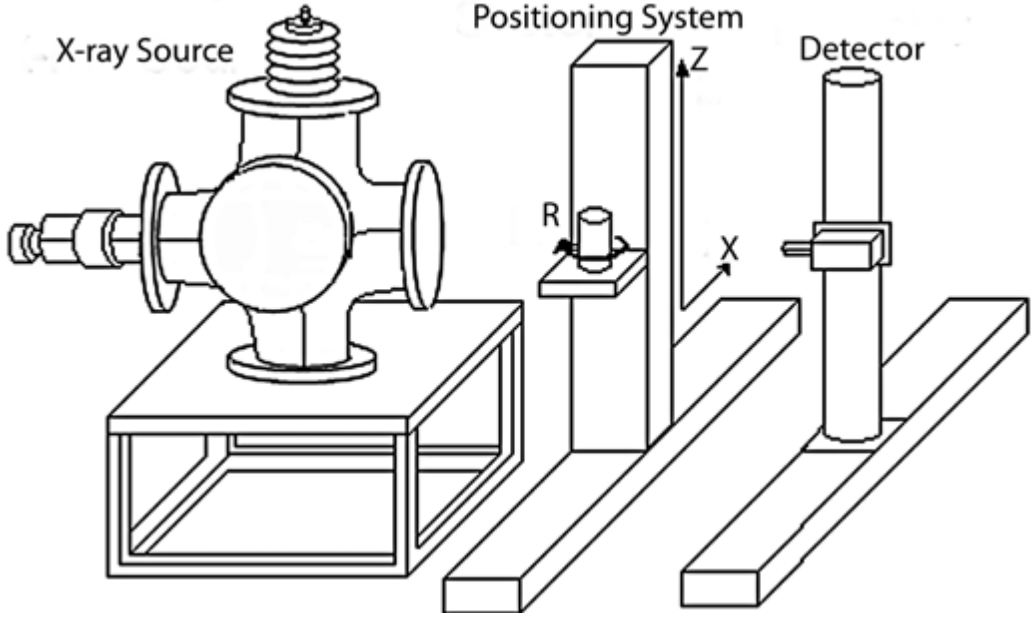

Figure 4.3: Physical layout of the system with the three principal components of the X-ray setup.

4.4.2. Experimental Procedure

The X-ray field is generated by applying a 45kV voltage to the anode and 3400 V gate voltage to generate the electric field over the cathode. The gate voltage is pulsed at 40 Hz with a 50% duty cycle resulting in a 100μA current. The gate voltage pulse is much faster

than the imaging capture time, which is 5 seconds. The gate voltage is pulsed rather than constant to reduce heating in the carbon nanotube sources. The field generated is functionally the same as a 45kV molybdenum source with a 100μA current. The use of 45kV is due to design limitations in the experimental system; the high-voltage feed-through is only rated to 50kV and we choose not to push this limit.

The object starts outside the projection line and the initial measurements create the incident X-ray spectrum, the blank scan. The object is translated using the horizontal x-direction Velmex linear slide 0.4mm at a time. The projection-ray increments were 0.4mm, and the corresponding reconstruction pixels are also 0.4mm. Each time the object is translated, a new projection ray is defined as the line through the part of the object that is in the projection line. Each translation of the object will produce a unique projection ray. This is repeated 81 times to allow for extra measurements on both sides of the object and 61 projection rays through the object. The object is then rotated 1.5° and the process is repeated to record a new set of projection rays. This is done 120 times to acquire an arc of 180°. The extra measurements on both sides of the object are used as the blank scan for each angle.

The AMPTEK detector can only record a single projection ray at a time, but translating the object in front of the detector simulates a strip detector in a parallel beam field. The spectrum is binned to 95 energy bins arranged from 10keV to 45keV with a bin width of .35keV. An equivalent strip detector would have to detect the entire X-ray spectrum for each material. The resulting data can be viewed as a set of 95 monochromatic sinograms through the object.

4.4.3. Phantom

To test the CT system and the algorithm an acrylic phantom was constructed, shown in figure 4.4. This is a cylindrical phantom with a diameter of 2.5cm and 5 cylindrical holes, each with a 5mm diameter, arranged circularly inside the phantom. Each of these holes can be left empty or filled with some agent to provide contrast with respect to the acrylic.

The materials used are: water, gold nanoparticle contrast solution, and iodine solution. The different materials were chosen based on their attenuation curve properties. Acrylic was used because its attenuation curve is very close to human soft tissue. Water is used because it is the principal compound in the human body and should have an attenuation curve very close to acrylic, but with some separation at low energies. We used non-ionized distilled water here and as a base for the other solutions.

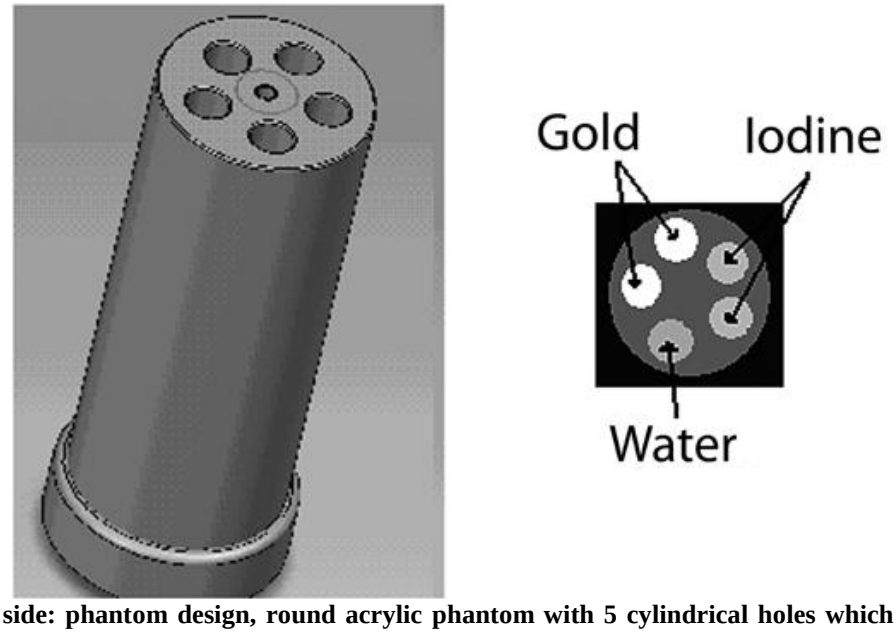

Figure 4.4: Left side: phantom design, round acrylic phantom with 5 cylindrical holes which are filled with some contrast agent. Right side: slice through phantom and location of different contrast agents.

Iodine was chosen because it is a common contrast agent used in cardiac CT and has a absorption edge within the energy range used in the experiment. Iodine has a greater

attenuation than bone after the absorption edge, so it also serves to test the response of the system on dense material. We used a 20mg/ml solution of VisipaqueTM (Visipaque) in non-ionized distilled water.

Gold nanoparticles are currently being investigated as potential X-ray contrast agent because they are non-reactive and have multiple absorption edges within normal X-ray energies (Hainfeld *et.al*, 2006; Kattumuri *et.al*, 2007). Gold is used in this experiment to demonstrate and study the effect of multiple absorption edges on the algorithm. Gold nanoparticles used in this experiment were 1.9nm gold nanoparticles, trade named AuroVistTM (AuroVist). We used an AuroVistTM 16mg/ml solution in non-ionized distilled water.

4.4.4. Reconstruction

The projection data is reconstructed to form an estimate of the linear attenuation coefficient for all 95 energy bins. There are two reconstruction methods use: Filtered back projection (FBP) and penalized weighted least squares (PWLS) (Section 4.3). FBP is implemented using the IRADON function in MATLAB (MATLAB). The program uses a Ram-Lak filter with a frequency response of $|f|$. We choose not to do any further spatial filtering in this stage; the goal is to maintain high spatial resolution, even at the cost of increased noise. The energy penalty has no effect on the spatial resolution, but it still suppresses the noise. FBP and PWLS are compared in figure 4.6 to demonstrate the improvement in noise while maintaining best possible spatial resolution.

4.5. Results

For this experiment there were 95 energy bins arranged from 10keV to 45keV. A projection sinogram corresponding to each of the energy bins was created, resulting in 95

sinograms. Each sinogram represents 120x81 projection rays corresponding to 120 angles and a simulated 81 pixel strip detector.

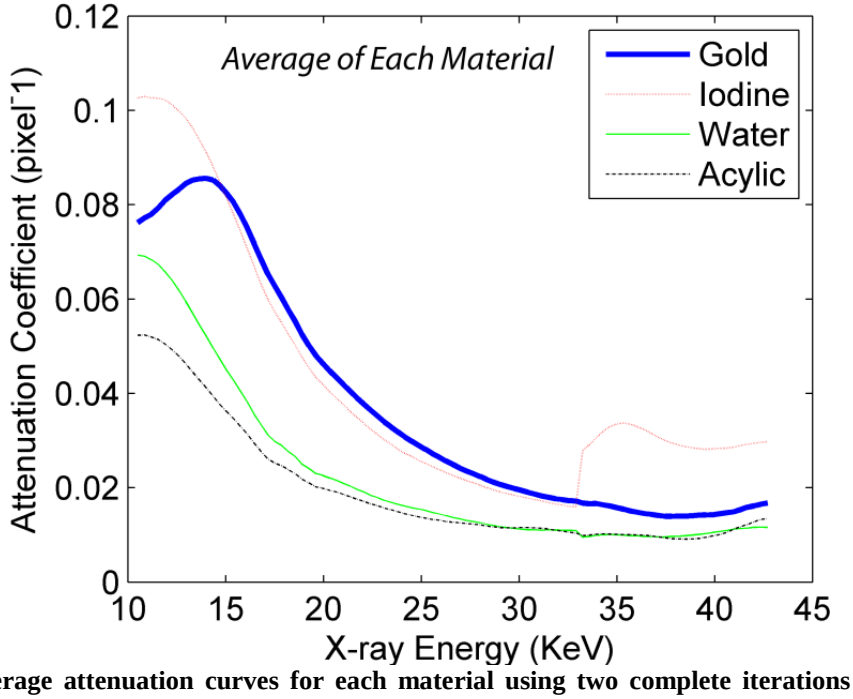

Figure 4.5: Average attenuation curves for each material using two complete iterations of the PWLS computed in the known locations of each material. The pixel size is 0.4mm.

Each sinogram is reconstructed to an attenuation map estimate using filtered back projection (FBP) and penalized weighted least squares (PWLS) Eq. (2). Attenuation curves are formed from these estimates by looking at the average value over a material as a function of energy (figure 4.5) or by taking a single pixel within a material as a function of energy. The average attenuation curve, figure 4.5, demonstrates that each material has a unique curve and that each material can be identified by its attenuation curve. There is a clear difference between water and acrylic at low energies.

The reconstructions of each sinogram at selected energies into an attenuation map image for both FBP and PWLS are shown in figure 4.6. This figure shows how single reconstructions look and demonstrates the clear improvement from FBP to PWLS. The FBP

reconstruction is sensitive to noise which makes it harder to identify the different materials in most of the images. The noise distorts the different material boundaries and prevents the user from seeing any change in material intensity as a function of energy. At the higher energies the noise increases due to photon starvation.

The PWLS reconstruction has been used with two complete iterations and demonstrates the effectiveness of the algorithm in suppressing noise. Two iterations offer the best visual quality, based on subjective assessment. The results remain very similar for 2, 3 or 4 complete iterations (data not shown). After 4 complete iterations, the noise begins to slowly increase (data not shown). The images appear much cleaner at every energy and the materials are well separated. In the PWLS-reconstructed images, it is clear how the intensity of gold and iodine change as a function of energy. The iodine absorption edge is clearly visible; the iodine suddenly becomes much brighter than the gold and the acrylic, as a result of iodine's absorption edge at 33KeV.

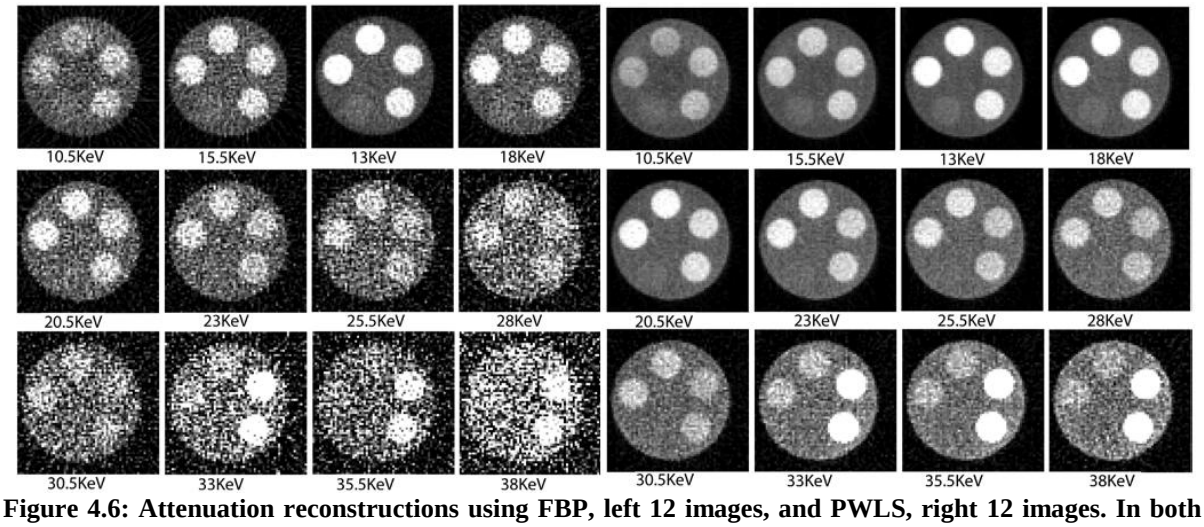

Figure 4.6: Attenuation reconstructions using FBP, left 12 images, and PWLS, right 12 images. In both the same energies have been reconstructed. Both are presented on the same scale. Left 12 images are very noisy from FBP. Right 12 images show how PWLS suppress the noise.

Sample pixels are taken out of gold, water, and iodine attenuation reconstruction at every energy to form the attenuation curves shown in figure 4.7. The left figure is from FBP and corresponds to the same data as the left 12 images in figure 4.6. This figure demonstrates how the noise is distributed along the energy curves. These curves fail to meet the properties proposed in Section 4.3.2; they are not smooth or always descending. The noise hampers the use of the curves in identifying the materials and even the strong iodine absorption edge is hard to identify.

The lower part of figure 4.7 shows how well the PWLS suppresses the noise in the attenuation curves. The curves in this figure are the same spatial pixels as the left image. Here the iodine absorption edge is very clear and the gold follows the expected pattern of starting below iodine and crossing over it. The small gold absorption edges in the 10-16keV range have been smoothed over.

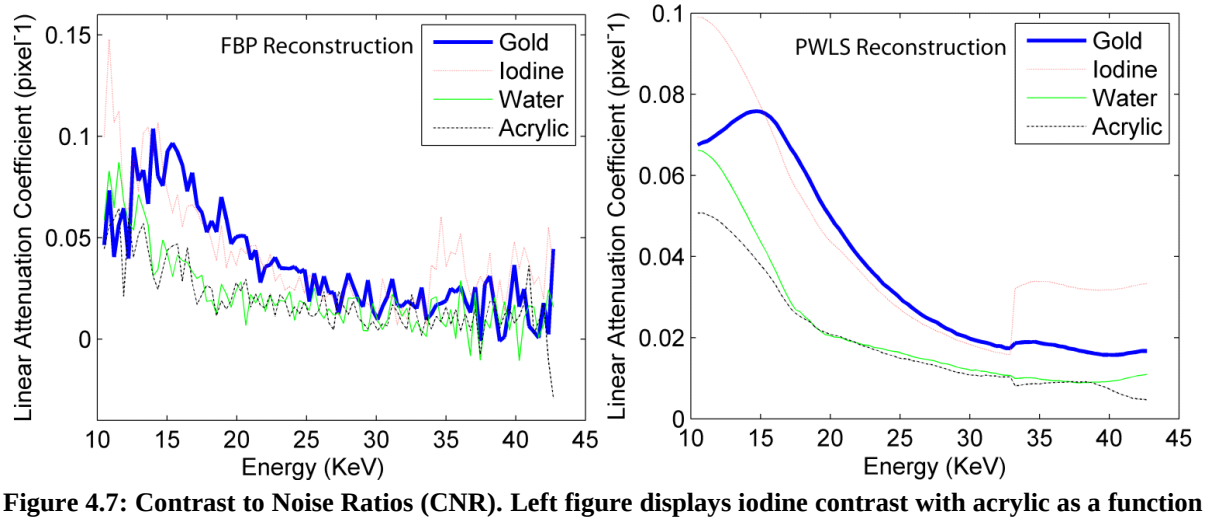

Figure 4.7: Contrast to Noise Ratios (CNR). Left figure displays iodine contrast with acrylic as a function of energy. Right figure displays water contrast with acrylic as a function of energy. Both images demonstrate that CNR is significantly improved using PWLS. The PWLS β=0 is defined as WLS and is displayed to demonstrate that it is the penalty which improves CNR.

These curves are close to the average curves presented in figure 4.5, showing how well all of the curves in a region follow the average of that region. This means that the algorithm suppresses the variance in each region without significantly biasing the average value in each region.

To further investigate the effect of noise suppression we defined a contrast to noise ratio (CNR) as the difference between the mean of two regions over the root sum of their combined variance. This demonstrates the algorithm's ability to identify materials, as the noise is suppressed. The CNR for iodine compared with acrylic and for water compared with acrylic are shown as a function of energy in figure 4.8.

An increase in CNR demonstrates a suppression of the noise and an increase in the potential ability to separate materials. The PWLS algorithm dramatically increases CNR for each material compared with the background acrylic. The CNR is shown here a function of energy because it changes with the changes in attenuation curves. This is most noticeable at the absorption edge in iodine, left image, and the low energies in water, right image. Water has a separation in attenuation from acrylic at low energies and the PWLS brings that out, making acrylic and water separable for some energies.

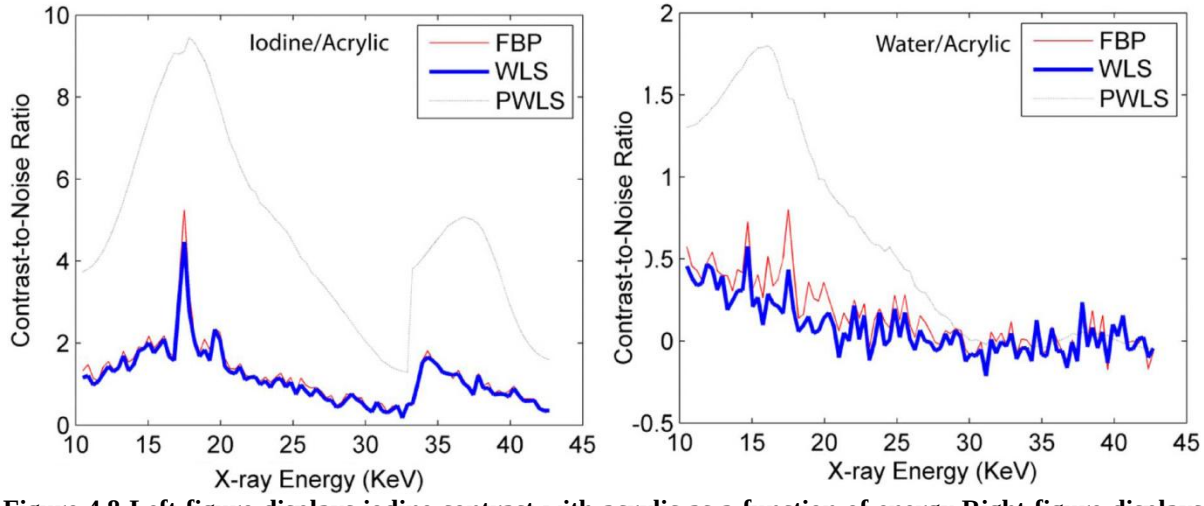

Figure 4.8 Left figure displays iodine contrast with acrylic as a function of energy.Right figure displays water contrast with acrylic as a function of energy. Both images demonstrate that CNR is significantly improved using PWLS. The PWLS $\beta = 0$ is defined as WLS and is displayed to demonstrate that it is the penalty which improves CNR.

PWLS is compared with FBP and WLS to show the effect of the penalty. The WLS data uses the same algorithm with to suppress the penalty. This demonstrates that it is the penalty function which improves the noise suppression and increases CNR. It should also be noted that as iterations of PWLS increase from 2 to 4, the CNR remains the same or slightly improves (data not shown). Frequently, CNR is degraded with iterations when spatial penalties are used; that behavior is not observed with the energy axis penalty until after four complete iterations. Although the algorithm suppresses the noise and maintains contrast in the reconstructions, preserving absorption edges is also very important so that attenuation curves can be used to identify materials. Fig. 9 demonstrates the capability of the PWLS to preserve absorption edges, compared with the standard values from the NIST data base. The NIST curves have been scaled to be comparable to the measured curves. The left image in Fig. 9 shows the gold absorption edges. The average FBP is shown to demonstrate how the original data looks before it is smoothed with PWLS. The PWLS with and without absorption edge correction is shown. The absorption edge correction used here includes the

edge in the expected slope based on the knowledge that gold was being imaged (method 2 Section 4.3.5). The edges in the measured data are much smaller than the edges in the predicted curve. This is because these edges exist at very low energies where most of the X-ray photons have been absorbed by the subject. The shape remains, but to get stronger edges the concentration of gold or the X-ray flux needs to be increased. The average FBP is included in figure 4.9 to show the data before PWLS is applied. The average over the regions is presented to reduce the effect of noise. The average demonstrates that the edge exists in the data and is not introduced by the PWLS. The PWLS pulls the data closer to the average without spatial blurring of the images.

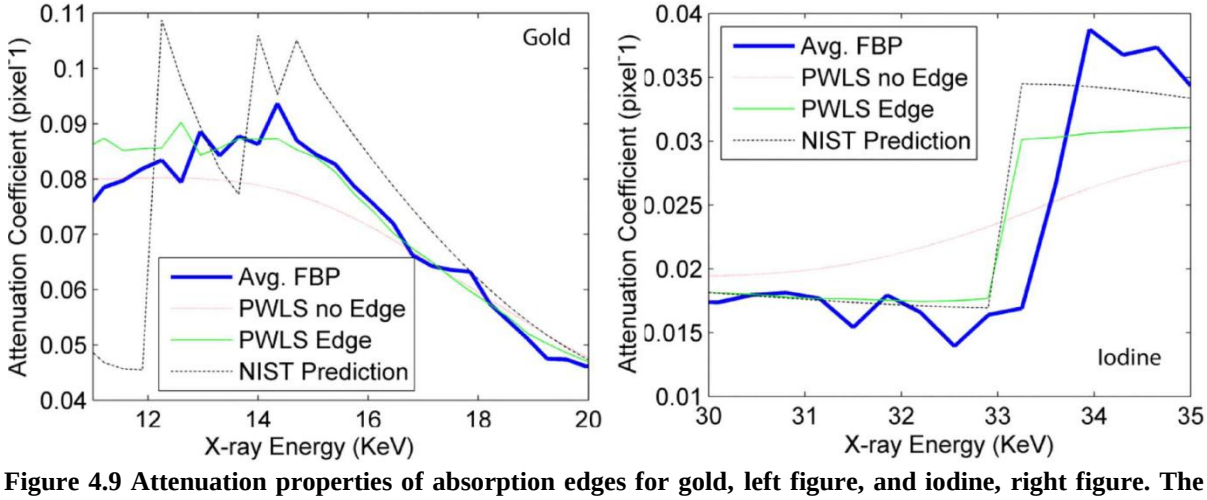

Figure 4.9 Attenuation properties of absorption edges for gold, left figure, and iodine, right figure. The solid line is the predicted value using NIST data bases. This is compared to the average FBP over the corresponding materials and to PWLS. The PWLS is shown with and without absorption edge correction. The pixel size for both images is 0.4 mm.

The lower image in Fig. 9 shows the iodine edge. This is a strong edge in a high X-ray flux region so it is very clear. The average FBP is shown to demonstrate that the edge exists the original measured data. The PWLS without edge correction smoothes over the sharp edge. The PWLS with edge correction follows almost exactly with the prediction from the NIST

database. To preserve this edge the curve is broken into two curves with the edge point left out (method 1 Section 4.3.5).

4.6. Discussion

The algorithm was designed to incorporate the effect of density and energy on a material's X-ray attenuation coefficient. This is expressed as an attenuation curve. The shape and slope of these curves are dependent on the composition and density of the material. The attenuation curves are measured by reconstructing the attenuation map of the X-rayed object at multiple energies.

The projection data is acquired using the system described in Section 4.4. This data is nearly complete parallel-beam Radon projection data. The detector measures the entire X-ray spectrum with 0.35keV accuracy. There is an energy-resolution effect, so it is not perfect. This means that each sinogram in the projection is effectively a monochromatic parallel beam projection. This represents the most complete dataset possible, apart from a noiseless system with perfect energy resolution.

The proposed algorithm assumes perfect energy resolution in the detector. Imperfect energy resolution will blur attenuation curves making transitions less distinct. In general, we do not expect energy resolution to impact the algorithm. In extreme cases, the energy resolution can be incorporated into the expected attenuation curves used to specify the penalty, such as in absorption edges. Absorption edges are the only locations where energy resolution may pose a problem. Incorporating absorption edges into the penalty estimation helps account for this (figure 4.9).

The system we propose takes a long time to acquire the energy data. Each projection ray must be independently measured taking 5 seconds each. An acquisition time of 5 seconds

is necessary to gather enough X-ray photons to build a complete spectrum. A longer time would decrease the noise present in the system but also extend the experiment. A 5 second measurement time was chosen because it was found to be fastest possible measurement time while still acquiring a strong signal across the spectrum.

With this detector, it is not possible to use this experimental set-up on a live subject due to the long measurement time. However, polychromatic strip detectors are currently being developed *(Ricq et.al, 2003)-(Giakos et.al, 1998)*. Presently they are only able to take 6 different energy measurements, which is not enough to measure complete attenuation curves. Hopefully this number will increase to a point where attenuation curves can be accurately measured. Our algorithm could be adapted for the six energy-bin detectors or any number. This would significantly reduce energy resolution, which would be an issue for materials with absorption edges. Further work is needed to study the effect of different numbers of energy bins and the impact of energy resolution on materials without absorption edges.

The reconstruction proposed in this paper uses the nearly monochromatic data at multiple energies to form a PWLS estimate. The monochromatic PWLS proposed in (Elbakri and Fessler, 2002) is used, but with a new penalty. The penalty accounts for the polychromatic nature of the projection data. The attenuation curve properties allow the penalty to suppress the noise in the reconstructed image with no effect on the spatial resolution. Figure 4.6 shows the improvement in appearance produced by the penalty. This improvement is in both the appearance of the different slices reconstructed at different energies and in the attenuation curves, (figure 4.7).

The penalty forces the data toward some slope δ_E which is the same for every pixel in the attenuation map. Different slopes were tried, but the one for figures 6 and 7 is simply the

average of the entire attenuation map at every energy. This does not pull the reconstructions away from the data because the weighted least squares part of the algorithm tracks with the original measured data. This balance, determined by β, allows the algorithm to suppress the data without significantly biasing the reconstructions.

We use a penalty which smoothes along the energy axis with no spatial smoothing. We could have introduced spatial smoothing into the prior but decided not to in order to demonstrate the effectiveness of the energy prior, independent of any spatial prior. Future work may include studying the effect of a spatially-varying slope estimate δ_{jE} and spatial smoothing.

The penalty we use is based on three assumptions which hold true for any material's attenuation coefficient. We modify these for absorption edges, which we assume exist at known energy locations. We wanted to create a penalty which would not require the prior knowledge of what materials where present so very simple assumptions are used. We only assume prior knowledge of contrast agents and assume that absorption edges only exist when contrast agents are used. A mixture model based on a number of biological materials might be a more useful model for attenuation curve assumptions. In the future, we will investigate the use of more specific mixture models.

X-ray contrast is critically important in medical imaging. To study the improvement in contrast, a contrast-to-noise ratio (CNR) is formed which compares the difference between two materials over the root sum of their combined variance. If this is small, it becomes more difficult to differentiate between materials because the intensity differences are less than the noise variation. Figure 4.8 shows the CNR for iodine and acrylic and for water and acrylic.

There is significant improvement for all CNR after one iteration of the PWLS. Both the gold and iodine show a long sweeping improvement for low energies and iodine a large one after the absorption edge. The water/acrylic comparison is more interesting because the attenuation curves for water and acrylic are basically identical after 25keV. However, due to the smoothing of the attenuation curve below this value there is some separation between water and acrylic and the CNR is above 1 for energies below 20keV. This means for the low energies it is possible to separate the water and acrylic pixels in the attenuation map. This demonstrates that the system may be able to differentiate very similar materials based on low energy differences in the attenuation curves. This should be studied in greater detail in the future.

The first and third attenuation curve properties used to create the penalty both have exceptions for absorption edges. Two possible solutions were proposed to preserve absorption edges: incorporating the edge into the slope estimate and creating a discontinuity in the attenuation curve smoothing at the kedge. The effect of these methods on the data is shown for iodine and gold in figure 4.9.

Iodine has a very sharp absorption edge so the discontinuity method works much better. This method stops the penalty before the edge and starts it again after the edge. Including the penalty in the slope smoothes out the edge because the penalty is applied over a second order neighborhood and the edge only exists at a single energy. The NIST prediction of the iodine attenuation curve is included to demonstrate that the penalty actually pulls the data closer to the expected value. This remains true through multiple iterations and iterating the algorithm does not have a strong affect on the iodine edge when a discontinuity is used.

However, if the absorption edge is included in the slope iterations in the algorithm force a longer slower curves pulling the data away from the edge.

has a collection of edges at low energies. To preserve all of these edges it is easier to add the gold edges, to the estimated slope . If no estimate is included, all information about the gold edges is rapidly lost, shown in figure 4.9. Even with the estimate included, the gold edges are slowly smoothed over. This means that these edges are lost with more iterations. Part of the problem is the input data, shown as averaged FBP, does not capture the edges. This is seen by comparing the FBP to the expected edges. At low energies so many X-ray photons are attenuated that it becomes harder to see differences in attenuation. One can still make out the gold edges, but they are small. This could be solved by increasing the measurement time or by increasing the concentration of gold. Higher-energy gold edges are not studied because the system presently only operates at 45keV.

The experimental system we used is limited by the high-voltage feed through which is only rated to 50KV. The system was originally designed to study low energy x-rays before it was modified by adding the AMPTEK detector. This work should be extended to study the effects of higher voltage. In principle, our proposed method should be feasible for clinical CT energies as well; however at high voltage there is less separation in the attenuation curves of biological materials. Future work should address performance of the method under these conditions.

The use of expected attenuation curves from the NIST database in figure 4.9 demonstrates that the reconstructed attenuation curves are very close to the predicted curves for these materials. This means that it might be possible to use these curves to identify specific materials or concentrations of specific materials in an imaged object using this

reconstruction method. This would be particularly interesting in contrast agent images, to see how much of different contrast agents are absorbed by different tissues. For example, gold nanoparticles could be functionalized with a target agent and this method might be used to find the exact concentration of the gold in a tissue. Future work will include differentiating concentrations of the same material using this system and a similar phantom.

4.7. Conclusion

This paper demonstrates a working polychromatic energy differentiating X-ray CT system and reconstruction algorithm. Attenuation curves are reconstructed which closely follow the expected value for a given material and energy. Using attenuation curve properties, noise is suppressed with no spatial blurring. This work will serve as a justification for future energy differentiating photon counting X-ray detector development as it demonstrates the potential of polychromatic reconstruction.

4.8. References

Alvarez R. and Macovski A., 1976, "Energy-selective reconstructions in X-ray computerized tomography," *Phys. Med. Biol.*, vol. 21, no. 5, pp. 733-744.

AuroVist™, A Nanoprobes Product, Information available: http://www.nanoprobes.com/AuroVist.html

Bazalova M., Carrier J., Baulieu L. and Verhaegen F., 2008, "Tissue segmentation in Monte Carlo treatment planning: A simulation study using dual-energy CT images," *Radiotherapy and Oncology*, vol. 86, no. 1, pp. 93-98.

Bazalova M. and Verhaegen F., 2007, "Monte Carlo simulation of a computed tomography X-ray tube," *Phys. Med. Biol.*, vol. 52, no. 19, pp. 5945-5955.

Christ G., 1984, "Exact treatment of dual-energy method in CT using polyenergetic X-ray spectra," *Phys. Med. Biol.*, vol. 29, no. 12, pp. 1501-1510.

Claesson T., Kerek A., Molnar J. and Novak D., 2001, "A CT demonstrator based on a CZT solid state detector," *IEEE Nuclear Science Symposium Conference Record*, vol. 3, pp. 1644-1646.

Elbakri I. and Fessler J., 2002, "Statistical image reconstruction for polyenergetic X-ray computed tomography," *IEEE Trans. Med. Imag.,* vol. 21, no. 2, pp. 89-99.

Elbakri I. and Fessler J., 2003, "Segmentation-free statistical image reconstruction for polyenergetic X-ray computed tomography with experimental validation," *Phys. Med. Biol.*, vol. 48, pp. 2453-2477.

Gao B., Yue G., Qiu Q., Cheng Y., Shimoda H., Fleming L. and Zhou O., 2001, "Fabrication and electron field emission properties of carbon nanotube films by electrophoretic deposition," *Advanced Materials,* vol. 13, no. 23, pp. 1770-1773.

Geman S. and Geman D., 1984, "Stochastic relaxation, gibbs distributions, and bayesian restoration of images", *IEEE Trans. Pattern Anal. Mach. Intel.*, vol. 6, pp. 721-741.

Giakos G., Guntupalli R., Vedantham S., Chowdhury S. and Pillai R., 1998, "A computed tomographic CdZnTe based Scanning Detector," *IEEE Instrumentation and Measurement Technology Conference*, pp. 462-465.

Gleason S., Sari-Sarraf H., Paulus M., Johnson D., Norton S. and Abidi M., 1999, "Reconstruction of multienergy X-ray computer tomography images of laboratory mice," *IEEE Trans. Nucl. Sci.*, vol. 46, no. 4, pp. 1081-1086.

Goh K.L., Liew S.C. and Hasegawa B.H., 1997, "Correction of energy-dependent systematic errors in dual-energy X-ray CT using a basis material coefficients transformation method," *IEEE Trans. Nucl. Scie.*, vol. 44, no. 6, pp. 2149-2154.

Hainfeld J., Slatkin D., Focella M. and Smilowitz H., 2006, "Gold nanoparticles: a new X-ray contrast agent," *British Journal of Radiology*, vol. 79, no. 939, pp. 248-253.

Hoheisel M., 2006, "Review of medical imaging with emphasis on X-ray detectors," *Nuclear Instruments and Methods in Physics Research Section A Accelerators Spectrometers Detectors and Associated Equipment*, vol. 563, no. 1, pp. 215-224.

Hubbell J.H. and Seltzer S.M., 2006, "Tables of X-Ray Mass Attenuation Coefficients and Mass Energy-Absorption Coefficients from 1 keVto 20 MeV for Elements Z = 1 to 92 and 48 Additional Substances of Dosimetric Interest", *National Institute of Standards and Technology*, Tech. Rep. 43NANB412756 Available: http://www.physics.nist.gov/PhysRefData/XrayMassCoef/cover.html

Hudson H.M. and Larkin R.S., 1994, "Accelerated image reconstruction using ordered subsets of projection data," *IEEE trans. Med. Imag*., vol. 13, pp. 601-609.

Kattumuri V., Katti K., Bhaskaran S., Boote E., Casteel S., Fent G., Roberston D., Chandrasekhar M., Kannan R. and Katti K.V., 2007, "Gum Arabic as a

Phytochemical Construct for the Stabilization of Gold Nanoparticles: In Vivo Pharmacokinetics and X-ray-Contrast-Imaging Studies," *Small*, vol. 3, no. 2, pp. 333-341.

Lasio G., Whiting B., and Williamson J., 2007, "Statistical reconstruction for X-ray computed tomography using energy-integrating detectors," *Phys. Med. Biol.*, vol. 52, no. 8, pp. 2247-2266.

Lohan D.G, Motamedi K., Chow K., Habibi R., Panknin C., Ruehm S.G. and Seeger L.L., 2008, "Does dual-energy CT of lower-extremity tendons incur penalties in patient radiation exposure or reduced multiplanar reconstruction image quality?," *American Journal of Roentgenology*, vol. 191, no. 5, pp. 1386-1390.

Marshall W., Alvarez R. and Macovski A., 1981, "Initial results with prereconstructed dual-energy computed tomography (PREDECT)," *Radiology*, vol. 140, pp. 421-430.

MATLAB version 7.7.0.471 2008 B Natick, Massachusetts: The MathWorks Inc., 2008.

Matsumoto M., Miyajima S., Yamamoto A., Yamazaki T. and Kanamori, 2000, "Measurement of diagnostic X-ray spectra using CdZnTe detector," *Proceedings of the Second International Workshop on EGS*, pp. 242-249.

Paulus M., Sari-Sarraf H., Gleason S., Behel J., Thompson L. and Allen W., 1998, "A new X-ray computed tomography system for laboratory mouse imaging," *IEEE Trans. Nucl. Sci.*, vol. 2, pp. 1259-1263.

Ricq S., Glasser F. and Garcin M., 2001, "Study of CdTe and CdZnTe detectors for X-ray computed tomography," *Nucl. Instrum. Methods Phys. Res. A*, vol. A458, pp. 534-543.

Schlomka, Roessl E., Dorscheild R., Dill S., Martens G., Istel T., Baumer C., Herrmann C., Steadman R., Zeitler G., Livne A. and Proksa R., 2008, "Experimental feasibility of multi-energy photon-counting K-edge imaging in pre-clinical computed tomography," *Phys. Med. Biol.*, vol. 53, no. 15, pp. 4031-4047.

Sukovic P. and Clinthorne N., 2000, "Penalized weighted least-squares image reconstruction for dual energy X-ray transmission tomography," *IEEE Trans. Med. Imag.*, vol. 19, no.11, pp. 1075-1081.

Szeles C., 2003, "CdZnTe and CdTe materials for X-ray and gamma ray detector applications," *Phys. Stat. Sol. (b)*, vol. 241, no. 3, pp. 783-790.

Taibi A., Fabbri S., Baldelli P., DiMaggio C., Gennaro G., Marziani M., Tuffanelli A. and Gambaccini M., 2003, "Dual-energy imaging in full-field digital mammography: a phantom study," *Phys. Med. Biol.*, vol. 48, no. 13, pp. 1945-1956.

Talbert A.J., Brooks R.A. and Morgenthaler D.G., 1980, "Optimum energies for dual-energy computed tomography," *Phys. Med Biol.*, vol. 25, no. 2, pp. 261-269.

Tsunoo T., Torikoshi M., Ohno Y., Endo M., Natsuhori M., Kakizaki T., Yamada Y., Ito N., Yagi N. and Uesugi K., 20004, "Measurement of electron density and effective atomic number using dual-energy X-ray CT," *IEEE*, pp. 3764-2768.

Visipaque™ (iodixanol), A GE Product, Information available: ttp://md.gehealthcare.com/visipaque/

Webb S., 1996, "The Physics of Medical Imaging (Medical Science Series)", *IOP Publishing*.

Whiting B., Massoumzadeh P., Earl O., O'Sullivan J., Snyder D. and Williamson F., 2006, "Properties of preprocessed sinogram data in X-ray computed tomography," *Med. Phys.*, vol. 33, pp. 3290-3303.

Yan C., Whalen R., Beaupre G., Yen S. and Napel S., 2000, "Reconstruction algorithm for polychromatic CT imaging: application to beam hardening correction," *IEEE Trans. Med. Imag.*, vol. 19, no. 1, pp. 1-11.

Yue G., Giu Q., Goa B., Cheng Y., Zhang J., Shimoda H., Chang S., Lu J. and Zhou O., 2002, "Generation of continuous and pulsed diagnostic imaging X-ray radiation using a carbon-nanotube-based field-emission cathode," *Appl. Phys. Lett.*, vol. 81, no. 2, pp. 355-357.

Zhang J., Cheng Y., Lee Y., Gao B., Qiu Q., Lin W., Lalush D., Lu J. and Zhou O., 2005, "A nanotube-based field emission X-ray source for microcomputed tomography," *Review of Scientific Instruments*, vol. 76, pp. (094301)1-4.

5. SECOND PAPER: EIGENVALUE DECOMPOSITION OF FULL-SPECTRUM X-RAY COMPUTED TOMOGRAPHY.

This is the second paper we submitted for publication based on new energy-sensitive CT system presented in this dissertation. The paper was submitted in January, 2011, to IEEE Transactions on Medical Imaging. The paper presents a second method for noise suppression along the energy axis using a set of basis functions derived from the known attenuation curves using Eigenvalue decomposition. Noise suppression is the first step in analyzing the energy-sensitive CT data.

5.1. Abstract

Energy-discriminated x-ray Computed Tomography (CT) data are projected onto a set of basis functions to suppress the noise in filtered back-projection (FBP) reconstructions. The x-ray CT data are acquired using a novel x-ray system which incorporates a single-pixel photon counting x-ray detector measuring the x-ray spectrum for each projection ray. A matrix of the spectral response of different materials is decomposed using Eigenvalue decomposition to form the basis functions. Weights corresponding to basis functions show the distribution of the materials within the imaged object. Final reconstructions show significant noise suppression while preserving important energy-axis data. We conclude that the noise-resolution trade off along the energy axis is significantly improved using the eigenvalue decomposition basis functions.

5.2. Introduction

Medical x-rays are polychromatic in nature. The energy spectrum is expressed as the distribution of x-ray intensity with respect to x-ray energy; the energy is typically between 15KeV-150KeV for medical applications (Valais *et.al*, 2007). Current computed tomography

(CT) systems use integrating detectors to measure the x-ray intensity (Borisov *et.al*, 2006). These detectors assign an averaged value to the entire incident x-ray spectrum at each detector element. This value is the weighted sum of the measured x-ray energies (Lasio *et.al*, 2007).

In CT, the measured x-ray spectrum intensity is ratioed with the emitted x-ray spectrum intensity and back-projected to create an estimate of the x-ray attenuation for the imaged object, typically represented as a Hounsfield number corresponding to a spatially-varying linear attenuation coefficient for a slice through the object (Ambrose and Hounsfiel, 1974). The spatial variation of this value represents the distribution of different materials within the object based on the different materials' ability to absorb and scatter x-rays. The estimated attenuation value for a material represents several different interactions between the material and the x-ray spectrum. To separate these different interactions, the x-ray spectrum must be sampled with multiple energies (Hubbel and Seltzer, 1996).

As x-rays pass through a material, the material affects the shape (the distribution of intensity with respect to energy) of the x-ray spectrum. This is primarily due to the Compton scatter and the photoelectric absorption of the material. Both these processes are dependent on x-ray energy, resulting in a change in apparent attenuation. The mass-attenuation coefficients as a function of x-ray energy for elements Z=1-93 and selected biological compounds are available at the National Institute of Standards and Technology (NIST) database (Hubbel and Seltzer, 1996).

The Compton scatter and photoelectric absorption for a material can be estimated by measuring separate x-ray spectra centered at two different x-ray energies; a low x-ray energy, typically around 40KeV, and a high x-ray energy, typically 80-100KeV (Talbert *et.al*, 1980).

This is called dual-energy computed tomography (DECT) (Marshall *et.al*, 1981). DECT allows one to estimate the electron density and effective atomic number of a material from the Compton scatter and photoelectric absorption respectively (Rutherford *et.al*, 1981; Tsunoo *et.al*, 2004). However, finding these values for more than two materials is not possible with DECT (Shikhalie, 2008) as it would require solving for more than two unknowns with only two attenuation measurements.

To compensate for the two energy limit, dual-energy algorithms focus on tissue segmentation rather than measuring photoelectric absorption and Compton scatter (Shikhalie, 2008; Shikhalie, 2008; Uotani *et.al*, 2009; Goh *et.al*, 1997; Bazalova *et.al*, 2008). Tissue segmentation divides the reconstructed x-ray attenuation based on density; indentifying the distribution of dense material and soft material. In medical imaging, the dense material is commonly bone or contrast agent and the soft material is soft tissue, i.e. fat, muscles, organs, etc. (Shikhalie, 2008; Uotani *et.al*, 2009). This is done to improve the contrast and reduce the effects of beam hardening (Sukovic and Clinthorne, 2000). Tissue segmentation uses the differences in x-ray measurements at two energies (Shikhalie, 2008; Shikhalie, 2008; Goh *et.al*, 1997; Uotani *et.al*, 2009; Bazalova *et.al*, 2008). This can be done using simple image subtraction (Shikhalie, 2008; Uotani *et.al*, 2009) or more complicated iterative algorithms. The low-energy scan contains a greater portion of soft-tissue information; at high energies these soft tissues attenuate less of the signal. Subtracting the low energy scan from the high-energy scan segments the dense tissue; reversing the order of subtraction segments the soft tissue (Shikhalie, 2008). This simple form of tissue segmentation does not suppress beam hardening (Sukovic and Clinthorne, 2000).

Iterative algorithms reconstruct the two energy measurements based on some criterion which is chosen to optimize the segmentation of materials (Shikhalie, 2008; Shikhalie, 2008; Uotani *et.al*, 2009; Goh *et.al*, 1997; Bazalova *et.al*, 2008). In (Sukovic and Clinthorne, 2000; Kalender *et.al*, 1988) the segmentation is based on the mass-attenuation for bone and soft-tissue and the reconstructions are segmented into corresponding mass of the different materials for each pixel of voxel location. This segmentation uses penalized weighted least squares (PWLS) criterion (Sukovic and Clinthorne, 2000) or adaptive filtering (Kalender *et.al*, 1988). The two segmented images correspond to the distribution of the two materials rather than an attenuation distribution. In (Goh *et.al*, 1997) linear attenuation coefficients are used for segmentation. The authors of (Goh *et.al*, 1997) assume that the two linear attenuation coefficients are independent and decompose a set of weights using the linear attenuation as basis functions defining the segmentation of the materials. This method fails to account for the significant correlation between the attenuation coefficients for most biological materials (Hubbel and Seltzer, 1996). In (Bazalova *et.al*, 2008) a variation of Compton scattering and photoelectric effect is used; dividing the reconstructions based on an estimate of the atomic number and atomic density. This assumes prior knowledge of materials present in the object. All of these algorithms are limited to two materials.

There has been increased interest in extending dual energy imaging concepts to energy-discriminated imaging (Shikhalie, 2008. This includes both simulation and algorithm design (Shikhalie, 2008), (Elbakri and Fessler, 2002) along with some experimental work (Shikhaliev, 2008). The experimental work uses new energy- differentiating x-ray detectors capable of sampling the incident spectrum with five averaged energies rather than a single averaged energy (Szeles, *2003*; Matsumoto *et.al*, 2000; Ricq *et.al*, 2001). The experimental

work is focused on incorporating new detectors and acquiring energy-discriminated x-ray data. There is little discussion of reconstruction methods or the incorporation of the added energy dimension in the reconstructions (Shikhaliev, 2008; Paulus *et.al*, 1998; Glease *et.al*, 1999; Szeles, 2003).

The energy-discriminating algorithms are extensions of the dual-energy algorithm concepts using simulated data (Elbakri and Fessler, 2002; Roessl and Proksa, 2007; Yan *et.al*, 2000; Bazalova and Verhaegen, 2007). The authors of (Elbakri and Fessler, 2002) extend the idea in (Sukovic and Clinthorne, 2000) to an undefined number of energy measurements and reconstruct based on mass of the different materials for each pixel or voxel location using a PWLS algorithm. The authors of (Roessl and Proksa, 2007) use multiple contrast agents and use a method similar to (Uotani *et.al*, 2009) with simple subtraction. The authors of (Yan *et.al*, 2000) use the added energy dimension to remove beam-hardening artifacts. These algorithms focus on tissue segmentation and suppression of beam-hardening.

Recently we have developed an energy-discriminating x-ray CT system capable of segmenting the incident x-ray spectrum into as many as 512 energy bins (Gonzales and Lalush, 2010). This system has a high degree of energy axis resolution; however, the division of the x-ray spectrum introduces a large amount of noise into the estimated attenuation reconstructions. As the number of energy bins increase, the x-ray intensity in each becomes smaller and the measurement becomes more susceptible to noise. Therefore, we propose two noise suppression algorithms: a PWLS algorithm (Gonzales and Lalush, 2010) and the Eigenvalue decomposition algorithm presented in this paper.

The data collected in this new system are represented in either the x-ray spectrum for each projection ray (figure 5.1A) or as a sinogram for each sampled energy bin (figure 5.1C). In this paper, these data are reconstructed using filtered-back-projection to form an estimate of the x-ray attenuation of the imaged object as a function of energy. This attenuation is represented as either a spatially varying attenuation for a slice through the object (called an "attenuation map") (figure 5.1D) or an attenuation varying along the energy axis for a single location in space (called an "attenuation curve") (figure 5.1B). In this algorithm we suppress the noise in the energy axis rather than in the spatial dimensions.

We propose an algorithm which decomposes the reconstructed attenuation curves along a set of orthogonal basis functions defined to separate the signal from the noise. The existence of as many a 512 x-ray energies enables us to create as many basis functions as we deem necessary, significantly extending the two energy limit in DECT. The basis functions are derived from the mass-attenuation curves (Hubbel and Seltzer, 1996) corresponding to the known materials within the imaged object. This allows us to suppress the noise and to separate materials in the image object based on their properties of attenuation with respect to the x-ray energy

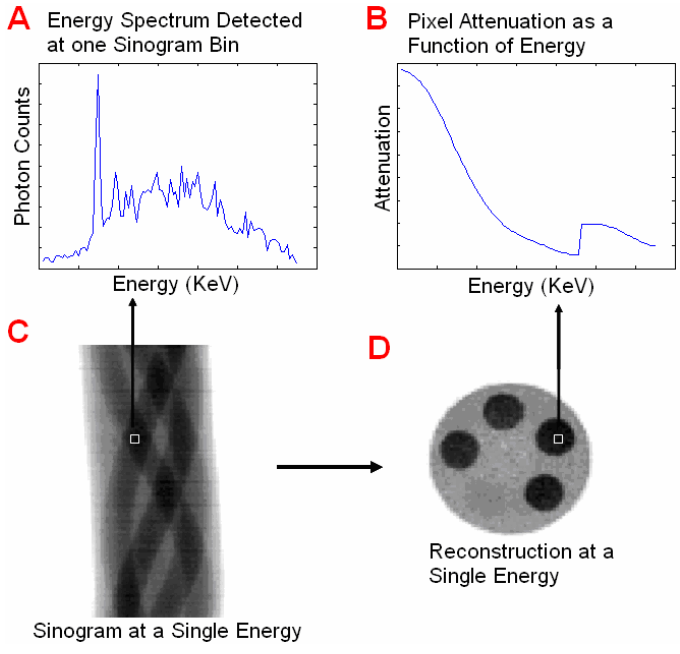

Figure 5.1: Data types for polychromatic X-ray CT. Data are collected as an x-ray spectrum for each projection ray (A). The projection rays are arranged as a sinogram (C) for each energy bin. Then each sinogram is reconstructed into an attenuation map for each energy bin (D). Each pixel in the attenuation map can be represented as an attenuation curve (B).

In this paper we present the Eigenvector decomposition algorithm for noise suppression (Section II). We also present a brief overview of the new energy-discriminating x-ray CT system we have developed (Section III). We then present a set of data validating the algorithm's ability to suppress the noise and significantly increase signal-to-noise ratio (SNR) (Section IV). The results are discussed and future directions for this research are presented in Section V.

5.3. Algorithm

The x-ray projection data are reconstructed using filtered back-projection (FBP) to an estimate of the attenuation. We define the estimated attenuation as μ_{jE} where the index j indicates the image-space pixel and the index E indicates the energy bin. We assume that there are K energy bins: $E = [1,2,\cdots,K]$. We express an attenuation curve as μ_{j*} which is the estimated attenuation for all energy at pixel *j*. We will determine a set of orthogonal basis

functions for the attenuation curves by regarding the attenuation curve for any pixel as a sample from a random process governing the set of all attenuation curves found in the subject. We define the composition of any location in the object to be a mixture of *M* known materials. Therefore, the attenuation curve at any location is a weighted sum of the mass attenuation relations of the M known materials:

$$\mu_{jE} = \sum_{m=1}^{M} w_{jm} \left(\left(\frac{\mu}{\rho} \right)_E \right)_m \tag{5.1}$$

The weight term w_{jm} encompasses the average density of material m within pixel or voxel *j*. Since all pixels are uniformly sized, this relates directly to the mass of material *M* within pixel *j*. The term in the parentheses represents a K-length vector (with index E for each vector element) of mass attenuation coefficients for material M across the defined energy range.

The random elements in this mixture model are the weights; the mass attenuation coefficient term is merely a collection of physical constants. So, the (E_1, E_2) element of the $K \times K$ autocorrelation matrix, designated as the expectation$\mathbb{E}$ of two energies for the attenuation curve at any location j in the object. The autocorrelation is:

$$\mathbb{E}\left[\mu_{jE1}\mu_{jE2}\right] = \sum_{m=1}^{M}\sum_{l=1}^{M} \mathbb{E}\left[w_{jm}w_{jl}\right] \left(\left(\frac{\mu}{\rho} \right)_{E1} \right)_m \left(\left(\frac{\mu}{\rho} \right)_{E2} \right)_l \tag{5.2}$$

The expectation term $\mathbb{E}\left[w_{jm}w_{jl}\right]$ is the autocorrelation of the weights (masses) associated with materials l and m at pixel j. It is related to the joint probability of certain amounts of each material being present at the given location. To simplify, we assume that (expression 5.1) this probability is independent of location and that (expression 5.2) the

amount of any material at a location is independent of the amount of any other material at that location. If we do not make these simplifying assumptions, there are some interesting implications. For example, maintaining a location-dependent model would allow one to model an increased likelihood of one material being present at a location based on some prior knowledge. Introducing dependence between materials would permit one to model materials that are more or less likely to co-locate: a contrast agent that cannot go to bone, for example. Initial results show that these assumptions have little effect on the basis functions derived, but more work remains in this area.

With the simplifying assumptions thus made, the expectation on the weights becomes a general constant w, which is factored out of the matrix, and we have a K × K square matrix U proportional to the autocorrelation of the attenuation curves μ_*. The * indicates a vector encompassing all energies $E = [1,2,\cdots,K]$. Thus, the autocorrelation matrix is a weighted sum of all M attenuation curves at every energy bin.

$$\mathbb{E}[\mu_*\mu_*^T] = \sum_{m=1}^{M}\sum_{l=1}^{M} w\left(\left(\frac{\mu}{\rho}\right)_*\right)_m \left(\left(\frac{\mu}{\rho}\right)_*\right)_l^T = U \tag{5.3}$$

We use a value of 1 or ½ for w:

$$w = \begin{cases} 1 & m = l \\ \frac{1}{2} & m \neq l \end{cases}$$

The T indicates a vector transpose so the multiplication of the vectors results in a scalar. A value of $\frac{1}{2}$ is used when $m \neq l$ because each combination of m and l is repeated twice in (expression 5.3) but $m = l$ only once. This makes every possible combination of

attenuation curves equally likely. An orthogonal set of basis functions is then derived by taking the Eigen decomposition of the matrix *U*:

$$U = V \cdot \Sigma \cdot V^{-1} \tag{5.4}$$

Where *V* is a K × K matrix of the Eigenvectors of *U* and ∑ is a K × K diagonal matrix comprised of the corresponding Eigenvalues. The K Eigenvectors, each of length K, represent a complete basis set to describe and decompose any K-length attenuation curve. However, since *U* was constructed from only *M* different attenuation curves, it will generally only require M Eigenvectors (those with the highest Eigenvalues) to describe any legitimate (i.e., composed of *M* known materials) attenuation curve. The remaining K-*M* Eigenvectors represent components of the orthogonal basis set that should not exist in the object (i.e., not legitimate attenuation curves), so these are considered to map to noise and are discarded. Thus, we have only M Eigenvectors used to describe the K-dimensional attenuation curve space. Noise suppression is achieved by projecting the attenuation curves from the raw reconstruction onto the *M* orthogonal basis functions by taking the inner production, designated by the brackets:

$$a_{jn} = \langle V_*^n, \mu_{j*} \rangle \tag{5.5}$$

Where a_{jn} is the weight associated with basis function n at pixel j, and V_*^n is the K-length basis function n extracted from matrix *V*. The noise-suppressed final estimate of the attenuation comes from reconstituting a new attenuation curve from the linear combination of the *M* basis functions:

$$\mu_{j*} = \sum_{n=1}^{M} a_{jn} V_*^n \tag{5.6}$$

The Eigenvector basis functions V_*^n describe the combinations and differences of the M known mass-attenuation curves. The weights a_{jn} give the spatial distribution of these basis functions, the contribution of basis function n at pixel location *j*.

5.4. Experimental Setup

The x-ray spectrum is sampled as a vector of photon counts for each projection ray (figure 5.1A); each element in the vector is an "energy bin". To acquire this sort of x-ray data, we use an AMPTEK single-pixel photon-counting detector (Gonzales and Lalush, 2011).

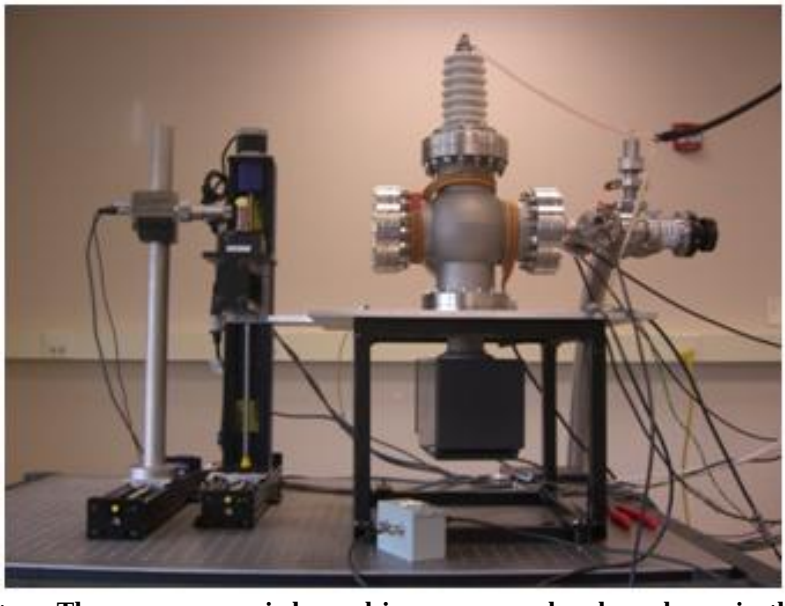

Figure 5.2: X-ray System. The x-ray source is housed in a vacuum chamber, shown in the right of the image, and controlled via the cables shown coming from the chamber. Velmax positioning slides, shown in the left of the image, are used to generate the CT motion. An AMPTEK detector, far left mounted on a stand, is used to sample the x-ray spectrum.

This is similar to the system proposed in (Claesson *et.al*, 2001). The system proposed in (Claesson *et.al*, 2001) also uses an AMPTEK single pixel detector using it with a monochromatic gamma source. This system uses a polychromatic carbon-nanotube (CNT) x-ray source (Gao *et.al*, 2001) instead. The rest of the system is designed around the incorporation of the AMPTEK single-pixel detector (figure 5.2).

5.4.1. Experiment Design

The carbon-nanotube (CNT) x-ray source is designed to be used with any detector; it uses CNT to generate free electrons which are accelerated into a molybdenum anode to generate x-rays. This x-ray source is housed in a steel vacuum CT system with a beryllium window; this window is the only filtering. The CNT sources replace a tungsten filament to generate the free electrons necessary to produce x-rays. These experimental CNT sources have many unique properties (Gao *et.al*, 2001; Yue *et.al*, 2002; Zhang *et.al*, 2005); however, we do not use them in any special way and a standard thermionic source could also be used in this system. The voltage sources are all controlled via a computer with Labview code.

The X-ray source has a 45kV voltage applied to the anode and a 3500V gate voltage to the gate electrode. The 3500V gate voltage is pulsed at 40Hz with a 50% duty cycle to preserve the CNT cathode. This creates an x-ray field which is equivalent to a 100mA field emitted from a tungsten filament. These settings are used for the entire experiment. The 45kV anode voltage is used because of limitations on the high voltage feed-through.

The imaged object is moved through this field, between the source and detector, to create a CT slice through the object. This movement is controlled by a set of Velmex linear slides and rotational table. The Velmex slides are capable of computer-controlled motion as small as 10μm step size in both horizontal and vertical directions. The object is rotated during imaging rather than the source-detector pair spinning around a stationary object.

An AMPTEK XR-100CR photon-counting detector with a PX4 signal processor samples the incident x-ray spectrum. The detector has a 36mm tungsten collimator with a 300μm hole in front of a 50μm tungsten pinhole to reduce the scattered x-rays and to define a projection ray from the source through collimator and pinhole to the detector. This detector

records each x-ray photon that makes it through the collimator and assigns it to an energy bin. The energy binning has approximately 0.35KeV steps covering an energy range from 10 to 45KeV.

The detector is set to record the x-ray photons incident upon it in a 5 second period. The distribution of x-ray photons with respect to energy over the period creates the x-ray spectrum the detector sees at that specific location. A single five second measurement determines the x-ray spectrum for a specific projection across all energies. Complete CT data are measured for every projection location.

5.4.2. Phantom

To test the algorithm and experimental design a phantom with multiple contrast agents was designed. The phantom was constructed from an acrylic base and is cylindrically shaped to optimize for a straightforward computed tomography imaged slice. The phantom is an acrylic cylinder with a 2.5cm diameter and five circular holes 0.5cm in diameter arranged circularly around the 1cm radius; see figure 5.3.

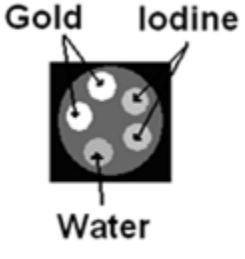

Figure 5.3: Cylindrical acrylic phantom and distribution of contrast agents within the phantom. This is a slice through the phantom corresponding to the reconstructed slice with distribution of different elements labeled.

We used an acrylic base because it has an attenuation curve very close to human soft-tissue and forms a good background material. One of the five holes is filled with distilled water. Water is also the base for the contrast agent solutions.

We focused on two contrast agents: iodine and gold nanoparticles. Iodine is commonly used in clinical applications for cardio-vascular imaging to increase contrast in vessels. Iodine has a very sharp absorption-edge at 35KeV making it appear denser than bone at energies larger than the absorption-edge. We use a 20mg/ml solution of Visipaque (Visipaque) to test the iodine contrast.

Gold nanoparticles are being investigated as potential contrast agents because they are non-reactive and have several absorption-edges at x-ray energies including a large one at 60KeV (Hainfield et.al, 2006; Kattumuri et.al, 2007). Gold nanoparticles may be tagged and used in functional imaging. We used a 16mg/ml solution of gold nanoparticles, trade named AuroVist (AuroVist).

5.4.3. Filtered Back Projection

The data are acquired in this method as a set of projection rays for 93 energy bins, and arranged as a sinogram for each energy bin (figure 5.1C). The imaged object is 2.5cm and there are 81 detector elements spaced 0.4mm; this leaves 20 pixels which pass through air in the sinogram. These pixels are used to form the blank scan, which represents the un-attenuated x-ray signal and is used to correct the data. The data are then back-projected using FBP with a Ram-Lak filter that has no low-pass roll off. We use the FBP attenuation map estimates as the initial estimate for the Eigenvalue decomposition method. We could have included spatial filtering into this step, but we choose not to in order to demonstrate only the effects of the decomposition method.

5.5. Results

The initial FBP estimate of attenuation is shown in two forms: as an attenuation map for each energy bin (figure 5.4) or as an attenuation curve for each pixel location (figure 5). Both

of these are only shown for selected energy bins or pixel locations respectively. Six different attenuation maps are shown and four attenuation curves (one for each material used). The FBP data are shown to demonstrate the noise distribution in the initial reconstructions. This noise is distributed spatially, as shown in the attenuation maps (figure 5.4), and along the energy axis (figure 5). Averaging along the energy axis would reduce the noise significantly, but would also result in the loss of energy axis detail.

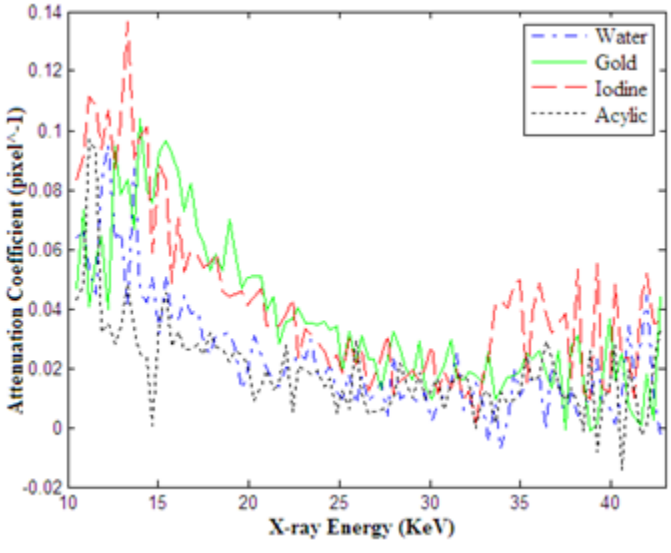

Figure 5.4: FBP reconstruction of attenuation maps at selected energy bins. Only 8 energy bins of the original 93 are shown. These are distributed over the entire energy range (13-43KeV) spaced every 3.85KeV.

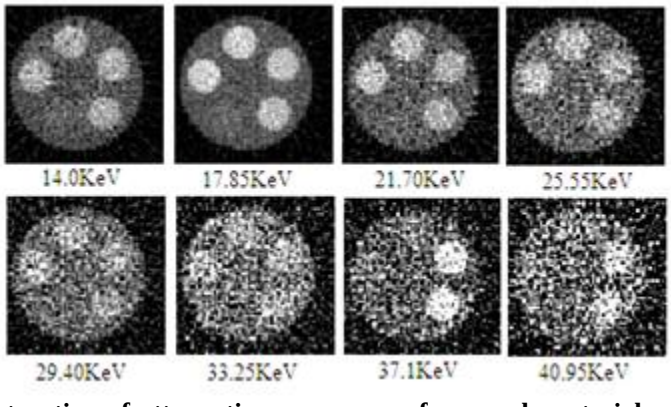

Figure 5.5: FBP reconstruction of attenuation curves, one from each material, at selected single pixels. Pixel size is 400μm

To suppress the noise along the energy axis, we use the Eigenvector decomposition algorithm proposed in Section III. The imaged object is composed of four materials (figure 5.2). Thus, we use M=4 for (expressions 5.1-5.3). The mass-attenuation curve $\left(\frac{\mu}{\rho}\right)_*$ for each of these materials is available online at the NIST database (Hubbel and Seltzer, 1996). We took the mass-attenuation values from (Hubbel and Seltzer, 1996) corresponding to the energy range of the AMPTEK detector. The curves were extended to be length K using shape-preserving piecewise cubic interpolation. These curves are displayed in figure 5.6A.

These four mass-attenuation curves were then combined using (expression 5.3) forming the $K \times K$ covariance matrix U which is decomposed using Eigenvector decomposition (expression 5.4). The top four Eigenvectors form the basis functions (figure 5.6B). The first basis function, basis 1, defines the negative average of all the different mass-attenuation curves. The second basis function, basis 2, is loosely interpreted as “gold and not-iodine”. The third, basis 3, is “iodine and not-gold”. The fourth is the remaining signal information. All other Eigenvectors form basis functions that map to features not found in the four materials, considered noise.

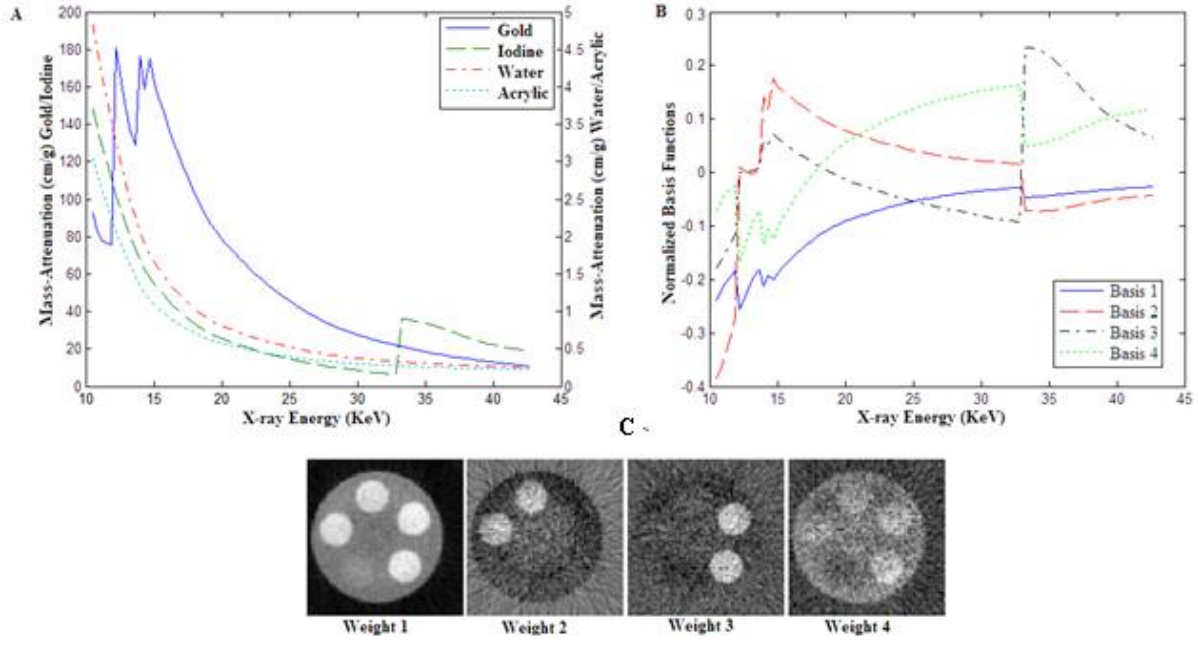

Figure 5.6: Eigenvector decomposition basis functions. (A) shows the mass-attenuation curves from the NIST database, shown on two axes. Iodine and gold have much larger mass-attenuation in this energy range and are shown on the left axis. Water and acrylic are shown on the right axis. These mass-attenuation curves are used as the *M* materials' curves to form eq. (3). These are decomposed eq. (4) to form four basis functions (B). (C) is the spatial distribution of each of these eq. (5). In (C) weight 1 is inverted to make it easier to see, it corresponds to an inverse average (basis 1 (B)).

The attenuation curve, corresponding to each pixel μ_{j*}, is projected onto each of the basis functions, eq. (5), forming a weight a_{jn} (figure 5.6C). Each weight is the spatial distribution of one of the basis functions. The first weight is the distribution of the average; weight 1 in Figure 5.6C has been inverted to make it easier to see. This corresponds to the negative average in basis 1. The second weight corresponds to the "gold and not-iodine basis" function. The third weight corresponds to the "iodine and not-gold". The final weight is a combination of the remaining signal space and focuses on the background material, mostly acrylic. The weights form a simple material segmentation for iodine and gold.

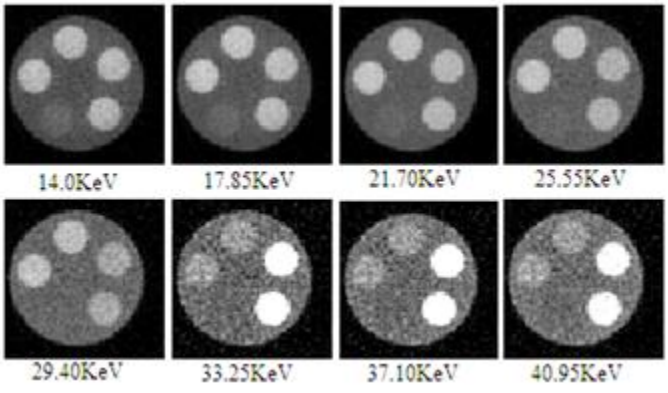

Figure 5.7: Attenuation map reconstructions at different energies after Eigenvector decomposition has been applied to the data, along each attenuation curve. These are the same energies and same scale as figure 5.4.

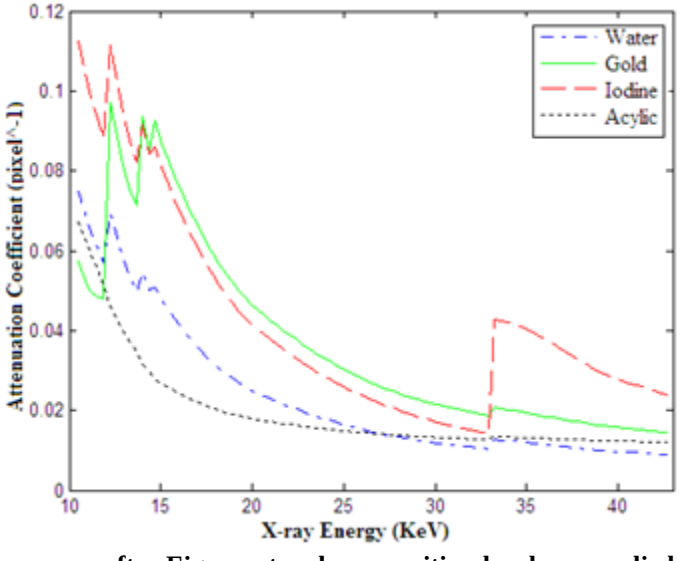

Figure 5.8: Attenuation curves after Eigenvector decomposition has been applied to reconstruction data, at selected single pixels, the same locations as figure 5. Pixel size is 400μm.

Multiplying each of the weights times the corresponding Eigenvector basis function and summing the result, eq. (6), returns a new estimate for the noise suppressed attenuation value. This new attenuation is shown for attenuation maps and attenuation curves (figures 7 and 8) corresponding to the same energy bins and pixel locations as figures 4 and 5 respectively.

The Eigenvector decomposition method suppresses the noise along the energy axis; however, this noise is distributed both spatially and along the energy axis (as shown in

figures 4 and 5). Thus, suppressing the noise along the energy axis also suppresses it in space. Figure 5.7 shows the noise suppression improvement in the attenuation maps (spatial distribution). The scale in both figure 5.4 and 5.7 is the same, so the improvement in appearance is entirely due to the Eigenvector method.

A single attenuation curve is selected for each material, from the known distribution of materials (figure 5.2), and shown (figures 5.5 and 5.8) to represent the way the Eigenvector decomposition method affects the noise along the energy axis. Figure 5.5 shows the noise along each of these curves, the general shape of each attenuation curve is visible, but only if one knows what to look for; the noise makes it difficult to use the attenuation curves to indentify the specific materials based on the known shape of the curve (figure 5.6A). Figure 5.8 shows the same attenuation curves after the noise suppression. The same shape remains, but the noise has been mostly removed and it is now possible to use these curves in indentifying the specific materials based on their shape (comparing the figures 6A and 8).

Comparing figure 5.4 to 5.7 and 5.5 to 5.8 demonstrates the noise suppression spatially and along the energy axis. This is also shown as an improvement in the signal-to-noise ratio (SNR) (figure 5.9).

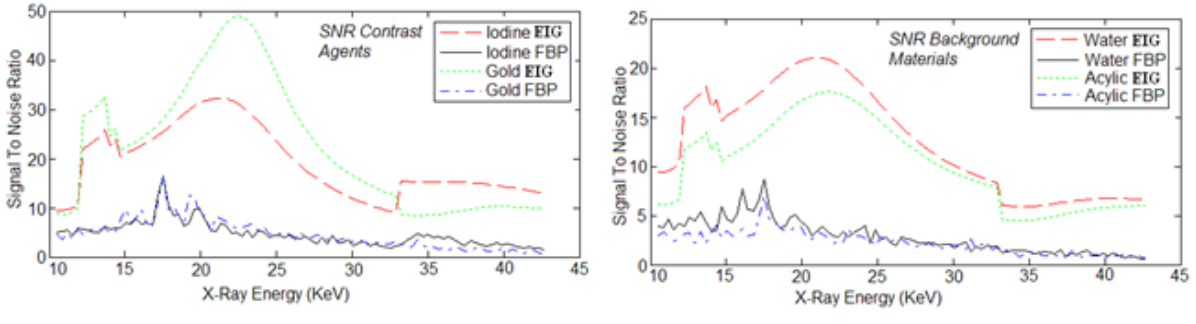

Figure 5.9: Signal-to-Noise ratio as a function of X-ray energy. Comparing Eigenvector decomposition (EIG) with filtered back-projection (FBP) Top figure: for the two contrast agents gold and iodine. Bottom figure: the background materials of water and acrylic.

This figure shows the SNR as a function of x-ray energy; calculated separately for each energy bin or for each attenuation map. The SNR is calculated by averaging the attenuation in each material at each energy bin and dividing by the variance within that material. The SNR is shown for the FBP and Eigenvector decomposition for each of the materials used in the experiment. Figure 5.9 shows the significant improvement across all energy bins and all materials due to the proposed method.

5.6. Discussion

X-ray data are collected using a new system which replaces the standard digital integrating detector with a single pixel photon-counting detector. This allows us to sample the complete x-ray spectrum through the imaged object. The only limiting factors are the sample size (energy binning size) and the noise.

The noise in the system is the result of photon counting and is distributed across energy in the initial projection estimates. Each energy bin in each projection ray will have some noise affecting the photon count in that specific bin. This noise is back-projected onto the attenuation estimate in the attenuation maps (figure 5.4) and the attenuation curves (figure 5.5). There are a number of different places we could have addressed the noise: in the projection space, in the initial reconstruction, across the attenuation maps, or in the attenuation curves. It makes sense to suppress noise along the energy axis rather than in space to maintain spatial resolution. We have prior knowledge about the attenuation curves from the NIST database; this means that we know more about attenuation effects with respect to energy than the sampled spectra with respect to energy.

To suppress the noise, we introduce the assumption that the attenuation curve in each pixel is a combination of a discrete number of M materials' attenuation curves (expression 5.1). We then take those known attenuation curves and combine them in a single covariance matrix (expression 5.3) which is decomposed using Eigenvalue decomposition. The top M Eigenvectors of this matrix form basis functions which we use to separate the signal from the noise in the reconstructed attenuation curves (expression 5.5).

The attenuation curves selected to form the covariance matrix (expression 5.3) are the mass-attenuation curves (figure 5.6A) for the four materials in the phantom (figure 5.2). The covariance matrix is decomposed, forming four basis functions (expression 5.5) (figure 5.6B). These are orthogonal basis functions interpreted as: the inverse average (basis 1), gold and not-iodine (basis 2), iodine and not-gold (basis 3), and the remaining data not defined by the other basis functions (basis 4). These interpretations of the basis functions are based on the shape of each basis function, i.e. the gold and not-iodine has a positive gold absorption edge and negative iodine absorption edge. These interpretations focus on the existence of absorption edges and more work needs to be done to investigate the effects if no absorption edges are present. The principal differences in the attenuation curves seem to be the absorption edges; if no edges exist it may be difficult to use this method.

Projecting each estimated attenuation curve onto the basis functions (expression 5.5) creates four spatially variant weights (figure 5.6C). Each weight is the distribution of the corresponding Eigenvector basis function. Thus, the first weight is the distribution of the average and appears as an average of the imaged slice (figure 5.6C.1). The distribution of bases 2 and 3 corresponds to the distribution of gold and iodine respectively. This demonstrates that this method may be used for tissue decomposition. However, it is apparent

that each basis function describes a combination of materials rather than a single material, thus this is not true image segmentation. Both gold and iodine have absorption edges which increase their separation; to be certain of this method's capability of partial tissue segmentation, more work is needed.

The distributions of the weights (figure 5.6C) are shown in image form, but the precise meaning of these weights is not clear. With only a single concentration of each material we cannot identify if the weights truly correspond to concentration. Future experiments will seek to quantify the relationship between the concentration of a material within a pixel and the weight of the basis functions.

Multiplying each of the weights times the corresponding basis function and then adding the results yield the new estimate of attenuation (expression 5.6). This new estimate shows significant noise suppression along the energy axis (figure 5.8) and attenuation maps (figure 5.7). This improvement is also shown as an improvement in the SNR as function of energy (figure 5.9). These results all demonstrate the basic success of the proposed algorithm. Our goal was to suppress noise from photon-counting along the energy axis, while preserving energy axis data.

Key energy axis data includes the location of absorption edges and general shape of the attenuation curves. Comparing figures 8 and 5 demonstrates that for each sampled attenuation curve, the basic shape is preserved. If one overlays the new attenuation curves (figure 5.8) over the old ones (figure 5.5), the new ones will be an average along each curve, except at absorption edges. The absorption edges for gold and iodine exist in figure 5.5, but are difficult to separate from the noise. This is also true when averaging the FBP for all attenuation curves for each material (data not shown). These edges remain in the new

attenuation curves (figure 5.8). This is a preservation of key energy axis data. If one simply averaged along the energy axis, these edges would be lost or reduced in size.

The only significant problem with the estimated attenuation curves (figure 5.8) is that a small part of the absorption edge, for both gold and iodine, is imposed on the other materials' attenuation curves. This is most apparent for the gold absorption edges. These are multiple edges close together and the algorithm confuses the noise in water and iodine to be a small amount of gold in each material. This is not a large problem in these reconstructions, but if the concentration of gold was smaller, this may become a significant problem. It may be possible to change the joint weights in (expression 5.2) to partially account for this; i.e. it is not possible to have both gold and iodine in the same attenuation curve.

We have recently proposed a second method for suppressing the noise along the energy axis using a penalized weighted least squares (PWLS) (Gonzales and Lalush, 2011). The PWLS method takes much longer: it is an iterative method and Eigenvector decomposition is a single step method. Both methods show a significant improvement in SNR over FBP. Both methods also preserve the key attenuation curve data. The PWLS method does not impose the absorption edges on other materials and seems less dependent on materials with absorption edges. A detailed comparison of the two methods for noise suppression and accuracy was recently presented at the IEEE conference of medical imaging 2010 (Gonzales and Lalush, 2010).

Extending this method, as it exists now, to preclinical imaging is not possible. For this experiment, section III, we are using a single-pixel photon counting detector. The projection at each pixel must be measured individually. This takes 5 seconds per pixel. This means that a single slice, which has 120*81 pixels takes 120*81*5 seconds. This is too long

for any practical experiments on any live subject. However, we are developing designs for a more efficient small animal system that could make use of these techniques.

Current digital strip detectors can segment the measured spectrum into 5-6 energy bins *(Szeles, 2003; Matsumoto et.al, 2000; Ricq et.al, 2001)*. Such a system could be used with the methods detailed here; however, it is not clear what the optimum number of bins would be to maximize sensitivity and quantitative accuracy. Having five energy bins may allow us to use this method for a similar phantom, because the number of bins is more than the number of materials. The work in this paper provides justification to extend detector work to be able to separate the x-ray spectrum into a greater number of energy bins.

5.7. Conclusion

A novel x-ray computed tomography system is proposed which uses a single-pixel photon counting detector to sample the entire x-ray spectrum for each projection ray. Data are reconstructed using simple filtered back-projection and noise is suppressed using an Eigenvector decomposition approach with a model autocorrelation matrix based on known mass-attenuation curves. Noise is successfully suppressed while preserving important energy axis data. The weights of the Eigenvector basis functions form a simple image segmentation based on the existence of absorption edges in the materials present in the phantom. Further work is needed to identify the relationship between material concentration and weights.

5.8. References

Ambrose J. and Hounsfield G., 1974, "Computerized Transverse Axial Tomography," *British Journal of Radiology,* vol. 46, no. 542, pp. 148-149.

AuroVist™, A Nanoprobes Product, Information available: http://www.nanoprobes.com/AuroVist.html

Bazalova M., Carrier J.F., Beaulieu L. and Verhaegen F., 2008, "Tissue segmentation in monte carlo treatment planning: a simulation study using dual-energy CT images," *Radiotherapy and Oncology*, vol. 86, pp. 93-98.

Bazalova M. and Verhaegen F., 2007, "Monte Carlo simulation of a computed tomography X-ray tube," *Phys. Med. Biol.*, vol. 52, no. 19, pp. 5945-5955.

Borisov A.A., Veip Y.A., Mazurov A.I., and Elinson M.B., 2006, "Two technologies for designing digital X-ray image detectors," *Biomedical Engineering*, vol. 40, no. 5, pp. 219-222.

Claesson T., Kerek A., Molnar J. and Novak D., 2001, "A CT demonstrator based on a CZT solid state detector," *in IEEE Nuclear Science Symposium Conference Record*, vol. 3, pp. 1644-1646.

Elbakri I. and Fessler J., 2002, "Statistical image reconstruction for polyenergetic X-ray computed tomography," *IEEE Trans. Med. Imag.*, vol. 21, no. 2.

Gao B., Yue G., Qiu Q., Cheng Y., Shimoda H., Fleming L. and Zhou O., 2001, "Fabrication and electron field emission properties of carbon nanotube films by electrophoretic deposition," *Advanced Materials*, vol. 13, no. 23, pp. 1770-1773.

Gleason S., Sari-Sarraf H., Paulus M., Johnson D., Norton S. and Abidi M., 1999, "Reconstruction of multienergy X-ray computer tomography images of laboratory mice," *IEEE Trans. Nucl. Sci.*, vol. 46, no. 4, pp. 1081-1086.

Goh K.L, Liew S.C., and Hasegawa D.H., 1997, "Correction of energy-dependent systematic errors in dual-energy X-ray CT using a basis material coefficients transformation method," *IEEE Trans. Med. Imag.*, vol. 44, no. 6, pp. 2419-2424.

Gonzales B. and Lalush D., 2010, "Performance of Reconstruction and Processing Techniques for Dense Full-Spectrum X-ray Ct," *Proceedings of the 2010 IEEE Nuclear Science Symposium and Medical Imaging Conference*, Knoxville, TN, M09-131.

Gonzales B. and Lalush D., 2011, "Full-Spectrum CT Reconstruction Using a Weighted Least Squares Algorithm with an Energy-axis Penalty," *IEEE Trans. Med. Imag*., vol. 30, pp. 173-183.

Hainfield J., Slatkin D., Focella M. and Smilowitz H., 2006, "Gold nanoparticles: a new X-ray contrast agent," *The British Journal of Radiology*, vol. 79, pp. 248-253.

Hubbell J.H. and Seltzer S.M., 1996, "Tables of X-Ray Mass Attenuation Coefficients and Mass Energy-Absorption Coefficients from 1 keVto 20 MeV for Elements Z = 1 to 92 and 48 Additional Substances of Dosimetric Interest", *National Institute*

of Standards and Technology, Tech. Rep. 43NANB412756 Available: http://www.physics.nist.gov/PhysRefData/XrayMassCoef/cover.html

Kalender W., Klotz E. and Kostaridou L.,1998, "An algorithm for noise suppression in dual energy CT materail density images," *IEEE Trans. Med. Imag.*, vol. 7. no. 3, pp. 218-224.

Kattumuri V., Katti K., Bhaskaran S., Boote E., Casteel S., Fent G., Roberston D., Chandrasekhar M., Kannan R. and Katti K.V., 2007, "Gum Arabic as a Phytochemical Construct for the Stabilization of Gold Nanoparticles: In Vivo Pharmacokinetics and X-ray-Contrast-Imaging Studies," *Small*, vol. 3, no. 2, pp. 333-341.

Lasio G.M., Whiting B.R., and Williamson J.R., 2007, "Statistical reconstruction for X-ray computed tomography using energy-integrating detectors," *Phys. Med. Biol.*, vol. 52, pp. 2247-226.

Marshall W.H., Alvarez R. and Macovski A., 1981, "Initial results with prereconstruction dual-energy computed and tomography (PREDECT)," *Radiology*, 421-430.

Matsumoto M., Miyajima S., Yamamoto A., Yamazaki T. and Kanamori, 2000, "Measurement of diagnostic X-ray spectra using CdZnTe detector," *in Proceedings of the Second International Workshop on EGS*, pp. 242-249.

Paulus M., Sari-Sarraf H., Gleason S., Behel J., Thompson L. and Allen W., 1998, "A new X-ray computed tomography system for laboratory mouse imaging," *IEEE Trans. Nucl. Sci*., vol. 2, pp. 1259-1263.

Ricq S., Glasser F. and Garcin M., 2001, "Study of CdTe and CdZnTe detectors for X-ray computed tomography," Nucl. *Instrum. Methods Phys. Res*. A, vol. A458, pp. 534-543.

Roessl E. and Proksa R., 2007, "K-edge imaging in x-ray computed tomography using multi-bin photon counting detectors," *Phys. Med. Biol.*, Vol. 52, 4679-4696.

Rutherford R.A., Pullan B.R., and Isherwood I., 1976, "Measurement of Effective Atomic Number and Electron Density Using and EMI Scanner," *Neuroradiology*, Vol 11. No. 1 15-21.

Shikhaliev P.M., 2008, "Energy-Resolved computed tomography: first experimental results," *Phys. Med. Biol*., Vol. 53, pp. 5595-5613.

Shikhalie P., 2008, "Computed Tomography with energy-resolved detection: a feasibility study," *Phys. Med. Biol.*, Vol. 53, pp. 1475-1495.

Sukovic P. and Clinthorne N.H., 2000, "Penalized weighted least-square image reconstruction for dual energy X-ray transmission tomography," *IEEE Trans. Med. Image.,* Vol. 19, No. 11, pp. 1075-1081.

Szeles, 2003, "CdZnTe and CdTe materials for X-ray and gamma ray detector applications," Phys. Stat. Sol. (b), vol. 241, no. 3, pp. 783-790.

Talbert A.J., Brooks R.A., and Morgenthaler D.G., 1980, "Optimum energies for dual-energy computed tomography," *Phys. Med. Biol.,* vol. 25, no. 2, 261-269.

Tsunoo T., Torikoshi M., Ohno Y., Endo M., Natsuchori M., Kakizaki T., Yamada T., Ito N., Yagi N., and Uesugi K., 2004, "Measurement of electron density and effective atomic number using dual-energy x-ray CT," *IEEE.*

Valais I.G., David S., Michail C., Nomicos C.D., Panayiotakis G.S., and Kandarakis I.S., 2007, "Comparative evaluation of single crystal scintillators under x-ray imaging conditions," presented at *4th International Conference on Imaging Technologies in Biomedical Sciences*.

Visipaque™ (iodixanol), A GE Product, Information available: ttp://md.gehealthcare.com/visipaque/

Uotani K., Watanabe Y., Higashi M., Nakazawa T., Kono A., Hori Y., Fukuda T., Kanzaki S., Yamada N., Itoh T., Sugimura K. and Naito N., 2009, "Dual-energy CT head bone and hard plaque removal for quantification of calcified carotid stenosis: utility and comparison with digital subtraction angiography," *European. Radiology*. vol. 19, pp. 2060-2065..

Yan C., Whalen R., Beaupre G., Yen S. and Napel S., 2000, "Reconstruction algorithm for polychromatic CT imaging: application to beam hardening correction," *IEEE Trans. Med. Imag*., vol. 19, no. 1, pp. 1-11.

Yue G., Giu Q., Goa B., Cheng Y., Zhang J., Shimoda H., Chang S., Lu J. and Zhou O., 2002, "Generation of continuous and pulsed diagnostic imaging X-ray radiation using carbon-nanotube-based field-emission cathode," *Applied Physics Letters*, vol. 81, no. 2, pp. 355-357.

Zhang J., Cheng Y., Lee Y., Gao B., Qiu Q., Lin W., Lalush D., Lu J. and Zhou O., 2005, "A nanotube-based field emission X-ray source for microcomputed tomography," *Review of Scientific Instruments*, vol. 76, pp. (094301)1-4.

6. COMPARING TWO METHODS

The new system (Chapter 3) is a novel x-ray computed tomography (CT) system capable of dense spectral measurements along the energy axis a using a photon-counting single-pixel detector. The reconstructions have excellent energy axis resolution but suffer from noise resulting from the nature of photon counting. We have developed two methods to suppress the noise along the energy axis: a Penalized Weighted Least Squares Algorithm (PWLS) (Gonzales and Lalush, 2011; Chapter 4) for iterative reconstruction along the energy axis and an Eigenvector Filtering Algorithm (EIGEN) for noise suppression in the energy domain using a set of basis functions (Gonzales and Lalush, 2010; Chapter 5). In this section we compare the two methods, including the methods' initial assumptions, the time the methods take to arrive at an estimate, and the shortcomings of each method. We investigate relationship between energy resolution and noise and the corresponding change in noise for the filtered-back-projection (FBP) reconstructions and both algorithms. We present a detailed comparison of the two algorithms focusing on the noise-energy resolution relationship. We compare the signal-to-noise ratio (SNR) ratio for both methods; the SNR is distributed differently across the energy spectrum for the two methods. We also examine the two methods to see how they retain key energy-axis information, specifically absorption edges for contrast agents. Both algorithms offer significant noise suppression while preserving key energy axis data; the PWLS algorithm is shown to be more dependent on the incident x-ray spectrum, whereas the EIGEN algorithm is more dependent on prior knowledge of materials in the imaged object. We study the combination of the two methods by forming a hybrid PWLS+EIGEN method. This hybrid method is shown to take advantage of both methods'

noise suppression. The hybrid method is shown to have improvements in the final reconstructed attenuation estimates and in the SNR.

6.1. Comparing Noise suppression Methods

A complete derivation for the two noise suppression methods can be found in chapters 4 and 5 for the PWLS and EIGEN methods respectively. In this section we focus on comparing the methods.

6.1.1. Initial Assumptions

The data in this new system are collected as an x-ray spectrum: a distribution of photon counts over some number of energy bins, for each projection ray. The projections are arranged into a sinogram for each energy bin. Each sinogram is reconstructed to an attenuation map corresponding to an energy bin. Each pixel in the reconstructed attenuation map can also be represented as an "attenuation curve" which we define as the attenuation for the spatial location, defined by the pixel location, as a function of energy. The reconstructed attenuation for all energy bins at a specified pixel represents a sample of the true attenuation curve at that pixel. Both noise suppression algorithms make key assumptions about the true attenuation curve sampled using the full-spectra CT system.

The two algorithms assume the attenuation curve sampled in each pixel is functionally independent of all other sampled attenuation curves. The algorithms smooth each pixel independent of all other pixels in the attenuation map. This means there is no spatial smoothing. This also means no prior assumptions about the distribution of the materials are made by either algorithm. This is an efficient assumption; it simplifies both algorithms, allowing them to impose assumptions independent of the spatial location of a given pixel. However, this assumption ignores the likelihood of similarities over spatial

neighborhoods. Initially, spatial independence was assumed to demonstrate the noise suppression along the energy axis only. Relaxing this assumption may improve the overall noise suppression for both algorithms.

The National Institute of Standards and Technology (NIST) has published a database describing the attenuation curves for elements with atomic number 1-93 and selected biological compounds (Hubbell and Seltzer, 1996). Both noise suppression algorithms use these data to form their initial assumptions for noise suppression. The PWLS algorithm uses some general properties common to most of the attenuation curves in the NIST database to smooth the sampled attenuation curves. The EIGEN algorithm uses the known attenuation curves from the NIST database to form a basis set defining the signal space to suppress the noise.

The PWLS algorithm makes three assumptions describing the properties common to most attenuation curves. These assumptions are: the attenuation decreases as energy increases, this decrease occurs with some slope, and this slope changes slowly. The PWLS forms a penalty function to impose these assumptions onto a set of energy neighborhoods. The energy neighborhood is penalized if the attenuation in the neighborhood is not decreasing as energy increases. The penalty drives the variation in the neighborhood to some slope defined by the user based on the second two assumptions. The slope is an average of all the sampled attenuation curves in the attenuation map. The PWLS algorithm makes an exception for all three assumptions if a contrast agent is used. Contrast agents have absorption edges: a point where the attenuation as a function of energy suddenly increases and the slope suddenly changes. These edges occur at know locations for specific contrast agents. The PWLS algorithm ignores the energy at the absorption edge to not penalize the

legitimate change in the attenuation slope. Thus, the PWLS method does not require any prior knowledge of what materials are present in the imaged object, other than a contrast agent.

The EIGEN method assumes the imaged object is composed of a limited known number of elements or compounds. The attenuation curves for these elements or compounds are used to form a set of basis functions defining the signal space. A matrix is formed with all possible combinations of the known attenuation curves, from the NIST database. This matrix is decomposed using eigenvector decomposition and the resulting eigenvectors are used as the basis functions. Each basis function describes some portion of the known attenuation curves. Each sampled attenuation curve is projected onto these basis functions to suppress the noise. This method requires prior knowledge of all elements or compounds present in the imaged object and prior knowledge of their attenuation curves.

The two methods both use the NIST database for their initial assumptions; the PWLS method only makes assumptions about the general nature of attenuation curves where the EIGEN method requires prior knowledge of elements or compounds present in the image object. The PWLS method has much broader initial assumptions: no prior knowledge of the elements in the imaged object is required unless contrast agents are used. Contrast agents are purposefully introduced into a subject, so if they exist in the imaged object, the agent and its properties will be known. If the object has a compound not found in the NIST database, this is not a problem for PWLS, so long as the compound's attenuation curve conforms to the basic assumptions. The EIGEN method requires knowledge of both the elements or compounds present and their attenuation curves. If a material is present in the object but not

in the NIST database a measurement of its attenuation curve must be done prior to imaging. Thus, the eigenvector method has more complicated initial assumptions.

6.1.2 Time for Each to Arrive at an Attenuation Estimate

The PWLS is an iterative reconstruction method; it projects and back-projects the data multiple times to converge on the best estimate for the true solution. Each projection and back projection will take some specified time depending on the program used to implement the algorithm. The EIGEN method projects the FBP data onto a set of basis functions once. This is a single projection, after an initial FBP. Thus, the eigenvector method will always be the faster method, since it only has one projection.

The time for each method to arrive at an estimate of the attenuation is demonstrated in the experiments which produced the data shown in chapters 4 and 5. For these experiments, the PWLS method took 15 minutes to arrive at a solution using MATLAB (MATLAB). The eigenvector method took only one minute to arrive at a solution using MATLAB. This included the initial FBP which took approximately 30 seconds. Using C or C++ instead of MATLAB would significantly reduce the time for both methods. However, PWLS will still take significantly longer to arrive at a solution. Thus, because the EIGEN method has a single projection step, it will always be faster. These times are based on a Dell Precision 670 3.80 Ghz computer, with 2GB of RAM. Running on a smaller computer would increase the time for each method.

The times presented for each method depends on the size of the experiment. There were 80 projection rays per projection angle over 120 angles reconstructed to a single 64x64 pixel attenuation map. Each projection ray was represented by 95 energy bins. The PWLS method must reconstruct an attenuation map for each energy bin and then apply the penalty

along the energy axis. The EIGEN method projects each attenuation curve, all energy bins at once, onto the basis functions. Therefore, for these experiments, EIGEN projects 64*64 attenuation curves four times onto basis functions and then sums the results. PWLS projects 64*64 attenuation maps 95 times (once for each energy bin) for each iteration. This represents a single slice through the imaged object. The size of the projections will increase by a factor of the number of slices.

6.1.3. Shortcomings of Each Method

The two methods each have key exceptions to their initial assumptions. The PWLS assumptions hold true unless there is an absorption edge. To account for the absorption edge, the energy at the edge must be ignored or the edge included in the expected slope. The distribution of the contrast agent in the object is unknown, so the expectation must be included for all attenuation curves, even ones with no contrast agent. This introduces an inconsistency into the reconstructions. This is a noticeable problem when an edge occurs in a region with high noise along the energy axis. The noise confuses the algorithm and it may assume an absorption edge exists where no contrast agents exists. The other key shortcoming of the PWLS is the time it takes to run.

The EIGEN method requires all elements or compounds and their attenuation curves to be known. Most objects imaged are composed of some set of known elements or compounds and the imaging is done to find the distribution of these elements or compounds. However, the NIST database only has attenuation curves for a limited number of elements and compounds. If an attenuation curve is not known, we could construct the attenuation curve based on the mass-attenuation properties of its constituent properties; assuming we know the compounds chemical makeup. The properties of the unknown attenuation curve can

also be identified by an independent measurement. This limits the EIGEN method to the set of known attenuation curves, which can be supplemented with additional measurements. The second key shortcoming of this method is the way basis functions are defined. The EIGEN method finds differences between attenuation curves to create orthogonal basis functions. However, the PWLS assumptions demonstrate that most of the time, the only difference between attenuation curves is small changes in the slope. Contrast agents introduce key differences in the attenuation curves in the form of absorption edges. Thus, the EIGEN method works better when contrast agents are used.

The PWLS is conceptually similar but much slower. EIGEN is more complicated but much faster. The use of contrast agents complicates one algorithm (PWLS) and is a requirement for the other algorithm (EIGEN); thus, the algorithms complement each other. However, both algorithms will suppress the noise along the energy axis while preserving energy axis data. This means that both can be used to identify a material based on its attenuation curve, even if that material is a contrast agent or some other material.

6.1.4. Combination of Both Methods

The two methods have been used for noise suppression independent of each other and both have shown to offer significant noise suppression, discussed in Chapters 4 and 5 for PWLS and EIGEN respectively. The next logical step is to use the two methods together. The data could be reconstructed using PWLS and then the EIGEN method could be applied to the result. Alternately, the PWLS could use the result of the EIGEN method as its initial estimate. It seems that either way the methods are combined; the final estimate should take advantage of the noise suppression of both methods.

To use both noise suppression methods, the initial assumptions for both methods must be satisfied. This means a combination method is more complicated in terms of initial assumptions than either of the methods individually. The combination of both methods will also take longer to arrive at an estimate; the total time is the sum of both methods' times. This is true regardless of which method is used first. Despite these shortcomings, a combination should offer some improvement over either method used independently.

6.2. Comparing Reconstructions

To compare the two different noise suppression methods, the final estimates of noise suppressed attenuation for each method are compared. A simple contrast phantom, designed to test the novel system and presented in both papers (Chapters 4 and 5), is used to investigate the differences between the methods. This phantom has five holes filled with gold, iodine and water (figures 4.4 and 5.3). The spectrum through the phantom is sampled with 95 energy bins arranged between 10keV and 43keV. The projection data are initially reconstructed using FBP (shown in figures 4.6 and 5.6). The final estimates are shown in figures 4.7 and 5.7. This section compares the results more carefully, placing the results side by side or overlapping in graphs to investigate the similarities and differences in each method.

The results of both methods are also compared with the estimates from the methods used together. The PWLS method is used instead of FBP to form an initial estimate which is then post-processed with the EIGEN method; this is labeled PWLS+EIGEN. This is one of two possible ways to use the two methods together. The second way uses FBP to form the initial estimate which is processed then using EIGEN method this result of which is used as

the initial estimate for the PWLS algorithm; this is labeled EIGEN+PWLS. These results are compared with the individual methods to give a full comparison of the methods.

6.2.1. Comparing Attenuation Maps

To compare the two methods more accurately, the estimated attenuation maps are placed next to each other in figure 6.1 for the same energies.

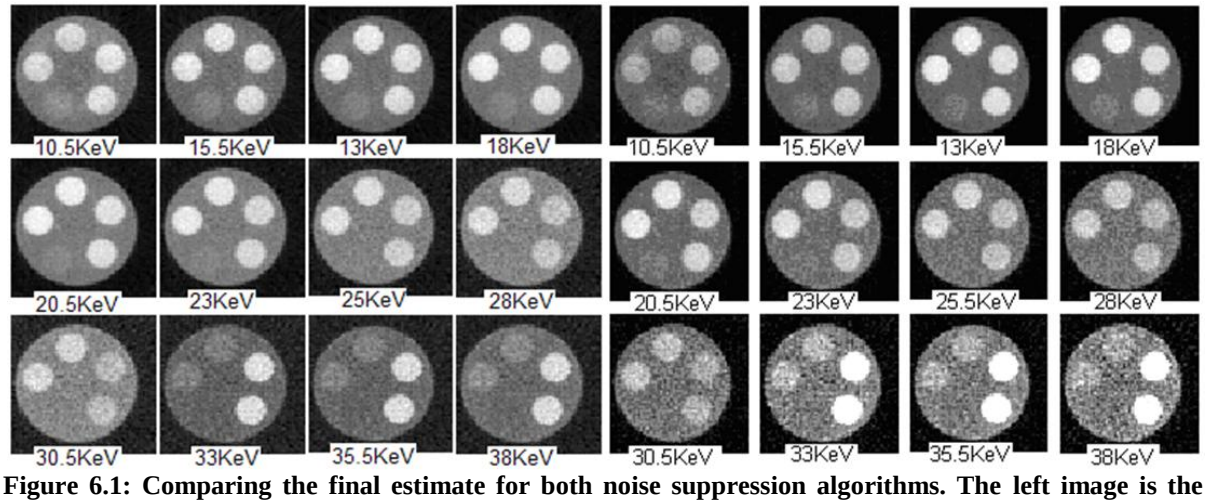

Figure 6.1: Comparing the final estimate for both noise suppression algorithms. The left image is the EIGEN method estimate. The right is the PWLS method estimate.

Both of the proposed methods suppress the noise while preserving spatial resolution in the attenuation maps. This is best demonstrated by the clear boundaries between each of the contrast agents and the background acrylic phantom and by the clear boundary between the acrylic phantom and the background air for energy bin. Each part of the phantom is clearly identifiable at almost every energy bin. This is a significant improvement over the initial FBP estimate (figures 4.3 and 5.4), especially since there is no spatial blurring in any of the images. Both methods also preserve the iodine absorption edge. The iodine contrast in both results increases noticeably after 33keV (the location of the iodine absorption edge), even though the other contrast agent does not. Thus, it is possible to identify contrast agents using both methods.

The same scale is used for all images in figure 6.1, a Hounsfield number approximation is applied to each image. The average of the background is set to -1000 and the average of the water region (figures 4.4 and 5.3) is set to 0. This is done for each energy bin independently, because this ratio will change for each energy bin depending on the attenuation curve of water. The first noticeable difference between the EIGEN method's reconstructions (left side of figure 6.1) and PWLS (right side of figure 6.1) is the suppression of all attenuation in the background. PWLS does a better job completely suppressing the background (air region outside the phantom) than the EIGEN method. This is demonstrated by how much darker the background is in the PWLS images compared with EIGEN, which is more gray and speckled. The EIGEN method is driving each pixel to an acrylic, water, iodine or gold attenuation curve, which preserves a small amount of the noise in the background. The simpler assumptions of PWLS allow the background to be more fully suppressed.

The second noticeable difference between the two methods is at higher energies PWLS appears more noisy throughout the reconstruction of the phantom and contrast agents. This is especially noticeable in the acrylic, gold, and water regions of PWLS at energies 30.5keV through 38keV when compared with the same regions and energies for the EIGEN method. The noise is not limited to these energies. It is just most apparent at these energies, but it does exist to some degree at all energy bins. The PWLS is noisier due to the way the algorithm defines each pixel's attenuation curve. Both methods assume independence of each pixel, but the EIGEN method is driving all attenuation curves toward some combination of four known attenuation curves. This reduces some of the spatial variance since there are only four curves. The PWLS method is driving all pixels toward an average slope but it allows for

more variance between each curve. The PWLS's toleration of variance is seen in the existence of spatial variation, especially at high energy bins.

The final noticeable difference is the attenuation of gold at multiple energy bins. This is much harder to see, but the gold of PWLS changes slightly more with respect to iodine than for the EIGEN method. Looking at energies 10.5keV through 25.5keV the gold becomes slightly brighter than the iodine for PWLS but remains basically equal to iodine for the EIGEN method. The gold becomes brighter than iodine because gold has low energy absorption edges in this energy range. The PWLS captures some of the absorption edges and they shows up as a slight brightening of gold. The EIGEN method imposes these edges on the iodine, mistaking noise in this energy region for legitimate edges. PWLS avoids this by incorporating the edges in the expected slope, which smoothes out the edges, but also prevents imposing them on iodine. These effects become clearer when examining the attenuation curves in the next section.

6.2.2. Comparing Attenuation Curves

To more accurately compare the two methods, and the combination of the methods, the estimated attenuation curves for each method are compared. There are 4096 attenuation curves in the estimated attenuation map; the attenuation map is represented with 64*64 pixels. There are approximately 120 attenuation curves in each hole in the acrylic cylinder, thus water is represented by approximately 120 curves and iodine and gold by 240 attenuation curves. The acrylic background has over 1000 attenuation curves. It is not practical to show all of the attenuation curves from each method when comparing the methods. Therefore, two comparisons are defined to reduce the data. The first is an average

of all attenuation curves for each element in the object. The second is a pixel chosen at random and compared with each method's estimate of that attenuation curve.

The average FBP attenuation curve is compared with the two methods and the combination of the two methods to demonstrate that the two methods do not add a bias into the estimated attenuation. Both methods return an estimate of attenuation which is very close to the original FBP data, with noise suppressed. By averaging the FBP attenuation curves, the noise in FBP is suppressed along the energy curves. The average FBP is also compared with the individual pixels selected at random from each material. A single pixel attenuation curve from FBP would have too much noise to be useful (see figures 4.5 and 5.4). This noise would dominate the figures and make it challenging to see other detail in the attenuation curves. Thus, the average FBP attenuation curve is used for all comparisons.

6.2.2.1. Gold Attenuation Curves

The attenuation curves for two noise suppression methods and two possible combinations of the methods are shown for gold in figure 6.2. The attenuation curves are shown as an average of all attenuation curves and from the same randomly selected pixel, compared with the FBP attenuation curve for gold.

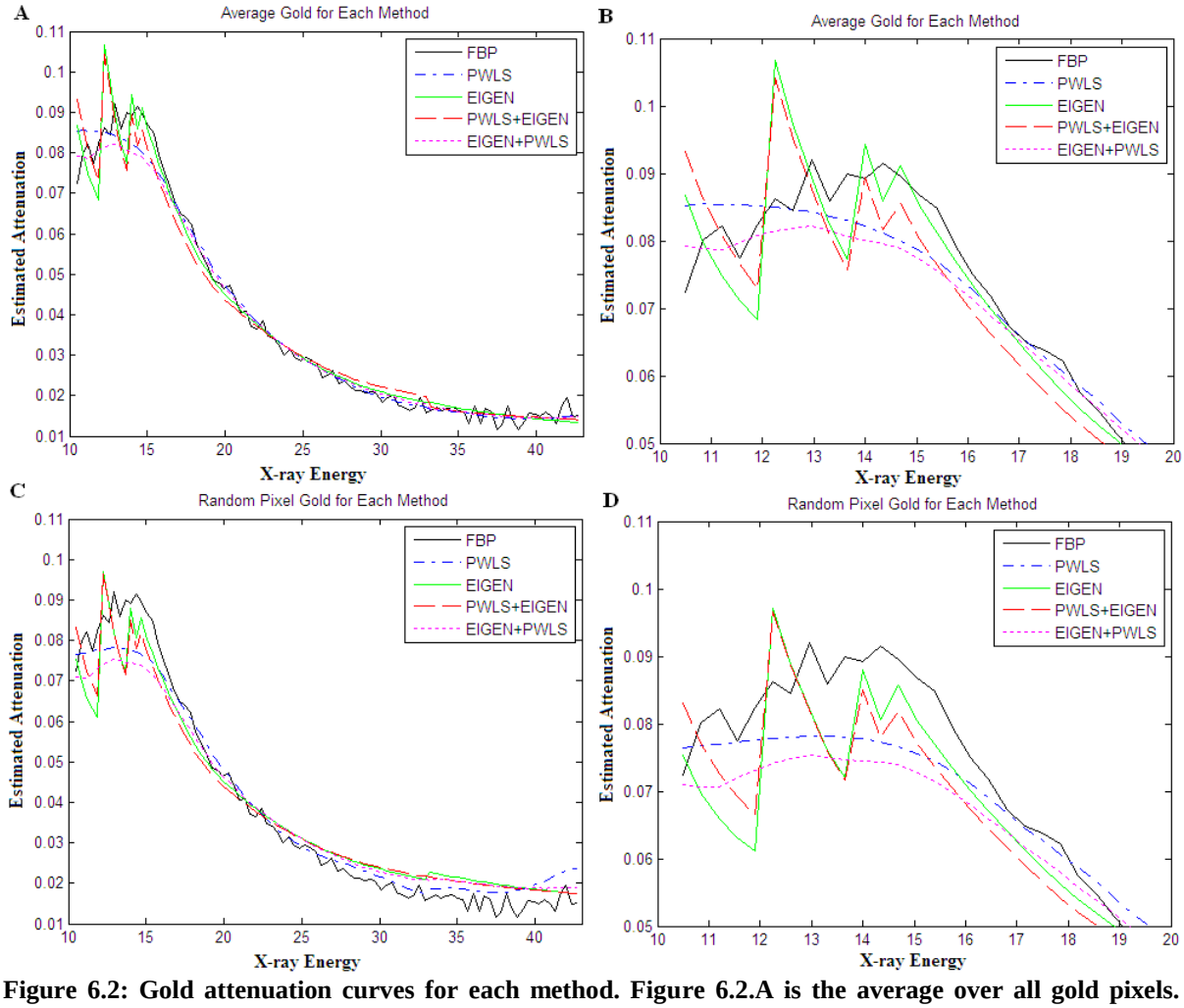

Figure 6.2: Gold attenuation curves for each method. Figure 6.2.A is the average over all gold pixels. Figure 6.2.B is the average at the absorption edges. Figure 6.2.C is a single pixel selected at random from gold. Figure 6.2.D is the single pixel at the absorption edges.

The average attenuation curves are grouped very close together for all methods above x-ray energy 20keV (figure 6.2.A). This means both methods are accurately reconstructing the smooth parts of the gold attenuation curve. Both the EIGEN and PWLS methods have curves in this region which are smoother than the FBP; even when averaged, the FBP still has noise along the energy axis. There is a little more separation between the averaged FBP, PWLS and EIGEN methods at energies below 20keV for the single pixel attenuation curves (figure 6.2.C). The EIGEN method produces slightly higher attenuation at these energies for the

randomly selected attenuation curve; this is also true for both combinations of the two methods. This likely reflects the true attenuation at this pixel, which might be slightly greater than the average, indicating some spatial variance in the gold region. The PWLS is between the average and the true attenuation. This is because the PWLS smoothes to the average. At these energies, combinations of the two methods EIGEN+PWLS and PWLS+EIGEN seem to follow the EIGEN estimates rather than the PWLS estimate; this is more noticeable for the single pixel attenuation curve.

The two methods address the absorption edges very differently; PWLS makes an exception in the penalty or incorporates them into the estimated slope and EIGEN incorporates them naturally as part of the basis functions. The absorption edges for gold are investigated more closely in figures 6.2.B and 6.2.D. In these figures, it is apparent the two methods have very different effects on the absorption edges. The average FBP shows that the overall group of edges has been detected; this is shown as a general increase in attenuation and as a few small edges. The PWLS method smoothes over these small edges and the attenuation slope in this region is sort of an average between the increase FBP and the overall average of all attenuation curves in this energy region. This is because these curves are included in the PWLS which smoothes them out over energy. There are multiple absorption edges in this energy range, if the PWLS ignored those energy bins there would be almost no low energy smoothing for other elements' attenuation curves. Therefore, because the PWLS includes the edges rather than ignoring the energy bins, the PWLS does a poor job preserving these edges. The EIGEN method imposes more of the edge than exists in the original data. The EIGEN attenuation curve has all three edges exactly where the NIST database shows them. This is artificially imposed on the data, but it matches the FBP fairly well (see figure

6.2.B); the green average EIGEN attenuation curve is very close to the black average FBP. In the single pixel attenuation curve, all the values are lower than the average. This is similar to the high energies where it was slightly larger. This simply represents a small amount of spatial variance in the attenuation map.

The combination of both methods depends on which method is done first. If the PWLS is used as the initial estimate which is then post-processes with EIGEN (PWLS+EIGEN) the final attenuation curve seems to look more like the EIGEN estimate. This is most apparent in the absorption edges (figure 6.2.B and 6.2.D). If EIGEN is used first (EIGEN+PWLS) then the final attenuation curve looks more like PWLS. Doing both pushes the edges down a little. For PWLS+EIGEN this makes sense, in fact it looks like the EIGEN attenuation curve but now averaged to the PWLS rather than FBP. This seems to indicate that for gold, PWLS+EIGEN capitalizes on the advantages of both methods, with slightly smaller absorption edges which are still well-defined and close to the average. EIGEN+PWLS seems to make the absorption edges worse, but is a little better along the rest of the attenuation curve compared with just EIGEN method. However, this is not really an improvement for gold, in fact EIGEN+PWLS seems to be the worst case for gold, combining the worst of both methods for absorption edges. This is because the PWLS sees the large edges introduced by EIGEN as noise and smoothes over them.

6.2.2.2. Iodine

The attenuation curves for two noise suppression methods and two possible combinations of the methods are shown for iodine in figure 6.3. The attenuation curves are shown as an average of all attenuation curves and from the same randomly selected pixel, compared with the FBP attenuation curve for Iodine.

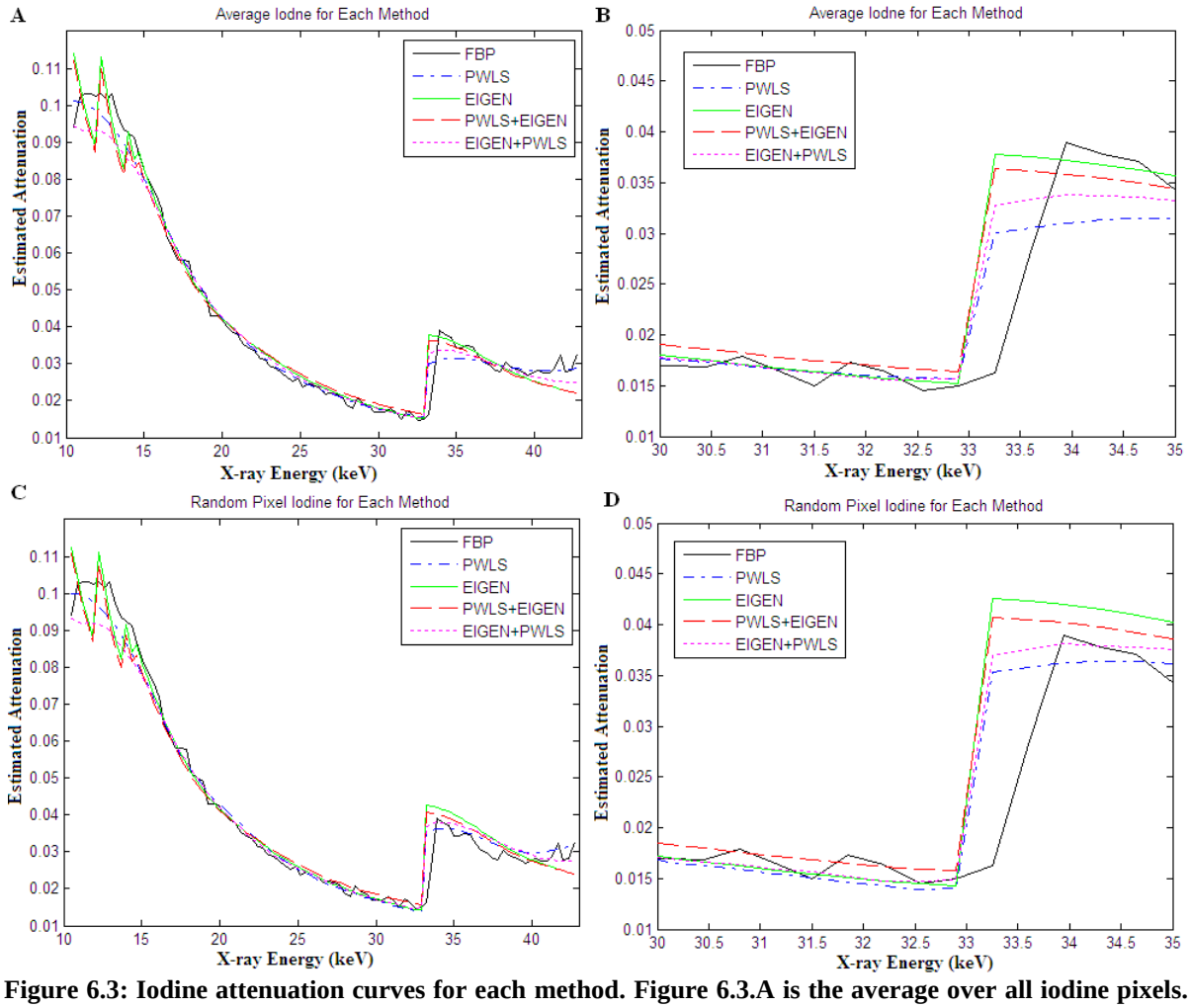

Figure 6.3: Iodine attenuation curves for each method. Figure 6.3.A is the average over all iodine pixels. Figure 6.3.B is the average at the absorption edge. Figure 6.3.C is a single pixel selected at random from iodine. Figure 6.3.D is the single pixel at the absorption edge.

The iodine attenuation curves can be divided into three energy regions: gold edges 10-15keV, middle 15-33keV, and iodine absorption edge 33-43keV. The middle region is the least interesting; in this region, attenuation curves for all methods are very close to average FBP. The most significant difference between the average FBP and the average for both methods and the randomly selected single pixel is the small amount of noise remaining in the average FBP. In the low energy region some of the noise in the initial reconstruction remains. The EIGEN estimated attenuation curve has the three gold edges, although these are smaller than the edges for the gold average or single pixel gold (figures 6.2.B and 6.2.D). This happens

because the EIGEN algorithm mistakes some of the noise for gold edges in the low energy reconstructions. The PWLS smoothes over the noise in this region, so these edges are not retained by the PWLS method. Both noise suppression methods in this region the estimate a lower attenuation because there is a lot of noise in this region and both noise suppression methods are looking for gold in this region. If some spatial smoothing was included in both methods, this noise might be reduced. An additional assumption could be introduced to each algorithm which only allowed the algorithm to pick one contrast agent. This additional assumption could be applied as part of the basis function definition or as an addition to the penalty in the PWLS. However, it is clear, for the average and for the selected pixel, that these are iodine attenuation curves due to the large absorption edge at 33keV.

The most important region of the attenuation curve is the iodine absorption edge (figure 6.3.B and 6.3.D). The edge in all of the noise suppressed attenuation curves is shifted slightly from the average FBP, the black attenuation curve. There are two reasons for this: the noise in the initial data distorts the location of the edge and the resolution in the AMPTEK detector is limited. The edge occurs between two energy bins; the initial FBP data assigns the edge to the bin following the edge, the noise suppression methods assign the edge to the bin preceding the edge. The same error occurs for both methods and the combination of both methods. This error is not significant because the two noise suppression methods place the edge where the NIST database indicates it should be. The average FBP places the edge one energy bin away from where it belongs, and both methods correct this.

The two noise suppression methods, and the combination of the two methods, look almost identical at the iodine edge for both the average and selected random pixel (figures 6.3.B and 6.3.D respectively). However, immediately after the edge, there is a difference

between the methods. The EIGEN method estimates attenuation after the edge which is significantly larger than the PWLS. The combination methods estimate a value between these two values, each pulling the attenuation closer to the second method used: EIGEN+PWLS pulls the value closer to PWLS and PWLS+EIGEN pulls the value closer to EIGEN. The PWLS algorithm has less change in the attenuation curve between 33keV and 43keV, and matches the average FBP for energies above 40keV (figures 6.3A and 6.3.C). The PWLS is averaging over a number of energy neighborhoods which removes the sharp increase in attenuation slope immediately after the edge, resulting in an attenuation slope which is almost flat in this region. The EIGEN method captures the full change in attenuation near the absorption edge, including the slope in the curve after the edge. This change exists in the original data, seen in the average FBP (figure 6.3.A). The PWLS+EIGEN also preserves the change in attenuation. The EIGN+PWLS does not preserve this change in attenuation, rather it looks more like the PWLS, with a more flat change in attenuation.

The PWLS and EIGEN+PWLS methods do a better job with low energy regions, their attenuation curves in this region are smooth and only descending; they do not show the gold edges in either the average or random pixel. The PWLS and EIGEN+PWLS methods adequately show the iodine absorption edge, but do not accurately demonstrate the attenuation in the region immediately after the edge; instead this region has a flat shape. The EIGEN method and PWLS+EIGEN do a good job with the absorption edge and immediately after the edge have a very accurate representation of the attenuation curve, both according to the average FBP and the NIST database. However, the EIGEN method and the PWLS+EIGEN have a noisy low energy region, mistaking some of the noise and the slow change in attenuation as indication of gold in these pixels. Overall the PWLS+EIGEN is the

best, a little less noisy in the gold region than just EIGEN, but also preserves the shape of the curve after the absorption edge.

6.2.2.3. Water and Acrylic

The attenuation curves for two noise suppression methods and two possible combinations of the methods are shown for both water and acrylic in figure 6.4.

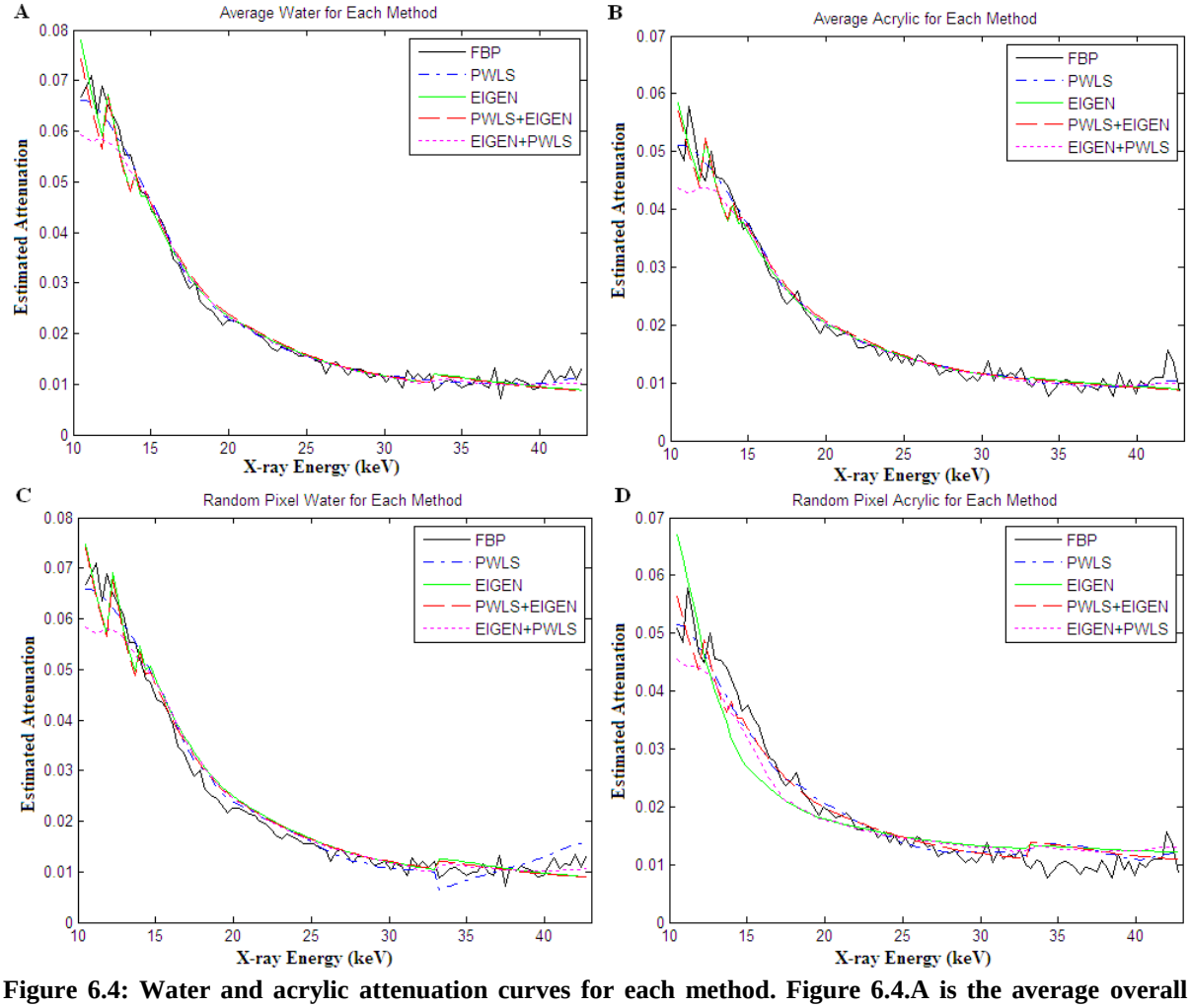

Figure 6.4: Water and acrylic attenuation curves for each method. Figure 6.4.A is the average overall water pixels. Figure 6.4.B is the average overall acrylic pixels. Figure 6.4.C is a single pixel selected at random from water. Figure 6.4.D is the single pixel selected at random from acrylic.

Both background compounds are shown in figure 6.4 because there are no absorption edges in either material, so there is space to show both attenuation curves. Both curves should

follow all of the initial assumptions for the PWLS; both water and acrylic should have an attenuation which always decreases as energy increase with a smooth slope. The attenuation curves for both of these elements are known from the NIST database. The initial assumptions for both methods are completely satisfied for both methods.

The average FBP attenuation curves for both water and acrylic both have a significant amount of noise, despite the fact that the curves are an average over multiple curves. This noise is most apparent at high energies, above 35keV, and at low energies, below 15keV, for water. The average FBP attenuation curve for acrylic has a large amount of noise all along the curve. This noise, both at the ends of the water curve and all along the acrylic curve, are due to a combination of lower x-ray flux, at the ends of the curve, and lower attenuation. A lower total x-ray flux decreases the projected signal, making the projections more susceptible to noise. A lower attenuation also decreases the projected signal. Both methods and the combination of both methods, smooth out this noise while preserving the basic shape for both compounds' attenuation curves; both the average attenuation curves and the randomly selected attenuation curves.

The PWLS and EIGEN methods estimated attenuation curves for water and acrylic share some of the same inconsistencies as the estimated gold and iodine curves. Both methods create a small error at the iodine absorption edge. For the average water attenuation curve (figure 6.4.A) this error is almost the same for each method, there is a slight increase in attenuation at 33keV. This means both methods and the combination of both methods impose a small amount of the iodine absorption edge on the water attenuation curve. However, when looking at the randomly selected water curve (figure 6.4.C), the PWLS estimate of water goes sharply negative and the EIGEN method and the combination methods retain the small

positive edge. The PWLS simply makes an exception at the absorption edge, so the negative edge occurs because of the noise in the attenuation curve at that pixel. The EIGEN method fits the noise to a small amount of iodine. The combination methods are both more like the EIGEN method because the PWLS does not impose an edge, it just ignores one. There is no iodine edge in the acrylic average attenuation curve (figure 6.4.B) for any method. However, there is a small iodine edge on the randomly selected acrylic attenuation curve (figure 6.4D). The PWLS also has a small edge, again due to fact that noise is allowed at edge energy. This noise is interpreted as an iodine edge by the EIGEN method in the combinational methods PWLS+EIGEN and EIGEN+PWLS. The EIGEN method does not impose an edge, but it changes the overall shape of the curve slightly (green line in figure 6.4.D). This change happens because the EIGEN is imposing an ideal acrylic attenuation curve onto the data.

The PWLS and EIGEN methods' estimated attenuation curves for water and acrylic also have inconsistencies at the gold absorption edges. PWLS and EIGN+PWLS have smooth curves in this region for both water and acrylic. PWLS has a smooth estimated curve which is near the average FBP for both materials. The EIGEN+PWLS curve is pushed down, similar to the EIGEN result for gold and iodine. The EIGEN and PWLS+EIGEN impose gold edges on both water and acrylic in this region. This happens because the EIGEN method mistakes the noise in this region for gold absorption edges. Interestingly, this does not happen for the randomly selected acrylic attenuation curve (figure 6.4.D). For the single acrylic pixel, the EIGEN method changes the overall slope of the curve to fit the ideal acrylic curve but it does not impose the gold edges on the curve. This means at this pixel, the EIGEN method has recognized this pixel as entirely acrylic.

6.3. Comparing Signal-to-Noise Ratio

The final way to compare the two methods is by looking at the signal-to-noise ratio (SNR) for each material for the two noise suppression methods and the combination of the two methods. To define the SNR, we first segment the reconstructions based on the known distribution of materials (figure 4.4). We then average material at each energy bin; this is the same as the averaged attenuation curves shown in figures 6.2-6.4. The standard deviation for each material is then calculated for each material over all energy bins. The SNR is then defined as the average for each material over the standard deviation of each material. This

The SNR is investigated as a function of energy. The SNR is defined as the average over the standard deviation of each material for each energy bin. This SNR will be a function of energy because the average and standard deviation are calculated at every energy bin. The SNR will change depending on the distribution of noise along the energy axis.

6.3.1. Signal-to-Noise Ratio: Gold

The SNR as a function of x-ray energy for each method and the combination of each method are compared with FBP for the gold region in figure 6.5.

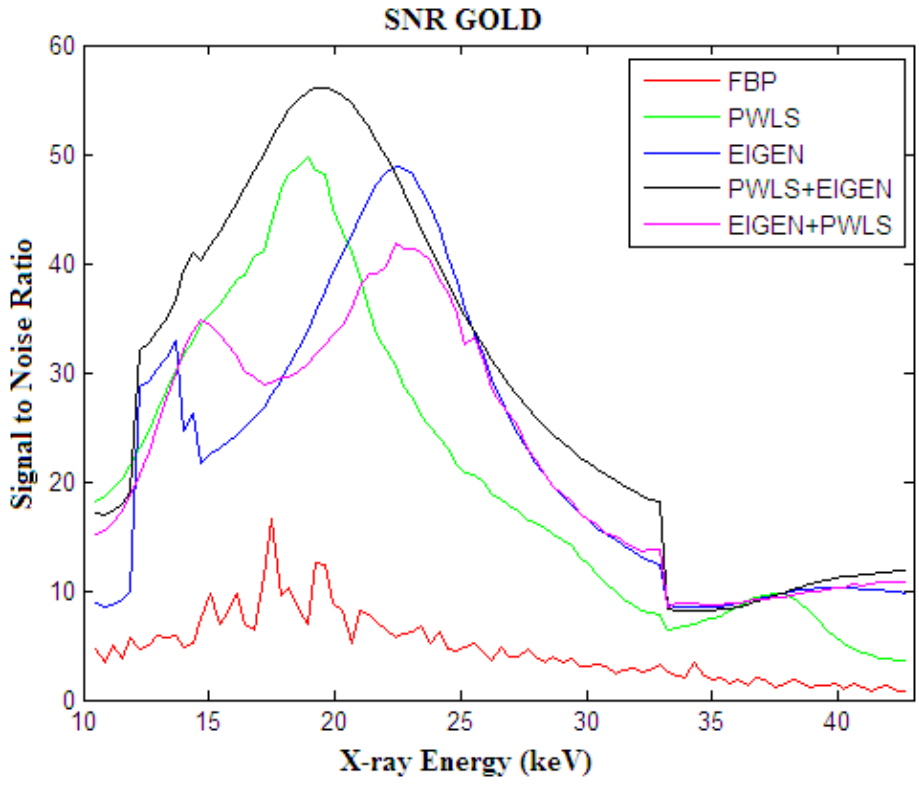

Figure 6.5: Signal-to-noise ratio as a function of x-ray energy for gold.

The SNR for FBP looks like a sample of the x-ray spectrum: it has a slightly triangular shape with two peaks at the characteristic peak locations of molybdenum (compare with figure 3.7). The spectrum is measured as photon counts for each energy bin; increasing the photon count increases the SNR, thus the SNR for FBP looks like the x-ray spectrum. The SNR for PWLS has a significant improvement over all the energy bins; the PWLS SNR peaks over the FBP SNR peaks. The PWLS spreads the FBP peak over all the energy bins, while retaining the initial SNR peak. The SNR for EIGEN also has an improvement over all energy bins, but it peaks near the center of the x-ray spectrum. This is because the estimated attenuation curves for gold have the least noise in the center of the energy range (figure 6.2). There is some noise in the EIGEN estimation of gold near the iodine and gold absorption edges. In the middle energies, the gold is smoothly descending and closely follows the average FBP

attenuation curve. In this region, EIGEN has successfully suppressed the noise while preserving the signal returning a maximum SNR. The SNR for the combination of both methods depends on which method was used first. The SNR for PWLS+EIGEN takes advantage of both methods and is the best overall method. The maximum SNR is between both maxima with a SNR which is almost always greater than the SNR for either method at every energy bin. The SNR for EIGEN+PWLS on the other hand is almost always below the SNR for either method for most energy bins. The PWLS+EIGEN combines the best of the both methods and EIGEN+PWLS combines the worst of both methods. This result is similar to what was seen with the estimated attenuation curves for gold (figure 6.2). The SNR for all methods decreases sharply at the location of the iodine absorption edge because all methods must account for the edge which allows some of the noise in the reconstructions to remain at these energies. All noise suppression methods' SNR for the energy bins above the iodine absorption edge are better than the FBP despite this overall decrease in SNR.

6.3.2. Signal-to-Noise Ratio: Iodine

The SNR as a function of x-ray energy for each method and the combination of each method are compared with FBP for the iodine region in figure 6.6.

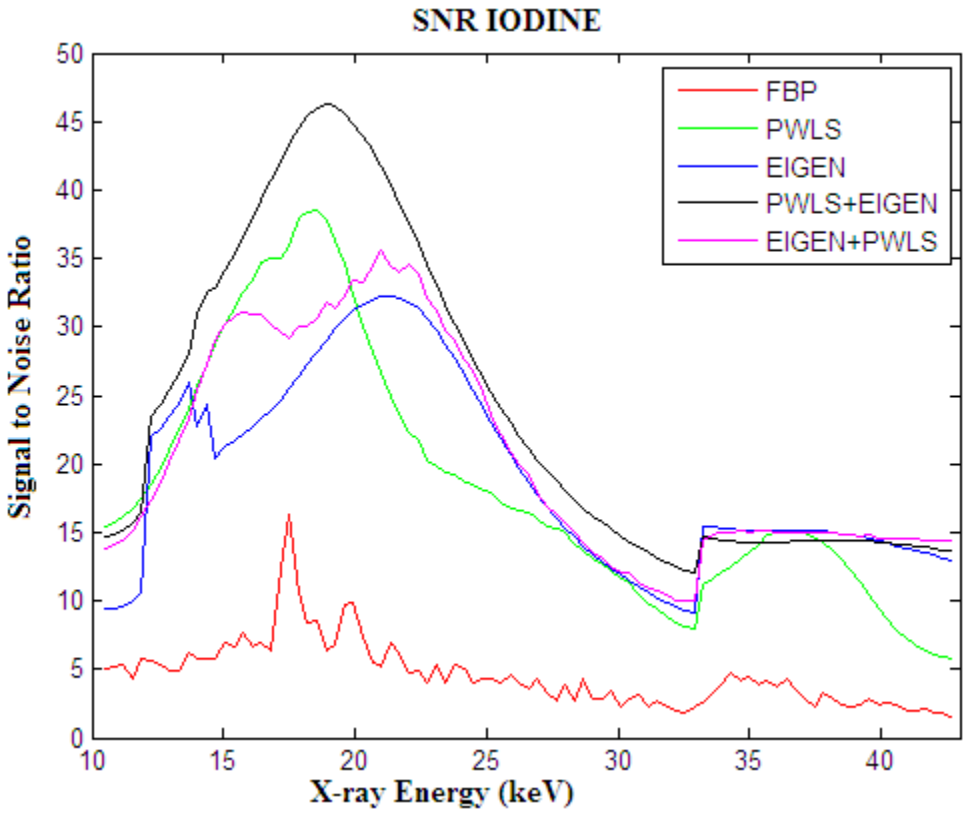

Figure 6.6: Signal-to-noise ratio as a function of x-ray energy for iodine.

The SNR for iodine for each method follows similar patterns as the SNR for gold. The SNR for FBP has a shape similar to the molybdenum spectrum. The SNR for PWLS peaks over the FBP peaks and spreads the peak over the rest of the energy bins. The SNR for EIGEN peaks over the center of the energy range. The SNR for PWLS+EIGEN is the best method, taking on the improvements for both methods. The SNR for EIGEN+PWLS has less improvement than PWLS+EIGEN; however, in the case of iodine EIGEN+PWLS is actually slightly better than just EIGEN and incorporates a small amount of the PWLS improvement. Iodine only has one absorption edge. It seems the multiple edges for gold allow more noise in the final reconstructions, especially for the EIGEN method; because these edges do not exits for the iodine, EIGEN+PWLS has a small improvement over just EIGEN at lower energy bins. All methods have a significant improvement over FBP in SNR for all energy bins.

The SNR after the iodine absorption edge, 33keV, improves slightly for all methods. The biggest improvement comes from the EIGEN method. The EIGEN method has the best improvement because the EIGEN method imposes the true iodine shape onto the data, successfully suppressing the noise after the edge. The least improvement comes from the PWLS method which increases to a small peak and then decreases again. The PWLS has the least improvement because the PWLS method simply ignores the edge, and this breaks up the smoothing of the penalty with respect to energy. The two combinations are closer to the first method used. The SNR for EIGEN+PWLS is closer to the SNR for EIGEN after the edge. The SNR for PWLS+EIGEN is in between the SNR for EIGEN and PWLS. This is similar to the estimations for the iodine attenuation curve.

6.3.3. Signal-to-Noise Ratio: Water and Acrylic

The SNR as a function of x-ray energy for each method and the combination of each method are compared with FBP for both water and acrylic regions in figure 6.7.

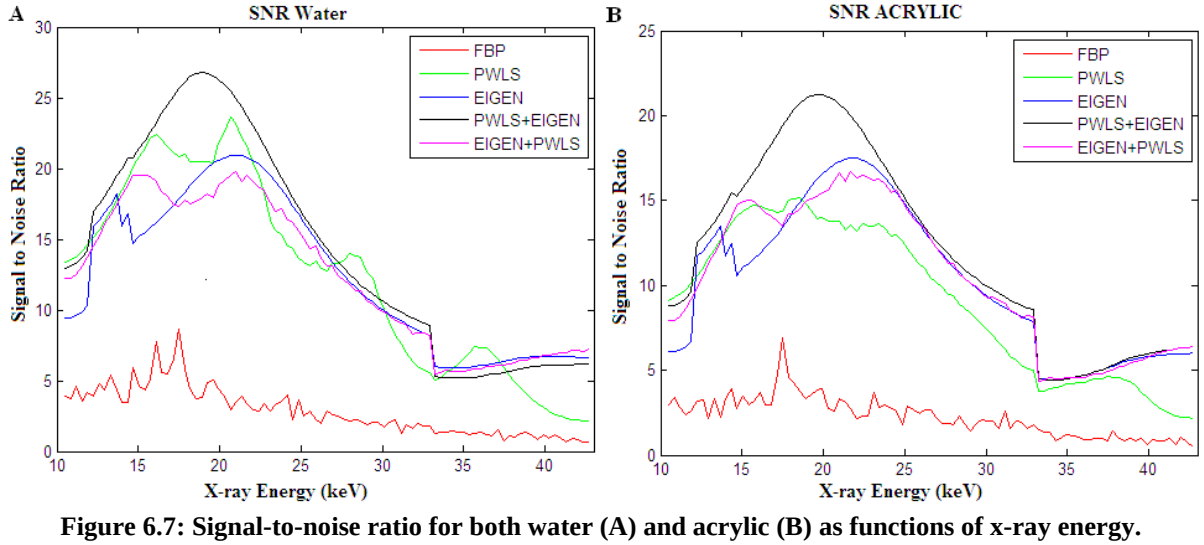

Figure 6.7: Signal-to-noise ratio for both water (A) and acrylic (B) as functions of x-ray energy.

The SNR for both water and acrylic follows the same patterns established by the SNR for gold and iodine. The SNR for FBP for both elements follows the molybdenum spectrum. The

SNR for PWLS peaks over the FBP peaks and spreads that peak over all energy bins. The SNR for EIGEN peaks in the center of the energy range. The SNR for PWLS+EIGEN is the combination of the better of the two methods. The SNR for EIGEN+PWLS is the worst overall method. The SNR after the iodine absorption edge drops off suddenly, similar to gold, but is still better than FBP. The noticeable difference in these elements' SNR is that PWLS has a less well-defined peak. The SNR for PWLS for both gold and iodine has a peak over the molybdenum peaks. The SNR for PWLS for both water and acrylic is flatter in this same region. This may be due to the lack of absorption edges in this region for both of these materials. The PWLS smoothed the gold absorption edges (figure 6.2), but the absorption edges increased the overall attenuation at low energies. This increased attenuation means a higher signal, resulting in a higher SNR. The water and acrylic attenuation curves simply descend, thus they do not have this increase in attenuation and increase in signal. The EIGEN method did not take advantage of this increase in attenuation because in imposing the actual edges, the EIGEN method allowed more noise in the final estimate. The PWLS+EIGEN got rid of the noise first then imposed the edges, thus it preserved the increase in SNR in lower energies. The SNR is improved for all methods for all energy bins for both methods for both water and acrylic when compared to FBP.

6.4. Discussion

The new x-ray photon counting single pixel CT system capable of dense spectral measurements proposed in chapter 3 allows a large amount of noise along the energy axis due to the nature of photon counting. Two noise suppression methods have been developed to suppress the noise along the energy axis, while preserving key energy axis data: a PWLS method with an energy axis penalty and an eigenvector decomposition (EIGEN) filtering

method. These two methods are compared in this section. The PWLS is shown to be simpler in terms of initial assumptions but it takes a long time to arrive at an estimate. The EIGEN method is shown to be more complicated since it requires prior knowledge of the elements or compounds in the imaged object and their attenuation curves, but it is much faster than PWLS. A detailed comparison is done by looking at the estimated attenuation produced by both methods.

Both noise suppression methods were developed to suppress the noise while preserving key energy axis data. Both methods are shown to have strong noise suppression, indicated by the increase in signal-to-noise ratio (SNR) over all energy bins for both methods (figures 6.5-6.7). The reduction in noise is also demonstrated by the identification of randomly selected attenuation curves (figures 6.2-6.5) when compared to the same randomly selected FBP attenuation curves (figures 4.5 and 5.4). This noise suppression is also demonstrated in the reconstructed attenuation maps (figure 6.1). Thus, both methods suppress much of the noise in the initial reconstructions.

The two methods approach the noise suppression and energy resolution very differently. The PWLS smoothes all measured attenuation curves to an average curve; the PWLS is focused on smoothing the energy axis. The PWLS algorithm has two ways to preserve the key energy resolution, identified as the absorption edges. In the first, the PWLS preserves an absorption edge by incorporating the edge into the estimated average curve. The PWLS smoothes over the energy neighborhoods which are five energy bins in size; thus, the PWLS smoothes a sharp edge to a continuous slope while preserving the general shape of the increase in attenuation, this is a apparent in the PWLS attenuation curve for gold (figure 6.2). Although the well-defined absorption edge is lost in this approach, the noise is strongly

suppressed. The second way the PWLS algorithm accounts for an absorption edge is to simply ignore the energy bin where the edge is located. This preserves a sharp curve and prevents the five energy bin neighborhoods from smoothing out the sharp curve, as the other approach does; this is apparent for iodine (figure 6.3). However, this breaking of attenuation curves is applied to every attenuation curve in the reconstruction. Breaking the curve at the absorption edge prevents any improvement in SNR from continuing past the break point. In both cases, the PWLS is making an exception to its smoothing to account for absorption edges.

The EIGEN approach is focused on recovering the ideal attenuation curves rather than just smoothing the attenuation along the energy axis. The EIGEN method projects the measured attenuation curves onto a set of basis functions defined by the eigenvectors of a matrix of all the possible attenuation curves. Thus, the EIGEN method restricts the estimated attenuation curves to a weighted sum of a limited number of attenuation curves. This means the EIGEN method is fitting each reconstructed attenuation curve to one or a combination of limited number of known attenuation curves. If the algorithm sees something that looks like an absorption edge, it will assume that some of the corresponding element exists in that pixel. This means that true absorption edges are very well preserved (see figure 6.5 for gold and figure 6.6 for iodine). In both these cases the edges are perfectly preserved. However, when the noise along the attenuation curves looks like absorption edges to this algorithm, the algorithm imposes an edge there. The EIGEN method restricts the final estimated attenuation curves to a limited number of known curves. This will reduce the variance in the final estimate and create a maximum in SNR located at the center of the energy range. The EIGEN

method tolerates a little more noise because it is more concerned with recovering the absorption edges than smoothing the energy axis.

The combination of the two methods says a lot about the individual methods. When PWLS is applied first, the result is the best of both methods. When EIGEN is applied first the result is the worst of both methods. The PWLS smoothes out most of the noise along the energy axis, the EIGEN method is then applied to return the absorption edges, but is a little less confused with the noise. Thus, PWLS+EIGEN suppresses the most noise, has the best SNR, but also preserves all of the absorption edges. On the other hand, when EIGEN is applied first, the edges appear as noise to the PWLS which then smoothes them. The SNR for EIGEN+PWLS is worse than either PWLS or EIGEN for all materials other than iodine. The EIGEN method suppresses the peaks in the SNR from FBP which PWLS spreads out over other energy bins. The PWLS then pushes down the improvement made by EIGEN in the middle energy bins. Thus, EIGEN+PWLS has a bad SNR and looses absorption edges, particularly at the gold edges, whereas PWLS+EIGEN has great SNR and preserves the absorption edges.

The EIGEN approach has one final advantage which has not yet been addressed: the image segmentation produced by the spatial distribution of the basis function weights (figure 5.6). Projecting each FBP attenuation curve onto the four basis functions produces a weight for each basis function. These weights are spatially distributed based on the pixel location of the FBP attenuation curve. The weights show how much each basis function contributes to the specified pixel attenuation curve. Thus the image is segmented based on the basis functions. Since the basis functions can be interpreted in terms of the material content, the segmented image contains material information. Figure 5.6 indicates that EIGEN

successfully segments the iodine and gold but not the water and acrylic. This is similar to what is seen in the estimated attenuation curves, where gold and iodine are easily identified based on the absorption edges.

Overall, both methods suppress noise much better than FBP while preserving some of the absorption edges. The PWLS algorithm is shown to have a more simple set of initial assumptions and to suppress the noise along the energy axis, but PWLS takes much longer and smoothes over more the absorption edges. The EIGEN method is shown to be faster and does a better job preserving the absorption edges, but EIGEN has a more demanding set of initial assumptions and suppresses less of the noise along the energy axis. A combination approach is slower and more complicated. When PWLS is done first the noise is suppressed better than either individually and the absorption edges are well preserved. When EIGEN is done first the noise is less suppressed and absorption edge detail is lost.

6.5. References

AMPTEK detector XR-100CT, product information available at: http://www.amptek.com/xr100cr.html

Gonzales B. and Lalush D., "Full-Spectrum CT Reconstruction Using a Weighted Least Squares Algorithm with an Energy-axis Penalty," IEEE Trans. Med. Imag., In Press.

Gonzales B. and Lalush D., "Performance of Reconstruction and Processing Techniques for Dense Full-Spectrum X-ray Ct," Proceedings of the 2010 IEEE Nuclear Science Symposium and Medical Imaging Conference, November, 2010, Knoxville, TN, M09-131.

Hubbell J.H. and Seltzer S.M., 1996, Tables of X-Ray Mass Attenuation Coefficients and Mass Energy-Absorption Coefficients from 1 keVto 20 MeV for Elements Z = 1 to 92 and 48 Additional Substances of Dosimetric Interest, National Institute of Standards and Technology, Tech. Rep. 43NANB412756 Available: http://www.physics.nist.gov/PhysRefData/XrayMassCoef/cover.html

7. QUANTIFICATION OF DATA

The work we have presented in this dissertation has been focused on acquiring densely sampled attenuation curves (Chapter 3) and suppressing the noise along the energy axis (Chapters 4, 5, and 6). Once we have suppressed the noise, we can use the attenuation curves to identify the elements or compounds in the imaged object; provided energy resolution has been sufficiently preserved. Once the elements or compounds have been indentified, the concentration of these elements or compounds in the imaged object can be estimated based on the shape and intensity of their attenuation curves. The distribution of the estimated concentrations will be an image segmentation which not only identifies where the elements are located, but how much of a specific element is in each location. The accuracy of this estimation is dependent on the amount of noise along the energy axis and the energy resolution. Increasing the noise or decreasing energy resolution will decrease the accuracy of this estimation. In this chapter we present the process of getting from the attenuation curves to concentration estimation.

7.1 Averaged Filtered Back-Projection Attenuation Curves

The initial estimated attenuation curves are reconstructed using FBP (see figure 4.8 for selected attenuation curves). These curves have a large amount of noise distributed along the energy-axis; however, if all the curves for a known element or compound are averaged, this noise is reduced and the underlying attenuation measurement is preserved. Since a technical phantom is used, the distribution for all elements and compounds are known. The averaged FBP attenuation curves are compared with an ideal attenuation curve for each element or compound from the NIST database (Hubbell, 1996).

7.1.1 FBP Water and Acrylic Attenuation Curves

The background materials: water and acrylic, are investigated first. The technical phantom (see figure 4.4) is made of acrylic with five holes; one of the holes is filled with deionized water. The average attenuation curve for water is defined as the mean of all attenuation curves for the pixels corresponding to the water hole and the average attenuation curve of acrylic is defined as the mean of all attenuation curves for the pixels corresponding acrylic phantom with the holes removed. These averaged attenuation curves are compared with the ideal attenuation curves from the NIST database in figure 7.1.

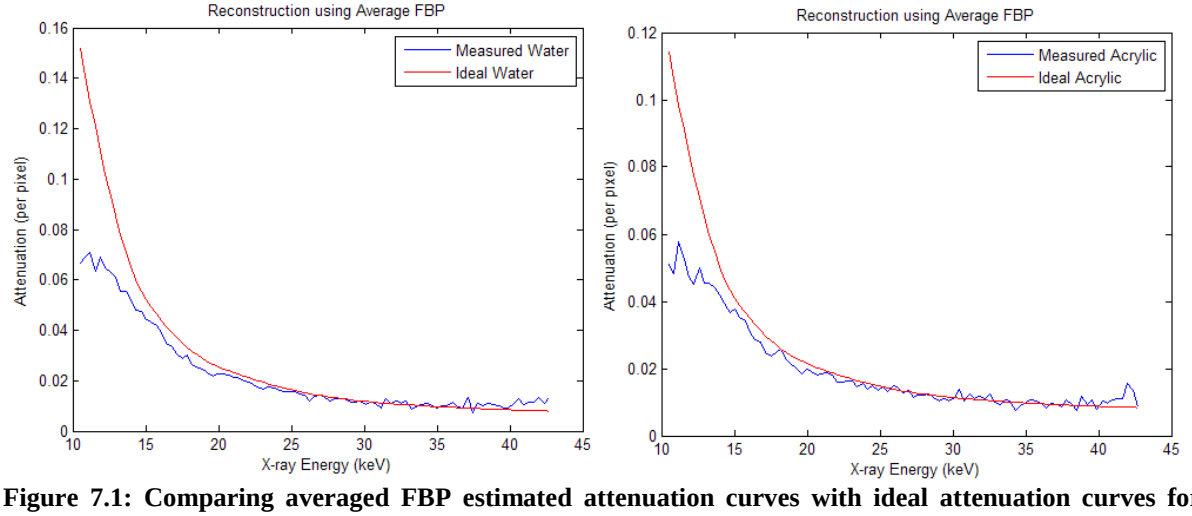

Figure 7.1: Comparing averaged FBP estimated attenuation curves with ideal attenuation curves for water and acrylic.

The NIST database (Hubbell, 1996) contains the mass-attenuation curve for both water and acrylic. The mass attenuation is expressed as: μ/ρ where μ is the linear attenuation coefficient and ρ is the density. The density has units of: g/cm^3 which means that density is the amount, or weight, of the element or compound per unit of volume. The density of water is one $(\rho_{water} = 1\ g/cm^3)$. The density of acrylic is 1.19 $(\rho_{acrylic} = 1.19\ g/cm^3)$. The

mass attenuation is given in units of: $^{cm^2}/_{g}$ so if the density is know, the linear attenuation coefficient is:

$$\mu = \frac{\mu}{\rho} \cdot \rho = \frac{cm^2}{g} \cdot \frac{g}{cm^3} = \frac{1}{cm} \quad (7.1)$$

To find the ideal attenuation curves for water and acrylic, for the experimental setup used in this dissertation, the volume must be known. The volume should be the voxel size in the reconstructed attenuation map. We only reconstruct a single slice through the imaged object, so we define the attenuation map in terms of pixels. Therefore, we define an area in place of a volume to define the ideal attenuation curve. The reconstructed pixel size is 0.4mm by 0.4mm. However, the detector has a 2mm pinhole. This means that the real area is circle with a diameter of 2mm, based on the size of the detector window. The area for each measurement is: $\pi \cdot r^2$, where $r = 1mm$. The area for each attenuation measurement is $\pi\ mm^2$. Thus, the ideal attenuation curve for water, accounting for the change in area is:

$$\mu_{Ideal\ Water} = \left(\left(\frac{\mu}{\rho}\right)_{water} \cdot \frac{Measure\ Area\ (cm^2)}{1cm^2}\right) \cdot \rho_{water} = \left(\left(\frac{\mu}{\rho}\right)_{water} \cdot \frac{\pi\ mm^2}{100mm^2}\right) \cdot 1 \quad (7.2)$$

This modification of the NIST database mass attenuation of water $\left(\frac{\mu}{\rho}\right)_{water}$ is done for all energies in the measured x-ray spectrum; this forms the ideal water attenuation curve (shown as red line in left image in figure 7.1). A similar modification is done to the NIST attenuation curve for acrylic, using the acrylic density $\rho_{acrylic} = 1.19$ but the same measured area.

When the measured average attenuation curves for water and acrylic are compared with the ideal attenuation curves, the curves match up almost perfectly above 15keV (figure 7.1). This confirms the initial speculations that the estimated attenuation curves can be used to identify the materials based on their specific shape. To compare the shape of the ideal

attenuation curves with the averaged FBP curves, a ratio is defined as the ideal attenuation over the measured attenuation. This ratio is shown as function of energy for both water and acrylic in figure 7.2.

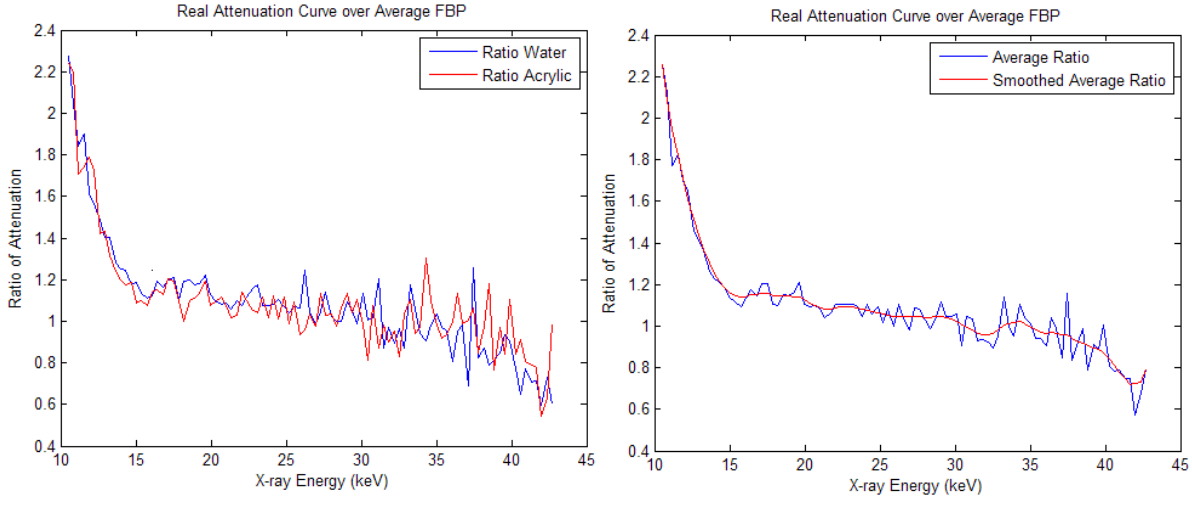

Figure 7.2: Ratio of ideal attenuation curve with measured attenuation curve for both materials. Right image is the average of both ratios and a smoothed ratio to give overall trend of ratio.

The ratio of the ideal to the measured attenuation curves shows a ratio of almost one for most of the energy range. A ratio close to one indicates the ideal and measured curves are almost identical. The ratio is larger at the low energies, below 15keV. This error could be the result a number of factors including: pulse-pileup, insufficient x-ray flux, or scatter. Pulse-pileup occurs when two photons are counted to close in time to each other and the detector assigns the count to the wrong energy bin; we see this problem at low energies (see figure 3.7). Insufficient flux occurs when not enough x-ray photons make it through the image object to accurately sample the true attenuation at those energies. Scatter is when the wrong x-ray photons are counted due to a scatter of photons in the image object.

The ratio at higher energies begins to fall below one (see the general trend of the ratio: red line left image in figure 7.2). This is because of the noise in these energy bins.

Overall, the ratio between the ideal and measured attenuation curves (Figure 7.2) and the curves themselves (figure 7.1) show that the estimated attenuation curves are very close to the ideal attenuation curves.

The smoothed water ratio can be used as a correction for all attenuation curves in the imaged object. Multiplying each attenuation curve by this ratio calibrates the attenuation curves to the water attenuation curve. This is a reasonable because water will nearly always be present in an imaged object. The calibrated water and acrylic attenuation curves are shown in figure 7.3.

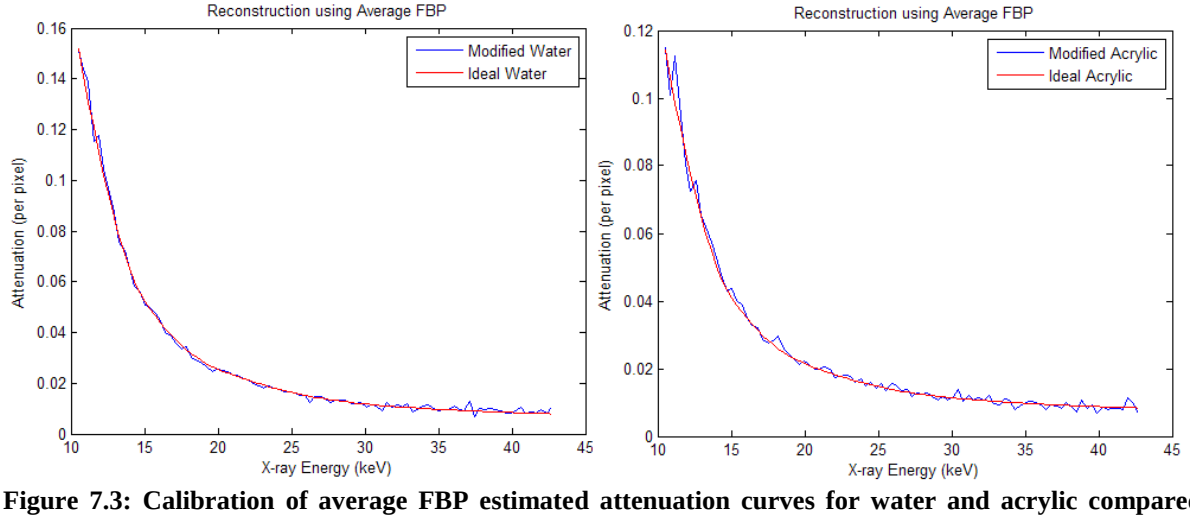

Figure 7.3: Calibration of average FBP estimated attenuation curves for water and acrylic compared with ideal attenuation curves.

The calibrated acrylic curve matches the ideal acrylic curve almost as well as the calibrated water curve matches the ideal water curve. This means that calibrating acrylic with the ideal water attenuation curve accounts of the loss difference between the measured acrylic and ideal acrylic seen in figure 7.1. This demonstrates that the new system proposed in this dissertation is capable of accurately measuring the attenuation curve, preserving the specific shape and intensity based on the measurement parameters, specifically the measured area. In the next section we demonstrate that this is also true for contrast agent attenuation curves.

7.1.2 FBP Iodine and Gold Attenuation Curves

The contrast phantom imaged has two contrast agents: gold and iodine, each is in solution with deionized water and each fills two of the holes in the phantom (figure 4.4). The average attenuation curves for gold and iodine are defined as the mean of all attenuation curves for the pixels corresponding to the gold and iodine holes respectively. The average attenuation curves for gold and iodine are compared with the ideal attenuation curves for gold and iodine in figure 7.4.

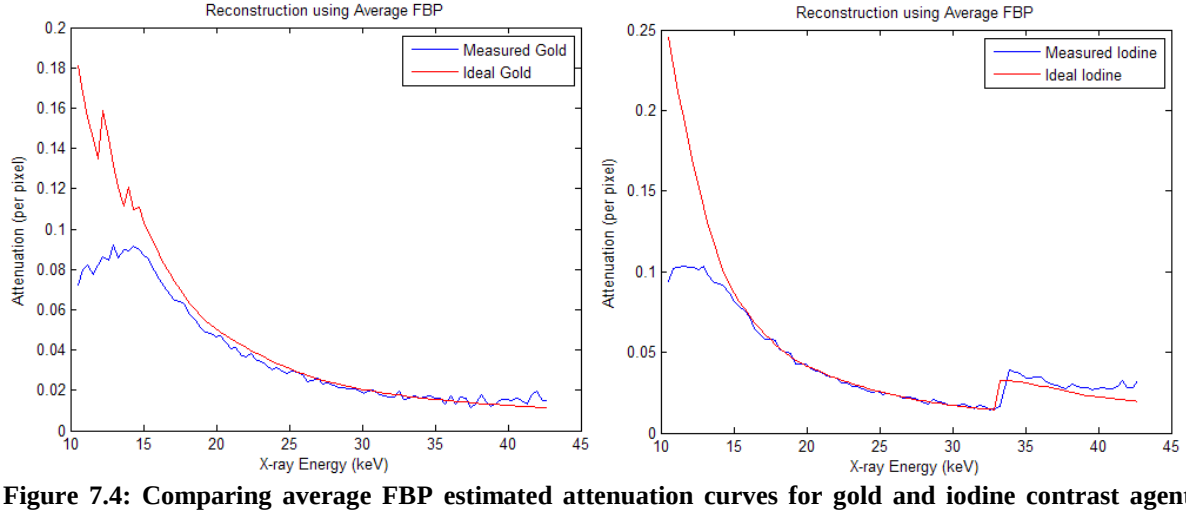

Figure 7.4: Comparing average FBP estimated attenuation curves for gold and iodine contrast agents with the ideal attenuation curves.

The ideal gold and iodine attenuation curves are defined in the NIST database. The NIST database defines a mass attenuation curve for both gold and iodine (see figure 4.2); however, the elements in the phantom are in solution with water. Therefore, we define the ideal attenuation curve for gold as:

$$\mu_{ideal\ gold} = \left(\left(\frac{\mu}{\rho}\right)_{gold} \cdot \rho_{gold} \cdot \frac{\pi\ mm^2}{100\ mm^2}\right) + \left(\left(\frac{\mu}{\rho}\right)_{water} \cdot \rho_{water} \cdot \frac{\pi\ mm^2}{100\ mm^2}\right) \qquad (7.3)$$

The second term in expression (7.3) is the ideal attenuation for water because the gold is in solution with water. The first term is the gold in the solution; the density term is the

concentration of gold, defined as: $\rho_{gold} = 10\,{}^{mg}/_{ml} = .010\,{}^{g}/_{cm^3}$. A unit of g/ml is the same as a unit of g/cm^3; therefore, the density is the same as concentration, which is known and plugged into the expression for ideal gold attenuation. The ideal iodine attenuation curve is defined by the same expression (7.3) substituting the gold mass attenuation curve $\left(\frac{\mu}{\rho}\right)_{gold}$ with the iodine mass attenuation curve $\left(\frac{\mu}{\rho}\right)_{iodine}$ and using a known concentration of iodine: $\rho_{iodine} = 20\,{}^{mg}/_{ml}$.

The average FBP estimated attenuation curves for gold and iodine compared to the ideal gold and iodine curves (figure 7.4) follow a similar pattern as the estimated and ideal water and acrylic. The average attenuation curves match the ideal curves well at x-ray energies above 15keV and there is an error between the average measured curves and the idea curves below 15keV. To account for this error, the water calibration is applied to each of the contrast agent attenuation curves (figure 7.5).

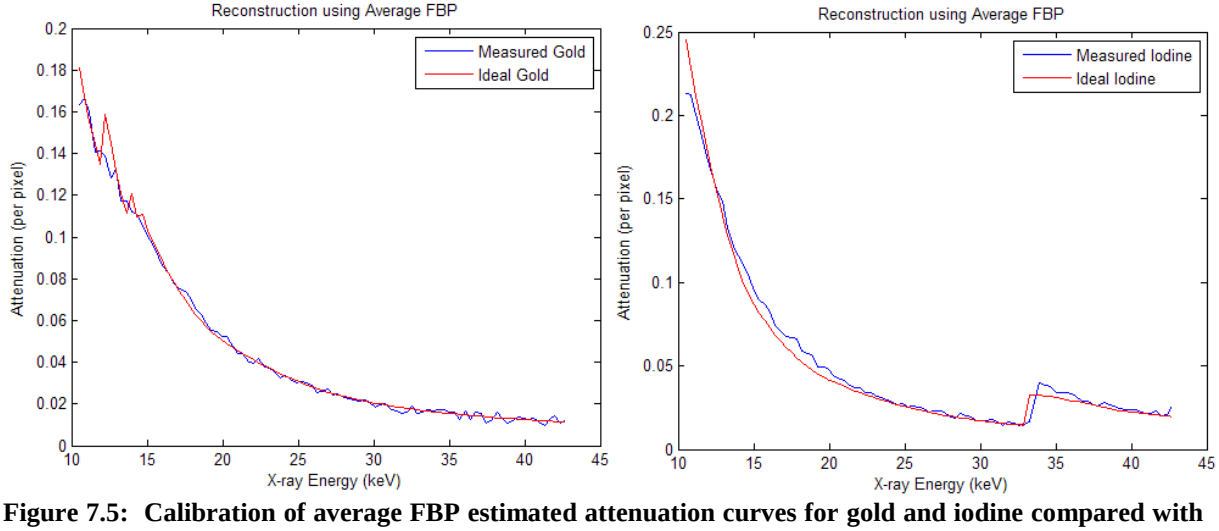

Figure 7.5: Calibration of average FBP estimated attenuation curves for gold and iodine compared with ideal attenuation curves.

The water calibrated average FBP estimated gold and iodine attenuation curves fit the ideal attenuation curves exceptionally well. This means that expression (7.3) is a good estimate of

the measured attenuation curve using the known concentration of the contrast agents. This also means that the water calibration works for the contrast agents.

7.2 Noise Suppression Attenuations Curves for single Pixel

The average FBP estimates for the different attenuation curves demonstrates that this new x-ray CT system is capable of estimating an attenuation curve which is nearly identical to the ideal attenuation curve for a given density and pixel size. However, this has been demonstrated by averaging a large number of known attenuation curves, requiring prior knowledge of the distribution of elements or compounds in the imaged object. An average is necessary because of the noise distributed along the energy axis. It has been shown that using the noise suppression algorithms, individual attenuation curves can be identified (Chapters 4, 5, & 6). These individual attenuation curves are compared with the ideal attenuation curves.

7.2.1 PWLS and EIGEN Water and Acrylic Attenuation Curves

The same randomly selected attenuation curves as figures 6.4.C and 6.4.D for water and acrylic respectively are compared with the same ideal attenuation curve shown in figure 7.1. These curves are reconstructed using PWLS or EIGEN for noise suppression and shown with the ideal curve in figure 7.6.

The randomly selected curves have been calibrated using the same water attenuation ratio used to average the FBP attenuation curves (shown in figure 7.2). This calibration was done after reconstruction, before the data was plotted. The calibration could have been done prior to the reconstruction. Calibrating prior to reconstruction may have improved the data slightly. However, this compares the same data shown in chapters 4, 5, & 6 compared with an ideal water and acrylic attenuation curve. Calibrating the PWLS would require calibration of all

the projections as well as the reconstructions, because the estimated attenuation is pulled toward the projections in the weighted least squares portion of the algorithm.

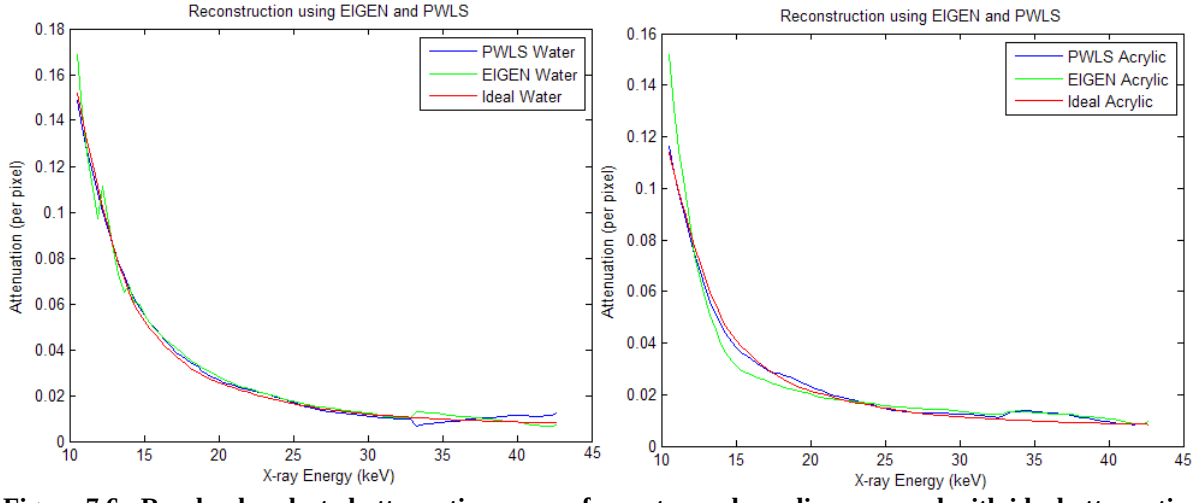

Figure 7.6. Randomly selected attenuation curves for water and acrylic compared with ideal attenuation curves. Noise has been suppressed using both proposed methods.

Although the attenuation curves in figure 7.6 are a single randomly selected attenuation curve, the estimated attenuation curve still matches the ideal curve very closely. This means the noise suppression algorithms suppress the noise while preserving the attenuation curves. It also means that after the noise has been suppressed, individual attenuation curves can be used to identify specific materials.

7.2.2 PWLS and EIGEN Gold and Iodine Attenuation Curves

The same randomly selected attenuation curves as figures 6.2 and 6.3 for gold and iodine respectively are compared with the ideal attenuation curves shown in figure 7.3. These curves are reconstructed using PWLS and EIGEN for noise suppression and compared with the ideal curves in figure 7.7.

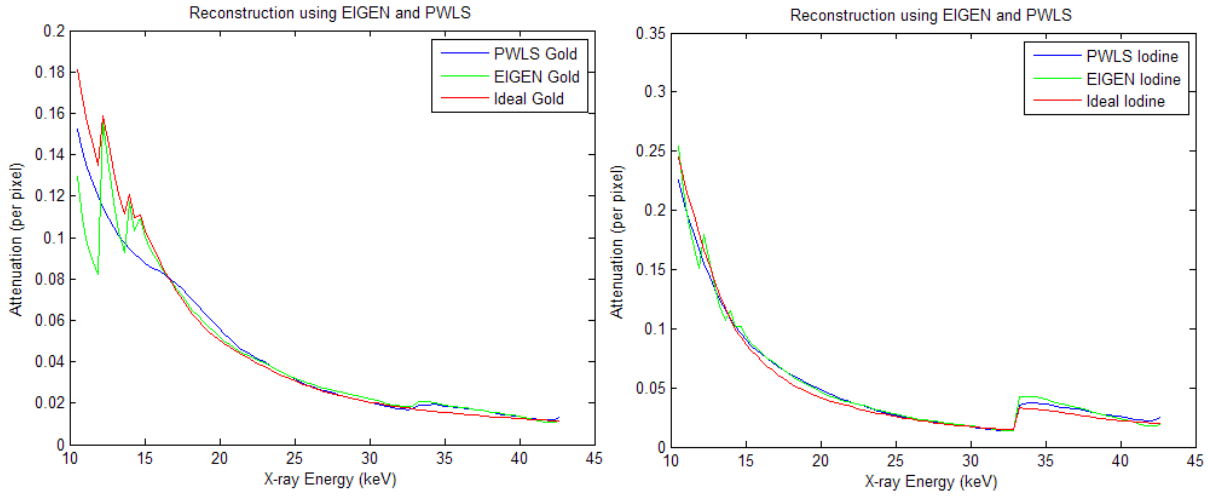

Figure 7.7. Randomly selected attenuation curves for gold and iodine compared with ideal attenuation curves. Noise has been suppressed using both proposed methods.

The randomly selected curves have been calibrated using the same water ratio shown in figure 7.2. Again, this calibration was done after reconstruction, before the data was plotted. The attenuation curves in this image match almost perfectly, similar to the average FBP attenuation curves. However, these are randomly selected single attenuation curves. This means that for a single pixel, the estimated attenuation matches very closely with the ideal attenuation. Thus, both noise suppression algorithms have preserved the attenuation curve in each pixel enough to match an ideal curve. If the concentration of either gold ρ_{gold} or iodine ρ_{iodine} changes, the ideal curves would change and no longer match the estimated curves as closely. This means that the estimated attenuation curves not only match the shape of the correct attenuation curve but also the intensity, which is correlated to the density or concentration. Once the noise has been suppressed, both the materials and the concentration of those materials, in a single pixel can be identified.

The most significant error in the estimated attenuation curves for gold and iodine (figure 7.7) is in the low energies, below 15keV. This is most apparent in the PWLS estimate

for gold. The absorption edges are missing and the curve is below the ideal curve until after the absorption edges. This difference was greater before the curves where calibrated; the calibration brings the gold curve closer to the ideal. This error may be due to pulse-pileup, insufficient x-ray flux, or scatter.

7.3 Identifying Concentration Distribution

The average FBP attenuation curves (figures 7.3 & 7.4) match the ideal attenuation curves from the NIST database based on know concentrations of the contrast agents. This demonstrates that the new system proposed in this dissertation is capable of accurately measuring the attenuation curve in a tomographic reconstruction. The increased energy resolution also increases the noise along the energy axis. However, the two proposed noise suppression algorithms (Chapters 4 & 5) not only suppress the noise, they also preserve the shape and intensity of the attenuation curves; this is demonstrated by the how closely the noise suppressed attenuation curves match the ideal attenuation curves (figures 7.6 and 7.7). The ideal attenuation curves for the contrast agents are defined by expression (7.3) which incorporates the density or concentration of the contrast agents with water. Once the noise has been suppressed it is possible to use the attenuation curves to estimate the concentration of a contrast agent in the imaged object.

The first step in using the attenuation curves to estimate the concentration of a contrast agent is to calibrate the attenuation curves using the water calibration. This calibration forms an attenuation curve we label $\widetilde{\mu}_{jE}$ for each pixel j in the attenuation map. In expression (7.3) we defined the ideal contrast attenuation curve as a mixture of the contrast agent and water; so the second step is to subtract the water attenuation curve from the calibrated attenuation curve for each pixel.

$$\bar{\bar{\mu}}_{jE} = \tilde{\mu}_{jE} - \mu_{water} = \tilde{\mu}_{jE} - \left(\left(\frac{\mu}{\rho}\right)_{water} \cdot \frac{\pi\, mm^2}{100\, mm^2}\right)_E \tag{7.4}$$

Expression (7.4) defines a new difference attenuation curve $\bar{\bar{\mu}}_{jE}$ which will be the remaining contrast attenuation curve, based on expression (7.3). The difference curve is then divided by the ideal contrast agent curve to identify the concentration ρ_{jE} of the contrast agent at the specific pixel location *j*.

$$\rho_{jE} = {\bar{\bar{\mu}}_{jE}}/{\mu_{contrast}} = \bar{\bar{\mu}}_{jE} \Big/ \left(\left(\frac{\mu}{\rho}\right)_{contrast} \cdot \frac{\pi\, mm^2}{100\, mm^2}\right)_E \tag{7.5}$$

The estimated concentration ρ_{jE} for a specific pixel location *j* will be dependent of the attenuation curve at the same location and the x-ray energy. Ideally, the estimated concentration will be the same for all energy bins, since the concentration is not a function of energy. However, the estimated concentration will vary with energy due to the noise in the sample attenuation curves. To arrive at a single concentration estimate $\hat{\rho}_j$ from expression (7.5), the estimated concentration ρ_{jE} is averaged over some number of energy bins.

$$\hat{\rho}_j = \frac{1}{K}\sum_{E=1}^{K} \rho_{jE} \tag{7.6}$$

The energy bins $E = [1,2,\cdots,K]$ can span the entire sampled x-ray spectrum or a specific part of the spectrum. The energy bins used to estimate the concentration of a contrast agent depend on where the contrast agent is best represented. For gold this seems to be the low energy region between 10keV and 20keV, where there is good separation between water and gold. For iodine, this seems to be directly after the iodine abortion edge, after 33keV, where the iodine has the most separation from the other attenuation curves.

We test the estimation of density $\hat{\rho}_j$ with the contrast phantom described in Chapters 4 and 5. Using the contrast phantom (figure 4.4) we first estimate the concentration of gold. There is an estimated density for each pixel j in the attenuation map. This spatially distributed estimated density $\hat{\rho}_j$ is shown for each reconstruction method in figure 7.8.

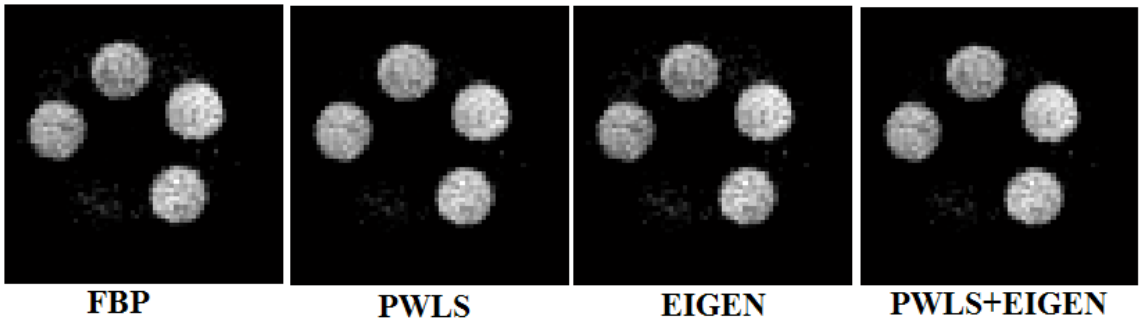

Figure 7.8: Spatial distribution of estimated gold concentration $\hat{\rho}_{j,gold}$

The spatial distribution of estimated gold concentration shows four regions, corresponding to the four holes filled with contrast agent. The mean and standard deviation of gold concentration for each of these regions is given in table 7.1. Regions are labeled as: far left hole is Region 1; holes are then counted clockwise in reconstruction.

Table 7.1: Average estimated gold concentration for each region in phantom.

Units (mg/ml)	Region 1	std 1	Region 2	std 2	Region 3	std 3	Region 4	std 4
FBP	9.94	2.54	10.07	1.97	12.64	2.98	11.80	2.10
PWLS	9.96	2.78	10.27	1.75	12.16	2.89	11.75	1.76
EIGEN	9.36	2.42	9.47	1.95	12.46	2.95	11.52	2.11
PWLS+EIGEN	9.23	2.62	9.47	1.74	11.78	2.83	11.26	1.79

The gold is estimated for energy bins corresponding to energies 10keV-20keV. This energy region is where the gold absorption edges are located and should be able to identify the gold. Region 1 and Region 2 in table 7.1 represent the locations of actual gold with a true concentration of 10mg/ml. The estimated concentration of gold for all methods is very close

to this value. This confirms the results seen in attenuation curves from these regions (figure 7.5). The iodine shows up as gold in this estimation because the gold edges were not sufficient to separate the iodine from the gold (figures 4.8 and 5.8).

The estimated iodine concentration uses energy bins 33keV-43keV and has a better separation from the gold concentration. The spatial distribution of estimated iodine concentration is shown in figure 7.9.

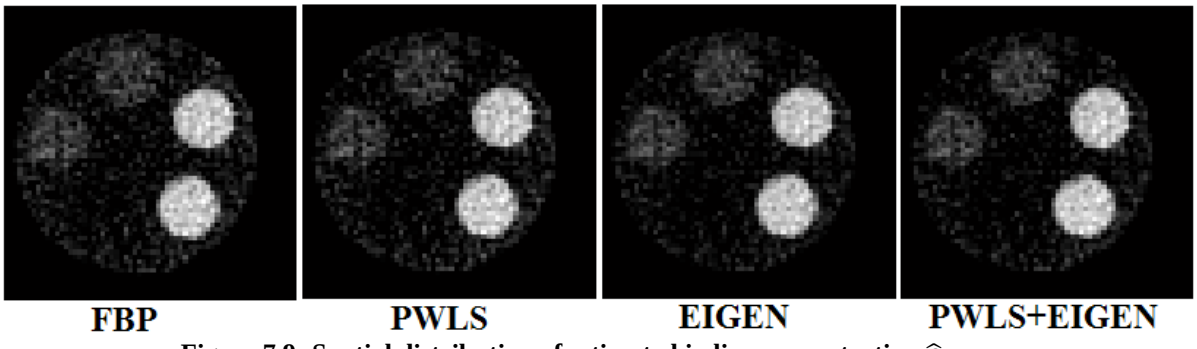

Figure 7.9: Spatial distribution of estimated iodine concentration $\hat{\rho}_{j,iodine}$

The spatial distribution of iodine distribution in figure 7.9 follows the known distribution of iodine. The two iodine regions are much brighter, corresponding to a higher concentration, than all other pixels in the images. The mean and standard deviation of estimated iodine concentration of each for the regions is given in table 7.2. Regions are labeled as: far left hole is Region 1; holes are then counted clockwise in reconstruction.

Table 7.2: Average estimated iodine concentration for each region in phantom.

Units (mg/ml	Region 1	std 1	Average 2	std 2	Average 3	std 3	Average 4	Std 4
FBP	5.38	2.55	5.19	2.12	18.90	3.81	19.67	2.53
PWLS	4.92	2.64	4.81	2.14	18.29	3.91	19.36	2.58
EIGEN	5.12	2.89	4.98	1.78	17.93	3.62	18.68	2.19
PWLS+EIGEN	4.96	2.38	4.98	1.84	17.35	3.66	18.44	2.33

Region 3 and Region 3 in table 7.2 represent the locations of actual iodine with a true concentration of 20mg/ml. The estimated concentration of iodine for all methods is very close to this value. This confirms the results seen in attenuation curves from these regions (figure 7.5). The gold regions (regions 1 and 2) are much lower iodine estimations, making it easier to separate them based on the estimated concentration.

The estimated concentrations for each region (in tables 7.1 and 7.2) is an average over a large number of pixels; approximately 120 pixels per average. This reduces the noise in each region. Thus, the FBP has an accurate estimate of concentration. The remaining noise is demonstrated in the standard deviation in each regions estimated concentration. This standard deviation is always less than the average concentration. This standard deviation indicates that there will be error when estimating the concentration in a single pixel.

The contrast agents in this phantom were clearly separated from each other. If the contrast agents were mixed in the same region, it would be difficult to separate their concentrations. We show in figure 7.9 and table 7.2 that it we can estimate the concentration of iodine fairly accurately based the absorption edge. The gold edges were not cleanly recovered, due to their low energy location. If the anode voltage of the system were increased to 100kV, the single gold absorption edge at 80keV could be recovered. Using this edge, it might be possible to separate the gold better. Using the gold absorption edge at 80keV and the iodine edge at 33keV, it might be possible accurately estimate the concentration of both gold and iodine mixed in the same region.

These initial distributions of gold and iodine concentrations (figure 7.8 and 7.9) demonstrate that, using the attenuation curves, it is possible to estimate the concentration of a contrast agent in an imaged object with a fairly high degree of accuracy. This estimate is

based on the measured data, it exists in the FBP; this means it is not imposed by the noise suppression methods.

7.4 Identifying Multiple Concentrations

The original phantom (figure 4.4) had two contrast agents in solution with water. There was only a single concentration for each of these contrast agents. To investigate the accuracy of concentration estimates more closely, two new experiments were conducted using multiple concentrations of the same contrast agent. An overview of these new experiments is presented, including both the initial FBP attenuation maps and the noise-suppressed attenuation maps. The estimated distribution of concentration is then presented for both experiments. Finally, the reconstructed attenuation curves are compared with the true attenuation curves for both experiments.

7.4.1 New Experiments

Two new experiments with multiple concentrations of a single contrast agent were done using the new x-ray system presented in this dissertation; both of these experiments used the cylindrical acrylic contrast phantom with the five holes filled with different concentrations of a single contrast agent. The first experiment used five concentrations of iodine contrast agent in solution with deionized water. The second experiment used four concentrations of gold nanoparticles in solution with deionized water and deionized water with no added concentration of gold. The new source had a problem with long term x-ray flux stability (section 3.3). There was some variance in the x-ray flux over the course of each experiment, increasing the noise the reconstructions.

7.4.1.1 Iodine Contrast Phantom

The first new experiment used the cylindrical acrylic phantom (figure 4.4) with all five holes filled with a different concentration of iodine (Visipaque) contrast agent in solution with deionized water. The distribution of the different iodine concentrations and the specific concentrations used are show in figure 7.10.

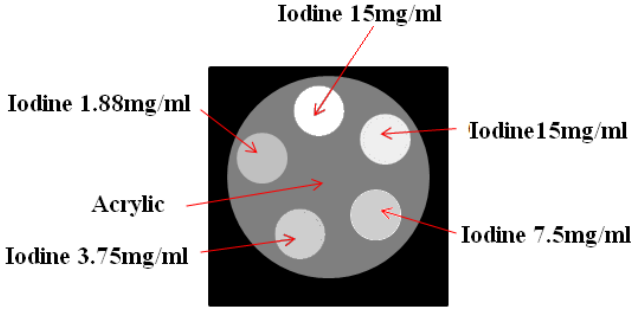

Figure 7.10: Distribution of iodine contrast solutions in acrylic contrast phantom

The iodine contrast phantom was imaged using 40kV applied to the tungsten anode. A 40Hz pulse signal with a 50% duty cycle and 1600V was applied to the gate. The focusing elements had a direct 2000V signal applied to each of them. These setting resulted in a low, but measurable, x-ray flux. The x-ray was run at low flux to prevent arcing or a charge from building in the vacuum chamber over the course of the experiment. This low x-ray flux resulted in an increased noise in the sampled x-ray spectrum. This noise is apparent in the initial FBP reconstructions. The FBP reconstructed attenuation maps for the iodine contrast phantom are shown for selected energy bins in figure 7.11.

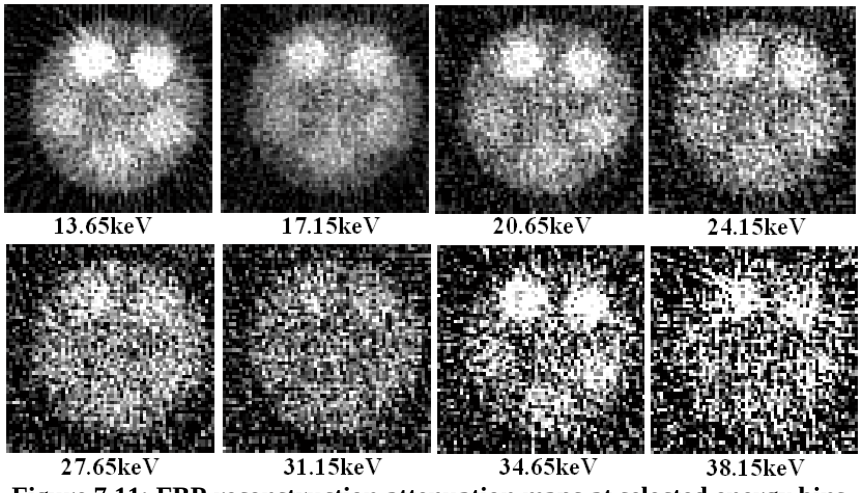

Figure 7.11: FBP reconstruction attenuation maps at selected energy bins

The initial FBP attenuation maps for the iodine experiment show the different concentrations of iodine as a difference in the brightness in the different the regions, compare figure 7.11 to 7.10. The FBP reconstructions show the iodine absorption edge, the iodine appears brighter at energies after 33keV. The FBP also shows that the concentration of iodine impacts the estimated attenuation around the iodine absorption edge. There is a slight misalignment of the phantom apparent in the FBP reconstructions; the reconstructed phantom is not perfectly circular.

To suppress the noise along the energy axis, the two noise suppression algorithms presented in this dissertation, PWLS (Chapter 4) and EIGEN (Chapter 5), where applied to this data. The results, after noise suppression, are shown in figure 7.12.

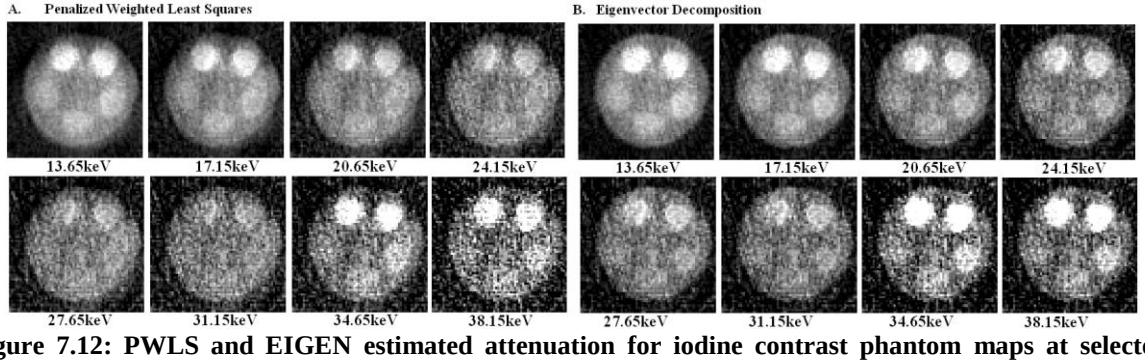

Figure 7.12: PWLS and EIGEN estimated attenuation for iodine contrast phantom maps at selected energies.

Despite the remaining noise, the distributions of different iodine concentrations are now more apparent in the attenuation maps (compare 7.11 and 7.10); indicating energy axis noise suppression. This improvement is most apparent in the low iodine concentration regions. The improvement is significant at low energies where the x-ray flux was higher (13.65-24.15keV) and after the iodine absorption edge (above 33keV). These noise-suppressed attenuation maps demonstrate the successful use of the two noise suppression algorithms on another set of data; both methods suppress a large amount of the noise while preserving the original attenuation, making it easier to identify materials in the attenuation maps.

The noise-suppressed attenuation curves are not show in this section. The noise along the energy axis is suppressed using either PWLS or EIGEN; but this has already been shown in Sections 4 and 5 for each method respectively. The attenuation curves for this experiment are investigated in section 7.4.2.1 with a focus on estimating the concentration in each iodine region.

7.4.1.2 Gold Contrast Phantoms

The second new experiment used the cylindrical acrylic phantom (figure 4.4) with four holes filled with different concentrations of gold nanoparticles in solution with deionized water and the fifth hole with deionized water. The distribution of the different gold concentrations is show in figure 7.13.

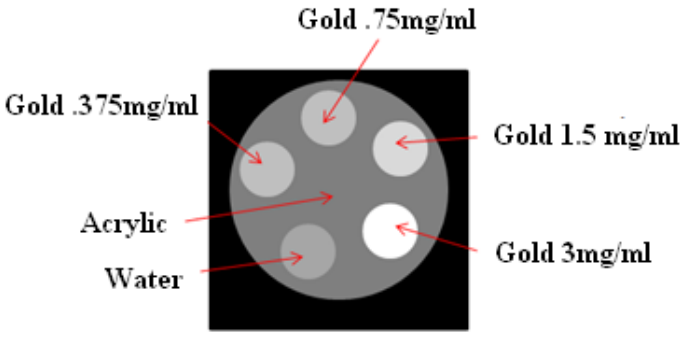

Figure 7.13: Distribution of gold nanoparticle solutions in acrylic contrast phantom

This gold contrast phantom was imaged using the new x-ray system presented in this dissertation (Section 3.3). A 40kV was applied to the tungsten anode. The gate had 1600 volts applied with a 40Hz pulse and a 50% duty cycle. The focusing elements both had 2000 volts applied to them. The x-ray was run at low flux to prevent arcing or charge building in the vacuum chamber during the experiment. This low x-ray flux resulted in an increase in noise in the sampled x-ray spectrum The molybdenum peaks in the previous experiment provided increased signal-to-noise ratio (SNR) at the characteristic peak energies; the tungsten anode has no characteristic peaks in the 10-40keV energy window used for this experiment (figure 3.8) so there is no energy with improved SNR. The FBP estimated attenuation maps for the gold contrast phantom are shown for selected energy bins in figure 7.14.

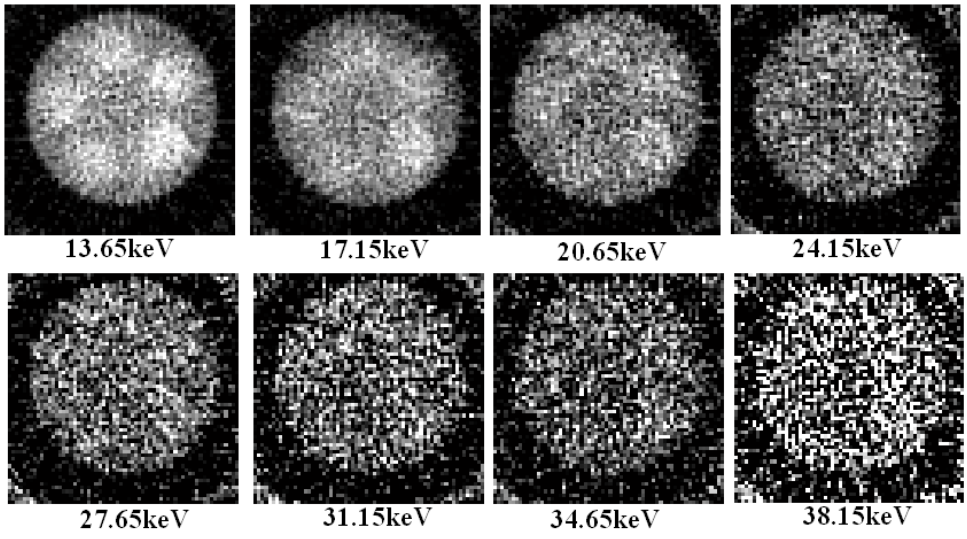

Figure 7.14: FBP estimated attenuation maps at selected energy bins.

The gold nanoparticles have a collection of low energy absorption edges; at the low energies, some gold variance can be identified in the initial FBP reconstructions (figure 7.14). This variance is rapidly lost to the noise in the FBP reconstructions. Both noise suppression algorithms were applied to the estimated attenuation curves for the gold attenuation. The noise suppressed attenuation maps for the same energy bins are shown in figure 7.15 for both noise suppression methods.

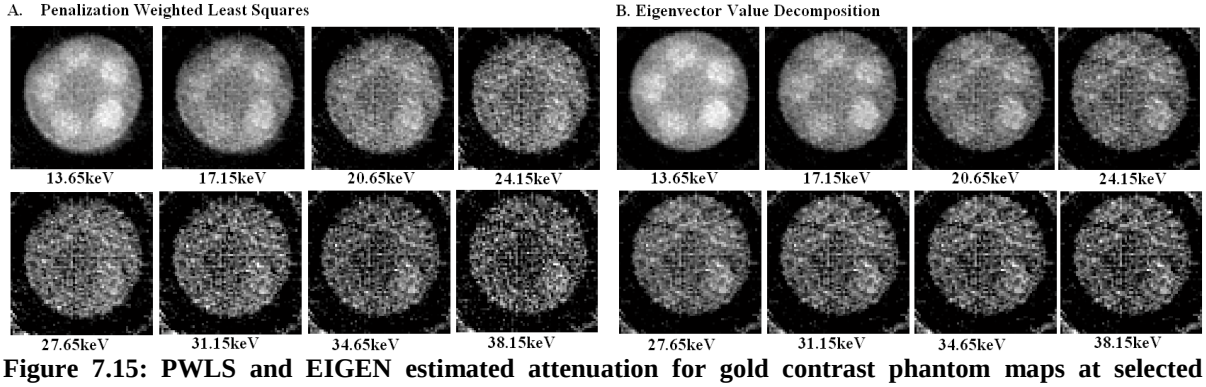

Figure 7.15: PWLS and EIGEN estimated attenuation for gold contrast phantom maps at selected energies.

The distribution of the different concentrations of gold is more obvious at the lower energies after noise suppression (figure 7.15). This distribution is indicated by variance in the attenuation map corresponding to the different concentrations of gold (compare figure 7.15 to

7.13). However, this distribution disappears at higher energies due to lack of gold absorption edges and the remaining noise. The EIGEN method seems to suppress a little more of this noise, preserving the highest concentration of gold through all energies and some of the spatial attenuation variance to 30keV. The EIGEN method is forcing all the attenuation curves to one of only three known curves (See discussion in section 6) reducing a little more of the noise.

7.4.2 Distribution of Concentration

The two new experiments (sections 7.4.1.1 and 7.4.1.2) focus on a single contrast-agent with multiple concentrations to test the accuracy of the concentration estimation. The initial FBP estimated attenuation maps for both experiments have so much noise that it is difficult to identify the specific distribution of different materials based on the spatial distribution of attenuation. The noise suppressed attenuation maps for both contrast agents (figures 7.11 and 7.15) still a significant amount of noise remaining. To reduce the impact of this noise on the estimation, the concentration is averaged over each known contrast region rather than of looking at the estimation along a single attenuation curve. The averaged attenuation curves are shown for each contrast region and are compared with a true attenuation curve, which is defined in the same way the true attenuation curves in the concentration estimates for the original experiment were (section 7.1). The distribution of this estimate and the average estimated concentration for each contrast region are presented and discussed in this section for both of the new experiments.

7.4.2.1 Estimating the Concentration of Iodine

The iodine contrast phantom (figure 7.10) has multiple concentrations of iodine in solution with water. The spatial distribution of estimated iodine concentration $\hat{\rho}_{j,iodine}$ is shown for each reconstruction method in figure 7.16.

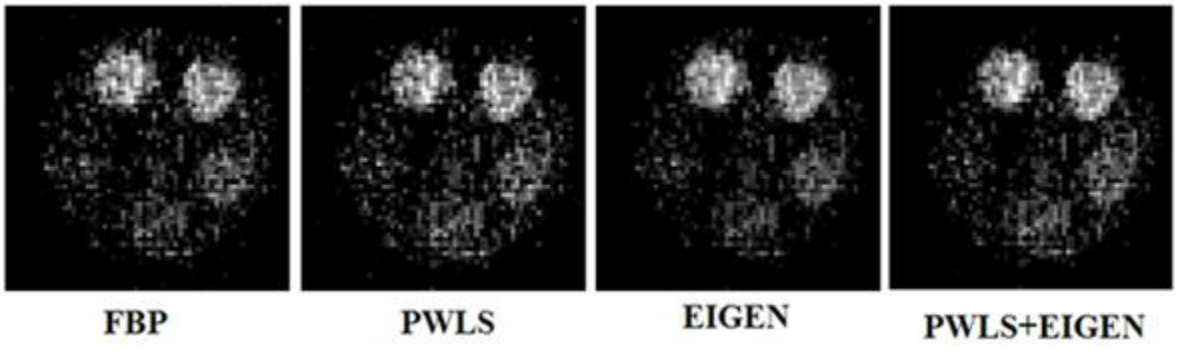

Figure 7.16: Spatial distribution of estimated iodine concentration of each method

The iodine concentration $\hat{\rho}_{j,iodine}$ is estimated using the method described in section 7.3. The estimated concentration $\rho_{jE}$is averaged over the 33keV-40keV energy range. The spatial distribution of the estimated iodine concentration follows the known distribution of iodine (compare figure 7.16 and 7.10). The average estimated iodine concentration for each region is shown plotted as a function of the true iodine concentration in figure 7.17. The averaged estimate and the standard deviation for each region are given in table 7.3. In this table regions are labeled as: upper left hole is Region 1, holes are then counted clockwise in reconstruction.

Table 7.3: Average estimated iodine concentration for each region

Units (mg/ml)	Region 1	std 1	Region 2	std 2	Region 3	std 3	Region 4	std 4	Region 5	std 5
FBP	15.1	7.7	15.5	6.7	8.2	5	4.3	5.1	2.3	5
PWLS	14.6	7.7	15.3	6.8	8.7	5.1	5.5	5.3	2.3	5.2
EIGEN	15.1	6.9	15.4	5.6	7.8	3.9	4.1	3.9	2	4.2
PWLS+EIGEN	15	6.4	15.6	5.4	7.5	3.9	4.9	4.2	1.5	4.1

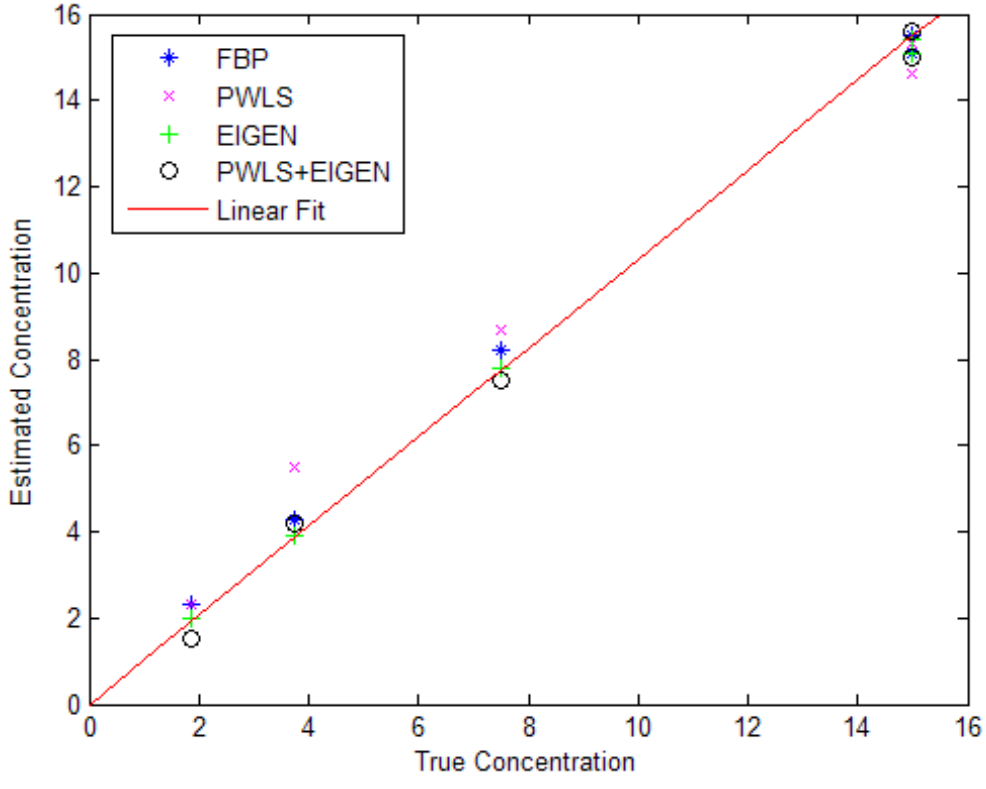

Figure 7.17. Average estimated iodine concentration for each region for each method plotted as function of the true iodine concentration.

The estimated iodine concentration is plotted as a function the true iodine concentration (figure 7.17) to demonstrate the accuracy of the concentration estimation. The estimated points are all tightly group along a line with a slope of one, indicating that the as concentrations double, the concentration is still accurately estimated. However, at lower concentrations, the standard deviation is greater than the estimated concentrations (table 7.3). This indicates that at these low concentrations it is more difficult to accurately estimate the concentration. This is confirmed by the spatial distribution of iodine concentration (figure 7.16); where it is more difficult to identify the specific shape of the lower concentration regions. The actual slope of the estimated concentration with respect to the true concentration is not actually one. A linear fit is applied to the data (shown as linear fit in figure 7.17) for

reconstruction method. The slope of the fit for each method and the r-squared error of the data with respect to that fit are given in table 7.4. The fit uses a linear line with slope shown in table and crosses y-axis at zero. The r-squared measure of error is also shown for each method.

Table 7.4: Linear fit to each method's concentration estimate

	FBP	PWLS	EIGEN	PWLS+EIGEN
Slope	1.033	1.028	1.022	1.024
R-squared	0.995	0.965	0.999	0.99

The linear fit assumes a y-interest of zero because there should be a zero estimated concentration for zero true concentration. The slopes are all close to one (table 7.4) with a very smaller error indicated by the r-squared. This means that the method is accurately estimating the concentration of iodine.

To further investigate the accuracy of each reconstruction method, the average attenuation curves for each concentration of iodine for each method are compared with the true attenuation curve in figure 7.18.

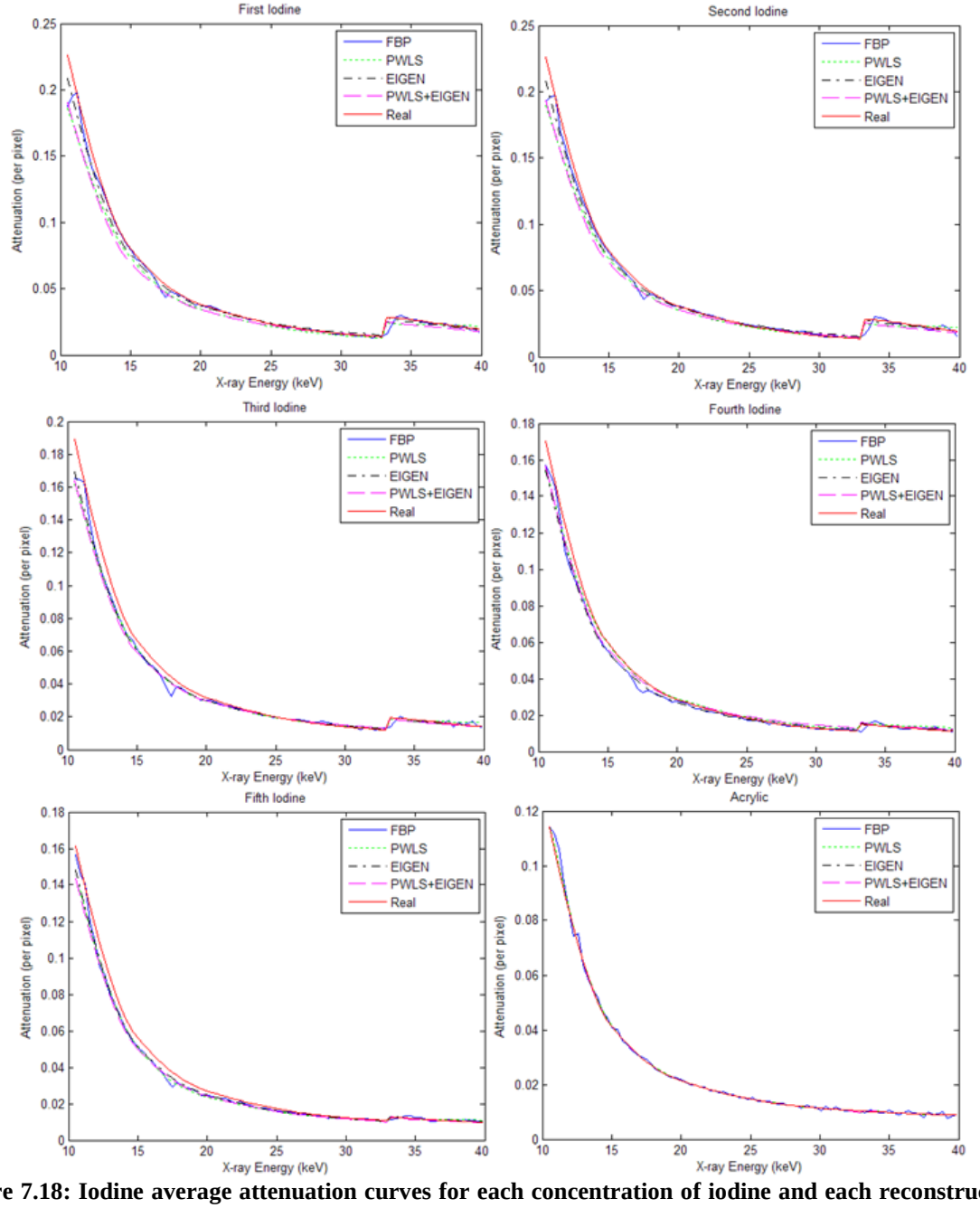

Figure 7.18: Iodine average attenuation curves for each concentration of iodine and each reconstruction method. True concentrations of each are: first iodine: 15mg/ml, second iodine: 15mg/ml, third iodine: 7.5mg/ml, fourth iodine: 3.75mg/ml, fifth iodine: 1.88mg/ml.

The average attenuation curve for each concentration of iodine for each reconstruction method closely follows the true attenuation curves. This means that the new system presented in this dissertation has accurately measured each concentration of iodine

and both noise suppression methods have preserved this measurement. It is interesting that the EIGEN method and the FBP method attenuation curves are closer to the true attenuation curve at low energies than the PWLS and PWLS+EIGEN curves for most regions of iodine. This means that FBP accurately samples the original attenuation curve. The EIGEN method is imposing just iodine onto a mixture of iodine and water, so this keeps more of the iodine shape to the curve. The PWLS is pulling the curves toward an average of all attenuation curves; at least half the curves are acrylic, so the PWLS will pull the iodine curve slightly down. The PWLS+EIGEN method applies the PWLS first which pulls the curve down a little before the EIGEN is applied. This pulling down of attenuation curves generally occurs at lower energies, so it does not have a strong impact on the estimated iodine concentrations (table 7.3).

The second interesting observation from the attenuation curves (figure 7.18) is the effect of iodine concentration on the iodine absorption edge. As the concentration decreases, the size of the iodine absorption edge also decreases. This is most apparent in the 1.88mg/ml concentration of iodine (figure 7.18, labeled fifth Iodine); an absorption edge still exists but it is very small. This means that it is possible to identify iodine contrast based on the absorption edge with an iodine concentration of 1.88mg/ml. It may be possible identify an even lower concentration of iodine if the x-ray flux was increased. This shows that even with the large amount of noise present in this experiment (figure 7.11) a very small concentration of iodine is identifiable.

7.4.2.2 Estimating the Concentration of Gold

The gold contrast phantom (figure 7.13) has multiple concentrations of gold in solution with water. The spatial distribution of estimated iodine concentration $\hat{\rho}_{j,gold}$ is shown for each reconstruction method in figure 7.19.

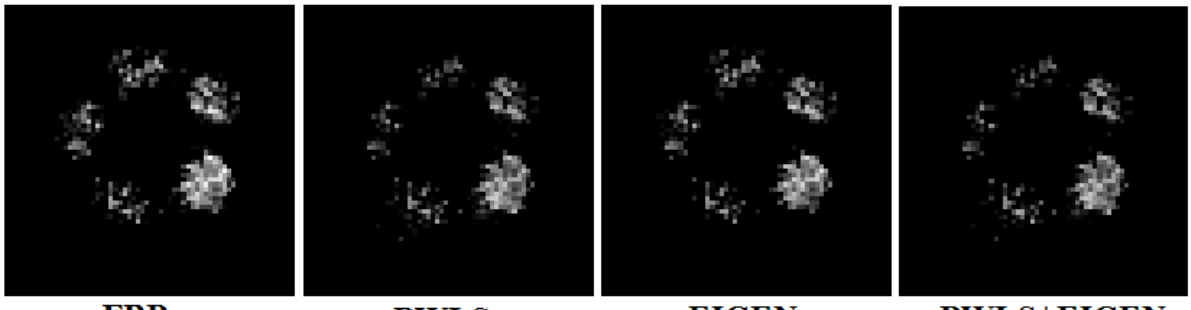

Figure 7.19: Spatial distribution of estimated iodine concentration of each method.

The gold concentration $\hat{\rho}_{j,gold}$ is estimated using the method described in section 7.3. The estimated concentration ρ_{jE} is averaged over the 10keV-20keV energy range. The general shape of the spatial distribution of estimated gold concentration follows the true distribution of gold concentration (figure 7.13). No additional segmentation has been applied to the distribution of gold concentrations; so figure 7.19 demonstrates that despite the remaining noise, the spatial distribution of estimated gold concentration clearly identifies regions of gold contrast agent. As the concentration decreases, these regions are less well defined, but still identifiable. The average estimated gold concentration for each region is shown plotted as a function of the true gold concentration in figure 7.20. The averaged estimate and the standard deviation for each region are given in table 7.5. For these values, the known distribution was used. Regions are labeled as: brightest region, in lower right hand corner labeled one and regions counted counter-clockwise from there following the general distribution of gold concentration (figure 7.13)).

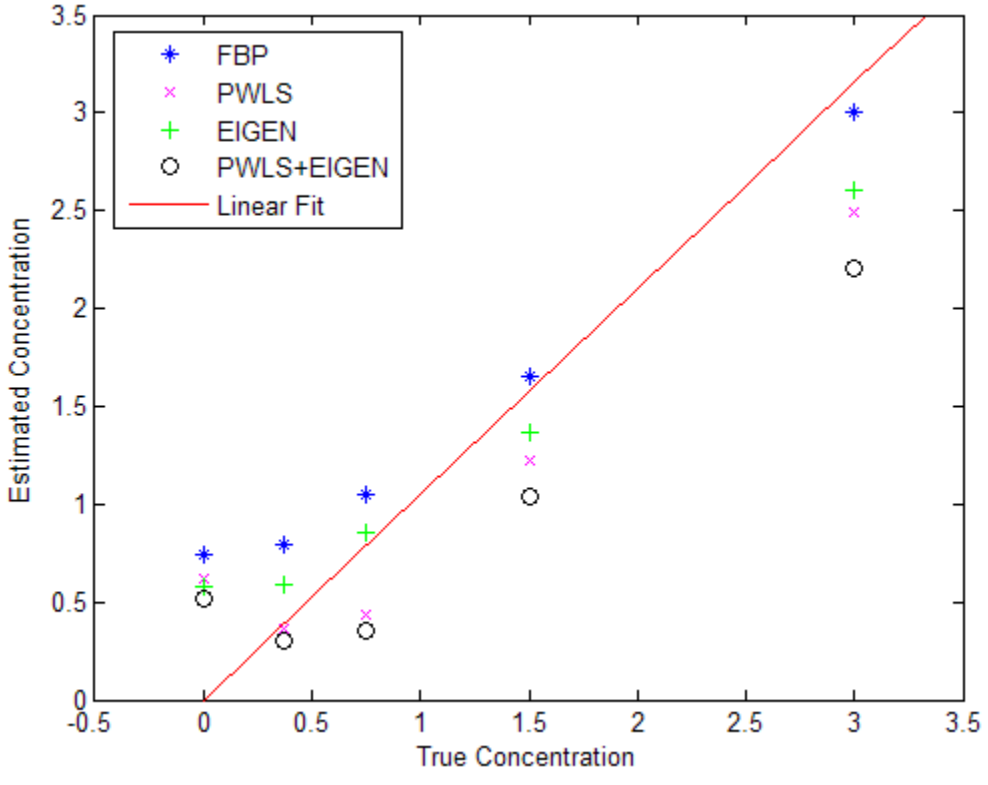

Figure 7.20. Average estimated gold concentration for each region for each method plotted as function of the true gold concentration.

Table 7.5: Average estimated gold concentration for each region in phantom.

Units (mg/ml)	Region 1	std 1	Region 2	std 2	Region 3	std 3	Region 4	Std 4
FBP	2.98	1.32	1.45	1.74	.66	1.62	0.33	1.61
PWLS	2.47	1.16	0.87	1.75	.84	1.83	0.52	1.54
EIGEN	2.55	1.32	1.09	1.73	.34	1.61	0.062	1.57
PWLS+EIGEN	2.37	1.18	0.81	1.74	0.88	1.83	0.57	1.55

The average estimated gold concentration plotted as function of true gold concentration (figure 7.20) is grouped along a line with slope one. The linear nature and grouping of the average estimate gold concentrations indicate that the system can accurately estimate very small concentrations of gold nanoparticles even in the presence of noise. We need an average to suppress this noise, but the averaged FBP gives the most accurate estimates. The standard

deviation for most of the regions is greater than the estimated concentration (table 7.5); due to the noise. The actual slope of the estimated concentration with respect to the true concentration is not actually one. A linear fit is applied to the data (shown as linear fit in figure 7.20) for reconstruction method. The slope of the fit for each method and the r-squared error of the data with respect to that fit are given in table 7.6. The fit uses a linear line with slope shown in table and crosses y-axis at zero. The r-squared measure of error is also shown for each method.

Table 7.6: Linear fit to each method's concentration estimate.

	FBP	PWLS	EIGEN	PWLS+EIGEN
Slope	1.051	0.798	0.800	0.770
R-squared	0.7737	0.905	0.957	0.854

The linear fit assumes a y-interest of zero because there should be a zero estimated concentration for zero true concentration. The lowest concentrations of gold are not accurately measured (see table 7.4). These inaccuracies distort the linear fit (table 7.6). This method is only measuring the first two concentrations. Below these two measurements, the noise is much larger, or standard deviation, is much larger then the estimate of concentration. However, the first two estimates of concentration are linear and have a slope very close to one for all methods.

To further investigate the accuracy of each reconstruction method, the average attenuation curves for each concentration of gold for each method are compared with the true attenuation curve in figure 7.21.

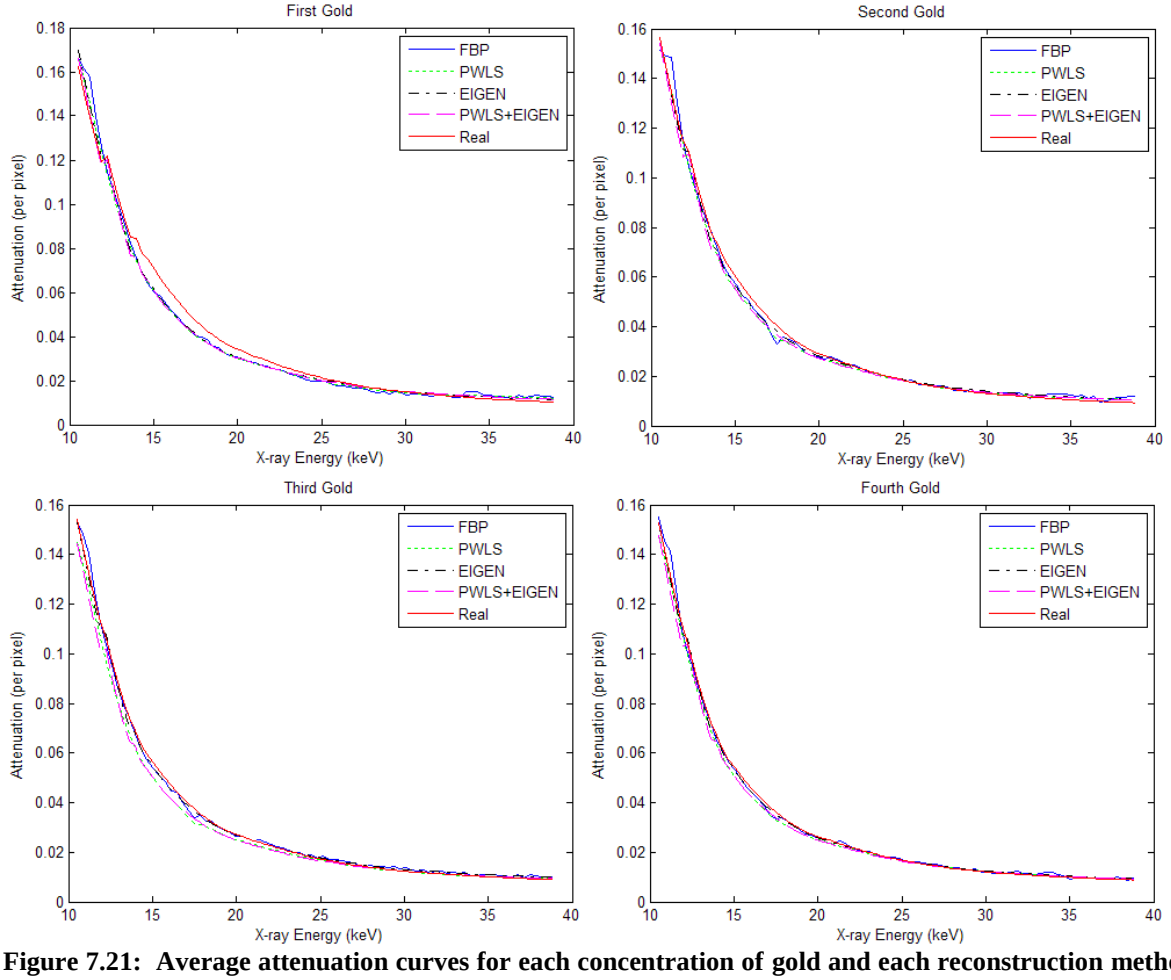

Figure 7.21: Average attenuation curves for each concentration of gold and each reconstruction method. True concentrations of each are: first gold: 3mg/ml, second gold: 1.5mg/ml, third gold: 0.75mg/ml, fourth gold: 0.375mg/ml.

The first important observation from the gold attenuation curves in figure 7.21 is the lack of large absorption edges. The very small concentrations of gold reduce the size of the ideal absorption edges; in fact the edges are only identifiable on the highest concentration gold (top left hand image figure 7.21). This makes it more challenging to accurately estimate the concentration of gold and may explain why the lower two concentrations are less accurately estimated (figure 7.20). If the energy limit of the system was increased to 100keV, another gold absorption edge (at 80keV) could be included; this absorption edge may be identified with lower concentrations of gold since it is a single large edge. The second

important observation from the gold attenuation curves is that all the curves for all reconstruction methods go below the true curve in the energy region between 15keV and 25keV. This is most apparent in the first gold curve (figure 7.21). This error is a byproduct of the water calibration, as the concentration of gold decreases, the estimated attenuation curves are more influenced by water and this error in the energy region between 15keV and 25keV decreases. The final observation from both the attenuation curves and estimated concentrations from FBP and EIGEN are slightly more accurate. An average estimate is used, the FBP is the measured data with no bias introduced in noise suppression, and the average suppresses the noise. The EIGEN method imposes the gold attenuation curve onto the data, so it will preserve the edges a little better, thus it yields a slightly more accurate concentration estimate; however, there is almost no apparent difference in average attenuation curves. The PWLS algorithm pulls the attenuation curves down a little, pulling the estimated concentrations down a little. This is most apparent for the lower concentrations of gold. The PWLS pulls the attenuation curves down a little because the PWLS is smoothing to an average attenuation curve. The PWLS+EIGEN method also pulls the estimates down a little because PWLS is applied first. Overall, the attenuation curves are accurately reconstructed for and the concentrations are accurately estimated for all concentrations of gold, although it is more accurate for higher concentrations. The estimate might be improved if the energy range was extended to include the next gold absorption edge at 80keV and/or the remaining noise was suppressed further.

7.4.3 Discussion of Multiple Concentrations of a single Contrast Agent

Two new experiments where conducted to investigate the accuracy of estimating a contrast agent's concentration based on the shape of the attenuation curve reconstructed

using a densely sampled x-ray spectrum. These experiments used multiple concentrations of two contrast agents in solution with deionized water in a simple contrast phantom. In both experiments, the phantom was imaged using the new x-ray source (section 3.3); this new source has not been fully optimized and was operated with a low x-ray flux, which increased the noise in the estimated attenuation. Despite the noise, it is possible to estimate the concentration of the contrast agents fairly accurately, as demonstrated by the average estimated concentrations plotted as a function of the true concentrations (figures 7.17 and 7.20).

The most accurate estimation of contrast concentrations came from the initial FBP. The estimate is based on an average over a large number of energy bins, so the noise along the energy axis has less of an affect. Only one contrast agent was used for each experiment, so being able to identify the attenuation curves prior to the estimation is less important. The noise suppression methods introduce a small bias, which has a small but noticeable affect on the estimation of concentration. However, if the distribution of contrast agent is not known, the FBP will return the worst estimate. Even if there is no second contrast agent, it is still necessary to know which attenuation curves to average to return an accurate average estimated concentration. If the distribution is not known, the concentration must be estimated along each individual attenuation curve, which makes the estimations more susceptible to noise; as is demonstrated in the standard deviation in tables 7.3 and 7.4.

The second most accurate estimation of contrast concentration seems to be generated by the EIGEN method. The fact that EIGEN imposes absorption edges onto the attenuation curves seems yield a better estimate, especially in regions where there is a lower concentration of contrast agent. This makes sense because EIGEN is specifically looking for

contrast agent. Previously, it seemed that by imposing absorption edges onto the attenuation curves, EIGEN was preserving more of the noise in the attenuation curves. However, this noise does not seem to affect the estimation of concentration. This may be because the estimation is based on both the existence of the edges and the overall shape of the curve.

The least accurate estimation of contrast concentration seems to be from the PWLS and PWLS+EIGEN methods. This seems to be due to the fact that the PWLS smoothes all attenuation curves to a single average attenuation curve. The WLS portion prevents this from introducing a significant bias into the attenuation curves. Until the concentration was estimated this bias was not noticeable. The PWLS+EIGEN method is also affected by this bias because it is introduced in the PWLS.

These two experiments demonstrate that using attenuation reconstructions based on a densely sampled x-ray spectrum it is possible to accurately estimate the specific concentration of a contrast agent in an imaged object. This is shown both as a distribution of the contrast concentrations (figures 7.16 and 7.19) and as average attenuation curves compared with the attenuation curve using the known concentrations (figures 7.18 and 7.21). This is a represents significant step toward functional x-ray CT, allowing a clinician to not only identify the distribution of a contrast agent, but also the distribution of concentration of the contrast agent. The average FBP estimates demonstrates this data exists in the original projections and that if noise is sufficiently suppressed very small concentrations of contrast agents can be identified. Although the noise suppression algorithms introduce some bias into the estimations, both algorithms fairly accurately estimate the distribution of contrast concentration and while suppressing the noise. This means that the additional noise

introduced by a dense sampling of the incident x-ray spectrum is accounting for without suppressing the usefully energy axis information.

7.5 Impact of Energy Resolution

This chapter has focused on the accuracy of the reconstructed attenuation curves and estimated the concentrations of contrast agents. The curves and estimated concentrations are based on the densely sampled x-ray projections. The first experiment had an anode voltage of 45kV and the spectrum was sampled with 95 energy bins. The second two experiments (with multiple contrast agents) had anode voltages of 40kV and the spectra were sample with 82 energy bins. Current x-ray detectors are incapable of sampling the energy axis this densely (Bazalova and Verhaegen, 2007). In this section, we look at how different number of energy bins affects the accuracy of the reconstructed attenuation curves and the estimation of the concentration of contrast agents.

7.5.1 How Different Number of Energy Bins Are Defined

The first step is to resample the energy axis. The original x-ray projection data consists of either 95 or 82 energy bins. The intensity in each energy bin corresponded to a photon count over a period of five seconds using the AMPTEK photon counting detector. To resample the energy axis, we assume a photon counting detector with some number N of energy bins. This allows us to simply re-bin the x-ray projection data into N energy bins. This is done for $N = [2,4,6,8,10,15,20,40]$ re-sampled energy bins. We based all of the re-sampling on the 82 energy bins because there is no significant contribution to any attenuation curve above 40keV. The re-sampled energy bins are defined according to table 7.5. # Energy bins is N re-sampled size, Bin Width is the energy range represented by each re-sampled bin, and Group Size is the number of original energy bins grouped to make the re-sampled bin.

Table 7.7: Re-sampling of energy bins.

# Energy Bins	Bin Width	Group Size
82	0.35 keV	1
40	0.7 keV	2
20	1.4 keV	4
15	1.75/2.1keV	5/6 (alternating)
10	2.8 keV	8
8	3.5 keV	10
6	4.55/4.9 keV	13/14 (alternating)
4	7keV	20
2	14kev	40

7.5.2 FBP reconstructions of Different Energy Resolutions

The FBP reconstructions of the first five re-sampled x-ray projections $N = [2,4,6,8,10]$ are shown for all energy bins in figure 7.22.

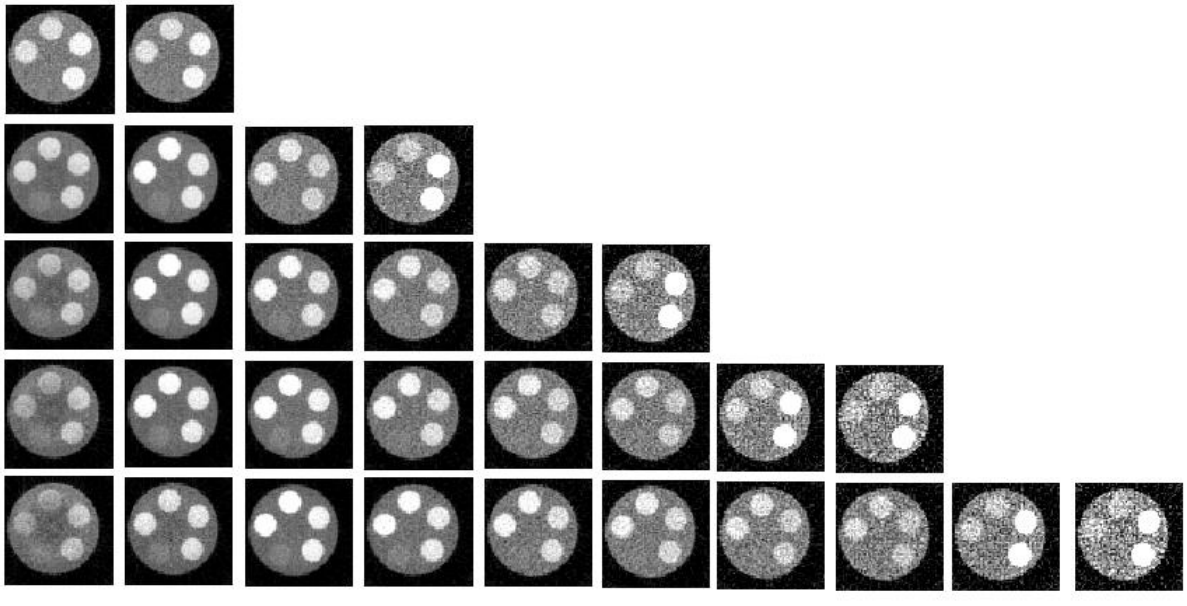

Figure 7.22 FBP attenuation map reconstructions for re-sampled x-ray projections for original phantom. X-rays are re-sampled into $N = [2, 4, 6, 8, 10]$ energy bins. Attenuation Maps are shown for all energy bins.

The first two FBP attenuation map reconstructions are for $N = 2$, this represents the broadest energy range (table 7.5). There is very little noise in these two images; increasing the photon

count has reduced the noise. However, these two images also appear almost identical, there is almost no variation along the energy axis; this is most apparent in the lack of any iodine absorption edge; the iodine regions have similar brightness. Increasing the number of energy bins from $N = 2$ to $N = 4$ increases the noise in the fourth energy reconstruction but also recovers a little of the energy axis information. The iodine in the fourth energy reconstruction is brighter than the third energy reconstruction in the $N = 4$ row. This indicates the absorption edge is preserved with four energy bins. Increasing from $N = 4$ to $N = 6$ energy bins introduces more noise in the fifth and sixth energy bin reconstructions, but now some of both the gold and iodine absorption edges are preserved. The final iodine is brighter than the fourth and fifth iodine reconstructions in the $N = 6$ row and the second gold is brighter than the first gold in the same row. Increasing energy sampling to $N = 8$ and then $N = 10$ continues this same pattern, noise continues to be affect the higher energy bins but absorption edges become more clear. To more accurately investigate the affect of energy resolution, the FBP reconstructed attenuation curves for $N = [2,4,6,8,10,15,20,40]$ are shown in figure 7.23 for each material in the phantom.

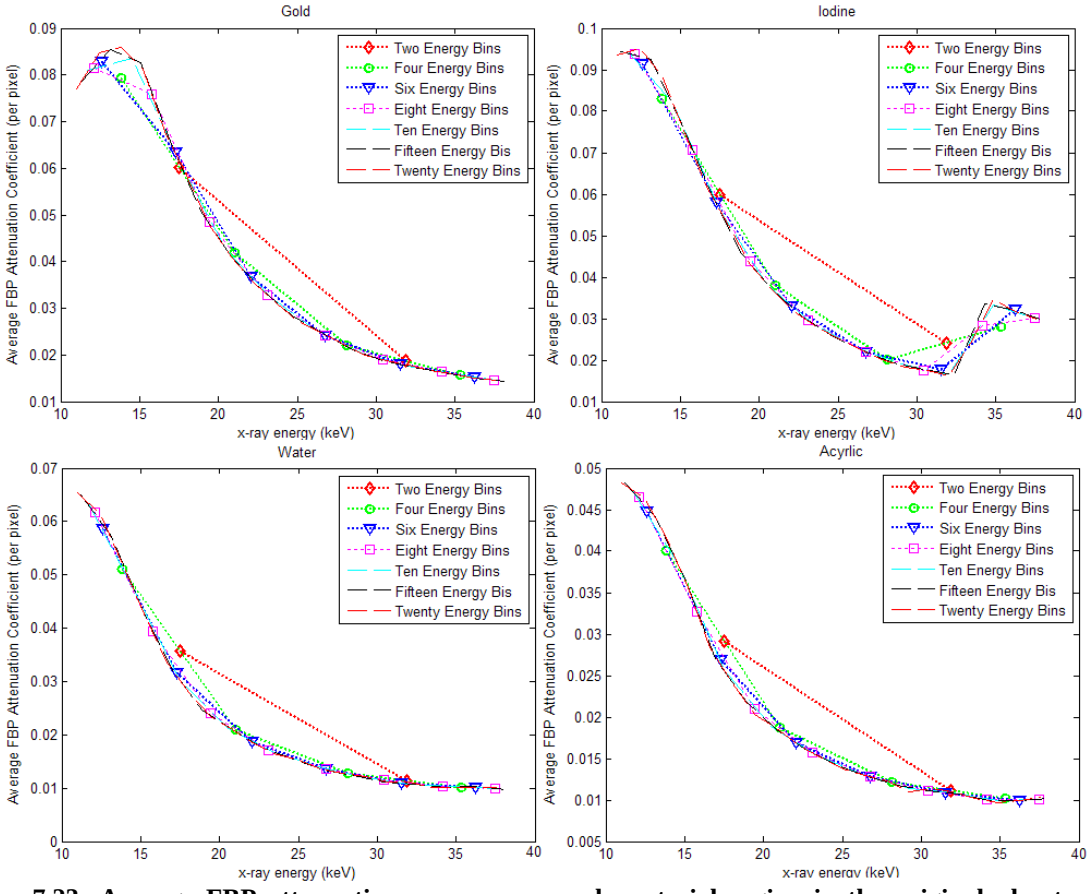

Figure 7.23: Average FBP attenuation curves over each material region in the original phantom for different energy resolutions. The attenuation for each energy bin is shown as the average energy in the bin.

The attenuation curves for the first four re-sample sizes, $N = [2,4,6,8]$, are plotted with markers because there is an insufficient amount of data to represent the points as a curve. The markers indicate that all estimations lie on, or very near, the same true attenuation curve. The lines connecting the markers demonstrate an estimated attenuation curve based on the limited energy samples. These curves become more accurate as the number of energy bins increase. The first energy sample ($N = 2$) does not capture any significant energy-axis information; specifically the absorption edges. The $N = 4$ sampled energy curve captures a little of the iodine absorption edge, the fourth marker has a greater attenuation than the third marker in the iodine image. However, it takes $N = 10$ energy samples to capture the gold absorption

edges; none of the energy samples smaller than $N = 10$ show any increase in the second gold energy sample, which we used to indicate an average of the gold absorption edges. Increasing to $N = 15$ and $N = 20$ improve the overall accuracy and detail in the reconstructed attenuation curves. However, these are small incremental improvements. Most of the relevant data in the attenuation curves are captured in $N = 10$ energy bins. This relevant data includes the location of the iodine absorption edge, a general increase in the gold curve around the gold edges, and the general overall shape of the individual curves. This means that with ten energy bins (in this energy range) it is possible to clearly separate and identify the two contrast agents based on their shape.

7.5.3 Estimated Concentrations for Different Energy Resolutions

The reconstructed FBP attenuation curves from the original phantom indicate that basic information about each material's attenuation curve is preserved in ten energy bins and subsequent energy bins only provide finer detail about the absorption edges and overall shape of the attenuation curves (figure 7.23). It was shown in the two experiments using a single contrast agent with multiple concentrations (Section 7.4) that these finer details are important in generating an accurate concentration estimate; a small bias introduced by PWLS created a noticeable change in this estimate. To investigate affect of energy resolution on the estimation of concentration, the two single contrast agent experiments where re-sampled in the same way as the original phantom was previously re-sampled (table 7.4) and the contrast concentration for each was estimated. The mass-attenuation curves used to estimate the concentrations (Section 7.3) are the known mass-attenuation (from the NIST database) re-sampled at the center of energy bin.

The spatial distributions of the estimated iodine concentrations (section 7.4.2.1) for different number re-sampled energy bins are shown in figure 7.24.

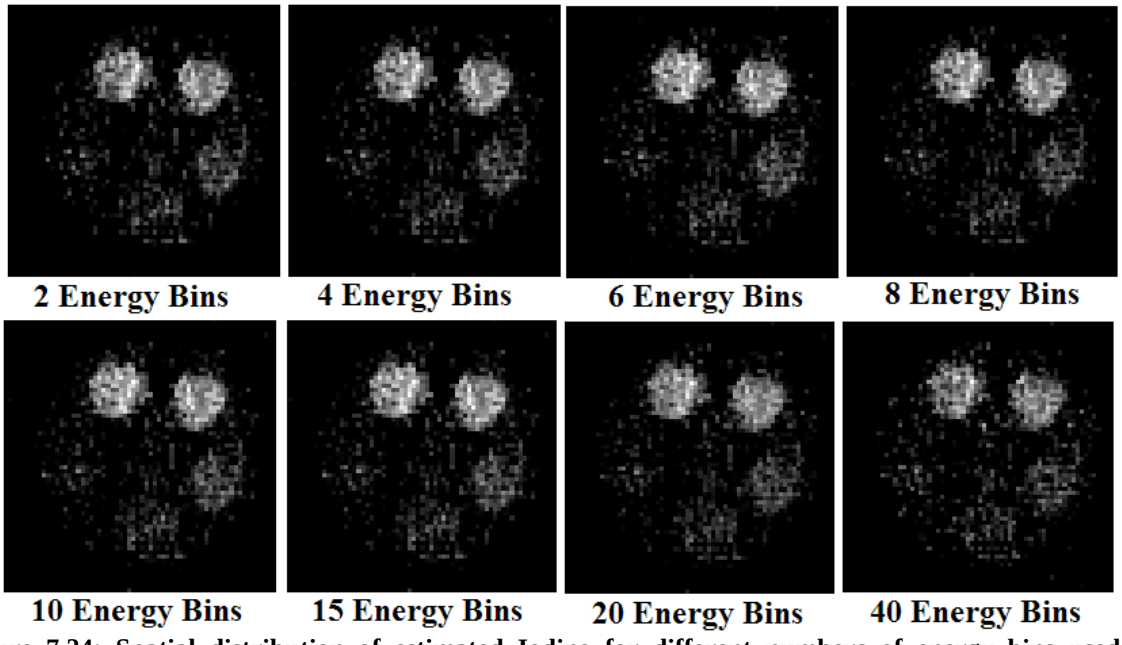

Figure 7.24: Spatial distribution of estimated Iodine for different numbers of energy bins used to resample the energy axis.

The spatial distribution of iodine seems to indicate that only two energy bins are necessary to create an accurate estimate of the concentration. The distributions all look remarkable similar. The spatial distribution of iodine is less noisy and segments the images better than any of the original fully sampled iodine distributions (figure 7.16). Re-sampling the energy axis significantly reduces the noise along the energy axis due to the increased photon counts. There is only one contrast agent in this image and the other materials are just water and acrylic which both have less attenuation than iodine at all of the energies in the energy range. Therefore, the estimated concentration easily identifies the location of iodine. However, the average estimate in each hole will change as the number of energy bins is increased. The average estimated concentration in each hole (numbered the same way as

figure 7.16) is shown plotted as a function of the number of re-sampled energy bins in figure 7.25.

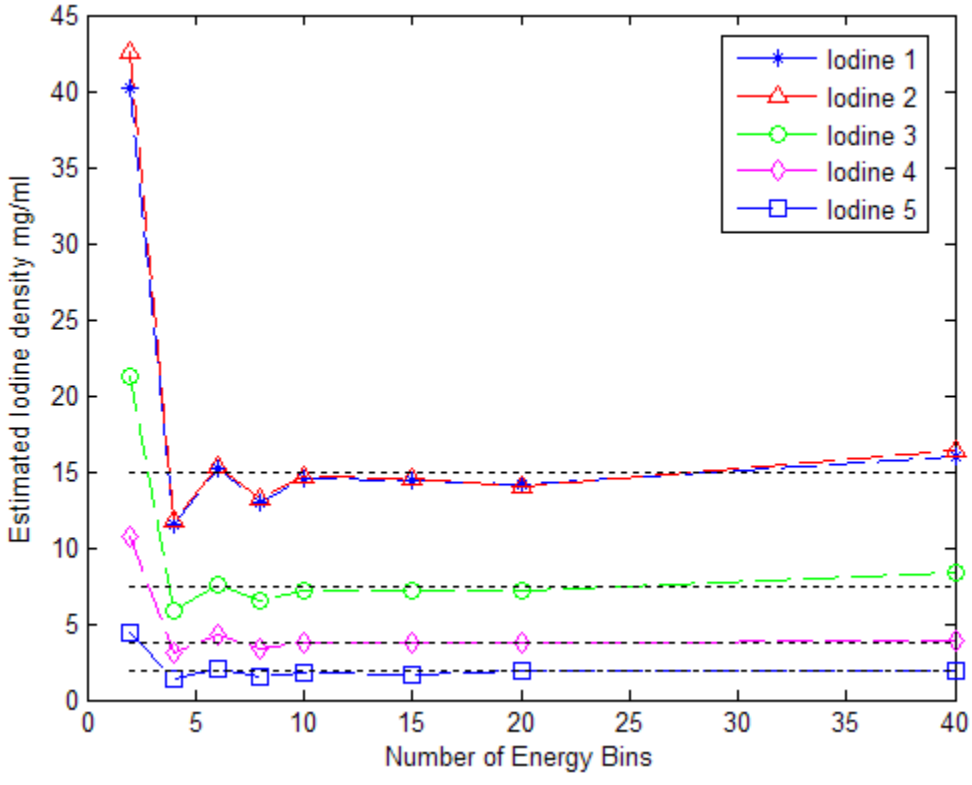

Figure 7.25 Estimated Iodine concentration plotted as function of re-sampled energy bins. Dotted lines indicate the true concentrations.

The average estimated iodine concentration for each contrast region changes in the same way for each number of re-sampled energy bins. The estimated concentration starts high then goes low and then settles near the true value. It only takes $N = 10$ energy bins to get an estimate which is close to the true concentration (shown as dotted lines) and after $N = 10$ there is very little change in the estimated concentration. This means that the attenuation curves were well sampled with $N = 10$ and subsequent energy bins only added small details.

The spatial distribution of the estimated gold concentrations (section 7.4.2.2) for different number re-sampling energy bins not shown because the results are similar to iodine

(figure 7.24). The gold distributions look like (figure 7.20). The estimated gold concentration for each contrast region in the phantom (figure 7.15) is shown as a function the number of re-sampled energy bins in figure 7.26.

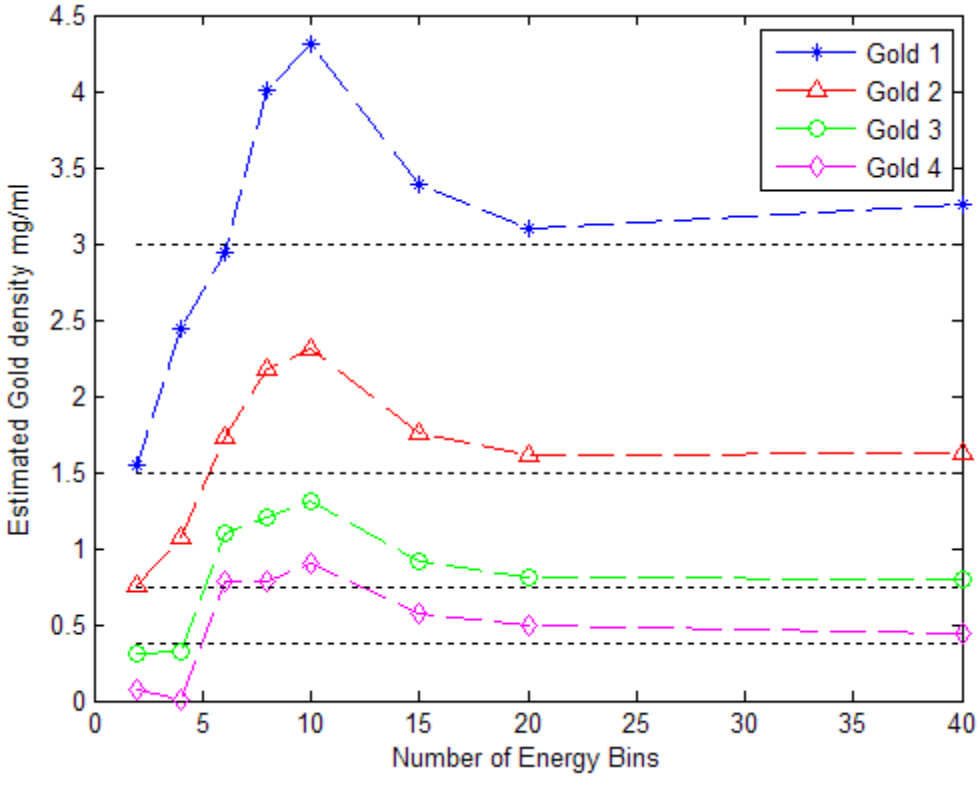

Figure 7.26 Estimated gold densities plotted as function of re-sampled energy bins. Dotted lines demonstrate the true concentrations.

The estimated concentration of gold in starts low at $N = 2$ energy bins for all regions of gold (figure 7.26). The key information in the gold attenuation curves is at low energies; the attenuation at these energies is not fully measured due to insufficient x-ray flux (figure 7.4). It was shown in (figure 7.5) that calibrating the attenuation curve to the ideal water attenuation curve recovers this low energy attenuation. However, it is more difficult to calibrate the curves if the curve is not accurately sample (N is small). As the number of samples increases, the estimated gold concentration increases because the low energy x-rays

are more accurately sampled. Iodine only requires $N = 10$ energy bins to create a fairly accurate estimate the concentration (figure 7.25) but gold seems to require $N = 20$ energy bins; there is a lot of change between $N = 2 - 20$ energy bins but very little change between $N = 20$ and $N = 40$ energy bins. This is due to the need to accurately sample both the gold attenuation curve and the water attenuation curve. If the anode voltage was increased to be greater than 90keV, the gold could be identified based on the gold absorption edge at 80keV. Identifying the concentration of an element based a single large absorption edge seems to require few energy bins based on comparing iodine and gold (figures 7.25 and 7.26 respectively).

The projections from the original two contrast agent phantom (figure 4.4) were re-sampled according to (table 7.5). The spatial distribution of estimated iodine is shown for the re-sampled FBP reconstructions in figure 7.27.

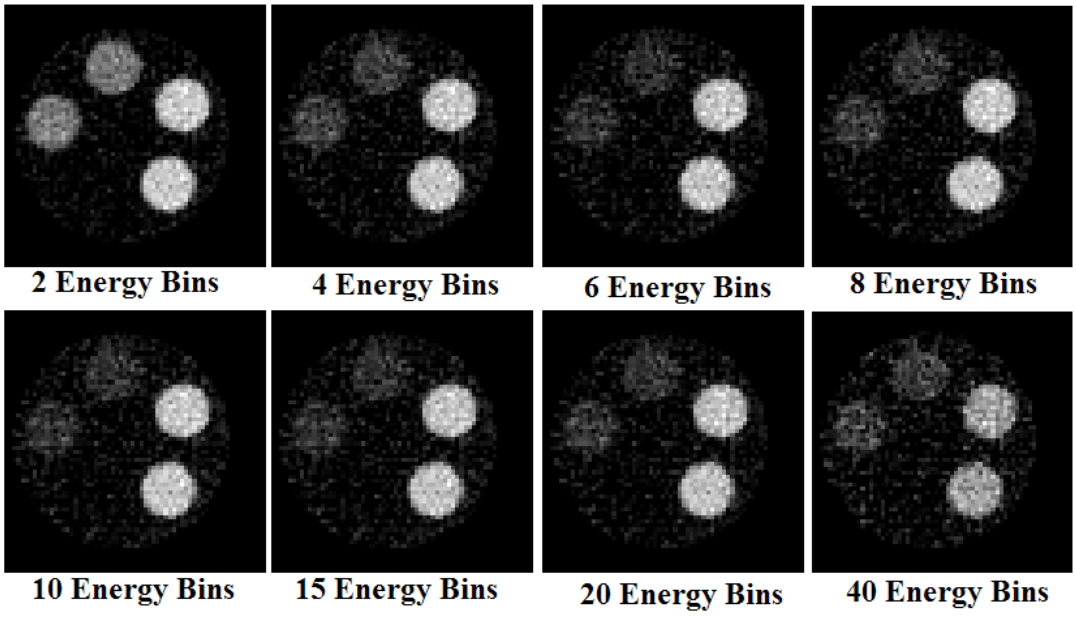

Figure 7.27: Spatial distribution of estimated Iodine for different numbers of energy bins used to resample the energy axis. Original two contrast agent phantom with gold and iodine (figure 4.4).

In (figure 7.9) we demonstrated that estimating the iodine concentration over an energy range from 33-40keV separated the iodine from the gold because the iodine absorption edge is well preserved. We repeat the same process in (figure 7.27) looking at the estimated iodine concentration in energy bins above 33keV. The number of energy bins above 33keV will depend on the density of the sampling. The N=2 energy sample's second sample was centered at: 31.8keV so is actually below the absorption edge; this is why there is less separation between estimated iodine in the gold and iodine regions. The rest of the energy samples $N = [4 - 40]$ are able to separate the iodine because the iodine edge is preserved, as was shown in the attenuation curves (figure 7.23). The estimated gold and iodine concentrations for the original contrast phantom (figure 4.4) are plotted as a function of the number of energy bins in the re-sampled spectrum in figure 7.28.

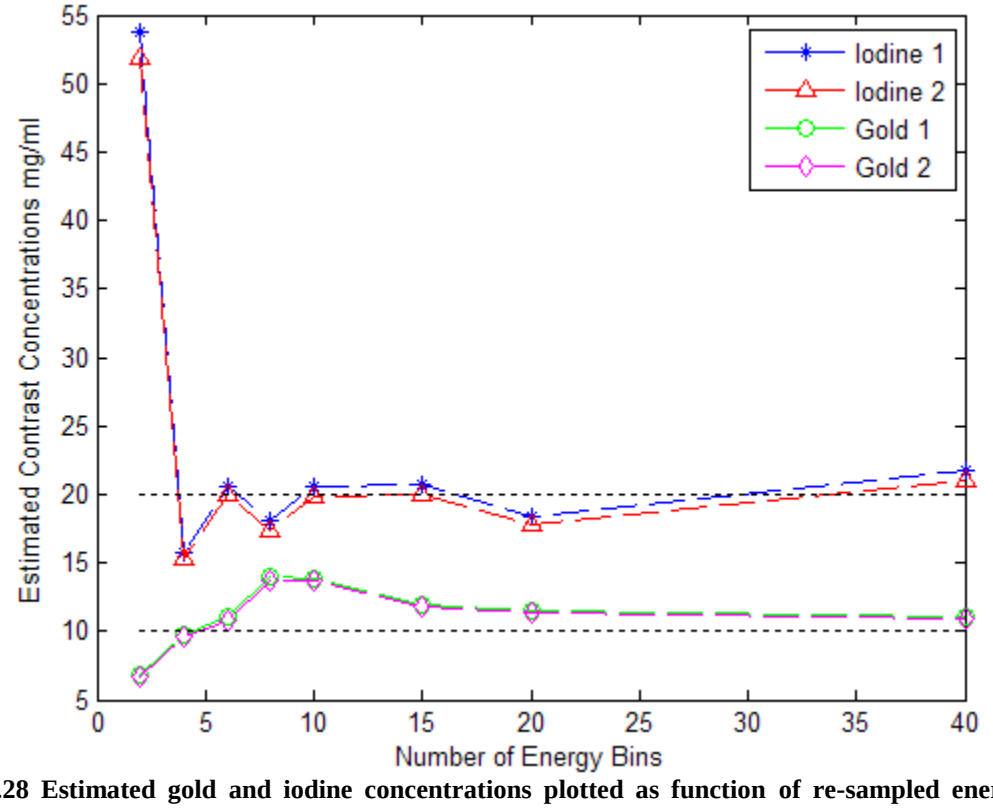

Figure 7.28 Estimated gold and iodine concentrations plotted as function of re-sampled energy bins. Dotted lines demonstrate the true concentrations.

The average estimated concentration for each of the regions is based on prior knowledge of the distribution of the contrast agents (figure 4.4). The shape of the estimated density of both iodine and gold with respect to the number of sampled energy bins is the same shape as individually sampled iodine and gold (figures 7.25 and 7.27 respectively). This demonstrates the consistency between the individual contrast measurements and the two contrast agent measurement.

7.5.4 Re-sampled EIGEN Reconstructions

Thus far, re-sampling the energy axis has only been applied for FBP reconstructions. In this section we investigate applying the EIGEN noise suppression method (chapter 5) to the re-sampled two contrast agent data. The EIGEN uses the re-sampled FBP attenuation maps (figure 7.22) as the input and the re-sampled mass-attenuation curves as the input to the basis functions. The EIGEN requires at least $N = 4$ energy samples to create four basis functions for the four materials in the imaged object. The $N = 4$ re-sampled mass-attenuation curves, corresponding basis functions, and the spatial distribution of the basis functions are shown in figure 7.29.

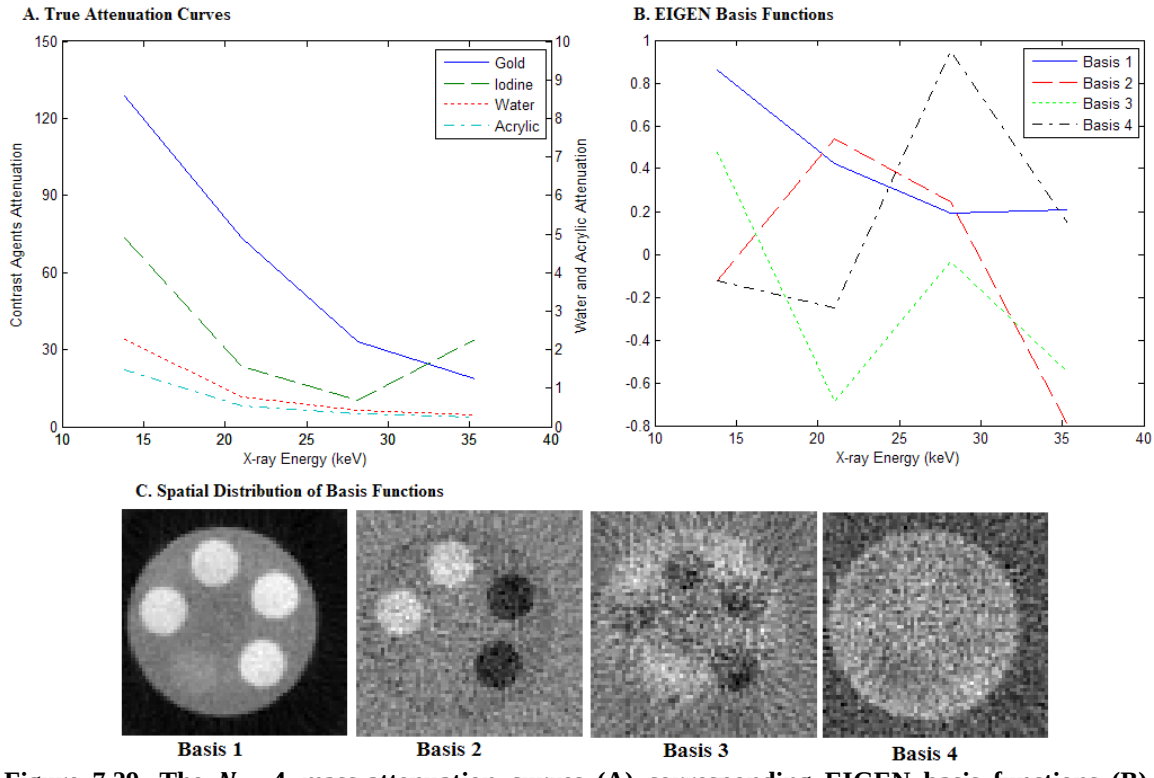

Figure 7.29. The $N = 4$ mass-attenuation curves (A) corresponding EIGEN basis functions (B) and spatial distribution of basis functions (C) from two contrast agent phantom.

The $N = 4$ mass-attenuation curves show an increase in iodine and gold is higher in general; this follows the sampled attenuation curves (figure 7.23). The $N = 4$ EIGEN basis functions are much harder to interpret than the fully-sampled attenuation curves (figure 5.6.B). Basis 1 seems to be an average. The rest are harder to interpret. The spatial distributions of basis functions are particularly interesting. The fist is an average, but the second two actually appear to segment the image a little. This is a surprising result for only $N = 4$ energy samples and indicates the EIGEN can be used to both suppress the noise and segment the image with as a little as four energy samples for four materials. The attenuation curves (figure 7.23) show that $N = 10$ accurately recovers most of the shape of the attenuation curves. We apply the EIGEN method to the $N = 10$ re-sampled attenuation maps (figure 7.30).

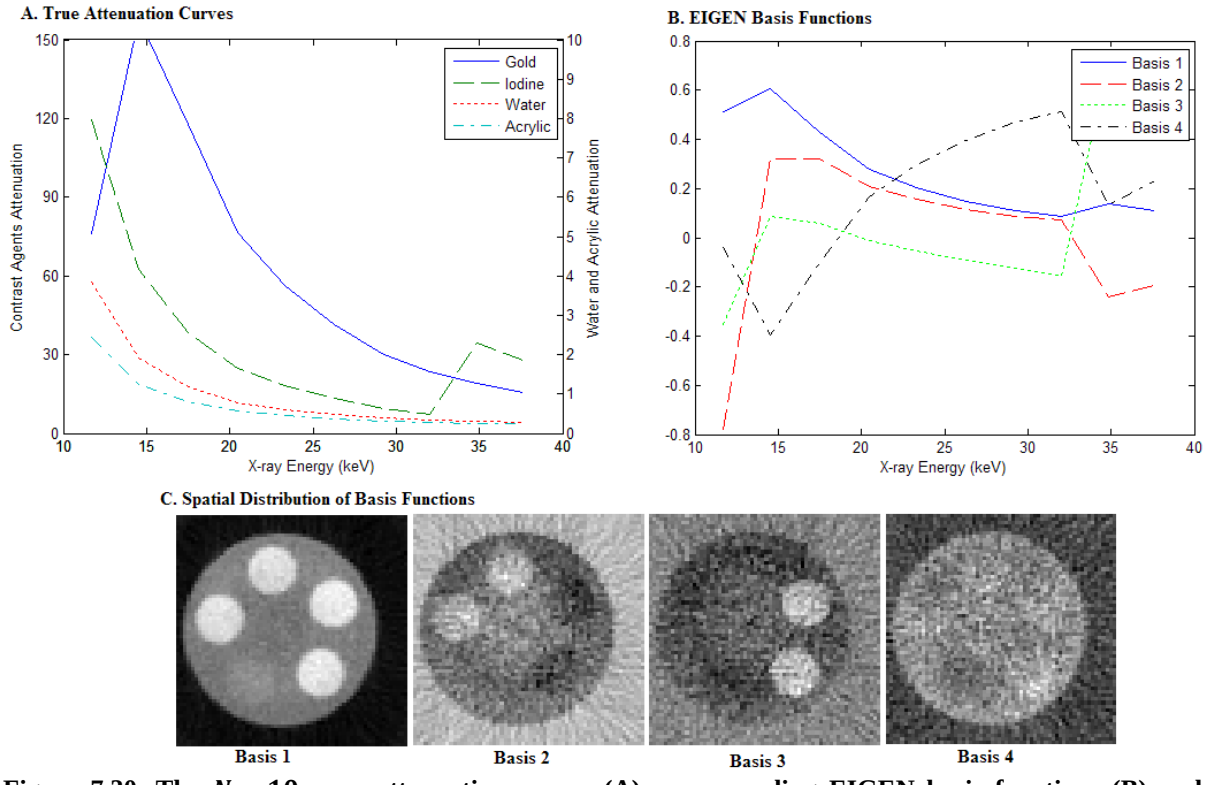

Figure 7.30. The $N = 10$ mass-attenuation curves (A) corresponding EIGEN basis functions (B) and spatial distribution of basis functions (C) from two contrast agent phantom.

The $N = 10$ mass attenuation curves now look like the attenuation curves we are used to seeing. The $N = 10$ basis functions are also much easier to interpret. The first basis function is an average of all attenuation curves. The second basis function is more gold and less iodine. The third basis function is more iodine and less gold. The final basis function is neither gold nor iodine. The spatial distributions of these basis functions now look very similar to the spatial distribution of the fully sampled basis functions (figure 5.6.C). The iodine and gold are separated in the spatial distribution of basis functions. This confirms the attenuation curves are accurately sampled with $N = 10$ for the energy range 10-45keV.

The EIGEN method is applied to every re-sample size $N = [4,6,8,10,15,20,40]$. The estimated contrast concentrations, after EIGEN has been applied, are shown plotted as a function of the number of energy samples in figure 7.31.

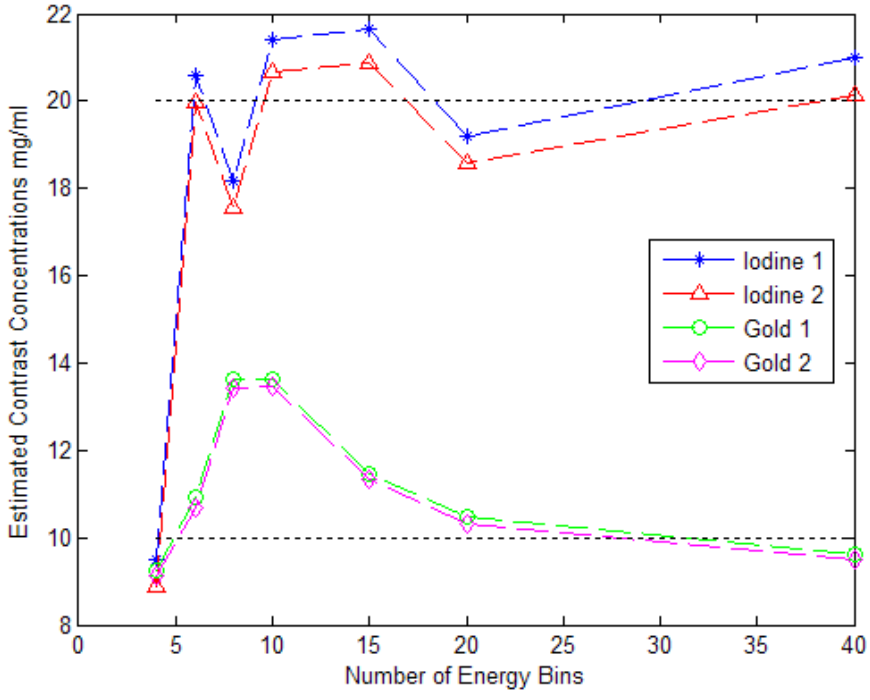

Figure 7.31. Estimated gold and iodine concentrations plotted as function of re-sampled energy bins. This is after the EIGEN method has been applied to the re-sampled data. Dotted lines demonstrate the true concentrations.

There is an odd iodine estimation at $N = 4$ which seems to indicate that more than four energy bins are required to accurately estimate the iodine concentration even though the iodine was identified by the EIGEN basis functions for $N = 4$ energy bins (figure 7.29). Other than this initial low iodine estimate, the general shape of the gold and iodine estimated concentrations with respect to the number of energy samples in figure 7.31 is very similar to the shapes of the FBP estimated concentrations (figures 7.25, 7.26, and 7.28). This is similar to the results shown in tables 7.1, 7.2, 7.3, and 7.4, where the estimation of contrast concentration is not very different between the average FBP and the average EIGEN. This indicates that the EIGEN method preserves the attenuation curves for most energy samples sizes.

7.5.5. Discussion of Re-sampled Energy Bins

The new x-ray CT system presented in this dissertation is capable of densely sampling the projected x-ray spectrum. This is done with a single pixel photon-counting detector which is not practical for a clinical CT. However, new photon-count strip detectors which are capable of binning the projected spectrum into as many as six energy bins have been developed (Medipix). Therefore, we investigated the affect of re-sampling the projected spectrum with different number of photon counting energy bins, N for $N = [2,4,6,8,10,15,20,40]$ energy bins. The sample sizes $N = [2,4,6]$ represent energy sampling currently achievable using the new photon counting strip detectors (Paulus *et. al*, 1998). The next two sample sizes after this, $N = 8$ and $N = 10$, represent potential future steps in x-ray detector development. The final three energy sample sizes, $N = 15$, $N = 20$, and $N = 40$, are included to demonstrate the impact of increasing number of energy bins.

The x-ray projections through the first original object (figure 4.4) were re-sampled and then reconstructed using FBP (figure 7.22). The FBP attenuation maps show that as the number of energy bins increases, the noise along the energy axis increases but the energy resolution also improves. As the number of energy bins increases, the sampling begins to recover the variance along the energy axis; this is seen as a recovery of both the gold and iodine absorption edges in the attenuation maps (indicated by increase in attenuation). It is difficult to see anything more than a subtle variation in attenuation and an increase in noise due to increasing the energy bins in the attenuation maps. To more carefully investigate the impact of number of energy bins on the energy axis the attenuation curves are studied.

The attenuation curves for each material in the original contrast phantom (figure 7.23) show a significant change as the number of energy bins is increased. As the number of

energy samples increases, the curves become more accurate, including the more of the full shape of the curve and the location of the absorption edges. This shape is important in identifying and quantifying the materials in an imaged object. The shape is also important in calibrating the reconstruction to the ideal water attenuation curve, which significantly improves the estimation of contrast concentration (figure 7.9). At least ten energy bins are required to preserve the shape of the attenuation curve for the contrast agents. The accuracy of the curve is improved a little as the energy sampling increases beyond $N = 10$, but most of the information is preserved with ten energy bins. It should be noted that the energy range in this experiment is 10keV-45keV and this range is represented with ten energy bins. If the range was significantly increased, say to 80keV or 100keV, ten energy bins would not accurately represent the entire energy spectrum. It is the density of the sampling rather than the specific number of energy samples which is necessary to preserve the specific shape of the attenuation curves. To achieve the same density of sampling for an x-ray spectrum distributed between 10keV and 80keV at least 20 energy bins are required.

The energy range for each bin, the number of energy samples in each re-sampled energy bin, is the same for each re-sampled energy bin. However, this does not have to be the case. As the energy-range increases, the noise in the bin decreases because the total photon count increases. The size of the energy bins could have been varied a little to make the high noise regions represented by more energy bins and the lower noise regions by fewer. The energy resolution is most significant near absorption edges. The size of the energy bins could also have been changed to make more of the energy bins near the known absorption edges. The energy bins' energy range are kept consistent to make measurements and comparisons

more simple. Future work could be done to investigate the optimization of the energy ranges for each number of energy bins.

One of the unique advantages of dense spectral sampling is estimating the specific density or concentration of a material in the imaged object. This has been shown for two contrast agents at the same time (section7.3.1) and for multiple concentrations of a single contrast agent (sections 7.3.2 and 7.3.3). It is important to see how the different number of energy bins affects the accuracy of the estimated concentration (figures 7.25, 7.26, and 7.29). The specific estimated concentration for each number of energy bins is based on an average over a specified region-of-interest corresponding to the known distribution of the contrast agents. Iodine (figure 7.24) only requires ten energy bins to accurately estimate the concentration. This is because the iodine absorption edge is well preserved with ten energy bins. Gold (figure 7.25) requires twenty energy bins to accurately estimate the concentration. This is because the gold absorption edges exist in a region where the attenuation is poorly estimated due to a lack of sufficient x-ray flux and the lower concentration of gold in the object. The full shape of the gold attenuation curve is more important because gold does not have a single large absorption edge. However, at ten energy bins, the difference between each gold region is preserved demonstrating an ability to identify different regions of gold contrast with only ten energy bins.

The re-sampled energy spectrum is reconstructed using both FPB and EIGEN. There is no a significant differences between the two method's estimated contrast concentrations after $N = 6$ energy bins (figure 7.31). The similarity in an average estimated concentration between FBP and EIGEN is demonstrated in (Tables 7.1, 7.2, 7.3, and 7.4). However, the EIGEN method begins to automatically segment the image at $N = 4$ (figure 7.29) and at

$N = 10$ has a basis function segmentation that is similar to the full $N = 93$ basis functions (figure 5.6). The estimated concentrations are all based on an average over a known distribution. If the distribution is known, the basis function segmentation provided by EIGEN may help create a more accurate estimate to the contrast agent concentrations.

Overall, only ten energy bins are required to estimate the attenuation curve and concentration for the two contrast agents if the energy range is 10keV-45keV. This provides a rough estimate of the attenuation curve but it preserves the important details. Increasing the number of energy bins beyond this preserves more the fine detail in the curves but also the increases the noise along the curves. The estimated concentrations for both contrast agents are close to their true concentrations at ten energy bins; these estimates continue to improve a little as the number increases. More work is required to see how this number will change if the anode voltage is increased. It seems likely that it is the density of energy bins more than the specific number which is the important factor for both accurate recovery of the attenuation curves and estimates of the contrast concentrations.

7.6 References

AMPTEK detector XR-100CT, product information available at: http://www.amptek.com/xr100cr.html

Bazalova M. and Verhaegen F., 2007, "Monte Carlo simulation of computed tomography X-ray tube," Phys. Med. Biol., vol. 52, pp. 5945-5955.

Hubbell J.H. and Seltzer S.M., 1996, Tables of X-Ray Mass Attenuation Coefficients and Mass Energy-Absorption Coefficients from 1 keVto 20 MeV for Elements Z = 1 to 92 and 48 Additional Substances of Dosimetric Interest, National Institute of Standards and Technology, Tech. Rep. 43NANB412756 Available: http://www.physics.nist.gov/PhysRefData/XrayMassCoef/cover.html

Medipix™ a Collaboration effort in photon counting detector development, information available at: http://medipix.web.cern.ch/medipix/index.php

Paulus M., Sari-Sarraf H., Gleason S., Behel J., Thompson L. and Allen W., 1998, “A new X-ray computed tomography system for laboratory mouse imaging,” IEEE Trans. Nuclear Science, vol. 2, pp. 1259-1263.

Rebuffel V. and Dinten J.M., 2007, “Dual Energy X-ray imaging: benefits and limits,” Insight, vol 49, no. 10.

Visipaque™ (iodixanol), A GE Product, Information available: ttp://md.gehealthcare.com/visipaque/

8. MOUSE KIDNEY

The final experiment using the novel energy-sensitive x-ray CT system presented in this dissertation imaged a mouse kidney which had been injected with gold nanoparticles. This is the first imaged object with an unknown distribution of elements or compounds studied on this system. Two mouse kidneys were imaged. The first was fixed in an epoxy setting and the second was set in a small sealed plastic test tube. The kidneys were prepared by Michael Altenburg (Department of Pathology at UNC Chapel Hill). The mouse was anaesthetized and the abdomen opened. Gold nanoparticles were injected into the superior mesenteric artery. After ten minutes the kidneys are removed from the mouse, washed, and fixed in epoxy or placed in a small test tube. We have previously demonstrated (in chapters 6 and 7) that we can identify gold nanoparticles based on the shape of the reconstructed attenuation curves. This was for known distributions of gold; the purpose of this experiment is to demonstrate the ability to identify the gold nanoparticles with an unknown distribution.

The mouse kidneys were imaged using a 40kV anode voltage and a 1700V gate voltage. The gate voltage was applied with a 40Hz pulse which had a 50% duty cycle to preserve the carbon nanotube sources. A 2000V voltage was applied to both of the focusing elements. These setting resulted in a low, but measurable, x-ray flux. The molybdenum anode was used to incorporate the two low energy characteristic peaks (figure 3.7) with the hope that this would increase the projection's SNR in the low energy region, where there are gold edges. The x-ray was run at low flux to prevent arcing or a charge from building in the vacuum chamber over the course of the experiment. This source has not been fully optimized, so there is some variance in the x-ray flux over time. This variance, and the low overall x-ray flux, causes a large amount of noise in the measured signal. This noise makes it

more challenging to identify the gold absorption edges in the reconstructed attenuation curves.

The mouse kidneys are smaller than the technical phantom. The first kidney was fixed in a cylinder-shaped epoxy setting of a 5mm diameter, and the second kidney was placed in a small test tube which also had a 5mm diameter. To capture the detail in the kidneys, a smaller step size is used in the translation of the object to simulate a strip detector (see section 3.2.2); this step size is 0.15mm. The detector had a 2mm pin-hole collimator; we tried using a smaller pin-hole, but we could not acquire sufficient flux with a smaller pin-hole. Using the 2mm pin-hole degrades the final resolution and introduces more scatter into final projections. Thus, the final projections will have a significant amount of noise and limited spatial resolution.

8.1 Filtered Backprojection

The FBP reconstructed attenuation maps for the mouse kidney fixed in epoxy for selected energy bins are shown in figure 8.1.

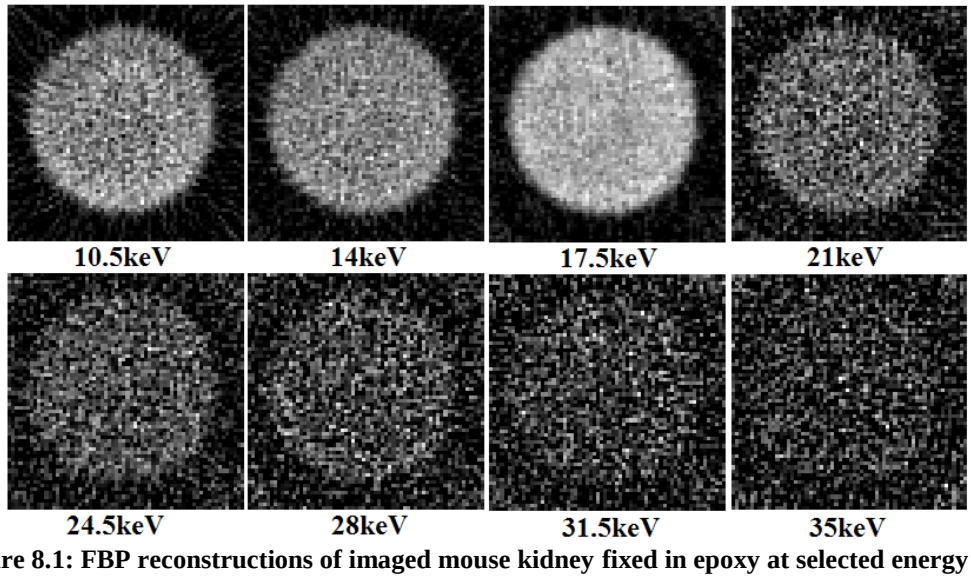

Figure 8.1: FBP reconstructions of imaged mouse kidney fixed in epoxy at selected energy bins

The FBP reconstructed attenuation maps for the mouse kidney placed in a small test tube for selected energy bins are shown in figure 8.2.

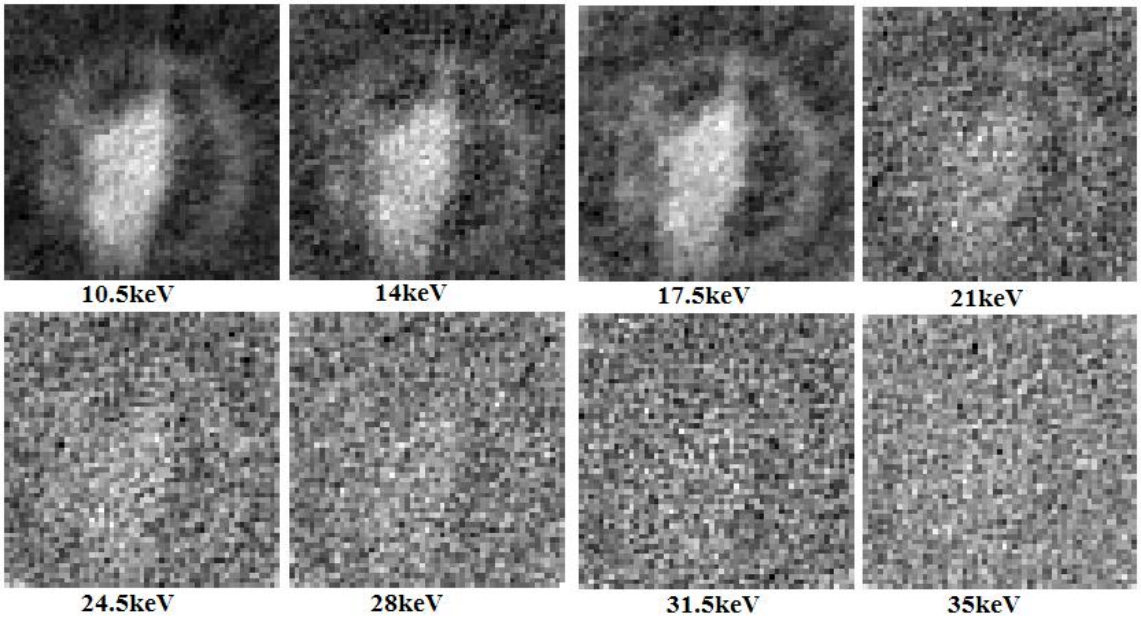

Figure 8.2: FBP reconstructions of imaged mouse kidney in test tube at selected energy bins

There is a significant difference between the initial FBP reconstructions of the two mouse kidneys (comparing figures 8.1 and 8.2). Both sets of reconstructions have a large amount of noise, but there is almost no identifiable spatial variation in the kidney fixed in epoxy (figure 8.1). The shape of the epoxy setting is the only identifiable attenuation distribution. The epoxy has a linear attenuation coefficient almost identical to soft tissue (Hubbel and Seltzer, 1996) and the epoxy has diffused through the entire kidney. Therefore, the first kidney experiment was not useful in identifying any distribution of gold nanoparticles. We only look at the second kidney for the rest of this chapter.

The FBP reconstruction of the second kidney (figure 8.2) has more spatial distribution and the general shape of the kidney and the outside test tube can be identified at lower energies. The noise at higher energy is due to the low photon counts in the detector.

Based on the FBP reconstructions it is not possible to identify any structure within the kidney or any distribution of gold nanoparticles. The attenuation curves for each material in the FBP reconstructions are shown and discussed below in section 8.4.

8.2 Penalized Weighted Least Squares

The initial FBP reconstructions of the mouse kidney (figure 8.2) have a large amount of noise, making it difficult to identify internal kidney structure based on the distribution of attenuation; particularly at energy bins above 20keV. To suppress the noise, the PWLS algorithm (Gonzales and Lalush, 2011) (Chapter 4) was applied. The results, after noise suppression, are shown in figure 8.3.

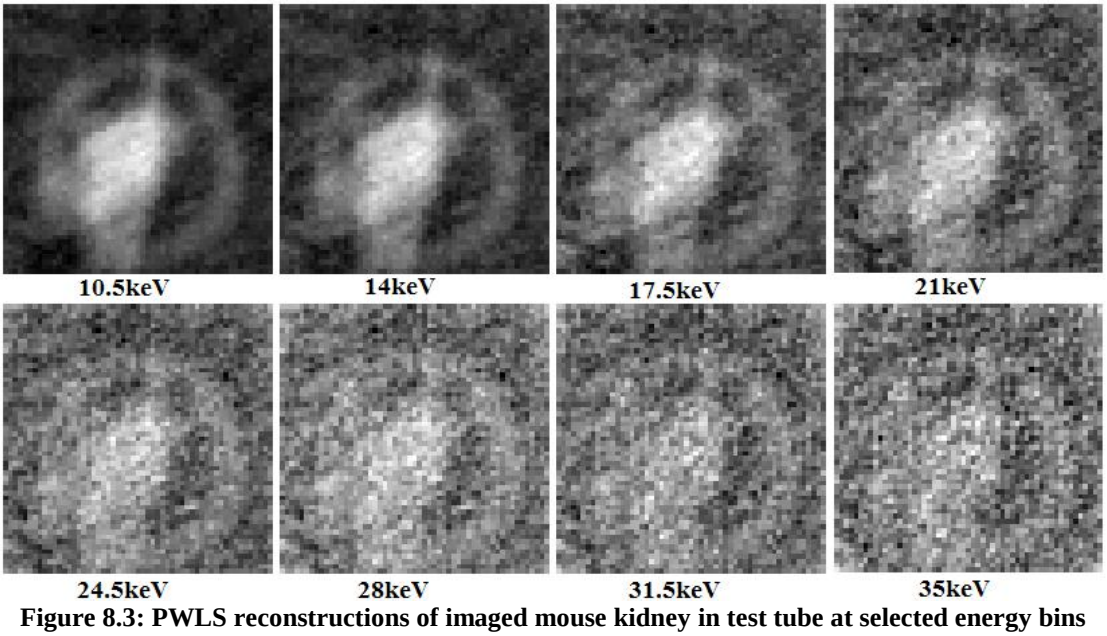

Figure 8.3: PWLS reconstructions of imaged mouse kidney in test tube at selected energy bins

The PWLS algorithm suppresses some of the noise in the FBP (compare figures 8.2 and 8.3); however, there is a significant amount of noise remaining in the reconstructions. The PWLS algorithm uses an average attenuation curve (chapter 4 expression **7**) to smooth the noise along the energy axis. For this experiment, the average attenuation curve is corrupted by the

large amount of noise at higher energies due to low photon flux. To account for this, the attenuation curve for plastic (from the NIST database) was used instead of an average attenuation curve. Using the plastic attenuation curve yields better noise suppression in the plastic and soft-tissue portions of the mouse kidney, but it preserves a little more of the noise in the air around the kidney; this makes the images appear more noisy. Suppressing the noise using a plastic attenuation curve will also suppress any gold absorption edges. However, if the gold attenuation curve is used, the noise is worse and it is still difficult to identify any distribution of gold nanoparticles in the reconstructions. There is a small brighter region in the upper corner of the kidney. It is difficult to identify exactly what this slight increase in estimated attenuation is due to because of the noise in the initial FBP reconstructions. The PWLS smoothes out any absorption edges which could be used to identify gold directly. The attenuation curves for each material in the PWLS reconstructions are shown and discussed below in section 8.4.

8.3 Eigenvector Decomposition

The PWLS algorithm was able to suppress the noise along the energy axis, but it was not able to clearly identify any gold in the reconstructions. The EIGEN method has been shown to preserve the absorption edges better (Chapter 6). The EIGEN method requires prior knowledge of the materials in the imaged object. We assumed the object was composed of plastic, blood, and gold. The plastic was assumed because we placed the kidney in a plastic test tube. The blood was assumed because kidneys are highly vascularized and blood and soft tissue have very similar attenuation curves over the imaged energy range. The gold was assumed because we are looking for gold nanoparticles which were injected into the kidney prior to its removal from the mouse. These three materials are characterized in the NIST

database (Hubbel and Seltzer, 1996) and their attenuation curves are shown in figure 8.4.A. The three attenuation curves are used to form the eigenvector basis functions (figure 8.4.B). The initial FBP reconstructions (figure 8.2) are projected onto these basis functions and the spatial distribution of these basis functions is shown in figure 8.4.C.

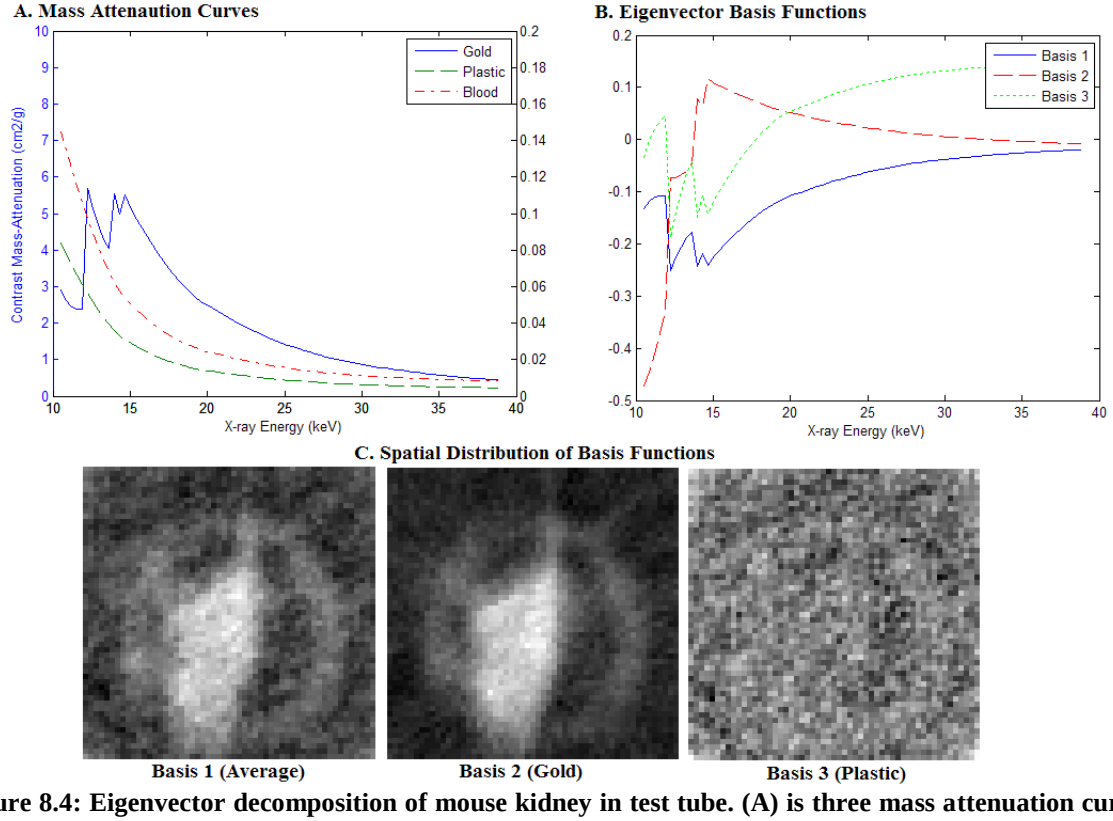

Figure 8.4: Eigenvector decomposition of mouse kidney in test tube. (A) is three mass attenuation curves of gold, blood, and plastic. (B) is basis functions based on the three mass attenuation curves. (C) is the spatial distribution of basis functions.

The three basis functions (figure 8.4.B) define the signal space based on the three mass attenuation curves (figure 8.4.A). The first basis function is an inverse of the average of all three mass attenuation curves. The second basis function is focused on the unique parts of the gold attenuation curve, or what makes the gold attenuation curve different from the average attenuation curve. The third basis function focuses on the plastic attenuation curve. The first spatial distribution (figure 8.4.C basis 1) is the average attenuation map. The second spatial

distribution should be gold; however, it seems to simply focus on the denser materials in the imaged object. The third spatial distribution is the distribution of plastic. The outline of the test tube is identifiable in the third distribution. This is an interesting result because it seems to indicate that the eigenvector method is indentifying a non-contrast agent material well.

The final eigenvector attenuation estimate (figure 8.5) is found by multiplying the spatial variation of each basis function (figure 8.4.C) by the corresponding basis function (figure 8.4.B) and summing the results.

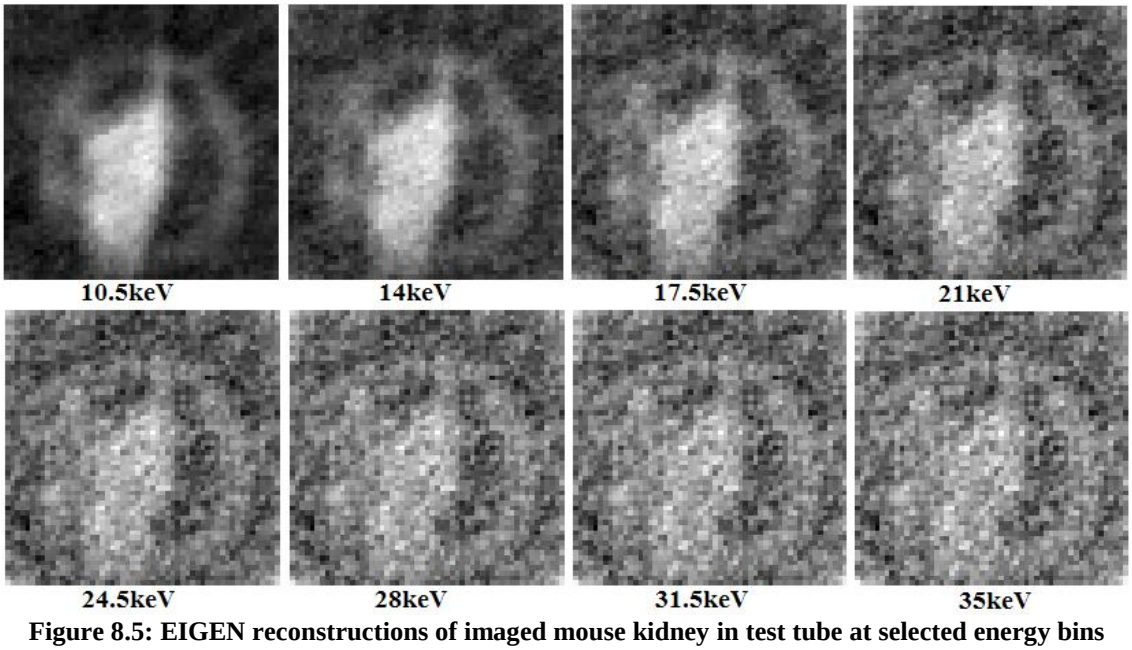

Figure 8.5: EIGEN reconstructions of imaged mouse kidney in test tube at selected energy bins

The EIGEN reconstructions have a large amount of noise remaining. This is not surprising since the PWLS also had a large amount of noise (figure 8.3). This noise is due to the low x-ray flux at energies above 20keV. The attenuation curves for each material in the EIGEN reconstructions are shown and discussed below in section 8.4.

In Chapter, 6 we showed that if PWLS was applied first and then EIGEN was applied to the result we achieve the best noise suppression. A combination of both methods, PWLS then EIGEN, is shown in figure 8.6.

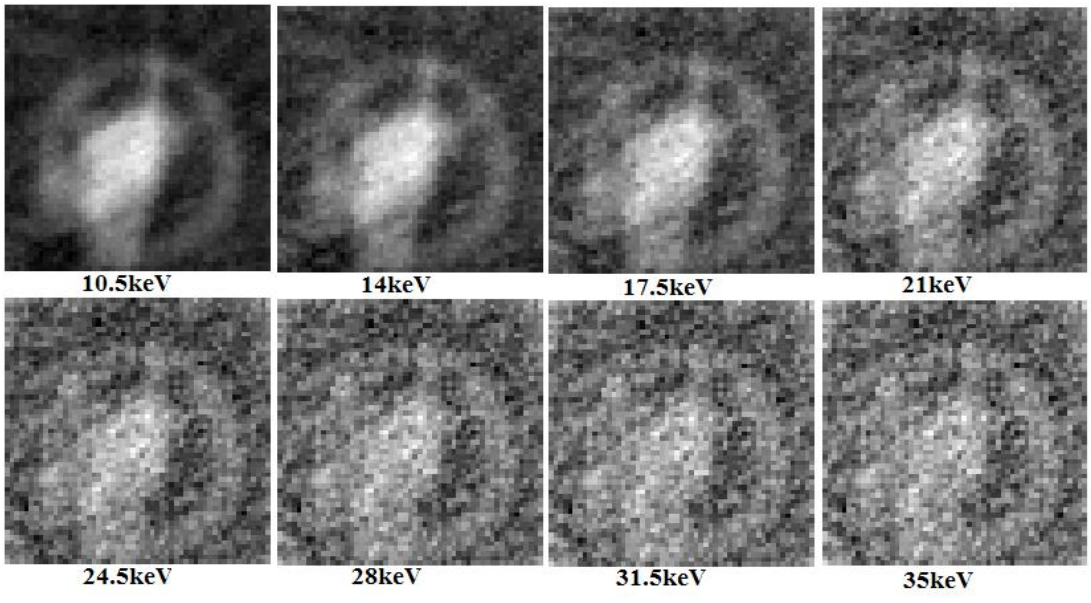

Figure 8.6: PWLS+EIGEN reconstructions of imaged mouse kidney in test tube

The combination of PWLS+EIGEN has a little more noise suppression than either PWLS or EIGEN, but there is still a large amount of noise. This noise is due to a low estimated attenuation at high energies (above 20keV), a low x-ray flux, and a variation in the x-ray flux over time. In both the EIGEN and the combination PWLS+EIGEN (figures 8.5 and 8.6) the basic shape of the mouse kidney and the plastic tube are easily identifiable. However, it is difficult to identify any distribution of gold in the reconstructions. There is one region inside the kidney with an increased attenuation, similar to PWLS (figure 8.3). This region also shows up brighter in the spatial distribution of the gold basis function (figure 8.4.c). However, it does not stand out enough compared to the surrounding material to be clearly identified as gold in the attenuation map reconstructions or basis function distribution.

8.4 Attenuation Curves

Three selected attenuation curves from each reconstruction method are shown in this section (figure 8.7). We decided to show and discuss the attenuation curves from each method together so that it would be easier to directly compare the curves.

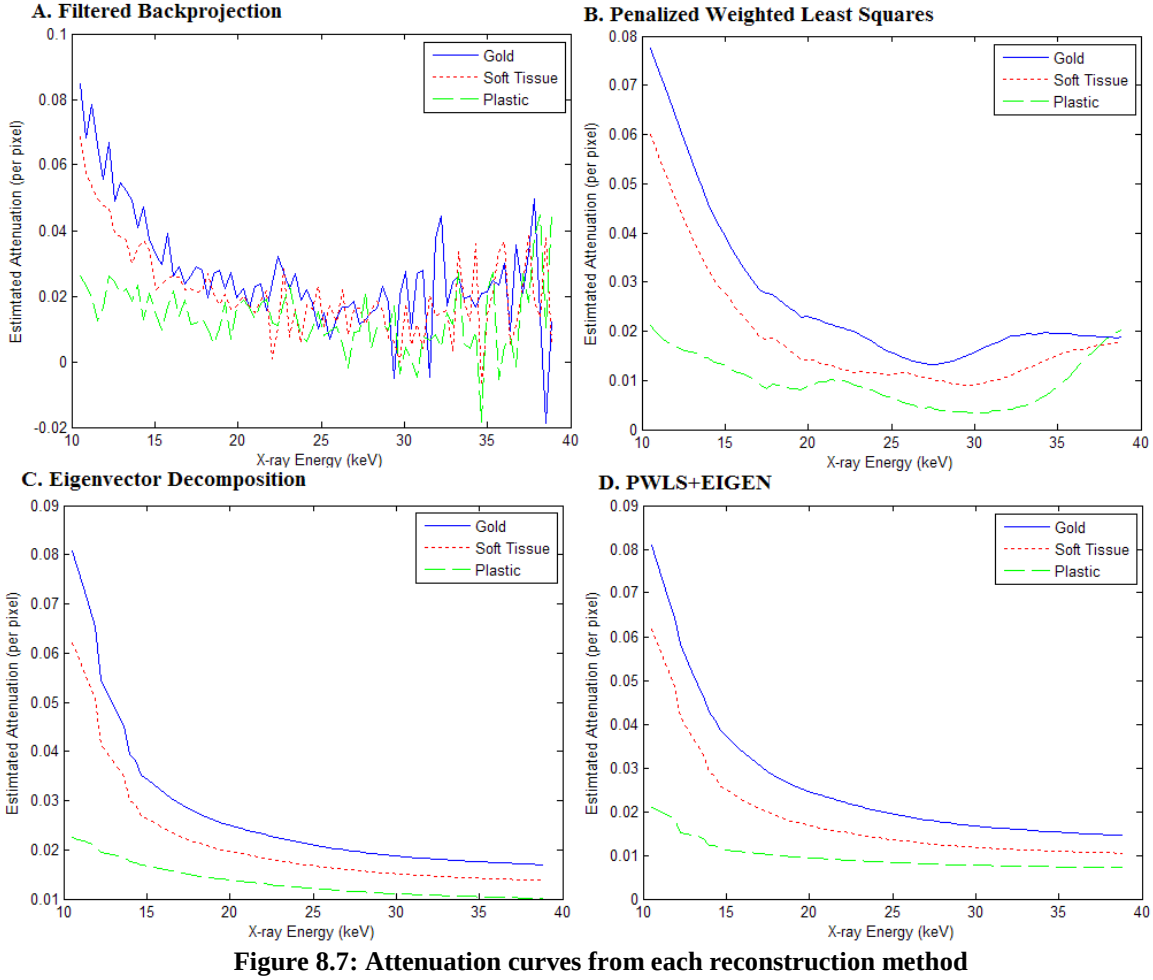

Figure 8.7: Attenuation curves from each reconstruction method

Three attenuation curves are labeled: gold, soft-tissue, and plastic. The plastic attenuation curve comes from a pixel in the outer plastic ring identified in all of the attenuation maps. The gold attenuation curve comes from the brightest region in the kidney. This does not mean the pixel is actually gold; it comes from a region we speculate might contain some gold nanoparticles because it has the largest estimated attenuation at low energies where the gold

absorption edges exist. The soft-tissue attenuation curve comes from the lower corner of the kidney where the estimated attenuation is lowest and seems least likely to contain gold nanoparticles. The same pixel is used from each reconstruction method.

The FBP attenuation curves (figure 8.7.A) show an increasing amount of noise along the energy axis. This follows the results shown in figure 8.2 where the noise dominated the high energy reconstructions. The FBP also shows an increase in attenuation along the energy axis for energy bins above 30keV. This means that there is so much noise in the reconstructions, the estimated attenuation is lost to the noise and the signal seems to increase at high energies.

The PWLS attenuation curves (figure 8.7.B) show a significant degree of noise suppression. There is separation between the three curves along the complete energy axis, indicating that some image contrast is preserved over all energy bins. This follows the results shown in figure 8.3 where the structure of the kidney and plastic wall are identifiable at every energy reconstruction. The increase in attenuation around 30keV seen in the FBP is preserved in the PWLS. This is because the PWLS is tracking with the FBP while attempting to suppress the noise. This may explain the large amount of noise in the PWLS reconstructions (figure 8.3). The gold attenuation curve has no identifiable absorption edges and has no clear indication that it is gold based on the shape of the curve.

The EIGEN attenuation curves (figure 8.7.C) show good noise suppression and have attenuation curves which do not increase at high energies. However, the EIGEN attenuation curves have an oddly shaped initial slope and then become almost identical with a small offset after 15keV. This may be because the algorithm is trying to fit the three known attenuation curves to the noise data (figure 8.4). This odd shape occurs in the region where

gold should be identified; the odd shape prevents us from identifying the gold attenuation curve.

The combination of PWLS+EIGEN attenuation curves (figure 8.7.D) have good noise suppression with high energy curves that look like the EIGEN curves; preventing the increase in attenuation seen in the FBP and PWLS. However, the low energy portion of the curves looks a little better, particularly the gold attenuation curve. The PWLS+EIGEN gold attenuation curve has a single small edge in the gold region. This would correspond to a very small concentration of gold (see chapter 7). However, this edge could be an imposed edge artificially added by the EIGEN method.

The attenuation curves (figure 8.7) demonstrate that both methods are successfully suppressing the noise along the energy axis. This is true even when there is a large amount of spatially distributed noise remaining (figures 8.3, 8.5 and 8.6). The attenuation curves also demonstrate that there is a limit to the improvement provided by the two noise suppression methods. If the initial data is too noisy, we can suppress some of the noise, but we may not be able to use the attenuation curves to clearly identify a material in imaged object.

8.5 Density Estimates

The initial goal of this experiment was to identify gold nanoparticles which were injected into the mouse before the kidney was extracted. We are not able to clearly identify gold based on the attenuation maps (figures 8.3, 8.5 and 8.6) or the spatial distribution of the EIGEN basis functions (figure 8.4.C). Using the combination of both PWLS and EIGEN we found an attenuation curve that might be gold (figure 8.7.D); but that could also be an artificial edge.

We demonstrated in chapter 7 that we can use the attenuation curves to identify the specific concentrations of contrast agents and that the process of identification yielded good contrast segmentation for a single contrast agent (figure 7.18). Therefore, we try to estimate the concentration of gold in each pixel in the reconstructed attenuation map to segment the pixels containing gold (see section 7.3 for an overview of the specific procedure). Previously, we assumed the gold was in solution with water, in the mouse kidney we assume the gold is in solution with blood. The kidney is composed of soft-tissue and blood, which have nearly identical attenuation curves (Hubbell, 1999) Each attenuation curve is calibrated with the sampled water attenuation curve (section 7.1). The spatial distribution of estimated gold in solution with blood is shown in figure 8.8 for all reconstruction methods.

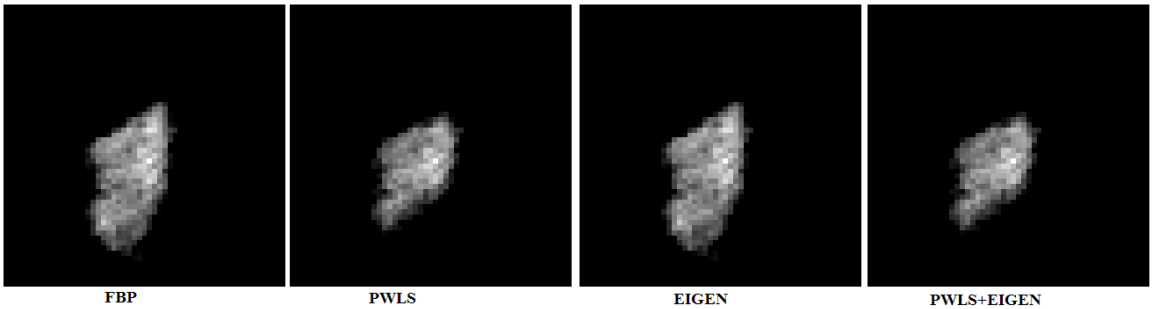

Figure 8.8: Spatial distribution of estimated gold after each noise suppression algorithm

Figure 8.8 graphs the positive estimated concentrations of gold based on the method proposed in section 7.3. All of the estimates correspond with part of or the entire kidney, but none of the plastic tube or surrounding air region. In the FBP and EIGEN methods the estimated gold concentration follows the basic shape of the kidney with the upper right corner appearing brightest. In the PWLS and PWLS+EIGEN graphs, only the upper right hand region shows up. These results seem to indicate that something denser than blood exists in this region of the kidney. This denser material may be gold nanoparticles.

The largest estimated gold concentration, the brightest point in figure 8.8, is approximately 1.3mg/ml of gold nanoparticles in solution with blood. This is a very small concentration, right near the lowest identifiable concentration demonstrated in chapter 7. The actual concentration of gold in the kidney may be too small to accurately estimate given the limitations of the system. To test possibility that gold might exist in the kidney, we compare the pixel's attenuation curve with the true attenuation curve based on the estimate gold concentration (figure 8.9).

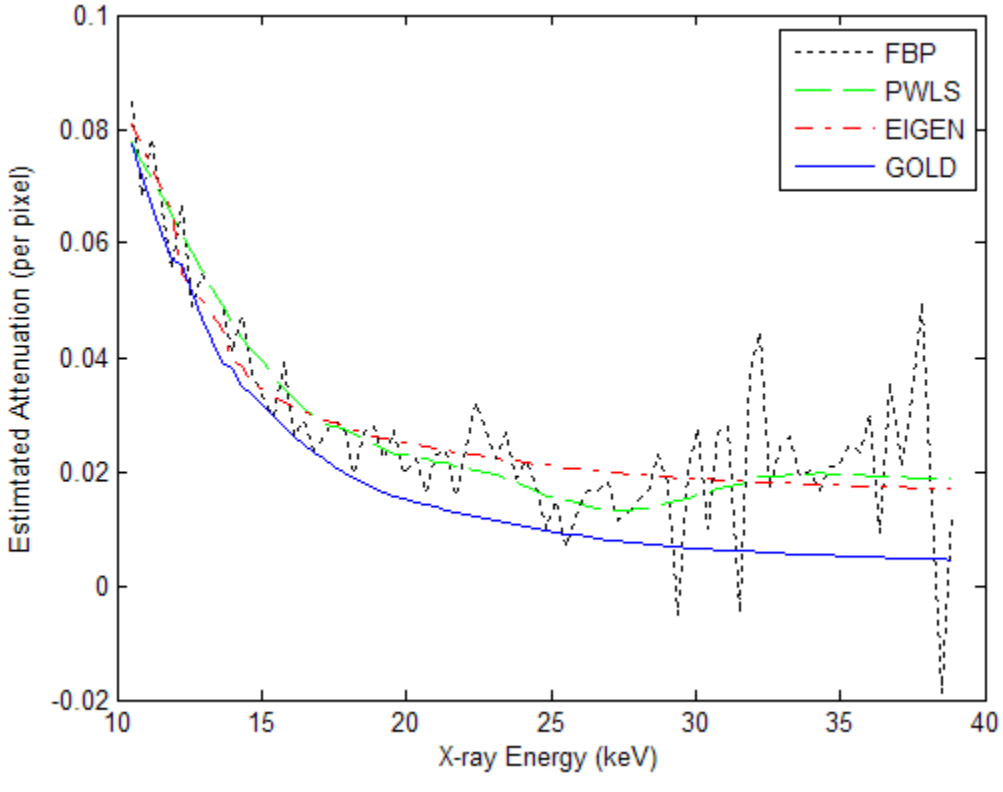

Figure 8.9: Different reconstruction method's attenuation curve compared with True Attenuation Curve from potential gold location in mouse kidney.

The true attenuation curve (labeled gold) is a 1.3mg/ml concentration of gold with blood. The true attenuation curve is close to the estimated attenuation at low energies but falls away from the estimated attenuation curves at higher energies. This follows the results seen in the

attenuation curves (figure 8.7); the estimated attenuation at high energies is corrupted by noise. This is apparent in figure 8.9, the FBP estimated attenuation increases around 30keV; the PWLS follows it as an average and the EIGEN compensates by being a little high in the middle region, but both follow the initial data. Since the initial data is corrupted by noise, the reconstructed attenuation curves do not look like gold above 20keV. The low energy correlation with gold seems to indicate that the dense region in the kidney (figure 8.8) might indeed be a very low concentration of gold nanoparticles.

8.6 Discussion

The goal of this final experiment was to identify gold nanoparticles based on their reconstructed attenuation curves. Two experiments with mouse kidneys were done to identify gold nanoparticles in the kidneys. The first experiment used a kidney fixed in epoxy (figure 8.1). The epoxy saturated the kidney and made it impossible to identify any variation in attenuation in the image, every pixel appeared to be epoxy. The second experiment used a kidney in a plastic test tube (figure 8.2). The kidney was identifiable but the noise and a very low concentration of gold prevented clear separation between gold and kidney (figure 8.9).

The initial data has a large amount of noise at high energies due to a low x-ray flux and small coefficient of attenuation. The imaged object was composed of plastic, soft-tissue, blood, and a possibly a small concentration of gold nanoparticles. All of these materials have small coefficients of attenuation resulting in a smaller signal. This small signal is more susceptible to noise. This noise results in a poor signal sample and a bad initial FBP estimate.

The two noise suppression methods successfully suppress the noise along the energy axis, but both drive the signal toward the FBP without noise (figure 8.9). The initial signal is poorly sampled, so the final noise suppressed signal is still poorly defined and it is difficult to

use the attenuation curves to identify materials in the imaged object (figure 8.6). This is an interesting result because it means there are some basic requirements for the sampling the energy spectrum before the reconstruction methods proposed in this dissertation can be effectively used. Identifying these basic requirements is a good next step for continuing this work.

It is not certain if we have identified gold nanoparticles in the mouse kidney. This seems to be because the concentration of gold may be very small, near 1mg/ml. The gold concentration is below the sensitivity limit of this measurement and processing system. This experiment is a low energy scan, with most of the x-ray energy below 30keV. In chapter 7 we discussed the limitation of identifying gold in the low energies due to the small absorption edges and large amounts of noise and we speculated that moving the anode voltage above the 80keV gold absorption edge may yield a better estimation of gold. It may be that we could identify the gold in the kidney better if we had a system capable of 90keV measurements.

It would be nice to speculate that we have identified some small concentration of gold nanoparticles in this experiment. However, without some other validation all we can say is there is one part of the kidney that is slightly denser than the rest of the kidney. Beyond that, all we can identify is the basic shape of the kidney and the plastic test tube. This is an improvement over the kidney fixed in epoxy, where all we could identify was the shape of the epoxy. Further work is necessary to identify an unknown distribution of gold in a mouse kidney.

8.7 References

Gonzales B. and Lalush D., 2010, "Performance of Reconstruction and Processing Techniques for Dense Full-Spectrum X-ray CT," *Proceedings of the 2010 IEEE Nuclear Science Symposium and Medical Imaging Conference*, Knoxville, TN, M09-131.

Gonzales B. and Lalush D., 2011, "Full-Spectrum CT Reconstruction Using a Weighted Least Squares Algorithm with an Energy-axis Penalty," *IEEE Trans. Med. Imag*., vol. 30, pp. 173-183.

Hubbell J.H. and Seltzer S.M., 1999, "Tables of X-Ray Mass Attenuation Coefficients and Mass Energy-Absorption Coefficients from 1 keVto 20 MeV for Elements Z = 1 to 92 and 48 Additional Substances of Dosimetric Interest", *National Institute of Standards and Technology*, Tech. Rep. 43NANB412756 Available: http://www.physics.nist.gov/PhysRefData/XrayMassCoef/cover.html

9. CONCLUSION

In this dissertation we present a new way to identify elements and compounds in an x-ray CT reconstruction based on their attenuation curves. These attenuation curves can then be used to identify the specific concentration of metallic contrast agents in the imaged object. The identification will lead to increased sensitivity in high-resolution molecular-targeted X-ray imaging of biological subjects. X-ray CT is one of the most ubiquitous imaging modalities. Thus, this increased sensitivity could open new research paths in fields such as drug delivery and cancer research. However, to identify the specific concentration of a contrast agent, the attenuation curve must be densely sampled and the noise along the attenuation curve must be adequately suppressed without significantly reducing the energy-axis resolution.

The work presented in this dissertation is separated into three main parts, each part contributing to the estimation of densely sampled attenuation curves in a CT reconstruction. The first part is the design and implementation of the x-ray CT system and the initial reconstruction into attenuation curves. The second part presents two noise suppression methods which control the noise along the energy axis while preserving the energy axis resolution. The third part is the identification of specific concentrations of different contrast agents based on the shape and intensity of the reconstructed attenuation curves. Each part is briefly discussed in this chapter, with a focus on its novelty and uniqueness. This chapter ends with a discussion of future work and direction for dense spectral CT.

9.1. Novel X-ray CT System

The spectral effects of x-rays on biological tissues and contrast agents are well understood (Christ, 1984) and mass-attenuation curves for some tissues and elements are

publically available (Hubble and Seltzer, 1996). X-ray Computed Tomography (CT) has existed for almost forty years (Hounsfield, 1973) and is one of the most widely used medical imaging modalities (Gonzalez et. al., 2009). Yet spectral CT, incorporating the spectral effects of x-rays into a CT measurement by sampling multiple x-ray energies, has generally been limited to dual-energy CT (Christ, 1984). More recently, some work has been done extending this to six-energy CT (Paulus *et. al*, 1998). In this dissertation we present a spectral CT system (Chapter 3) capable of dense energy sampling. This system is unlike other spectral CT systems because it samples the x-ray spectrum with close to one-hundred energy samples.

The novel x-ray CT system presented in this dissertation uses an x-ray source adapted from a design by Gouhua Cao (Cao et. al., 2009) and a detector purchased from Amptek (AMPTEK), so the physical system is not, by itself, new. The novel part is the way the system was implemented. The Amptek detector samples the entire x-ray spectrum through the imaged object, along all the projection rays. When these sampled spectra are back-projected, the spatial distribution of attenuation (attenuation map) becomes a spatial distribution of attenuation as a function of x-ray energy (attenuation curves). Thus, this system reconstructs an attenuation curve for each pixel (or voxel) in the attenuation map.

Representing the reconstructed attenuation as a collection of spatially distributed attenuation curves is a new approach to CT measurements. Attenuation curves have been identified for specific tissues or elements (Hubble and Seltzer, 1996) and used to visualize the effect of x-ray energy on different tissues (Elbakri and Fessler, 2002), but attenuation curves have not been reconstructed for every pixel in a back-projected attenuation map. Ordinarily, attenuation maps reconstructed at different energies are compared for spatial

variance in attenuation (typical to current spectral CT), which is a good way to identify significant variation due to energy, such as the existence of an absorption edge. However, the reconstructed attenuation curves capture more of the fine detail which separate similar tissues. The reconstructed attenuation curves can then be used to identify specific tissues or contrast agents based on how they match the known mass-attenuation curves from the NIST database.

The new system presented in this dissertation takes a long time, approximately 40 hours for a single slice, to collect tomographic data, sampling the spectrum along a single projection ray for each measurement. A full CT measurement for a single two-dimensional slice requires 80*90 projection ray measurements. Thus, this system is a proof-of-concept rather than a realistic system. The system proves the usefulness of dense spectral measurement sampling and reconstructing those spectra into attenuation curves.

9.2. Noise Suppression Algorithms

Increasing the energy axis resolution by sampling the projected x-ray spectrum with a large number of energy bins also increases the noise distributed along the energy axis. As the number of energy bins increases, the total x-ray flux in each bin decreases, increasing the noise in each sample. However, the principal contribution of the new system is increased energy axis resolution; specifically, the shapes of the attenuation curves. Thus, preserving energy resolution while suppressing the increased noise is important before a system like the one presented in this dissertation could be implemented for clinical applications. In this dissertation, we present two new noise suppression algorithms (Chapters 4 and 5). The first has been published in IEEE Medical Imaging (Gonzales and Lalush, 2011) and the second has been submitted for publication.

The first noise suppression method presented in this dissertation is a Penalized Weighted Least Squares (PWLS) iterative reconstruction algorithm with an energy axis penalty (Chapter 4; Gonzales and Lalush, 2011). The unique part of this algorithm is the energy axis penalty. Typical penalties smooth a pixel to an average defined over a spatial neighborhood around that pixel (Elbakri and Fessler, 2002); this penalty smoothes a pixel to a point on a curve defined by an energy neighborhood. This penalty is unique in two distinct ways: first it smoothes along the energy axis, and second it smoothes to a curve rather than an average.

The PWLS penalty introduces an assumption that all energy bins reconstructed at a single spatial location (pixel or voxel location) must belong to the same attenuation curve, and it smoothes the curve based on general properties of attenuation curves. This system represents the first time densely sampled attenuation curves have been reconstructed from a CT scan. Thus, it has never before been practical to smooth in the energy dimension. If there are only a few energy bins, smoothing along the energy axis may reduce the already limited energy resolution. However, with the increase in energy resolution, smoothing along the energy axis becomes not only practical but also preferable because new information can be introduced. This information is the attenuation curve properties which justify smoothing to a curve rather than an average. These properties ensure the preservation of energy resolution, even while suppressing most of the noise. This novel approach to noise suppression will grow in significance as the number of detector energy bins is increased.

The second noise suppression method presented in this dissertation is an Eigenvector Decomposition filtering method (EIGEN) (Chapter 5). This creates a set of orthogonal basis functions, based on the known attenuation curves, which are used to define the signal and

separate it from the noise. The unique part of this method is the way the basis functions are defined. The basis functions are the eigenvectors of a correlation matrix composed of the known attenuation curves in the imaged object. This is similar to a singular value decomposition (SVD) approach (Vozalis and Margaritis, 2005), where the attenuation curves are used as the known signal.

In the EIGEN method, attenuation curves from the NIST database are used to form the basis functions. This means that all the relevant information about the size and shape of each element in the imaged object (the attenuation curves) is preserved in the final noise suppression. This is only possible if the energy resolution is sufficient, similar to the PWLS method. The number of energy bins must be greater than or equal to the number of elements, plus any unique traits belonging to these elements' attenuation curves, specifically absorption edges.

In this dissertation, both noise suppression algorithms have been shown to significantly improve the signal-to-noise ratio on data collected from the new CT system. Both of these algorithms are also shown to preserve key energy axis information; both are able to differentiate between two contrast agents in the same object based on the differences between these two agents' attenuation curves. The two noise suppression algorithms present two unique new ways to incorporate known information about the energy axis to suppress the noise along the axis while preserving the energy resolution. Both of these methods are only practical when a densely sampled attenuation curve has been reconstructed. Both reduce the limiting factor noise places on future energy resolving x-ray systems. Overall, these algorithms provide a guideline for energy resolving CT systems, introducing the idea that the energy axis can be used to suppress the noise.

9.3. Identifying the Concentration of Contrast Agents

The new system presented in this dissertation is capable of reconstructing the attenuation curve for each pixel in the attenuation map. The two noise suppression algorithms suppress the noise along the energy axis, while preserving the energy resolution. The final step is using the attenuation curves to identify specific elements or compounds and their concentrations in the imaged object (Chapter 7). This entire step, for x-ray CT, is unique to densely sampled x-ray CT. Typically CT identifies elements or compounds by their reconstructed attenuation coefficient and physical density (Bazalova *et. al.*, 2008). In this new system, we also identify elements or compounds based on the shape and size of their reconstructed attenuation curves.

To identify an element or compound by the shape and size of its attenuation curve, the attenuation curve must be densely sampled and there cannot be much noise along the curve. The new system satisfies the first requirement and the noise suppression algorithms satisfy the second. Previous spectral CT systems have used properties of attenuation curves to identify a specific element or compound. Dual energy CT commonly uses the existence of an absorption edge to identify a contrast agent or the difference between bone and soft-tissue attenuation curves (Bazalova *et. al.*, 2008). However, using a densely sampled attenuation curve to identify multiple elements or compounds in the same image object is only possible when imaging with a system similar to the one presented in this dissertation.

The reconstructed attenuation curves can also be used to identify the specific concentration of a metallic contrast agent in an imaged object (Chapter 7). This represents an exciting step in x-ray CT research. Current CT systems estimate the attenuation based on how physically dense the elements or compounds in the imaged object are (Chantler, 2000).

Different concentrations of a contrast agent will make the attenuation appear with different densities, but it is hard to quantify the exact concentration of these contrast agents based on these estimates. We clearly demonstrate the accurate identification of contrast concentration of multiple concentrations of both iodine and gold nanoparticle contrast agents in solution with water (Sections 7.4.2.1 and 7.4.2.2 respectively).

We end with showing how the energy resolution relates to the accuracy of the concentration estimates. As the energy resolution increases, the accuracy of the estimations is shown to increase. We show that for iodine in the 10-40keV energy range, only ten energy samples are required. We show that for gold nanoparticles in the 10-40keV energy range, twenty energy samples are required. I also show that as energy samples increase beyond this, the accuracy of the estimate concentrations continues to improve slightly. This justifies continuing x-ray detector research to create fast photon counting strip detectors capable of sampling the energy axis with at least ten energy bins. As these detectors are developed, it will become possible to accurately estimate the concentration of multiple contrast agents in a biological subject.

9.4. Future Direction

The x-ray system presented in Chapter 3 is limited to a 50kV anode voltage. This limit is based on the high-voltage feed through mounted on the vacuum chamber (figure 3.11). This limits the x-ray range to less than half the typical medical range of 15kV-150kV (Valais et.al, 2007). Increasing this voltage limit by replacing the high-voltage feed-through would allow us to measure more of the attenuation curve and to investigate the effect of energy sampling on larger objects, which requires more flux and energy to image. It may be that longer attenuation curves classify specific tissue better, given that more of the overall

shape of the attenuation curve can be estimated. This would be particularly true for dense biological tissues such as bone, which has not been investigated in this dissertation. If the anode voltage is above 90kV, the gold absorption edge at 80keV would be included. This would improve gold identification and may improve the estimated concentration of gold.

The x-ray source in the system was replaced near the end of this research with a new one designed by Gouhua Cao (Section 3.3). This source was never fully optimized to reduce the slight flux variation over time, which increased the noise (Section 7.4). Over the course of an experiment, the source experiences arcs, sometimes large enough to trip the voltage sources. Addressing these arcs and finding a stable cathode voltage to run an experiment at slightly higher flux needs to be completed before another experiment is done with this system. Stabilizing the source and/or increasing anode voltage are simple changes which will further demonstrate and test the significance of reconstructing attenuation curves rather than only attenuation maps.

Optimizing the source and changing the anode voltages are important steps to improving the system design. However, the system still takes a long time to create a single slice through the imaged object. This is due to the Amptek detector, which is a single pixel detector which takes five to ten seconds per measurement. To successfully reconstruct attenuation curves from a biological subject, a faster multi-element detector is required. This requires an improvement in existing detector technology which currently only measures six energy bins. In chapter 7, it was shown that at least ten energy bins are required to accurately sample an attenuation curve for a 10-45keV energy range. The work in this dissertation proves the usefulness of spectral CT and justifies continued research in energy-resolving x-ray detectors.

The two noise suppression algorithms have been well-tested and compared (Chapters 4, 5, and 6). These two algorithms have been implemented with no spatial smoothing. This was done to clearly demonstrate that all noise suppression only came from the energy axis smoothing. However, in the future it would be useful to add spatial smoothing to both algorithms to further improve the overall noise suppression. This spatial smoothing can be done by applying a spatial filter to the result of each algorithm. Spatial smoothing could also be incorporated into the initial assumptions of each algorithm.

The PWLS penalty could be modified to incorporate a spatial penalty. This could be as an independent penalty or as part of the energy penalty. An independent penalty would be a typical spatial smoothing penalty added to the PWLS. This would simply be another penalty added to each iteration. Adding a spatial penalty to the energy penalty means smoothing attenuation curves to a spatially varying set of curves. The EIGEN method could be done first to estimate the distribution of materials in the object and then the ideal attenuation curves could be used for each region. This might improve the overall energy axis resolution a little. Another way to add a spatial penalty to the energy penalty is to run the PWLS for one complete iteration and then segment the image based on absorption edges. If an absorption edge exists, the contrast agent attenuation curve could be used for those specific attenuation curves and the average curve for the rest. These are just two ideas of how to incorporate a spatial penalty into the PWLS. More work is required to investigate the effect of each method on the data.

The EIGEN method could be modified by applying a spatial penalty prior to implementation or to incorporate some spatial information into the algorithm. Implementing a spatial penalty prior is similar to the PWLS+EIGEN (shown in Section 6.4). This would

simply smooth the attenuation maps a little before the EIGEN method is applied and is not really all that new. Incorporating spatial information into the algorithm has to do with the way the initial correlation matrix is defined (expression 5.4). Currently, it is assumed that all elements are equally likely and can mix at any pixel location. This assumption could be changed to indicate certain elements cannot mix, such as gold and iodine in the original phantom. This might be a reasonable assumption given it is unlikely that bone and an iodine contrast agent would mix in a patient CT. However, this sort of spatial information requires more prior knowledge and may be difficult to actually implement.

The estimated concentrations of different contrast agents were shown to be accurate using the reconstructed attenuation curves (Chapter 7). This was done with an acrylic phantom and different concentrations of contrast agents in well-defined and separated regions. In the future it will be important to see how other dense materials affect the estimation of concentration. A new contrast phantom should be designed to better model a real subject. This phantom should allow for dense materials (either bone or something that looks like bone) to be included. This new system should have no problem separating the bone and contrast agent based on the attenuation curves. Once the bone and contrast agent are separated, the concentration of contrast can be estimated.

In the future it would also be interesting to investigate the effect of two contrast agents mixed in the same solution. This would be a good example of the unique benefits of using the attenuation curve to identify and quantify the contrast agents. If the region around the absorption edge was used, rather than the whole curve, it seems likely that an accurate estimate of the concentration of each contrast agent in the solution can be made (Section 7.3). However, if gold were mixed with iodine this would require imaging the system with an

anode voltage above 90kV to capture the gold 80keV absorption edge. The iodine experiment (Section 7.4.2.1) showed how accurate using a single absorption edge was compared with the multiple, poorly imaged, low-energy gold edge. It seems reasonable to assume that the same accuracy can be achieved with the higher energy gold absorption edge. If this is the case, the size of this edge can be used to estimate the concentrations of each in solution.

It was shown that in the 10-40keV energy range, the attenuation curves were preserved with 10 energy bins. In the future, the anode voltage should be moved to 100kV or 120kV to see how many energy bins are required to accurately estimate concentrations and to preserve the specific shape of attenuation curves. It was speculated that it was the density, rather than number, of energy bins which made the difference. This should be tested in the future.

Along with all this proposed work, we feel it is important to simply collect more data with the present system. This takes a great deal of time, due to the Amptek detector, but as the amount of data increases, the effect of dense energy sampling will be better understood. The two noise suppression algorithms and concentration estimations developed after we began taking data with this new system. As more data is acquired, new ideas about the nature and possibility of spectral CT will become apparent. As new x-ray energy differentiating detectors are developed, this information will be very useful because it represents a spectral sampling which is much denser than any detector.

9.5. Final Thoughts

The work presented in this dissertation is a detailed investigation into a densely sampled full spectrum x-ray CT. The uniquely dense spectral samples have allowed us to propose two new noise suppression algorithms and to clearly demonstrate the potential in

energy-differentiating CT. We show that it is possible to clearly differentiate between two contrast agents in a single scan and to quantify the specific concentration of those contrast agents. This work will lead to increased sensitivity in high-resolution molecular-targeted X-ray imaging of biological subjects. This increase justifies further x-ray detector development and we foresee a future where the noise suppression algorithms presented here and the concentration estimations are used in a clinical setting.

9.6. References

AMPTEK detector XR-100CT, product information available at: http://www.amptek.com/xr100cr.html

Bazalova M., Carrier J.F., Beaulieu L. and Verhaegen F., 2008, "Tissue segmentation in Monte Carlo treatment planning: a simulation study using dual-energy CT images," *Radiotherapy and Oncology*, vol. 86, pp. 93-98.

Chantler C.T., 2000, "Detailed Tabulation of Atomic form Factors, Photoelectric Absorption and Scattering Cross Sections, and Mass Attenuation Coefficients in the Vicinity of Absorption edges in Soft x-ray (Z=30-36, Z=60-89, E=0.1 KeV-10KeV, addressing Convergence Issues of Earlier Work," *Journal of Physical Chemistry*, vol. 29, No. 4.

Cao G., Lee Y.Z., Peng R., Liu Z., Rajaram R., Calderon-Colon X., An L., Phan T., Sultana S., Lalush D.L., Lu J.P., and Zhou O., "A dynamic micro-CT scanner based on carbon nanotube field emission source," Phys. Med. Bio., vol. 54, pp. 2323-2340, 2009.

Christ G., 1984, Exact treatment of dual-energy method in CT using polyenergtic x-ray spectra, Phys. Med. Biol., vol 29, pp. 1501-1510.

Elbakri I. and Fessler J., 2002, "Statistical image reconstruction for polyenergetic X-ray computed tomography," IEEE Trans. Med. Imag., vol. 21, no. 2, pp. 89-99.

Gonzales B. and Lalush D., "Full-Spectrum CT Reconstruction Using a Weighted Least Squares Algorithm with an Energy-axis Penalty," IEEE Trans. Med. Imag., In Press.

Gonzalez A.B., Mahesh M., Kim K.P., Bhargavan M, Lewis R., Mettler F., and Land C., 2009, "Projected cancer risks from computed tomographic scans performed in the United States in 2007," Ach. Intern. Med., vol. 169, pp. 2071-2077.

Hubbell J.H. and Seltzer S.M., 1996, Tables of X-Ray Mass Attenuation Coefficients and Mass Energy-Absorption Coefficients from 1 keVto 20 MeV for Elements

Z = 1 to 92 and 48 Additional Substances of Dosimetric Interest, National Institute of Standards and Technology, Tech. Rep. 43NANB412756 Available: http://www.physics.nist.gov/PhysRefData/XrayMassCoef/cover.html

Hounsfield G.N., 1973, "Computerized transverse axial scanning (tomography).1. description of system," British Journal of Radiology, vol. 46, pp. 1016-1022.

Paulus M., Sari-Sarraf H., Gleason S., Behel J., Thompson L. and Allen W., 1998, "A new X-ray computed tomography system for laboratory mouse imaging," IEEE Trans. Nuclear Science, vol. 2, pp. 1259-1263.

Valais I.G., David S., Michail C., 2007, Nomicos C.D., Panayiotakis G.S., and Kandarakis I.S., "Comparative evaluation of single crystal scintillators under x-ray imaging conditions," presented at 4th International Conference on Imaging Technologies in Biomedical Sciences, Sept.

Vozalis M.G. and Margaritis K.G., 2005, "Applying SVD on Item-based Filtering," IEEE Proceedings on Intelligent system design and applications, pp. 1-6, 2005.